# SORPTION OF RADIONUCLIDES ON GLAUCONITE OF THE NEOGENE

Yaana BRUNEEL

Supervisors:

Prof. E. Smolders
Dr. L. Van Laer

Members of the
Examination Committee:

Prof. A. Maes (chair)
Prof. J. Elsen
Dr. R. Adriaens
Prof. R. Swennen
Prof. C. Kirschhock
Dr. N. Maes

Dissertation presented in partial fulfilment of the requirements for the degree of Doctor of Bioscience Engineering

May 2021

Doctoraatsproefschrift nr. 1702 aan de faculteit Bio-ingenieurswetenschappen van de KU Leuven



Uitgegeven in eigen beheer, Yaana Bruneel, Alfons Roelandtsstraat 8 bus 4,
3010 Kessel-Lo

## Acknowledgements

Dear reader, thank you for your interest in my work. I hope this booklet can carry out the knowledge I gathered during this thesis until long after my defence. With this thesis I conclude more than four years of PhD work, work that has given me great pleasure, curiosity for research and many sleepless nights. I had the honour of working among a wonderful group of people both in the Soil and Water management group at KU Leuven and the Waste and disposal group of SCK CEN in Mol. I have had the opportunity to learn, grow and challenge myself during this PhD. However, you wouldn't be reading this thesis without the help of so many people on my way.

First I want to thank prof. Dr. Erik Smolders, my promotor in this work and Dr. Liesbeth, my mentor. Erik, it was a privilege to have you as my promotor. I have had a wonderful time as part of your group. Your endless amount of new ideas and enthusiasm kept me inspired and motivated for every part of the PhD. Thank you for the advice, for making time discuss the experimental data, to listen to the problems I couldn't find a solution to and for reading all my reports and papers so thoroughly. You gave me freedom to find my way in research and helped me see when to let go of the details. Liesbeth, thank you for the wonderful time together, for being with me every step of this PhD. Thank you for always making time for me and for reading every iteration of the reports, articles and thesis that were written in these last four years. I have learned a lot from you and I hope our collaboration does not end here.

I would like to thank Dr. Michèle Coeck and the scientific counsel of the Academy at the Belgian nuclear research centre (SCK CEN) to give me the opportunity to start this PhD. I would like thank the chairman and jury members of my examination committee for their time and effort to improve my manuscript to finalise this PhD. Thank you Dr. Stéphane Brassinnes from ONDRAF/NIRAS for the great collaboration on this PhD project and ONDRAF/NIRAS for the financial support for this PhD topic. At SCK CEN I would like to thank Dr. Christophe Bruggeman en Dr. Norbert Maes for including me in their research group and sharing their suggestions and advise for the project. My PhD labwork would have been much harder without the support, analyses and guidance by the technical staff at all the different labs where part of my labwork took place (lab from the waste & disposal at SCK CEN, the Soil and Water lab and the mineralogy lab at KU Leuven). Thank you Marc, Serge, Frank, Tom, Dorien, Anneleen, Kristin, Karlien, Karla, Dries, Elvira and Nancy. Also a great thanks to my master students, Stef, Hedwig and Karen for catching the enthusiasm for the topic (sometimes temporary) and conducting experiments with me. I want to thank Dr. Diederik Jacques for the help with the reactive transport modelling.

To my colleagues in Mol, Nancy, Yana, Yulia, Anna, Jente, Min, Laurent, Lander, Antoine, Gabriel & Saeid, and Leuven, Charlotte, Ruth, Claudia, Siyao, Mieke, Kris, Toon & Maarten thank you for all those talks over lunch, laughs in between work, the running, the shared frustration and joy in the lab and

the friendships that remain after this common PhD adventure. Dr. Wanna, I am lucky to have you as a friend.

A special gratitude goes to my family. Dearest Moeke, Vake en Hilke, thank you for the warm nest I was born in, for giving me the opportunity to study and for supporting me all these years. Without you, without the summers in the tent all over the world, without the international visitors as part of our day to day life I would not be the person I am today. Thank you for having the confidence in me I often didn't have myself and for creating the space I can still call home today. Hilke, I look up to you, my little sister. I admire your mind set and mental power to keep going even if every cell in your body works against you. Compared to you my life is only sun and rainbows. Thank you for being there for me among all of it. Anders and Susanne, my extra parents, thank you for offering me a warm home with good food to escape to whenever I need (or can). Thank you for listening, for always being there for me and for helping me find my way. Peter, my Love, I could not have done it without you. Thank you for supporting me through grumpy mornings and stressful days, to help me understand it will all be ok. I look forward to what the future holds for us.

## Summary

The safe disposal of radioactive waste is one of the key aspects in the risk assessment of nuclear energy. A safe disposal requires that the long-term dispersion of the radionuclides (RN) from the waste to the environment is minimal. Disposal facilities are designed to contain the radioactive waste by engineered and natural barriers without the intention of retrieval. The assessment of RN dispersal requires a thorough understanding of the processes and mechanisms controlling the radionuclide transport around these barriers. This PhD is dedicated to a specific aspect of such assessments, i.e. the sorption of two medium-lived radionuclides, i.e. caesium-137 ($^{137}Cs$) and strontium-90 ($^{90}Sr$) on glauconite sands of the Paleogene and Neogene formations (Fm) in Belgium. Glauconite sands are not considered as a primary host for radioactive waste disposal in geological formations. The sands are highly permeable and facilitate high pore water flow rates. Glauconite sand is, however, one of the options for the complementary sorption sink below the surface disposal at the Dessel site in Belgium for the short-lived and low-level waste (Cat-A). For the high-level and/or long-lived radioactive waste (Cat-B & C), a geological disposal is considered. Host rocks that might qualify for long-term disposal are poorly indurated clay (Boom Clay or Ypresian clays) 200 to 600 m below the surface. Both Boom Clay and Ypresian clays are enclosed in glauconite rich sands or silts.

Glauconite is an iron rich clay mineral formed in marine sediments and occurs mainly as coarse pellets, sizing up to 1 mm, and, to a smaller extent, as minerals in the clay size fraction (< 2 µm). The term glauconite refers to a mineral composition (end-member) similar in structure as illite. Glauconite sands are the dominant lithology in the Neogene succession with often high pelletal glauconite content (20-30 %). The glauconite is characterised by a dark green well rounded pellet, resembling sand rather than clay. In this thesis the term glauconite is used for the description of the green grains.

First, the sorption of $^{137}Cs^{+}$ on glauconite was characterised. Glauconite sands were collected from several drilling cores in the Campine subsurface and from outcrops in the Hageland region, the latter representing weathered and oxidised samples. The radiocaesium interception potential (RIP) on glauconite sands was measured in batch in a background solution of 0.1 M calcium ($Ca^{2+}$) and 0.5 mM potassium ($K^{+}$). The log transformed $^{137}Cs$ distribution coefficient ($K_D$, L kg$^{1}$) after 30 days reaction ranged 3.4-4.3, surprisingly high for a sand formation and close to the $K_D$ of $^{137}Cs^{+}$on the Boom Clay (3.5). Variations in the RIP among the sands can be explained by the glauconite content and the cation exchange capacity (CEC). Isolated glauconite fractions have $^{137}Cs$ sorption potentials that are a factor of about 2 smaller than the reference Illite du Puy. A comparison of intact and milled pellets shows that the pellets reduce the sorption rate and sorption potential, suggesting that not all $^{137}Cs^{+}$ binding sites inside the pellets are accessible. In strongly weathered pellets, the cracks in the grain surface increase the accessibility of the inner sorption sites which increases the rate and extent of $^{137}Cs$ sorption. Sorption equilibrium on intact glauconite sands is reached after 1 month, though slow reactions lead to an 1.6-

1.8 fold increase in the $K_D$ between equilibrium and 8.5 months. A desorption experiment showed that $^{137}Cs$ sorption is not fully reversible.

The similarity of $Cs^+$ sorption on isolated glauconite fractions to illite suggests similar sorption sites characteristics. Caesium sorption on illite can be described by a three-site exchange model: frayed edge sites (FES) type I, FES type II sites and planar sites. The ammonium ($NH_4$) - K selectivity on the FES was determined as a fingerprint for the highly selective FES. The selectivity ranged between 3.8-5.0 for three glauconite sands, in the range reported for illite and clay formations. This suggests that the glauconite sands have highly selective sites that bind $^{137}Cs^+$ with similar properties as in illite. The $Cs^+$ sorption isotherms for glauconite sands were determined between $10^{-8}$ and $10^{-4}$ M $Cs^+$ in the equilibrium solution. The experimental isotherms were fitted with a three-site model. The FES type I capacities of the sands ranged from 0.04 to 0.06 % of the CEC (versus 0.25 % for illite) and the FES type II site from 1.7 to 2.2 % (versus 20 % for illite). The difference in the FES fractions between illite and glauconite is attributed to the smectite content on glauconite. Smectite interlayers increases the CEC and decreases the fractions of FES type I and type II sites.

Glauconite has a RIP that is comparable to illite, suggesting that glauconite containing sands may be an effective geological barrier for radiocaesium. However, the combination of the presence of glauconite as coarse pellets (~ 0.25 mm diameter) and slow sorption indicates considerable sorption non-equilibrium may occur during reactive transport in these permeable sands. A breakthrough (BT) experiment was set up with 13 saturated columns at variable flow rates. The columns, all filled with the same Diest Fm glauconite sand, were leached with $10^{-6}$ M $Cs^+$ for 154 days. The BT was observed in the columns with the higher flow rates after 890-1170 pore volumes. Breakthrough at smaller cumulative pore volume was only observed in the column with the highest flow rate (2.4 m $d^{-1}$), indicating chemical non-equilibrium, but these flow rates are unrealistically large for the Neogene and Paleogene Fm. The BT curves were modelled with HP1 (Hydrus-PhreeqC), based on batch sorption data obtained at 90 days and assuming local reaction equilibrium. The BT curves were well predicted with this model, corroborating local equilibrium unless at the highest flow rates. Caesium sorption on highly permeable glauconite sands is sufficiently fast to delay breakthrough in realistic flow rates for the Neogene and Paleogene Fm (Diest, Berchem and Voort Fm).

The adsorption of radiostrontium ($^{85}Sr^{2+}$) was determined for 45 subsurface and naturally weathered (surface) glauconite sands. The $K_D$ for $^{85}Sr^{2+}$ in a background solution of 1 mM $Ca^{2+}$ ranged 23-65 L $kg^{-1}$ for the intact sands and 50-144 L $kg^{-1}$ for the glauconite fractions. Sorption equilibrium was reached within 48 hours. The $K_D$ values for intact and milled pellets are nearly identical, i.e. the sorption of $^{85}Sr$ is not hindered by the glauconite pellet in contrast to observations for $^{137}Cs$. The $K_D$ values corresponded well with predictions of the $K_D$ by two existing models calibrated to soils based on the CEC. It is

concluded that glauconite sands have a suitably high retention of radiostrontium and the sorption strength is in line with that of other geological barriers when judged from the CEC.

An accelerate weathering study was performed to evaluate how weathering of glauconite can affect the radiocaesium ($^{137}Cs$) retention given that redox or pH dependent transformation may change the Fe speciation, leaching of K and, hence, affect clay mineralogy. Three different glauconite sands were artificially weathered at ambient temperature during 27 months in four different scenarios: continuously purged with oxygen (oxidation), under cement water at pH = 13 in the absence of oxygen, in an acid solution of pH = 4 and in an anoxic setup at pH = 7 under $N_2$ atmosphere. The CEC increased by factors 1.1-1.2 under alkaline conditions whereas it decreased by similar factors in the oxic and acid samples. The $Fe^{2+}$ to $Fe_{tot}$ ratio doubled under anoxic conditions and remained similar in the other treatments. The RIP enhanced by factor 1.1-1.3 under alkaline conditions consistent with the changes in CEC, however no decreases in RIP were detected in the oxic samples. These analysis suggests that glauconite sand is not highly sensitive to weathering under these conditions and that the effects on the radiocaesium sorption are marginal within the conditions used here.

To summarise, this study shows that the glauconite sands exhibit strong sorption potential for radiocaesium and radiostrontium. The $^{137}Cs$ sorption potential of a sand with 25-30% glauconite appeared surprisingly as high as that of Boom Clay with 30-60 % clay, which is one of the candidate hosts for category B and C waste. From the research work performed in this PhD, it is concluded that glauconite can act as an additional sorption sink for Cs and Sr.

## Samenvatting

De veilige berging van radioactief afval is een belangrijk aspect bij de risico analyse van kernenergie. Een bergingsinstallatie is ontworpen om radioactief afval af te zonderen van mens en milieu door middel van kunstmatige en natuurlijke barrières. Laag- en middelactief afval (Cat-A) kunnen in een oppervlakte berging veilig bewaard worden. Voor hoogradioactief en/of langlevend afval (Cat-B & C) is een geologische berging de beste optie. Hiervoor bestuderen we de processen en mechanismen die de migratie van radionucliden (RN) door de barrières en het milieu bepalen. Dit doctoraat is gewijd aan een specifiek aspect van dergelijke studies, namelijk de sorptie van twee middellanglevende radionucliden, namelijk caesium-137 ($^{137}Cs^{+}$) en strontium-90 ($^{90}Sr^{2+}$) op glauconiet zand van de Cenozoïsche (Paleogeen en Neogeen) formaties (Fm) in België.

De glauconiet zanden zijn geen optie voor geologische berging. De zanden zijn zeer doorlatend waardoor de hoge poriewater stroomsnelheden mogelijk zijn en voor snel transport van radionucliden kunnen zorgen. Glauconiet zand kan echter gebruikt worden als extra barrière onder een oppervlakteberging. Bovendien is glauconiet zand aanwezig in de nabijheid van enkele formaties die in aanmerking komen voor geologische berging (Boomse Klei of Ieperse klei). Glauconiet is een ijzerrijk kleimineraal dat gevormd wordt in mariene sedimenten en zowel voorkomt als grove korrels, met een grootte tot 1 mm, en, in mindere mate, als mineralen in de kleifractie (< 2 µm). De donkergroene goed afgeronde glauconiet korrels lijken meer op zand dan op klei, maar de structuur van glauconiet is vergelijkbaar met illiet. Glauconiet zanden vormen de dominante lithologie in de Neogeen successie met vaak een hoog glauconiet gehalte (20-30 %).

In een eerste stap werd het $^{137}Cs$ sorptie potentiaal bepaald. Glauconiet zand werd verzameld uit verschillende boorkernen uit de regio Kempen en uit ontsluitingen in het Hageland, waarbij de laatste verweerde en geoxideerde monsters vertegenwoordigden. De radiocaesium-interceptiepotentiaal (RIP) op werd in batch gemeten in een achtergrondoplossing van 0,1 M calcium ($Ca^{2+}$) en 0,5 mM kalium ($K^{+}$). De log-getransformeerde $^{137}Cs$ distributiecoëfficiënt ($K_D$, L kg 1) na 30 dagen reactie varieerde van 3,4 tot 4,3, verrassend hoog voor een zandformatie en dicht bij de $K_D$ van de Boomse Klei (3,5). Variaties in de RIP tussen de zanden kunnen worden verklaard door het glauconiet gehalte en de kation uitwisselingscapaciteit (CEC). De geïsoleerde glauconiet fracties hebben een RIP met een factor 0,5-0,7 kleiner dan dat van de referentie, Illite du Puy. Een vergelijking van intacte en gemalen pellets laat zien dat de pellets de sorptiesnelheid en de sorptiepotentiaal verminderen, wat suggereert dat niet alle $^{137}Cs$ bindingsplaatsen in de pellets toegankelijk zijn. Dit geldt niet in sterk verweerde pellets. Waarschijnlijk vergroten de scheurtjes in het korreloppervlak van de verweerde korrels de toegankelijkheid van de binnenste sorptieplaatsen. Sorptie-evenwicht op intact glauconiet zand wordt na 1 maand bereikt, hoewel langzame reacties leiden tot een 1,6-1,8-voudige toename van de $K_D$ tussen het evenwicht en 8,5 maanden. Een desorptie-experiment toonde aan dat de sorptie van $^{137}Cs$ niet volledig omkeerbaar is.

De overeenkomsten tussen de sorptie van $Cs^+$ op glauconiet en illiet suggereren vergelijkbare eigenschappen van de sorptie sites. De sorptie van caesium aan illiet kan worden beschreven met een uitwisselingsmodel met drie sites: de Frayed edge sites (FES) type I, FES type II en planaire sites. De ammonium ($NH_4^+$) - K selectiviteit op de FES kan gezien worden als een vingerafdruk voor de zeer selectieve FES. De selectiviteit varieerde van 3,8 tot 5,0 voor drie glauconiet zanden, vergelijkbaar met gerapporteerde waarden voor illiet en kleiformaties. Dit suggereert dat de glauconiet zeer selectieve sites heeft die $Cs^+$ binden met vergelijkbare eigenschappen als in illiet. De $Cs^+$ sorptie-isothermen voor glauconiet zanden werden bepaald tussen $10^{-8}$ en $10^{-4}$ M $Cs^+$ in de evenwichtsoplossing. De experimentele isothermen werden gemodelleerd met een drie site-model. De FES - type I-capaciteit van de zanden varieerde van 0,04 tot 0,06 % van de CEC (tegenover 0,25 % voor illiet) en de FES - type II-capaciteit van 1,7 tot 2,2 % (tegenover 20 % voor illiet). Het verschil in de FES-fracties tussen illiet en glauconiet wordt toegeschreven aan het smectiet gehalte. Smectiet tussenlagen verhogen de CEC en verlagen de fracties van FES type I en type II sites. De hoge RIP van glauconiet suggereert dat glauconiet-houdend zand een effectieve geologische barrière voor radiocaesium kan zijn. De combinatie van het voorkomen van glauconiet als grove pellets en langzame $Cs^+$ sorptie wijst er echter op dat sorptieonevenwicht kan optreden tijdens reactief transport in deze zanden. Dit kan zorgen voor een vroegtijdige doorbraak van $Cs^+$. Er werd een doorbraak experiment opgezet met 13 verzadigde kolommen bij variabele stroomsnelheden. De kolommen werden gedurende 154 dagen uitgeloogd met $10^{-6}$ M $Cs^+$. Na 890-1170 porievolumes (PV) was er doorbraak in de kolommen met de hoogste stroomsnelheden. Vroege doorbraak werd alleen waargenomen in de kolom met het hoogste debiet (2,4 m $d^{-1}$), wat wijst op chemisch niet-evenwicht. Maar deze stroomsnelheid is onrealistisch groot voor de Neogene en Paleogene Fm. De BT-curves werden gemodelleerd met HP1 (Hydrus-PhreeqC), gebaseerd op batch sorptiegegevens verkregen na 90 dagen en uitgaande van lokaal reactie-evenwicht. Het model kan de doorbraak goed voorspellen, tenzij bij de hoogste stroomsnelheid. De sorptie van $Cs^+$ op zeer permeabele glauconiet zanden is bijgevolg voldoende snel om de doorbraak te vertragen bij realistische stroomsnelheden.

De adsorptie van radiostrontium ($^{85}Sr^{2+}$) werd bepaald voor 45 glauconiet zanden. De $K_D$ voor $Sr^{2+}$ in een achtergrondoplossing van 1 mM $Ca^{2+}$ varieerde van 23 tot 65 L $kg^{-1}$ voor de intacte zanden en van 50 tot 144 L $kg^{-1}$ voor de glauconiet fracties. Sorptie-evenwicht werd binnen 48 uur bereikt en de $K_D$-waarden voor intacte en gemalen pellets zijn vrijwel identiek, d.w.z. dat de sorptie van $Sr^{2+}$ niet wordt gehinderd door de korrel, in tegenstelling tot waarnemingen voor $^{137}Cs$. De $K_D$-waarden kwamen goed overeen met voorspellingen van de $K_D$ door twee bestaande modellen die geijkt zijn op bodems op basis van de CEC. Glauconiet zand heeft een voldoende hoge retentie van radiostrontium in gelijkaardig aan die van andere geologische barrières wanneer men uitgaat van de CEC.

Er werd een versnelde verweringsstudie uitgevoerd om na te gaan hoe verwering van glauconiet de retentie van radiocaesium ($^{137}Cs$) kan beïnvloeden. Drie verschillende glauconiet zanden werden

gedurende 27 maanden kunstmatig verweerd bij omgevingstemperatuur in vier verschillende scenario's: continu gespoeld met zuurstof (oxidatie), onder cementwater bij pH = 13 in afwezigheid van zuurstof, in een zure oplossing van pH = 4 en in een anoxische opstelling bij pH = 7 onder $N_2$ atmosfeer. De CEC nam onder alkalische omstandigheden met een factor 1,1-1,2 toe. In de oxiderende en zure monsters nam de CEC met eenzelfde factor af. De verhouding $Fe^{2+}$ tot $Fe_{tot}$ verdubbelde onder anoxische omstandigheden en bleef vergelijkbaar in de andere behandelingen. De RIP nam onder alkalische omstandigheden toe met een factor 1,1-1,3, in overeenstemming met de veranderingen in CEC, maar in de oxische monsters werd geen afname van de RIP waargenomen. Deze analyse suggereert dat glauconiet zand onder deze omstandigheden niet erg gevoelig is voor verwering en dat de effecten op de sorptie van radiocaesium marginaal zijn onder de hier gebruikte omstandigheden.

Deze studie toont aan dat het Cenozoïsche glauconiet zand een sterk sorptievermogen heeft voor radiocaesium en radiostrontium. Het sorptiepotentieel voor $^{137}Cs$ van een zand met 25-30 % glauconiet bleek verrassend genoeg even hoog te zijn als dat van Boomse Klei met 30-60 % klei, een van de kandidaat-gastheren voor afval van categorie B en C. Bijgevolg kan geconcludeerd worden dat glauconiet kan fungeren als een extra sorptie barrière voor $^{137}Cs$ en $^{90}Sr$.

## List of abbreviations

AAS Atomic Absorption Spectroscopy

$A_s$ Activity in solution

BC Boom Clay

BT Breakthrough

Ca Calcium

CDE Convection-dispersion equation

CEC Cation Exchange Capacity

Cs Caesium

D Dispersion coefficient

Eh Redox potential

EW Exempt waste

FANC Federaal Agentschap voor Nucleaire Controle

Fe Iron

FES Frayed Edge Sites

FES – type I high affinity, low capacity sites, in literature often referred to as FES

FES – type II low affinity, high capacity sites, often referred to as type II sites

Fm Formation

GL Glauconite

GLM Milled Glauconite fraction

HEC Hydrated exchangeable cations

HLW High level waste

HP1 Hydrus-PhreeqC

IAEA International Atomic Energy Agency

ICP-MS Inductively Coupled Plasma Mass Spectrometry

ICP-OES Inductively Coupled Plasma Optical emission spectrometry

IdP Illite du Puy

ILW Intermediate Level Waste

IS Ionic Strength

K Potassium

$K_c$ Selectivity coefficient

$K_D$ Solid-liquid distribution coefficient

LEA Local Equilibrium Assumption

LLW Low Level Waste

LSC Liquid Scintillation Counting

MLM Mixed Layer Mineral

$NH_4^+$ Ammonium

NIRAS Nationale Instelling voor Radioactief Afval en verrijkte Splijtstoffen

PV Pore Volume

Qz Quartz

RIP Radiocaesium Interception Potential

RN Radionuclides

SCK CEN Studiecentrum voor Kernenergie-Centre d'etude nucleair

SD Standard Deviation

SEM Scanning Electron Microscopy

Sr Strontium

SRM Standard Reference Materials

TM Ter Munck

UV-Vis Ultra Violet Visible Spectrometer

VLLW Very Low Lived Waste

VSLW Very Short Lived Waste

XRD X-ray Diffraction

$\lambda$ Dispersivity

## Table of contents

# Chapter 1. Introduction, context and objectives

The safe disposal of radioactive waste is one of the key aspects in the risk assessment of nuclear energy. The aims of disposal are to contain the waste, to isolate the waste from the biosphere, to inhibit, reduce and delay the migration of radionuclides (RN) and to ensure that the radiological consequences of RN reaching biosphere are acceptably low at all times (IAEA, 2011). The assessment of long-term dispersion of the RN from the waste requires a thorough understanding of the processes and mechanisms controlling the radionuclide transport in the environment. This PhD is devoted to a specific aspect of such assessments, i.e. the sorption of two medium-lived radionuclides, caesium-137 ($^{137}$Cs) and strontium-90 ($^{90}$Sr) on glauconite and glauconite sands of the Cenozoic (Paleogene and Neogene) formations in Belgium.

The glauconite sands are generally not considered as a primary host for radioactive waste disposal in geological formations. The sands are highly permeable and facilitate high pore water flow rates and fast radionuclide transport. Glauconite sand is, however, one of the options for the complementary sorption sink below the surface disposal at the Dessel site (Cat-A). Glauconite is an iron rich clay mineral formed in marine sediments and occurs both as coarse pellets, sizing up to 2 mm, and in the clay fraction (< 2 µm). Glauconite sands are the dominant lithology in the Neogene succession with often high pelletal glauconite content (> 30 %). Interest for this topic came from a question from FANC (Federaal Agentschap voor Nucleaire Controle) on the geochemical characteristics of the site in Dessel in the context of the safety analysis of surface disposal (*veiligheidsanalyse-oppervlakteberging*). In addition to the cementitious materials, a complementary sorption sink or embankment was requested by FANC to delay and attenuate the release of RN. Additionally, it is important to enhance knowledge about the sorption of various RNs onto different clay materials. Potential clayey host rock formations and surrounding rocks in various geological settings are still being evaluated for the disposal of radioactive waste. The knowledge may help at a later stage to select a geological formation, optimise the design of the repository or in the remediation of RN contaminated soils.

The term glauconite refers to a mineral composition (end-member) similar to illite in structure. In sedimentology the term is often used to describe green pellets with a variable mineralogical composition typically found in marine deposits. In the Cenozoic glauconite sands in the northeast of Belgium, the glauconite is characterised by a dark green, well rounded pellet, resembling sand rather than clay. The occurrence of glauconite is not unique to the Cenozoic formations. The topic of glauconite genesis and mineralogical variation remains controversial and opinions often differ.

The introduction of this thesis focusses on the context of radioactive waste, on the mineralogy of glauconite and on radionuclide sorption ($^{137}$Cs and $^{90}$Sr) on clays.

# 1. Radioactive waste

Radioactive waste is generated by a wide range of activities, from hospitals to nuclear power plants to mines and mineral processing facilities (IAEA, 2011). Radioactive waste is divided in six different categories according to the International Atomic Energy Agency - IAEA (IAEA, 2009).

- Exempt waste (EW)
- Very short lived waste (VSLW)
- Very low level waste (VLLW)
- Low level waste (LLW)
- Intermediate level waste (ILW)
- High level waste (HLW)

The exempt waste, very short lived and very low level waste are waste types with decay times over a limited period of up to a few years, or waste that does not need high level of containment and isolation. These waste types are stored in waste facilities until the activity is sufficiently reduced and the waste can be cleared from regulatory control for uncontrolled disposal or disposal in near surface landfill type facilities with limited regulatory control (IAEA, 2009).

In the Belgian context, the radioactive waste requiring long-term storage is divided in three different categories.

**Category** A

The category A contains conditioned short-lived low- and intermediate-level radioactive waste containing limited amounts of long lived isotopes. A radionuclide is considered short-lived if its half-life is less than 5 years and medium-lived with a half-life of 5-100 years. The cat-A waste corresponds to the LLW classification from IAEA (2009). This type of waste requires robust isolation and containment for periods of up to a few hundred years. Engineered near-surface facilities are suitable for disposal of cat-A waste. The cat-A waste contains less than 0.5% of the total activity of the waste in Belgium and consists for almost 75% of dismantling waste. The total volume of the cat-A waste is currently about 50 000 m³. The cat-A waste contains about 80.8 TBq $^{137}$Cs and 3.19 TBq $^{90}$Sr, based on the inventory of radioactive waste of 2013 (NIRAS, 2019b).

**Category B**

The category B contains long lived radionuclides (half-life > 100 years) requiring long-term separation from the biosphere and is equivalent to ILW according to IAEA (2009). The content of long lived radionuclides requires long-term containment and isolation that cannot be provided in a near surface disposal. This type of waste contains about 2% of the total activity of the waste in Belgium and its cumulative volume is 10 900 m³ (NIRAS, 2019b).

**Category C**

The category C waste is conditioned high level waste, HLW according to IAEA (2009). It should be isolated from the biosphere for thousands or up to millions of years. In addition to the large amount of long lived radionuclides in the waste, the activity concentration in the waste generates significant amounts of heat due to radioactive decay. For disposal, stable, deep geological formations are suggested at several hundred metres below the surface. In the disposal concept the heat production has to be taken into account. The high level waste consists of reprocessed and unprocessed spent fuel from commercial power plants containing mixed fission products with typical activities of 104 TBq $m^{-3}$. At the time of disposal, a cooling time of a few decades is needed before the cat-C waste can be moved to a geological disposal site (IAEA, 2009). The high level waste of Belgium contains most of the activity (~98 %) though it represents the smallest volume, 250 $m^3$ of the vitrified waste and 3800 ton heavy metals (spent fuel from nuclear power plants) (ONDRAF/NIRAS, 2020).

## 2. Disposal of radioactive waste

**Surface disposal**

A (near) surface disposal is recommended for the category A radioactive waste. In this type of disposal facility a series of engineered barriers are constructed on the ground surface to contain the radioactivity (IAEA, 2011). Such a facility must be able to contain the radioactive waste for several hundreds of years.

In Belgium, a political decision on the type of disposal - surface disposal - was taken on the 6th of January 1998, the site location was decided on the 23rd of June 2006. A surface disposal is planned for the category A waste in Dessel; the cAt project (Figure 1.1). The waste will be placed in caissons (concrete crates) and will be encapsulated in mortar forming a monolith. The monoliths enclose the radionuclides and contain the ionising radiation. The monoliths are placed in modules constructed out of reinforced concrete. During the exploitation the modules are covered by a roof structure. At the end of the exploitation the roof will be replaced by a permanent cover (NIRAS, 2010).

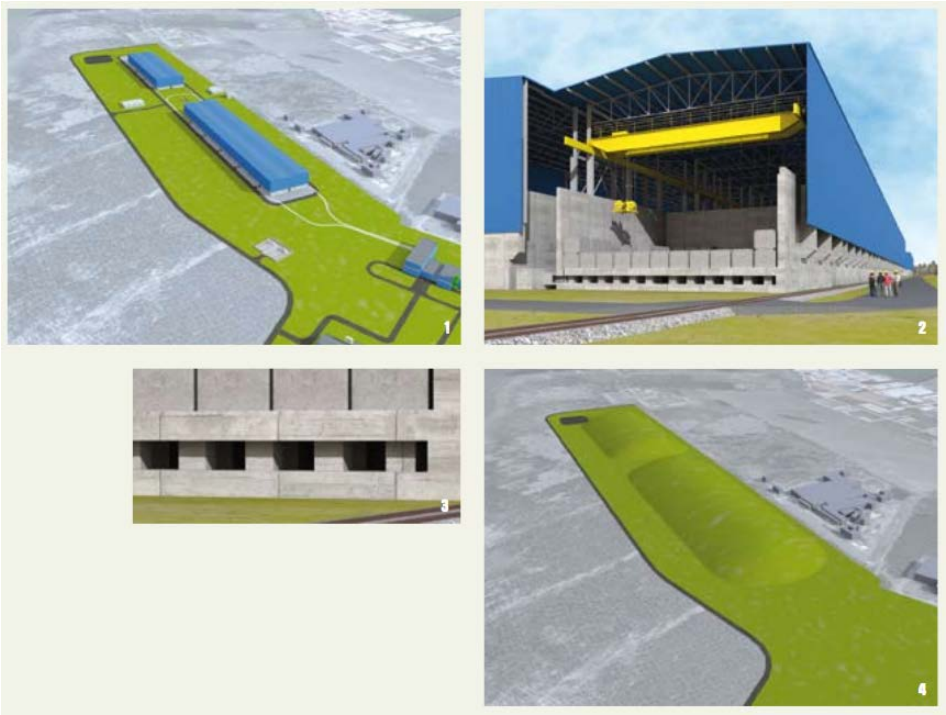

Figure 1.1 The planned surface disposal for the cAt project in Dessel with 1. the disposal modules, 2. the roof that will cover the disposal modules during the exploitation, 3. the inspection space below the modules, 4. the permanent cover of the disposal facility (NIRAS, 2010).

Below the surface disposal a drainage layer and additional sorption sink will be added. The additional sorption sink must be sufficiently permeable to allow the drainage water to flow through the barrier rather than over it, while still maintaining RN sorption properties (NIRAS, 2019a). On the short list for the sorption sink of the cAt project were glauconite, bentonite, zeolite, oxyhydroxides and geopolymers. A decision has recently been made in favour of a “non-swelling” bentonite enriched soil layer for the sorption sink in the cAt project.

**Geological disposal**

In the case of category B and C waste, geological disposal is recommended (IAEA, 2011). The safety of a geological disposal system depends on many barriers, both engineered and natural barriers. In this type of disposal system waste is hosted in a stable geological formation able to retain radionuclides and prevent their migration to the biosphere, without the need of repeated human intervention. The RN must be isolated from the biosphere during the entire decay time of the radioactive waste, several 100 000 years or even up to one million years.

Several types of host formations qualify for geological disposal. Internationally three types of host formations are being studied: evaporites, crystalline rocks and clay formations. A good host is characterised by sufficient depth, homogeneous formation without structural features that improve RN transport (e.g. fractures), mechanical compatiblity with a disposal facility (for stability, heat transport etc.), reduced water movement in the formation, retention of RN and uninfluenced by climate change, seismicity or volcanism.

For a geological disposal on Belgian territory, several formations can be considered: crystalline rock, poorly indurated clay formations, argillites and slate (ONDRAF/NIRAS, 2020; Vandenberghe et al., 2014; Vandenberghe, 1996). The Ypresian clay and Boom Clay are poorly indurated clay formations under consideration for geological disposal. In both cases glauconite sands are overlying, or present in the vicinity of, the clay formations. For category B and C waste a depth of several hundred meters is advised (IAEA, 2009). The activity and the half-live of the radioactive waste determine the degree of isolation and containment required in the disposal system. The spacing of the galleries and the density of the disposal is determined by the gamma radiation and the emission of decay heat. The fission products $^{137}Cs$ and $^{90}Sr$ are the dominant heat emitting radionuclides in the vitrified fraction of the HLW (U and Pu are separated from this fraction in PUREX). In spent fuel, Pu and the minor actinides (Am, Cu, Np) are the main contributors to the heat emission and radiotoxicity. The design of the geological disposal can be optimised by cooling the waste for an extended time before the disposal. Also, for the disposal concept itself there are still two options: a facility with galleries[1] or borehole[2] disposal (IAEA, 2011). The borehole disposal is no longer considered for geological disposal in Belgium.

**History of radioactive waste management in Belgium**

In 1966 the Belgian government decided that nuclear energy was to be introduced in Belgium. In 1974 it was decided that research into reprocessing, storage and disposal of high level radioactive waste was one of the conditions coupled to the construction and exploitation of nuclear power plants. In 1976 a commission of scientists "*Commissie van Beraad inzake Kernenergie*" concluded that the radioactive waste problem is inherent to nuclear power plants and that the problem of high level waste was underestimated (*Comité van het Nationale Programma*, 2015). In the initial years a partial disposal program was in place. Between 1960 and 1982, 30 000 ton of the Belgian short-lived low- and intermediate-level radioactive waste (category A) was disposed in the North-Atlantic Ocean (until the moratorium in 1983). Sea disposal was no option for the high level waste due to the extremely long decay times and strongly ionising radiation. The remaining options for the cat B&C waste proposed by the scientific commission are long-term surface disposal or controlled disposal in geologically stable layers. A long-term surface disposal will require monitoring and human intervention every 50 to 100 years, a complex situation for waste that has to be isolated up to 1 million years.

[1] "Geological disposal: Disposal in a facility constructed in tunnels, vaults or silos in a particular geological formation (e.g. in terms of its long term stability and its hydrogeological properties) at least a few hundred metres below ground level. Such a facility could be designed to receive high level radioactive waste (HLW), including spent fuel if it is to be treated as waste." - IAEA, 2011. Disposal of Radioactive Waste. INTERNATIONAL ATOMIC ENERGY AGENCY, Vienna.

[2] "Borehole disposal: Disposal in a facility consisting of an array of boreholes, or a single borehole, which may be between a few tens of metres up to a few hundreds of metres deep. Such a borehole disposal facility is designed for the disposal of only relatively small volumes of waste, in particular disused sealed radioactive sources. " ibid.

Today in Belgium, over 20 000 m³ of radioactive waste is housed in interim storage facilities awaiting final disposal. The Belgian radioactive waste management organisation, ONDRAF/NIRAS, is responsible for the long-term management of radioactive waste in Belgium. Category A waste is suitable for near surface disposal and is planned to take place in a surface disposal facility in Dessel (FANC, 2019). In order to realise this disposal concept, ONDRAF/NIRAS has developed the cAt-project (category A project) for which the planning permit has been submitted in 2019 (Figure 1.1). An extended Strategic Environmental Assessment was published by NIRAS in April 2020 containing all possible disposal options for cat-B & C waste and different possible host formations. The location and host formation have not been selected yet. The long timeframe of radioactive waste disposal implies that not only an appropriate location needs to be selected, changes in the environment need to be taken into account as well. This means there is a need to evaluate the migration taking into account effects of climate change and associated changes in the landscape (IAEA, 2020).

**The role of glauconite sand**

The glauconite (sand) is considered to be used as a barrier in a radioactive waste disposal system or for remediation of contaminated land (Voronina et al., 2015b). Engineered barriers are designed to retain and delay the dispersal of radionuclides as much as possible. The low permeability in the clay barriers restricts the groundwater flow and thereby transport of RN. Bentonite (a smectite) is considered to be the best candidate due to a combination of high sorption capacity for ions in solution, low permeability and the rheological properties of wet smectite (Meunier, 2013). Illite has a much lower cation exchange capacity (20 $cmol_c\ kg^{-1}$ versus 90-100 $cmol_c\ kg^{-1}$ for smectite (Favre et al., 2006)) due to the collapse of the interlayer. However, $Cs^+$ sorption is much more selective in illite. Near the high level waste storage, smectite-to-illite transformation may occur due to the higher temperatures produced by radioactive decay.

In some cases the groundwater flow cannot be impeded and a reactive permeable barrier is needed, e.g. in the case of a sorption sink below a surface disposal site. Therefore, a porous mixture of glauconite/illite and chlorite could be an efficient filter enveloping radioactive waste storage sites (Meunier, 2013). The glauconite sand is highly permeable and the glauconite content gives it the high reactivity. Other options are pure clays (illite or bentonite) mixed with wood shavings or pure quartz sands (De Pourcq et al., 2015).

In case of accidents at nuclear fuel cycle plants, e.g. Fukushima, large areas of land can become heavily contaminated by radionuclides. Radionuclides such as $^{137}Cs$ and $^{90}Sr$ are major contributors to the contamination. Due to the resemblance with, respectively $K^+$ (potassium) and $Ca^{2+}$ (calcium), these radionuclides can be taken up by fauna and flora. The radionuclides migrate from soil to vegetation through the groundwater. To rehabilitate land the radionuclides must be removed or fixed in the soil. The best option is in most cases the removal of (top-)soil. However, this leads to enormous amounts of

contaminated soil to be disposed of. Moreover, the soil fertility and structure can be lost by removing the soil. Another option is mixing the soil with a strong sorbent to fix the radionuclides. One of these possible sorbents is glauconite (Voronina et al., 2015b; Voronina et al., 2013).

## 3. Glauconite

Glauconite is an iron rich clay mineral that is formed in marine sediments. Glauconite has a specific mineralogical composition but the term  is often used for describing *green grains*. Glaucony refers to green grains made up of mainly glauconite crystal flakes. The glauconite in the glaucony grains can vary in composition between a smectite and mica like structure (Gaudin, 2005; Odin, 1981). Glaucony and glauconite are mixed up in many publications. In this thesis we will use *glauconite* for the description of the green grains and the *glauconite fraction* for the fraction that can be magnetically separated from the glauconite sand.

**Mineralogy**

Glauconite is an iron (Fe) rich illite with the structural formula $K_{0.75}$ ($Fe^{2+}$ $Fe^{3+}$ Mg Al)$_2$ ($Si_{3.75}$ $Al_{0.25}$) $O_{10}$ $(OH)_2$. Glauconite is a dioctahedral clay mineral with a charge deficit originating from substitutions of $Si^{4+}$ by $Al^{3+}$ in the tetrahedral sheet and of trivalent ($Al^{3+}$, $Fe^{3+}$) by bivalent cations ($Mg^{2+}$, $Fe^{2+}$) in the octahedral sheet. The size of $Fe^{3+}$ and $Fe^{2+}$ ions is very different from $Al^{3+}$, substitutions in the octahedral layer, thereby causing distortions in the crystal lattice (Meunier, 2005). The charge of glauconite is predominantly octahedral and largely compensated by fixed $K^+$ in the interlayer. Compared to illite glauconite is $K^+$ deficient ($K_{0.75}$ to  $K_1$ in illite). (Bailey, 1980; Meunier, 2005). The remaining negative charge is compensated by hydrated exchangeable cations (Van Ranst and De Coninck, 1983).

Glauconite is an end member composition that forms a solid solution with celadonite. Celadonite can hardly be distinguished from glauconite (mineralogically), however, it only occurs in specific hydrothermal environments (Ivanovskaya et al., 2015; Meunier and El Albani, 2007). The glauconite compositional domain stretches from the solid solution glauconite-celadonite to a high- and low- charge beidellite (smectite) (end members, Table 1.1). The spread of the composition domain is related to four factors: (1) the $K_2O$ content ranging from 6-9 wt%, (2) the variable presence of $Al^{3+}$ ions in the tetrahedral positions (3) the variable content of  $Fe^{2+}$ in the octahedral positions and (4) the occurrence as a mixed layer mineral (MLM) glauconite-smectite (Meunier, 2005). Glauconite and illite are considered pure end-members if they contain < 10 % smectite (according to the Clay Mineral Society, Bailey (1980)). In practice nearly all glauconite and illite will contain smectite layers. The oxidation state of the Fe is mostly undetermined for glauconite. Adriaens et al. (2014) report a $Fe^{2+}$ to $Fe_{tot}$ ratio of 0.1 in the Neogene glauconite.

Table 1.1 The different end-members of Fe-bearing clay phases and compositions (Meunier and Albani, 2007) with $M^+$ representing interlayer cations and $R^{2+}$ and $R^{3+}$di- or trivalent structural cations.

| End-members | Structural formulae | |
|---|---|---|
| Celadonite | $K\ (Fe^{3+}\ Mg)\ (Si_{4-x}\ Al_x)\ O_{10}\ (OH)_2$ | with $x < 0.2$ |
| Glauconite (mica) | $K\ (R^{3+}_{1.33}\ R^{2+}_{0.67})\ (Si_{3.67}\ Al_{0.33})\ O_{10}\ (OH)_2$ | with $Fe^{3+}$>Al Mg>$Fe^{2+}$ |
| Glauconite (illite) | $K_{0.75}\ (R^{3+}_{1.5}\ R^{2+}_{0.5})\ (Si_{3.75}\ Al_{0.25})\ O_{10}\ (OH)_2$ | |
| Nontronite (high charge) | $M^+_{0.6}\ Fe^{3+}_2\ (Si_{3.4}\ Al_{0.6})\ O_{10}\ (OH)_2$ | |
| Nontronite (low charge) | $M^+_{0.3}\ Fe^{3+}_2\ (Si_{3.7}\ Al_{0.3})\ O_{10}\ (OH)_2$ | |
| Fe-montmorillonite (high charge) | $M^+_{0.6}\ (Fe^{3+}_{1.4}\ Mg_{0.6})\ Si_4\ O_{10}\ (OH)_2$ | |
| Fe-montmorillonite (low charge) | $M^+_{0.3}\ (Fe^{3+}_{1.7}\ Mg_{0.3})\ Si_4\ O_{10}\ (OH)_2$ | |
| Beidellite (high charge) | $M^+_{0.6}\ Al_2\ (Si_{3.4}\ Al_{0.6})\ O_{10}\ (OH)_2$ | |
| Beidellite (low charge) | $M^+_{0.3}\ Al_2\ (Si_{3.7}\ Al_{0.3})\ O_{10}\ (OH)_2$ | |
| Al-montmorillonite (high charge) | $M^+_{0.6}\ (Al_{1.4}\ Mg_{0.6})\ Si_4\ O_{10}\ (OH)_2$ | |
| Al- montmorillonite (low charge) | $M^+_{0.3}\ (Al_{1.7}\ Mg_{0.3})\ Si_4\ O_{10}\ (OH)_2$ | |

More recent research by Meunier and El Albani (2007) represented the compositions of the iron bearing clay phases by plotting the interlayer charge ratio over the ratio of octahedral Fe to the total octahedral positions (Figure 1.2). Mixed layer minerals occur in all compositional domains. Meunier and El Albani (2007) suggest a compositional division between the glauconite – Fe-illite – Fe-Al-smectite and the Fe-montmorillonite group. In the first group the continuity can be related to the glauconite incorporating smectite in the interlayers and isomorphic substitutions. The continuity also implies a possible solid solution between the three components. However, according to Meunier (2005) the chemical composition domain of glauconite suggests that substitutions of $Si^{4+}$ by $Al^{3+}$ in the tetrahedral positions take place only in the smectite component.

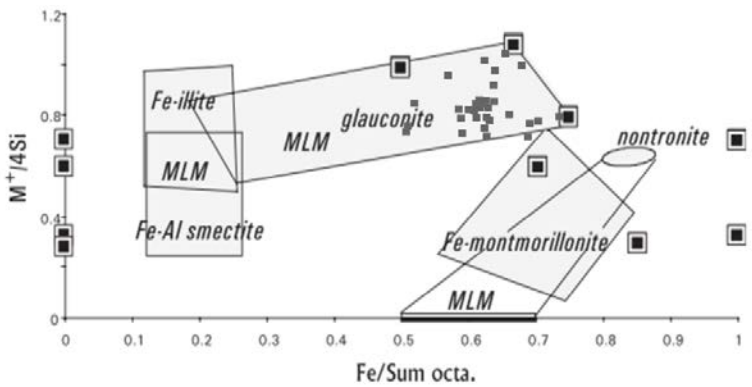


Figure 1.2 Different compositional domains for the Fe-bearing clays with indication of the identified mixed layer minerals (MLM). The $M^+$/4Si ratio corresponds to the interlayer charge of the combined Na, K and Ca divided by the $Si_4O_{10}$ content and the Fe/Sum octa represents the ratio of Fe versus the sum of the octahedral cations. The extension from the glauconite compositional domain suggests a Fe-Al smectite composition for the expandable layers in the mixed layer minerals (Meunier and El Albani, 2007) with data of the Neogene glauconite (Adriaens et al., 2014) (grey squares).

It is important to distinguish between solid solutions and mixed layering. Mixed layer minerals (MLM) are defined by a stacking sequence of several layers with different mineralogy. Solid solutions represent the variation in the layer, where ion substitution is the main contributor, implying that the structural formula is analogous and the space symmetry group stays the same. The ion substitutions make each layer compositionally different from the adjacent layers (Meunier, 2005). The smectite layers in the MLM cause an overall lower $K^+$ content. The studies of McCarty et al. (2004) and Huggett (2006) show that multiple clay minerals and mixed layer phases coexist in the glauconite grains or pellets. More specifically, glauconite, nontronite, vermiculite, muscovite, feldspar, illite and kaolinite layers were found. The mineral composition depends on the formation conditions. Feldspar and mica are often relicts from before the transformation. Detecting polymineralic particles through X-ray diffraction analysis is possible, but difficult, because the distortion in the crystal lattice will influence the cell parameters and thereby the position, intensity and shape of the peak in the diffraction pattern.

**Genesis of glauconite and formation of glauconite grains**

Most clay minerals are formed as weathering products or through diagenesis. Glauconite develops in a marine environment close to the sediment-water interface (Odin, 1988). The starting point is often a grain consisting of mud of the sediment and biogenic particles or a porous silicate grain in the presence of organic matter. The crystals develop in the pores of the grain leading to globule formation (Figure 1.3). The clay fraction glauconite mostly originates from disintegration of grain during reworking or weathering (Adriaens et al., 2014).

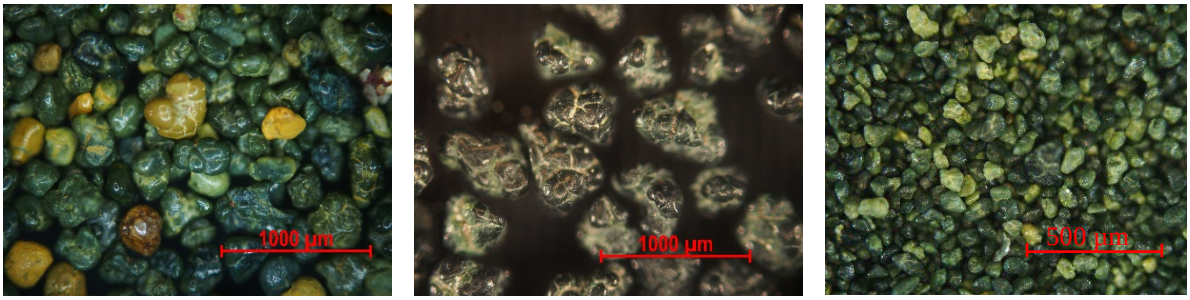


Figure 1.3 Gauconite grains from respectively the Diest, Berchem and Voort Fm.

To form glauconite – Fe-illite – Fe-Al-smectite minerals, a reductive environment (high concentrations of soluble $Fe^{2+}$) with an Al-bearing sediment is needed. The presence of organic matter and high concentration of soluble Fe and $K^+$ is vital for the formation. To achieve these conditions, slow sedimentation rates are required (Kelly and Webb, 1999). As sedimentation continues, the parent material gets buried under new sediment. The fresh sediment restricts the contact to the seawater and ion diffusion to the glauconite. The suboxic conditions in the early diagenesis cause partial reductive dissolution of the iron(III) bearing minerals (e.g. hematite, goethite) formed under oxic conditions and allow both $Fe^{2+}$ and $Fe^{3+}$ to be built into the glauconite structure. Iron is stable in minerals under a ferric form ($Fe^{3+}$) under oxic conditions with a neutral to alkaline pH (e.g. hematite, goethite, smectite).

However, under reducing conditions the stability of iron shifts to the soluble ferrous ($Fe^{2+}$) state. Reduction of the structural $Fe^{3+}$ to $Fe^{2+}$ and isomorphic substitutions of $Fe^{3+}$ and $Al^{3+}$ by $Fe^{2+}$ and $Mg^{2+}$ lead to an increased (negative) charge of the octahedral layer. Potassium ions are taken up into the interlayer to compensate this charge increase if available. Hydrogen ions are released into the environment during the fixation of $K^+$. The decrease in pH is buffered by the sediment, causing local dissolution. When the redox potential ($E_h$) drops further, sulphate reduction starts and the available iron is built into pyrite ($Fe_2S$) thereby ending the glauconite formation (Kelly and Webb, 1999).

Several theories are proposed for the formation of glauconite. The precipitation-dissolution-recrystallisation theory is widely accepted. According to this theory, pre-existing minerals are dissolved in the seawater and glauconite crystallises from the fluid to take its place (Odin, 1982). The nucleation crystal growth theory starts from the idea that marine clay species require solid support to grow on. For example, detrital minerals or biogenic debris, as long as the substrate is susceptible to alterations (Meunier and El Albani, 2007).

The glauconitisation process (Figure 1.4) is described as a continuous evolution with increasing $K^+$ (interlayer) and structural Fe ($Fe^{2+}$ and $Fe^{3+}$) content (Odin, 1981). These ions originate from the seawater and the surrounding sediment and reach the pore solutions through chemical diffusion. Four stages are distinguished. In the first or nascent stage glauconite minerals develops and the $K_2O$ content ranges from 2 to 4 %. The reaction rate in this phase depends on the original porosity and permeability to allow ion migration. Towards the second stage the biogenic material has dissolved and the original pores are being filled with authigenic clays. The $K_2O$ increases to 4 to 6 %. In the third phase, the evolved stage, a series of successive recrystallisations overprints the initial structure. The crystal growth is stronger in the centre of the grain and the $K_2O$ content ranges from 6 to 8 %. The pellet has reached a dark green colour and an increase in volume gives rise to cracks in the grain surface between the globules. In the last stage, the highly evolved state, the surface cracks are filled with authigenic minerals and the $K_2O$ content is larger than 8 %. The smaller grains often show a less evolved state of glauconitisation, while larger grains may have an unevolved centre (Odin, 1988; Pestitschek et al., 2012).

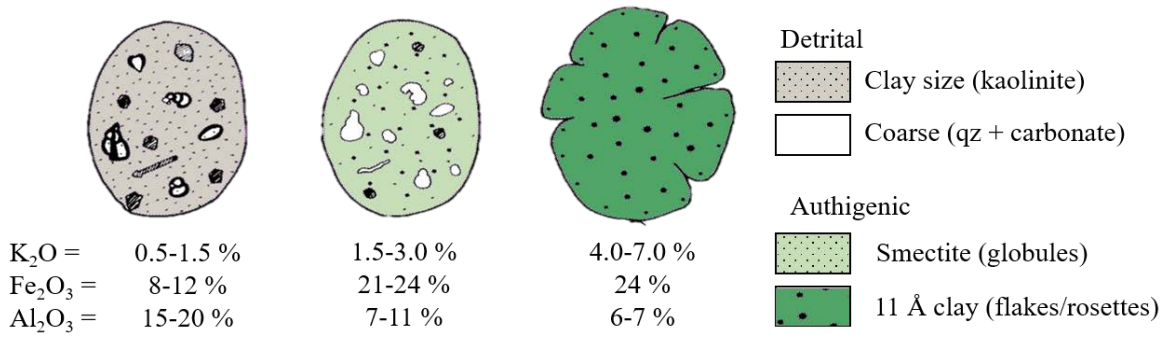


Figure 1.4 Glauconitisation process after Odin (1988)

The process continues as long as the glauconite pellet remains close to the sediment surface and sufficient ions are present (Odin, 1982) and during diagenesis. In the detrital minerals, iron is present as $Fe^{3+}$. Iron must be in a soluble $Fe^{2+}$ state to be able to migrate into the glauconite pellet. The reductive microsystem no longer exists if the organic matter is mineralised or the bacterial activity stops. The subsequent oxidation causes a silicate phase to form (Baldermann et al., 2017; Meunier and El Albani, 2007).

**Weathering**

Weathering can be considered as the process opposite to glauconitisation. Alteration and reworking can change the appearance and mineralogy of the glauconite grains. As the glauconite forms in shallow marine environments, the sediment is often reworked. The reworking can disintegrate the glauconite grains. Clay-sized glauconite has a very similar clay mineralogy to the pelletal glauconite but logically has an increased expandability and is more reactive. The origin of the clay-sized glauconite is often debated, however mineralogical and chemical analysis prove that it is related to pellet abrasion and disintegration during transport, implying that the amount of glauconite in the clay fraction will give an indication as to the distance and intensity of the pellet transport (Adriaens and Vandenberghe, 2020; Adriaens et al., 2014).

Glauconite formed under reducing conditions is not stable when subjected to oxic conditions, e.g. during reworking of the sediment. Weathering can induce zoning in glauconite grains, where the outer rim is depleted in $K^+$ and Fe, resulting in a lighter green colour. The weathering is accelerated by oxidising and mild acidic conditions. The oxidation of $Fe^{2+}$ to $Fe^{3+}$ causes a layer charge reduction.

In soil profiles, the weathering of glauconite rich sands has been described as a gradual transformation into mica-nontronite and smectite (Van Ranst and De Coninck, 1983). In a first phase the glauconite grains disintegrates into clay-sized particles with limited changes to the mineralogical structure. Over time the clay fraction glauconite is transformed into Fe-rich mixed layer illite-smecite and even to smectite and amorphous iron is released. In the case of larger glauconite grains, the oxides deposit in cracks in the grain or as a (amorphous) layer on the grain surface. The oxide layer can restrict ion exchange between the pore water and the glauconite grain and protect the grain from further weathering. In a subsequent step the MLM evolves to smectite, kaolinite, and Al mixed layer illite. The pellet itself can fully transform to an oxidised pellet consisting predominantly of goethite. The process is more pronounced in soils with alternating redox conditions associated with wetting and drying. Because of the fluctuating ground water table, the clay fraction migrates and forms argillic horizons in the soil. (Essa et al., 2016; Meunier, 2005; Pestitschek et al., 2012).

## 4. Lithostratigraphy: the Neogene and Paleogene glauconite sands

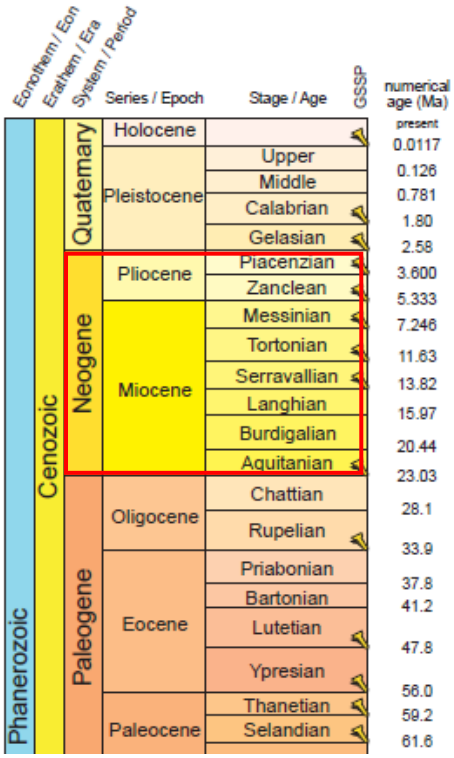


Figure 1.5 International chronostratigraphic time chart (2015) (stratigraphy.org)

During the Miocene (Figure 1.5) sedimentation was restricted to the north-eastern part of Belgium, specifically to the Campine area. The Miocene deposits are linked to a transgressive shallow-marine environment with minor estuarine to fluvial deposits, giving rise to sands with a high pelletal glauconite content separated by sedimentation stops and erosion. The sands are characterised by strong local differences in grain size and mineral content, and thin clay intercalations. In the formations several major stratigraphic unconformities are present (Adriaens et al., 2014). In Table 1.2, an overview of the Neogene units occurring in Belgium is given. The corresponding average glauconite content is added for each formation. The glauconite content in the Neogene sands is highly variable, average 20-30 %. The values given here are estimates, averages calculated based on investigated samples (Adriaens and Vandenberghe, 2020).

Table 1.2 Overview of the Neogene units from Adriaens (2015)

| Chronostratigraphy | Lithostratigraphic unit | | Average | Authigenic |
|---|---|---|---|---|
| | Formation (Fm) | Member | GL content | GL potential |
| Zanclean/Piacenzian | Mol Fm | | < 0.01 % | Very low |
| Piacenzian | Poederlee Fm | | 20 % | Medium |
| Messinian | Kasterlee Fm | | 3 % | Very low |
| Tortonian | Diest Fm | | 39 % | Very low |
| Serravallian | | Antwerp | 50 % | Medium |
| Langhian | Berchem Fm | Kiel | 35 % | Low |
| Burdigalian | | Edegem | 35 % | Low |
| Chattian | Voort Fm | | 20-30 % | Medium |

The sequence stratigraphy of the Neogene units is quite complex. Unconformities and reworking are common in the Neogene units. Most of the glauconite grains have been transported and reworked before re-deposition, except for the Antwerp Member of the Berchem Fm (Adriaens and Vandenberghe, 2020; Vandenberghe, 2014). Due to the higher density of glauconite (vs quartz grains) the glauconite grains were sorted during transport leading to large differences in glauconite content in the formation. In addition, gradual transitions make it difficult to recognise the unit and formation boundaries.

**Voort Formation**

The Voort Formation (Fm) is a fine grained and clay-rich sand characterised by a dark green colour due to the high glauconite content (up to 40 %). The formation is rich in fossil fragments (molluscs) with fossiliferous phosphatic sandstone concretions (Dusar and Vandenberghe, 2020). There is a gradual transition to the Eigenbilzen Fm without a noticeable boundary. The Voort Fm is a relatively homogeneous glauconite sand. The top of the unit is weathered and decalcified.

**Berchem Formation**

The Berchem Fm is divided among the Edegem, Kiel and Antwerp Members. Towards the east, the Bolderberg Fm replaces the Berchem Fm. The formations never touch because of a large erosion gully between them. The members of the Berchem Fm are separated due to a sedimentation stop as a result of fluctuating sea levels. The highest glauconite contents for the whole Neogene can be found in the Antwerpen Member, up to 87 % locally. The formation consists of a smectite-rich assemblage with varying content glauconite-smectite with high-expandable glauconite-smectite (Adriaens, 2015). The same clay mineral assemblage can be found in the Deurne and Dessel Member of the Diest Fm, suggesting reworking of the Berchem and Bolderberg Fm within the Deurne and Dessel Members. A description of the different members of the Berchem Fm can be found in Table 1.3.

Table 1.3 Compositional description of the different members of the Berchem Fm (Adriaens et al., 2014)

| | Member | Description | GL content |
|---|---|---|---|
| Berchem Fm | Antwerpen Member | Very glauconitic medium grained sands with disperse clays and variable shell layers, phosphate nodules, bones and shark teeth | Authigenic pelletal glauconite<br>47 ± 11 % |
| | Kiel Member | Glauconitic, medium- to coarse grained sandy unit. Subdued to post-depositional decalcification | Reworked pelletal glauconite<br>33 ± 8 % |
| | Edegem Member | Clayey, glauconitic, fine- to medium- grained sand unit with locally basal gravel | Reworked pelletal glauconite<br>37 ± 5 % |

**Diest Formation**

The Diest Fm occurs in the Campine region in the subsurface and at the surface in the Hageland region due to the East dipping formations. The subsurface Diest Fm shows a large variation in the composition and characteristics of its members. Overall, the formation exists mostly of loose coarse sands with a dark green to limonite brown colour. The sands are glauconite rich with glauconite content estimates ranging from 25 to 70 %, 39 % on average. The glauconite pellets are partially to completely weathered depending on the locality (based on microscope observations). Not all glauconite grains show the same weathering state. The base of the Diest Fm shows gullies, giving rise to varying thickness up to 90 m.

The base of the Diest Fm consists of a coarse basal gravel most probably reworked from the underlying Antwerp member of the Berchem Fm (Goolaerts et al., 2020). The basal gravel is not present over the full base of the Diest Fm. Still the base of the Diest Fm can be distinguished from the Berchem Fm by a significantly coarser sand. At the outcrops of the Diest Fm (Hageland region, e.g. Beniksberg, Wijngaardberg) the loose sand has been cemented by Fe minerals of the limonite group. Iron sandstone layers are alternated by loosely compacted glauconite sands.

The Dessel Member is characterised by its fine grained nature with a 26 % glauconite content in the lower Dessel Member. The base of the Diest sand Member can be distinguished by a significantly coarser sand with low expandable glauconite-smectite clay mineralogy. In this member about 38 % low-expandable glauconite-smectite is present. The coarse main body of the Diest Fm only occurs in the western part of the Campine basin. In the Mol-Dessel region the top of the Diest Fm is significantly more clay-rich with a fraction of Fe-vermiculite (Adriaens and Vandenberghe, 2020). This specific mineralogy is characteristic of a weathered origin of the sediment. Beside the Fe-smectite, high amounts of siderite, plagioclase, chlorite and pelletal glauconite typically occur in the top of the Diest Fm. The clay-sized glauconite is systematically more expandable than the pelletal glauconite.

**Kasterlee Formation**

The transition from the Diest to the Kasterlee Fm is gradual, implying an important reworking most likely related to the emersion of the Diest Fm during the late-Miocene (Adriaens and Vandenberghe, 2020). The Kasterlee Fm is characterised by a fine grained and well sorted sediment with less than 5 % glauconite pellets. The clay mineralogy is glauconite-smectite dominated. Micas are present. In the Mol-Dessel area the top of the Kasterlee Fm is covered by a sand facies with clay intercalations. The mineralogy of the clay fraction, however, remains dominated by glauconite-smectite. The Kasterlee sands overall have a pale green to brown colour. The formation reaches a thickness up to 12 meters.

**Mol Formation**

The start of the Mol Fm has been defined by the change of a glauconite-smectite to a kaolinite-dominated clay mineralogy. The Mol Fm is characterised by middle to coarse sands with sand lenses deposited in an estuarine environment (Broothaers, 2000). The leaching of the sands by acids originating from the lignite layers gave rise to very pure quartz sands. Glauconite and micas occur in small amounts (0.5 % pelletal glauconite). Though glauconite-smectite makes up 20-30 % of the clay fraction (< 2µm). The clay content is described as kaolinite and low expandable glauconite-smectite (Adriaens, 2015). The formation has a thickness of 15 meters maximum.

## 5. Radionuclide sorption

**Environmental aspects of radiocaesium and -strontium isotopes**

Neutron-induced nuclear fission reactions generate a mixture of fission products. The abundance of the fission productions is a function of the parent actinide nucleus' atomic number and the incident neutron energy. In light water moderated nuclear reactors, the principal fissile nuclides are uranium ($^{235}$U) and plutonium ($^{239/241}$Pu). The isotopes $^{137}$Cs and $^{90}$Sr are two of the most abundant in fission products of $^{235}$U and $^{239/241}$Pu reactions (Chan, 1992; Koning et al., 2006) (Figure 1.6). In the first 150 years from the discharge from the reactor, the heat and gamma radiation of spent nuclear fuel or highly active waste are dominated by the short- and medium-lived radionuclides with a half-life up to 100 years (mainly $^{137}$Cs and $^{90}$Sr) (Baetsle 2003).

The $^{134}$Cs ($t_{1/2}$ = 2.1 y) and $^{137}$Cs ($t_{1/2}$ = 30.2 y) isotopes are products of the $^{235}$U fission reaction with fission yields of 6.8 % and 6.1 %, respectively. The $^{135}$Cs ($t_{1/2} = 2.3 \times 10^6$ y) isotope is the progeny of the $^{135}$I, produced at 6.3 % fission yield. $^{134}$Cs, $^{135}$Cs and 5,6% of $^{137}$Cs undergo a $\beta^-$ decay into stable barium (Ba) isotopes, while 94,4% of $^{137}$Cs $\beta^-$ decays into the metastable nuclear isomer $^{137m}$Ba ($t_{1/2}$ = 2,6 min), which decays into the stable $^{137}$Ba with emission of a gamma ray (Chu et al., 1999). The long half-lives of $^{135}$Cs provide an additional challenge in the radioactive waste disposal. Transmutation of the Cs fraction ($^{135}$Cs separate or $^{135}$Cs and $^{137}$Cs) of the waste is not feasible for the moment. The different isotopes of Cs cannot be separated chemically or physically. Transmutation of $^{135}$Cs to stable $^{136}$Cs by irradiation would generate new $^{135}$Cs from the $^{133}$Cs and $^{134}$Cs.

The $^{90}$Sr ($t_{1/2}$ = 28.8 y) isotope is produced at 5.7 % fission yield, it undergoes $\beta^-$ decay into yttrium ($^{90}$Y, $t_{1/2}$ = 64 hours) which in turn undergoes $\beta^-$ decay into the stable zirconium ($^{90}$Zr). In the experiments described in this study, $^{85}$Sr is used as an analogue for $^{90}$Sr due to the much shorter half-life ($t_{1/2}$ = 64.8 days).

During nuclear accidents overheating of the fuel and failure of the cladding leads to the release of highly volatile radionuclides (such as I, Te, Cs, Xe, Kr) and particulates into the atmosphere (Mathieu et al., 2018). The airborne elements can subsequently be inhaled by humans or can be deposited on vegetation. The highly volatile I and Xe can diffuse through nuclear fuel and air and create radioactive Cs often far from the original fission site (Ishiwatari and Nagai, 1981). In the accidents at Chernobyl and Fukushima $^{131}$I, $^{137}$Cs and $^{90}$Sr were released and spread in the environment. The fate of anthropogenic caesium and strontium in the environment is mainly controlled by sorption on solid particles and the geochemistry of the groundwater (Comans and Hockley, 1992).

The radiological risk of an isotope is related to a combination of its inherent radiotoxicity, the half-life and its concentration. The isotopes with highest human risk are $^{129}$I and $^{137}$Cs, even though $^{137}$Cs is already 10 times less toxic than $^{129}$I (Baetsle, 2003). The $Cs^+$ and $Sr^{2+}$ isotopes have a large

environmental impact, they occur dominantly as the aqueous species $Cs^+$ and $Sr^{2+}$ and are part of the non-hydrolysing cations. The $Cs^+$ cation is stable over a very large $E_h$-pH domain (Takeno, 2005). The high solubility increases the potential mobility through the groundwater into the biosphere. In addition, $Cs^+$ is accumulated by plants and microorganisms due to its chemical similarity to $K^+$, a macronutrient. Caesium has no known biological role (Avery, 1995; White and Broadley, 2000). Caesium taken up by plants is then readily transferred to organisms higher in the trophic chain, including animals which may form important food sources for human populations, such as fish (Smith et al., 2002; Sundbom et al., 2003), grazing livestock (Andersson et al., 2001), game (Hanson, 1967; Crête et al., 1990) and mushrooms (Kalač, 2001; Guillén and Baeza, 2014). The divalent $Sr^{2+}$ ion generally occurs across a wide $E_h$-pH range in water but the neutral carbonate complexes become more dominant under alkaline conditions (Missana et al., 2014a). Strontium has properties similar to $Ca^{2+}$ and, hence, can be deposited in bone and marrow.

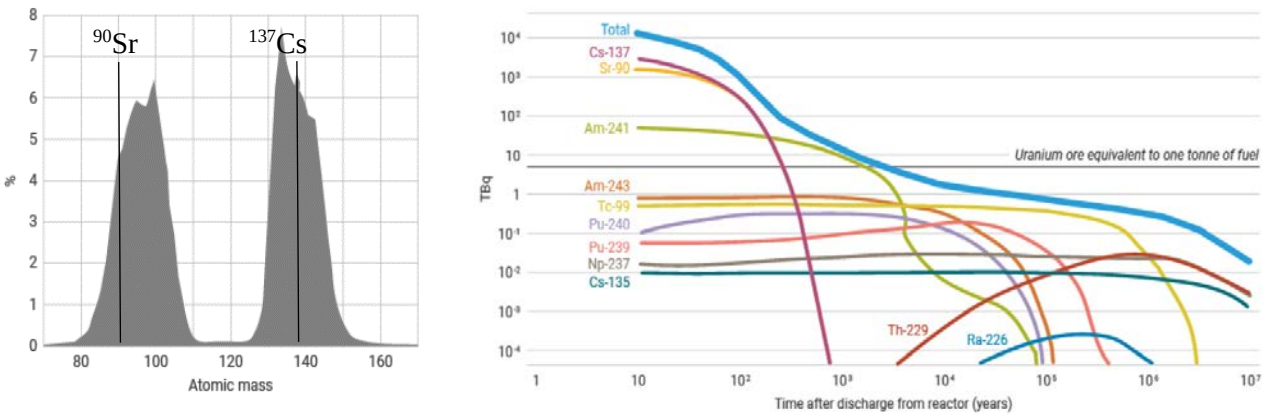


Figure 1.6 The distribution of fission products (left) and the activity of high level waste from one ton of used fuel (right) (Chan, 1992).

## Sorption of caesium and strontium onto micaceous minerals

### *Sorption sites and ion exchange*

Clay mineral surfaces have a permanent negative charge due to isomorphous substitutions in the structure. The excess charge is compensated by the electrostatic attraction of aqueous cations (Figure 1.7). The layer charge in glauconite originates from substitutions in the octahedral and tetrahedral layer, while in illite, the substitution in the tetrahedral layer determines the permanent layer charge (Meunier, 2005). This results for illite in a less diffuse layer charge and higher preference for inner-sphere complexes, i.e. unhydrated cations. The di-trigonal cavities in the interlayer correspond closely to the ionic radius of $K^+$. The interlayer $K^+$ is unavailable for ion exchange for most cations with exception for cations with similar ionic radius ($Cs^+$, $NH_4^+$, $Rb^+$). Upon illite weathering, some of the $K^+$ at the outer edges of the interlayer can be leached forming *frayed edge sites* (FES) and hydrated interlayer sections. In smectite, the permanent charge is largely the result of substitutions in the octahedral sheet ($Mg^{2+}$ and $Fe^{2+}$ for $Al^{3+}$ and $Fe^{3+}$). Compared to illite the charge is more diffuse over the tetrahedral layer leading to the formation of outer-sphere complexes (Bruggeman and Maes, 2016).

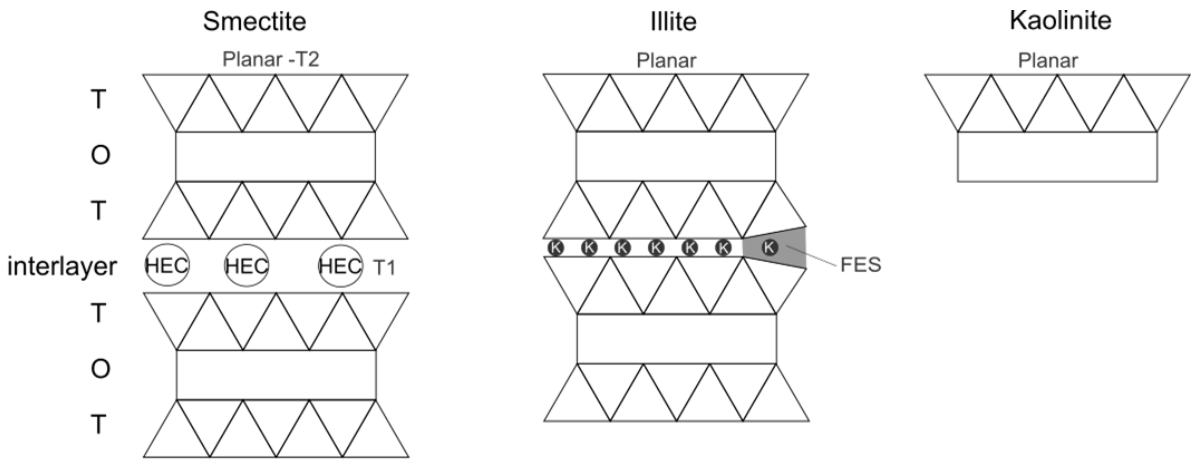


Figure 1.7 Schematic crystal structure of smectite, illite and kaolinite and the sorption sites of importance for Cs and Sr (T tetrahedral, O octahedral). From smectite to illite a collapse of the interlayer can be observed. The interlayer space is no longer accessible to hydrated exchangeable cations (HEC). Only cations with similar ionic radius to $K^+$ (non-hydrated) can exchange with $K^+$ in the interlayer.

On the illitic clay minerals, three main types of sorption sites can be distinguished: the planar sites and two types of frayed edge sites, i.e. the FES-type I and the FES-type II sites, in literature mostly referred as to FES and type II sites (Figure 1.8) (Brouwer et al., 1983; Eberl, 1980; Sawhney, 1972; Sawhney, 1970). The planar sites have a preference for outer sphere complexes to compensate the negative charge, the selectivity differences among the alkaline metals for sorption are small. By contrast, the type I and type II FES sites are highly selective and adsorb only dehydrated cations due to the size of the sites. However, they only represent a small fraction (~2 % in the type I and 20% in the type II) of the total cation exchange capacity (Bradbury and Baeyens, 2000). The FES (type I and type II) can be depicted as an entrance to the interlayer (Okumura et al., 2018). The illite interlayer has a thickness of about 1.0 nm compared to 1.0-1.4 nm for the FES (type I and type II) (Lee et al., 2017). In the current state-of-the-art characterisation methods (e.g. High Resolution Transmission Electron Microscopy) differences in structure between the type I and type II sites cannot be distinguished. It possible that rather than two discretised high affinity sites the FES might represent a continuum with variable selectivity. Over time ions can diffuse into the interlayer through direct exchange of interlayer $K^+$ or through the migration in a hydrated section of the interlayer. The exchange takes place over the full interlayer space, not just at the edges. Once $Cs^+$ has gained access to the interlayer, the interlayer is a fast path for diffusion (Fuller et al., 2015). Larger (hydrated) cations (e.g. $Na^+$ (sodium), $Ba^{2+}$ (barium), $Sr^{2+}$, $Ca^{2+}$) can cause an expansion of the interlayer though the presence of $K^+$ or $NH_4^+$ in solution can prevent the expansion or even cause a collapse.

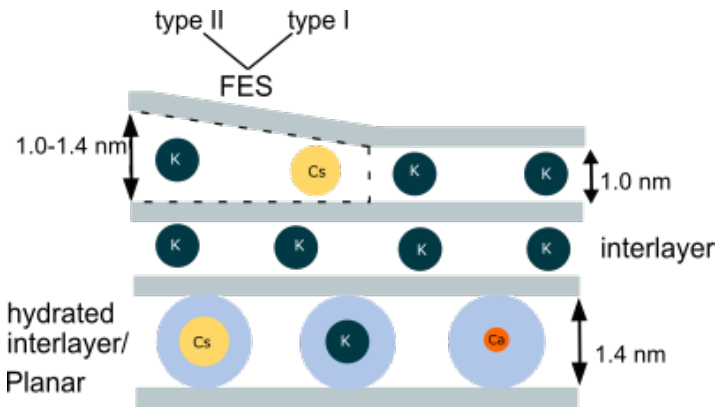


Figure 1.8 Schematic representation of the sorption sites on glauconite and illite-type clays.

Strontium is predominantly bound on the planar sorption sites, making it vulnerable to exchange by cations with higher charge density. The capacity of the planar sites represent about 80-98 % of the effective CEC in illite (Bradbury and Baeyens, 2000; Brouwer et al., 1982; Fuller et al., 2014; Missana et al., 2014a). Contrary to illite, the interlayer is accessible to (hydrated exchangeable) cations in smectite-like minerals leading to an increase of the planar sites to nearly 100 % of the CEC. Glauconite occurs mostly as a mixed layer mineral of illite-like and smectite-like end members (Meunier and El Albani, 2007). The CEC of illite ranges 20-40 $cmol_c\ kg^{-1}$, that of smectite 80-120 $cmol_c\ kg^{-1}$ (Meunier, 2005). The selected data for glauconite indicate an intermediate CEC suggesting that the $K_D$ of $Sr^{2+}$ is expected in the range between that of illite and that of smectite.

In the evolution from illite to smectite, the interlayer space becomes accessible leading to an increase in CEC (Drits et al., 1997). However, the fraction of FES and type II sites to the total CEC will decrease. In addition to the three types of sorption sites with ion exchange, pH depending sites are present at the broken edges of the phyllosilicate minerals as well. Depending on the pH they can be protonated or deprotonated by adsorption of $H^+$ or $OH^-$. Cations can form inner sphere complexes with the deprotonated sites. This sorption mechanism on these sites is surface complexation.

The affinity of cations for the sorption sites increases with the radius of the ion (non-hydrated) according to the Hofmeister series for most clays (Stumm et al., 1996) (Table 1.4). The $Cs^+$ has the most suitable hydrated ion size of the monovalent ions for the illite FES. The low hydration energy allows $Cs^+$ to dehydrate and enter the illite interlayer (Lee et al., 2017). The selectivity differences generally rank:

$$Cs^+ > NH_4^+ > K^+ > Na^+$$
$$Ba^{2+} > Sr^{2+} > Ca^{2+} > Mg^{2+}$$

Table 1.4 Ionic radius, hydrated radius and hydration free energy of the relevant cations. Hydrated and ionic radii after Tansel (2012), hydration free energy from Marcus (1994).

| Cations | $Cs^+$ | $NH_4^+$ | $K^+$ | $Na^+$ | $Ba^{2+}$ | $Sr^{2+}$ | $Ca^{2+}$ | $Mg^{2+}$ |
|---|---|---|---|---|---|---|---|---|
| Ionic radius (nm) | 0.174 | 0.148 | 0.152 | 0.102 | 0.136 | 0.125 | 0.100 | 0.072 |
| Hydrated radius (nm) | 0.329 | 0.331 | 0.331 | 0.358 | 0.404 | 0.412 | 0.412 | 0.428 |
| Hydration free energy (kJ/mole) | -264 | -307 | -343 | -365 | -1250 | -1380 | -1505 | -1830 |

Because of the environmental relevance of $^{137}Cs$ and $^{90}Sr$, their sorption on clay minerals has been extensively studied. The sorption strength of an element (ion or neutral species) can be quantified as the solid-liquid distribution coefficient ($K_D$) or the ratio of the concentration of element sorbed to the solid phase (mol $kg^{-1}$) to the equilibrium concentration in solution (mol $L^{-1}$) (*Eq 1.1*).

$$K_D = \frac{conc\ sorbed\ on\ solid}{conc\ in\ solution} \times \frac{V}{m} \quad Eq.\ 1.1$$

where V is the volume of the solution (L) and m the weight of the sorbent (kg). The $K_D$ depends on the sorption capacity, selectivity, competition and site heterogeneity of the solid or mineral in this case.

Table 1.5 Distribution coefficients ($K_D$) expressed in $log_{10}$ units of a series of clay mineral standards as reported in literature at pH 7 and an ionic strength (IS) of 0.01 M ($NaClO_4$), unless otherwise specified, for trace concentrations of Cs or Sr. The results for the same standard vary between authors and the differences in composition of the background electrolyte make the results not fully comparable.

| Mineral | CEC<br>$cmol_c\ kg^{-1}$ | Log $K_D$ Cs<br>L $kg^{-1}$ | Log $K_D$ Sr<br>L $kg^{-1}$ |
|---|---|---|---|
| Na-montmorillonite (SWy-1) | 87 [3] - 94 [1] | 3.4 [1] - 2.9 [3] | 4.3 [2] |
| Ca-montmorillonite | 94 [1] | 3.1 [1] | |
| K-montmorillonite | 94 [1] | 2.9 [1] | |
| Na-illite (illite du Puy) | 12.1 [5] - 30 [1] | 3.4 [5] - 4.5 [1] | 3.6 [4][5] - 3.9 [2] |
| K-illite | 30 [1] | 3.6 [1] | |
| Kaolinite (KGa-1b) | 2.0 [3] | 2.5 [3] | |
| Boom Clay | 13 - 27 [6] | 4.0<br>IS 0.02 M [6] | 2.5<br>IS 0.02 M [6] |
| Glauconite | 10-18[8][9] | 3.6 [7] -3.9 [8] | 1.9 [8] |

[1] (Staunton and Roubaud, 1997); [2] (Missana et al., 2008); [3] (Durrant et al., 2017) [4] (Bradbury, 2005); [5] (Poinssot et al., 1999b); [6] (Bruggeman and Maes, 2016; Maes et al., 2017); [7] (Belousov et al., 2019); [8] (Voronina et al., 2015b); [9] (Adriaens et al., 2014)

In Table 1.5 an overview is given of literature distribution coefficients ($K_D$) for $Cs^+$ and $Sr^{2+}$ for a series of clay mineral standards. The non-selective sorption of $Sr^{2+}$ on clay minerals makes the $Sr^{2+}$ $K_D$ a function of the background electrolyte. The $K_D$ values reported in literature have a large variation in background electrolyte composition, ionic strength and pH. The data selected for Table 1.5 was reported as measured at pH 7 in a 0.01 M $NaClO_4$ solution unless otherwise specified.

*The Radiocaesium Interception Potential of minerals, soils and sediments*

For $Cs^+$, the $K_D$ (L $kg^{-1}$) is highly dependent on the $K^+$ concentration. Therefore Cremers et al. (1988) developed the Radiocaesium Interception Potential (RIP) to quantify the $Cs^+$ interception at trace concentration taking into account the $K^+$ competition. At low $Cs^+$ concentrations (trace < $10^{-8}$ M) the sorption of $Cs^+$ is dominated by the FES. $Cs^+$ sorption at the FES is highly selective and will determine the (short term) $Cs^+$ retention (Valcke, 1993). The Cs-to-K selectivity in the FES can be written as *Equation 1.*2 on the assumptions that i) the amount of intercepted $Cs^+$ in the *FES* is only representing a very small fraction of the total *FES* capacity, ii) $K^+$ is the only competing cation, present in known concentration, and iii) the $Ca^{2+}$ background concentration prevents $Cs^+$ sorption on the planar sites (de Preter, 1990).

$$K_c^{FES}\,(Cs/K)(Z_{Cs} \rightarrow 0) = \frac{Z_{Cs} \times m_K}{Z_K \times m_{Cs}} = \frac{K_D^{Cs} \times m_K}{Z_K \times [FES]} \qquad \textit{Eq. 1.2}$$

with $K_c^{FES}$ (Cs/K) the Cs-K selectivity coefficient in the FES (type I) (-), Z the fractional loading in the FES (type I) (-), m the solution molarity (mol $L^{-1}$), $K_D^{Cs}$ the distribution coefficient (L $kg^{-1}$) of $Cs^+$ at trace concentration and [FES] the capacity of the FES (type I) sites (mol $kg^{-1}$). At trace loadings of $Cs^+$ the FES will be nearly fully occupied by $K^+$ and $Z_K$ can be assumed 1. *Equation 1.2* can be rewritten as:

$$K_D^{Cs} = \frac{K_c^{FES}\,(Cs/K) \times [FES]}{m_K} \qquad \textit{Eq. 1.3}$$

$$K_D^{Cs} \times m_K = K_c^{FES}\,(Cs/K) \times [FES] = \boldsymbol{RIP} \qquad \textit{Eq. 1.4}$$

The RIP at trace $Cs^+$ loadings is the product of the high affinity site capacity and its selectivity. The RIP is expected to be constant because both the FES and $K_c$ (Cs/K) have a given value. The linear *RIP* concept is theoretically valid in the 5-10 mmol $L^{-1}$ $K^+$ concentration range (de Preter, 1990). In the lower $K^+$ concentration domain the *RIP* is underestimated (Hisashi et al., 2013) (Wauters et al., 1996b). In Table 1.6 the RIP values are given for a series of clay mineral references.

Table 1.6 Radiocaesium interception potential values for a series of clay mineral references and the corresponding CEC value for that specific sample.

| Mineral | CEC $cmol_c\ kg^{-1}$ | RIP $mol\ kg^{-1}$ |
|---|---|---|
| Illite[1](Yong-koong illite Korea) | 14.2 | 25 |
| Illite[2] | 26.4 | 12.5 |
| Illite-smectite[2] | 59.4 | 7.5 |
| Montmorillonite[1] (Sigma Aldrich) | 58.0 | 20 |
| Montmorillonite[3] (Wyoming) | 87 | 3.6 |
| Muscovite[2] | 5.9 | 0.74 |
| Kaolinite[3] | 1.1-4.0 | 0.96-3.1 |
| Boom Clay[2] | 33.0 | 5.2 |

[1](Lee et al., 2017)
[2] (de Preter, 1990)
[3] (Ogasawara et al., 2013)

*Sorption kinetics*

The $Cs^+$ sorption on illite is described by two phases. A rapid initial adsorption phase (hours to days) followed by slow and continued sorption. The competition with $K^+$ and $NH_4^+$ controls the $Cs^+$ sorption in the rapid initial phase (Madruga, 1993). Sorption on the planar sites is considered instantaneous though reversible. The selective sorption sites have more heterogeneous sorption kinetics. Depending on the position, accessibility and current occupation of the site, the reaction rate will be different. The sorption on the FES is partially irreversible even at short time scales of hours to days (de Koning and Comans, 2004; Durrant et al., 2017). The $Cs^+$ migration into the interlayer is limited by the rate of diffusion. Therefore, the interlayer exchange is most often not taken into account, rather considered part of the slow reactions on the selective sorption sites. Slow sorption on illite can take months to years to reach equilibrium and lead to a factor 2 increase in the $K_D$ (Madruga, 1993). The $Cs^+$ in the interlayer is considered irreversibly sorbed (de Koning and Comans, 2004; Fuller et al., 2015).

The $Sr^{2+}$ sorption kinetics can be described with first order or pseudo second order kinetics (Akar et al., 2005), there is only a fast reaction, slow reactions are less pronounced, because $Sr^{2+}$ sorption only occurs as ion exchange on the planar ion exchange sites.

*Sorption models*

Sorption models aim to predict or describe the concentration dependent distribution of a solute between the solid and aqueous phases. For RN sorption, this concentration dependency has little environmental relevance, because the fission products occur at extremely small concentrations in the environment. For process understanding, however, this concentration dependent sorption is often experimentally addressed by adding (stable) carrier isotopes. Linear sorption is the simplest form and can be described by a one-site model. Non-linearity reflects site heterogeneity, or differences in selectivity and capacity.

The concentration dependent sorption of $Cs^+$ on kaolinite and smectite is generally linear (Durrant et al., 2017). If non-linearity is observed, it often reflects the presence of trace amounts of other clay minerals such as illite and vermiculite (Durrant et al., 2017; Missana et al., 2014b). Caesium sorption on illite is clearly non-linear, a two-site (Missana et al., 2014a) or three-site model provides a better fit with experimental data (Bradbury and Baeyens, 2000; Poinssot et al., 1999a). The model requires a sorption capacity and selectivity of each site. Bradbury and Baeyens (2000) developed a three-site sorption model for a theoretical illite based on experimental data (Table 1.7, Figure 1.9). Based on the mineralogical similarities between illite and glauconite a similar model with adjusted site selectivities and capacities should apply to glauconite.

Experimental data show linear to pseudo-linear sorption of $Sr^{2+}$ to clay minerals (Akar et al., 2005). A one-site model is sufficient to describe $Sr^{2+}$ sorption.

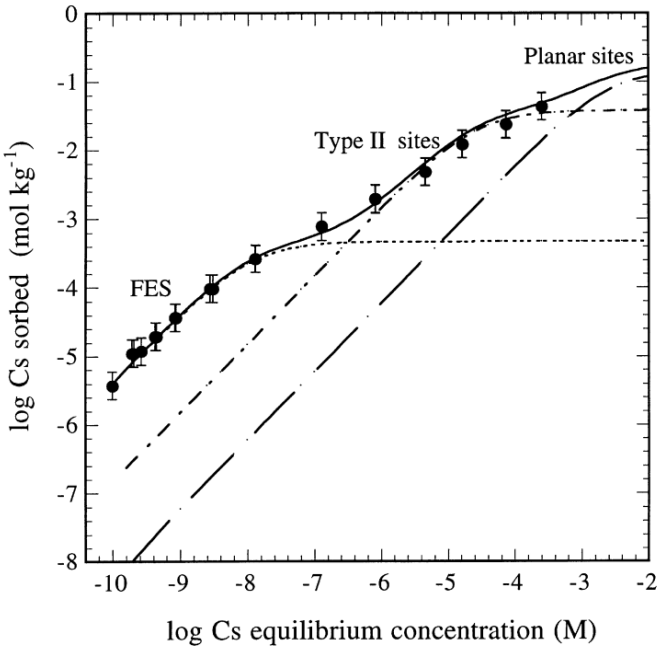


Figure 1.9 Cs sorption isotherm for a Na-conditioned Illite du Puy, measured in 0.1 M $NaClO_4$. The isotherm is denoted by the continuous line with the contributions of the FES (type I), type II and planar sites in respectively dotted, dot-dashed and dashed line (after Bradbury and Baeyens (2000)).

Table 1.7 Site capacities and selectivities for a three-site sorption model of $Cs^+$ to illite (Na Illite du Puy) (Bradbury and Baeyens, 2000).

| | FES – type I | FES – type II | planar |
|---|---|---|---|
| Capacity (% of the CEC) | 0.25 | 20 | 80 |
| Log $K_c$ Cs-Na | 7.0 | 3.6 | 0.5 |
| Log $K_c$ Cs-K | 4.6 | 1.5 | 0.5 |
| Log $K_c$ Cs-$NH_4$ | 3.5 | - | - |

*Reversibility of sorption*

Sorption of $Cs^+$ and $Sr^+$ on clay minerals takes place as ion exchange. Ion exchange is a reversible reaction implying that sorption is reversible. The extent and the rate of the desorption will depend on the intraparticle diffusion, the composition of competing cations in solution and the ion selectivity of the sorption site. The $Cs^+$ cation can be desorbed from montmorillonite and kaolinite at all concentrations. On illite, $Cs^+$ sorption is partially irreversible due to the high selective sorption on the FES type I and type II sites. At high surface loadings, approximately 40-45% of the $Cs^+$ can be desorbed (Durrant et al., 2017; Liu et al., 2003). At lower pH (~3) the desorbed $Cs^+$ fraction increases up to 60-80 %. The $Cs^+$ can be fixed by migration into the interlayer or by the collapse of the interlayer. In illitic minerals the interlayer (edges) can collapse trapping the $Cs^+$ at high concentrations of $K^+$. The fixation of $Cs^+$ in the interlayer limits the desorption to the rate of interlayer diffusion (Liu et al., 2003). The non-selective sorption of $Sr^{2+}$ to the planar sites increases the sensitivity for desorption. An increase of the ionic strength of the ground water can lead to the remobilisation of $Sr^{2+}$ (Wallace et al., 2012).

*Knowledge gap*

Sorption of radiocaesium and radiostrontium on glauconite has been studied before in the context of remediation of contaminated land (Belousov et al., 2019; Semenishchev et al., 2016; Voronina et al., 2015a; Voronina et al., 2015b; Voronina et al., 2013). However, the effect of natural variations in mineralogy were not taken into account. The Neogene glauconite has been studied from a mineralogical perspective, finding large variations in glauconite content, pellet size and morphology and to a lesser extent mineralogical composition. The effects of these variations on the sorption of $Cs^+$ and $Sr^{2+}$ are unclear. The mineralogical comparisons between glauconite and illite suggest similar sorption sites and capacities. However, the sorption sites have not been characterised and selectivity coefficients are unknown.

In addition, the classical sorption studies (mentioned above) have used milled glauconite in dilute concentrations (1 g $L^{-1}$). The pelletal occurance of glauconite in the Neogene sands suggests other sorption dynamics might be at stake, with possible effects of the pellet size on the sorption capacity and kinetics. The kinetics are highly relevant in scenarios with high pore water flow rates, as can be expected in the sands. Finally, little information is available on the stability or weathering susceptibility of the glauconite and the effect on RN sorption.

## 6. Objectives

This thesis is devoted to answer the question to what extent glauconite sand can act as a permeable geological barrier in a radioactive waste disposal system. The aim of this thesis is to provide a mechanistic understanding of sorption of radiocaesium and radiostrontium onto diverse natural glauconite (sands) from the Cenozoic (Paleogene and Neogene) formations. It is hypothesised that glauconite is a strong sorbent for $Cs^+$ and $Sr^{2+}$ based on the mineralogical similarities to illite, suggesting that selective sorption of $Cs^+$ sorption is possible. However, the density and size of the glauconite pellets can reduce and slow down sorption rate compared to dispersed clay minerals. Hence, the high pore water velocity that can be expected in highly permeable sand suggests that the permeable geological barrier may not be efficient, i.e. an early breakthrough could occur during RN transport because of local non-sorption equilibrium across pore water-pellet boundaries. Finally, the weathering of glauconite requires attention during storage, the glauconite minerals are redox active and can transform during oxidation or in reaction to alkaline conditions. Cement, and consequently cementitious pore water, will be omnipresent in the radioactive waste facilities from seals and buffer material to general construction (Mann et al., 2019). This requires studies on the longevity of Cs and Sr sorption on weathered glauconite.

The specific objectives of this thesis are

i. to assess the sorption of trace concentration $^{137}Cs$ on natural glauconite sands from the Cenozoic formations in Belgium. It is speculated that the $Cs^+$ sorption potential and kinetics are affected by the mineralogical composition of the glauconite sand, the size of the glauconite grains and the weathering grade;

ii. to characterise and model the concentration dependent selective $Cs^+$ sorption on a range of glauconite sands and relate the sorption parameters to the mineralogy. The $NH_4$/K selectivity coefficient on the frayed edge sites (FES) was used as a fingerprint of the highly selective sorption sites;

iii. to evaluate the validity of chemical equilibrium for $Cs^+$ sorption during transport in glauconite sand at a range of different realistic flow rates. Forward transport modelling will be used to reproduce experimental results;

iv. to assess the strength and kinetics of radiostrontium sorption on the natural (subsurface) and weathered (surface) glauconite sands;

v. to assess the effects of accelerated weathering of glauconite on RN sorption in order to evaluate the evolution of the sorption potential and retention over the time frame of radioactive waste disposal. For this naturally and artificially weathered glauconite sands will be used with four different weathering conditions: alkaline, acidic, oxic and anoxic.

To accomplish these objectives, experimental and computational studies were combined. This thesis is part of the larger investigation into the disposal of radioactive waste in Belgium. The glauconite sands of interest were, hence, those sampled below the planned surface disposal in Dessel (Cat. A) and surrounding the Boom Clay Fm. Therefore samples were taken from subsurface glauconite sands from drill cores and excavations in the Mol-Dessel region. In addition, weathered samples from the surface section of the Diest Fm were collected in outcrops in the region of Leuven. The sorption $K_D$ of $Cs^+$ and $Sr^{2+}$ in trace concentrations were measured in batch sorption with the radiotracers $^{137}Cs$ and $^{85}Sr$ on a large batch of glauconite sands. A linear regression analysis was used to determine the predictive factors for $Cs^+$ and $Sr^{2+}$ sorption (Chapter 2 and 5). An experimental determination of the sorption isotherm in a wide range of $Cs^+$ concentrations was used to identify the site capacities and selectivities (Chapter 3). The evaluation of chemical equilibrium of $Cs^+$ sorption was tested in a column set-up with variable flow rates (Chapter 4). Finally, a limited set of glauconite sands was subjected to four different environments, alkaline (young cement water), acidic, oxic and anoxic for a period up to 27 months. The material characteristics ($Cs^+$ sorption, CEC, Fe speciation, major elements) were determined before and after treatment (Chapter 6).

# Chapter 2. Radiocaesium sorption on natural glauconite sands

Adapted from Bruneel et al. (2020)

## Abstract

The Neogene-Paleogene glauconite sands of Belgium cover the Boom Clay deposits that are candidate host for radioactive waste disposal. It is unclear if the highly permeable sand formations may act as an additional barrier for radiocaesium ($^{137}Cs$) or could be added as a complementary sorption sink in a surface disposal concept. Glauconite is an Fe-rich phyllosilicate that is mainly present as 250-125 µm sized pellets in sand, it is unknown to what extent and how fast these pellets may bind $Cs^+$. Pelletised clays embedded in sand may have poorly accessible high affinity sites for $Cs^+$. The $^{137}Cs$ sorption potential on 11 different glauconite sands was measured in batch in a background solution of 0.1 M $CaCl_2$ and 0.5 mM KCl. The log transformed $^{137}Cs$ distribution coefficient $K_D$ (L $kg^{-1}$) after 30 days reaction ranged 3.4-4.3, surprisingly close to the $K_D$ of the Boom Clay (3.5). Isolated glauconite fractions exhibited similar $^{137}Cs$ sorption potentials (log $K_D$ 4.1-4.3) as the reference Illite du Puy (4.4). The small $K_D$ variation among the Neogene-Paleogene sands was explained by its glauconite content (r=0.82). The $^{137}Cs$ sorption kinetics (1-57 days) of milled pellets (<2 µm) confirmed slower reaction with intact (un-cracked) pellets than with milled samples. Additionally, the $K_D$ values of milled samples (57 days) sorption are 1.1-1.5 fold larger than the corresponding intact pellets, suggesting that not all $Cs^+$ binding sites are accessible in intact pellets. Strongly weathered pellets exhibited cracks (visible with SEM). In these pellets the $K_D$ was similar for milled and intact pellets suggesting that cracks increase the accessibility of the inner sorption sites. After 8.5 months the $K_D$ values were 1.6-1.8-fold above corresponding 1 month data and these long-term reactions were more pronounced as total sand $K^+$ content was larger. An adsorption-desorption experiment illustrated that $^{137}Cs$ sorption is not fully reversible.

## 1. Introduction

Radioactive waste needs to be stored securely for hundreds to hundreds of thousands of years. Sand formations are generally not considered a suitable host material for radioactive waste repositories due to their high permeabilities and low sorption potentials. This implies fast transport of radionuclides (RN) with the pore water, against any potential disposal concept. In Belgium, the Neogene-Paleogene glauconite sands are, however, being considered as natural barrier. These sands are highly permeable, but contain a strongly sorbing component, glauconite. These Neogene-Paleogene glauconite sands may be added as an extra embankment below the surface disposal for the short-lived and low-level waste. For the high-level and/or long-lived radioactive waste, deep geological disposal is proposed. Host rocks that might qualify for long-term disposal are poorly indurated clays 200 to 600 m below the surface (e.g. Boom Clay or Ypresian clays). Both Boom Clay and Ypresian clays are enclosed in glauconite-rich sands or silts. In the Neogene and Paleogene marine sands, glauconite is very abundant. Some formations have low percentages (< 5% e.g. Mol Fm), others have, on average 35-40% (e.g. Diest and Berchem Fm) and locally percentages up to 80% occur (Adriaens et al. 2014). In the NE of Belgium, the 100 m thick Boom Clay layer is situated below about 100 m of Neogene-Paleogene glauconite sands and above 175 m of Paleogene glauconite sands/silts.

Glauconite is a phyllosilicate, classified as a clay mineral, but mostly present as coarse pellets in the sand-silt fractions (2 – 0.002 mm), only minor amounts are found in the clay fraction (< 2µm). The term glauconite is often used for the description of green globular silt- to sand-sized pellets in sediments, without any mineralogical connotation. The mineral glauconite is described as an iron (Fe) - potassium ($K^+$) phyllosilicate, comparable to an Fe-rich illite with $K^+$ the main interlayer cation, with (K,Na) $(Fe^{3+}Fe^{2+},Al,Mg)_2(Si,Al)_4O_{10}(OH)_2$ the structural formula. Finding a pure glauconite is exceptional, most often glauconite pellets consist of one or more Fe-rich mixed layer glauconite-smectite phases (Meunier and El Albani, 2007). In this work the term ‘glauconite’ refers to the green pelletal fraction of the sands, unless stated otherwise.

The diverse composition of glauconite pellets stems from both the formation and weathering history. Glauconite is formed through diagenesis of granular substrates in marine sediment at shallow depth. During formation $K^+$ and Fe are incorporated in the structure. The $K^+$ content increases with maturity with $K^+$ > 8 wt% for mature glauconite (Meunier and El Albani, 2007; Odin, 1988). Due to the presence of both $Fe^{3+}$ and $Fe^{2+}$, glauconite is redox sensitive. During weathering Fe and $Mg^{2+}$ are removed from the structure and $K^+$ is leached from the interlayer by which glauconite evolves to a more smectitic form (Courbe et al., 1981; Van Ranst and De Coninck, 1983). Additionally, physical weathering can cause the disintegration of the glauconite pellets to the clay fraction glauconite. The Neogene-Paleogene glauconite mineralogy has been studied in detail by Adriaens et al. (2014) for both pelletal and clay-sized glauconite. On average, the glauconites have 6-12 % expandable layers and total Fe content of 16

– 23.5 wt% with an $Fe^{3+}/Fe^{2+}$ ratio of 9/1. The high $K^+$ content (5.5 – 7 wt% $K_2O$) makes the Neogene-Paleogene glauconites highly mature according to the classification of Odin (1988).

Sorption of RN on glauconite (sands) are not as widely studied as sorption on illite. This study focuses on the sorption of $^{137}Cs$ on glauconite sands. Caesium-137 poses a long-term radiation risk due to a combination of a half-life $t_{1/2}$ of 30 years and a large dose rate. Caesium is present in the environment as monovalent hydrated $Cs^+$ and is highly soluble under all $E_h$ and pH conditions. The mobility of $^{137}Cs$ in the environment is mainly controlled by sorption on clay mineral surfaces in soils (Fuller et al., 2015; Sawhney, 1972; Takeno, 2005). Just as illite, glauconite is expected to have strong sorption, but the pellet form might be an obstacle for fast and near complete immobilization. The $Cs^+$ sorption sites in glauconite are largely similar to the sites on illite due to the chemical and mineralogical resemblances between both minerals. This suggests a high sorption potential, however, sorption may be limited by slow intraparticle diffusion, i.e. slow or incomplete within realistic time frames.

The $Cs^+$ sorption on illite can be described by a three-site exchange model: frayed edge sites (FES) type I, FES type II sites and planar sites (Figure 2.1) (Bradbury and Baeyens, 2000; Fuller et al., 2015; Poinssot et al., 1999a). The FES (type I) and (FES) type II sites are often considered together as the highly selective sites, with Cs-K selectivity coefficients exceeding $10^4$. The FES have the highest specificity for $Cs^+$ over other monovalent cations (e.g. $K^+$, $NH_4^+$, sodium ($Na^+$)) and are responsible for strong sorption of $Cs^+$ in the low, but relevant, concentration domain. Larger ions simply do not fit in the limited space of the FES. Despite the high selectivity for $Cs^+$, the FES are only representing 0.25 % of the total CEC (cation exchange capacity) (Bradbury and Baeyens, 2000). The type II sites can be found at the edges of the layers. Here, the layers are sufficiently widened to be accessible to larger ions reducing the selectivity for $Cs^+$. The planar sites originate from the isomorphic substitutions in the structure. The permanently negative charged surfaces provide high capacity but low affinity sites (Bradbury and Baeyens, 2000). $^{137}Cs$ sorption on the planar sites of illite is fast, with only a few hours to reach equilibrium. On the frayed edge sites sorption equilibrium is only reached after 4-5 days, most probably due to the size and the accessibility of the sites compared to the planar sites (Poinssot et al. 1999).

Potassium has a perfect size to fit in the interlayer and due to the positive charge the negative clay layers are attracted. Increasing the $K^+$ content causes a stronger ‘bond’ between the clay layers or a so called layer collapse. When $K^+$ is leached from the interlayer, due to weathering for example, the layer edges open up and new frayed edge sites are available to $Cs^+$ sorption.

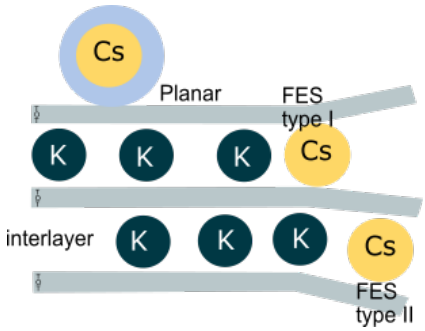


| | | FES | Type II sites | Planar sites |
|---|---|---|---|---|
| (Bradbury and Baeyens, 2000) | Capacity (meq $kg^{-1}$) | 0.5 | 40 | 160 |
| | (Cs-K) Log $K_c$ | 4.6 | 1.5 | 0.5 |
| (Fuller et al., 2014) | Capacity (meq $kg^{-1}$) | 0.004 | 1.6 | 65 |
| | (Cs-K) Log $K_c$ | 5.5 | 3.0 | 1.1 |
| (Missana et al., 2014b) | Capacity (meq $kg^{-1}$) | 0.46 | 39 | 155 |
| | (Cs-K) Log $K_c$ | 4.2 | 2.0 | 1.15 |

Figure 2.1 Three-site model with site capacities (meq $kg^{-1}$) and site selectivity coefficients (log $K_c$) for modelling Cs sorption on illite as described by three different authors (Bradbury and Baeyens, 2000; Fuller et al., 2014; Missana et al., 2014b).

This study aimed to assess the sorption of trace $^{137}Cs$ ([Cs] < $10^{-7}$ M) on natural glauconite sands from the Neogene-Paleogene formations in Belgium. It is assumed that glauconite is the main sorbing component in the sands. The sorption of $^{137}Cs$ on glauconite is expected to be similar to $^{137}Cs$ sorption on illite for clay-sized fractions, however, sorption might be slower or less complete for the pellet form due to restricted access to the inner sorption sites. In addition, the mineralogical and compositional variation in the glauconite sands among different formations is addressed, that mineralogy is expected to affect the $^{137}Cs$ sorption. A series of glauconite sands were sampled, their mineralogical compositions were characterised and $^{137}Cs$ sorption was measured with due attention to reaction kinetics. Pellet isolation and pellet grinding were used as experimental treatments to interpret sorption data of intact sands.

## 2. Materials and methods

### Sample selection

Table 2.1 Inventory of the selected glauconite sand samples from the Neogene-Paleogene formations for this study (GL glauconite fraction). The ON-Dessel5 31W370 borehole from the collection of NIRAS/ONDRAF was sampled at four positions to get a wider variability of samples in the section of Diest-Berchem Formation. The samples indicated with shaft excavation originate from the excavation of the second shaft to the underground lab HADES in Mol. The Boom Clay (BC) sample is a sample from a recent sampling campaign at HADES level. The sampling depth is expressed in mTAW, or the reference level in Belgium (Tweede Algemene Waterpassing).

| | Fm | Member | Origin | mTAW | Lithology | Intact | | Milled | |
|---|---|---|---|---|---|---|---|---|---|
| | | | | | | Sand | GL | Sand | GL |
| D1 | Diest | | Shaft excavation | -73 | Sand | X | X | X | X |
| D2 | Diest | | Shaft excavation | -91 | Sand | X | X | X | X |
| D3 | Diest | | ON-Dessel 5-30 | -95 | Sand | X | | | |
| D4 | Diest | Dessel | ON-Dessel 5-44 | -109 | Sand | X | | | |
| D5 | Diest | Dessel | ON-Dessel 5-48 | -113 | Sand | X | | | |
| B1 | Berchem | Antwerp | ON-Dessel 5-63 | -126 | Sand | X | X | X | X |
| B2 | Berchem | Antwerp | Shaft excavation | -134 | Sand | X | | X | |
| W14 | Berchem | Antwerp | BC quary Wienerberger Rumst | 30.5 | Sand | | X | | X |
| V1 | Voort | | Shaft excavation | -144 | Clayey sand | X | | X | |
| V2 | Voort | | Shaft excavation | -152 | Clayey sand | X | | | |
| V3 | Voort | | Shaft excavation | -140 | Clayey sand | X | X | X | |
| I | Na-illite du Puy | | Reference material | | Clay | X | | | |
| BC | Boom Clay | Putte | HADES sampling campaign 2017 | -197 | Clay | X | | | |

All experiments were performed using natural glauconite sands. A selection of 11 sand samples was made over the Voort, Berchem and Diest Formation (Fm) from the Neogene-Paleogene layer above the Boom Clay in Mol (NE Belgium). These formations have variable glauconite and total clay mineral content. Some sections of the formations have been reworked or eroded, leading to variable weathering states in the glauconite pellets. Samples were collected from the drilling core ON-Dessel5 and the shaft excavation. Two reference samples, i.e. purified Na-conditioned Illite du Puy and a Boom Clay sample, were included (Table 2.1). A full overview of all samples used in this work is given in the annex (Sample selection).

### In-situ pore water samples

Fresh in-situ pore water samples were sampled in several piezometers in the region to achieve pore water compositions in each formation. The piezometers (R-4b, L64a, L64b, R-4c and R-6d) were selected at corresponding depth and formation for the glauconite sand samples. Before sampling, the well volume

was pumped out three times to get fresh aquifer water. The pore water samples were acidified in the field with 1% $HNO_3$.

**Sample preparation**

The samples had been stored after sampling in vacuum sealed bags under variable conditions, i.e. in a freezer or cooled room. The samples were dried at 60 °C before use in the batch sorption experiments. Part of the experiments were performed on the separated glauconite fraction of the samples; Table 2.1 shows the selected samples. Glauconite can be separated from the matrix by magnetic separation (Frantz Isodynamic magnetic separator). Since the glauconite fractions contain quartz-clay-iron oxide aggregates that are also attracted by the magnet, wet sieving was done to break these aggregates up. The sieving is also needed to improve the isolation of glauconite from the glauconite sand. The attraction of the glauconite grain to the magnet depends on the grain size. Using a narrower grain size fraction (125-250 µm) improves the separation of the glauconite grains from the sand. The quality of the separation was checked under the microscope and separation was repeated until a glauconite content of 99 % was reached in the glauconite fraction. The remaining impurities are Fe-oxides and quartz. Static minerals such as muscovite often pose a problem for the separation as they are also attracted by the electromagnet. For samples containing a lot of muscovite, the platelets were separated from the glauconite with a thin plastic sheet.

A subset of the glauconite fraction samples (Table 2.1) was milled to clay size with a McCrone Micronizing mill, a wet milling to avoid damage to the crystal structure (Środoń et al., 2001 ). This sample preparation resulted in four types of samples: complete glauconite sand, glauconite fraction (magnetically separated from the 125-250 µm fraction of the glauconite sand), a milled complete sand and a milled glauconite fraction.

**Sample analysis**

*X-ray diffraction (XRD) analysis*

Powder X-ray diffraction analysis was used to determine the glauconite content and the total clay content of the glauconite sand. For the identification of the clay minerals clay slides were made from the < 2 µm fraction. The X-ray diffraction scans were measured using a Phillips PW1830 diffractometer with Copper (Cu) Kα radiation at 30 mA and 45 kV using a graphite monochromator and a scintillation detector. The diffractometer scans were recorded in Bragg-Brentano geometry, 5 to 65 º for bulk measurements and 2 to 47 º for clay measurements, each time with a step size of 0.02 º and 2 s counting time per step.

The presence of Fe in the sample (as for glauconite rich sands) can cause scattering of the Cu radiation and thereby an increase in background. Cobalt (Co) sources have the advantage of a longer wavelength

shifting the 00l diffraction peaks to higher angles and avoiding Fe-fluorescence. The current diffractometer set-up using Cu Kα radiation was optimised by Zeelmaekers (2011). By using a curved graphite crystal monochromator between the sample and detector the Cu Kβ radiation is blocked. The remaining intensity and resolution is more than sufficient for mineral qualification and quantification (Zeelmaekers, 2011).

To avoid preferred orientation, the samples were side loaded in the sample holders (Bruneel, 2016). Complete glauconite samples were milled (McCrone micronizing mill) to create fine random powders for XRD analysis. To the sample, 10 m% zincite was added as internal standard to calibrate the XRD pattern and avoid offset error. QUANTA (© Chevron ETC) was used for data interpretation and quantitative data analysis. QUANTA is pattern summation software that uses the concept of the Mineral Intensity Factor (MIF) to quantify the different mineral phases in a mixture. This concept attributes an intensity value to each mineral phase related to the stable reflection of the internal standard (zincite). For clay minerals the $d_{060}$ peak position is typically used. However, this implies that clay minerals with a similar $d_{060}$ peak position will be quantified together (e.g. glauconite, nontronite, Fe-smectite).

*Cation exchange capacity - cobalt(III) hexamine chloride*

The cation exchange capacity (CEC) quantifies the quantity of cations, expressed in molar charge units, that can be exchanged from negatively charged mineral surfaces. Clay minerals have a permanent negative charge and a large surface area. To evaluate the potential sorption of the cations $Cs^+$ and $Sr^{2+}$ the CEC is an important parameter. A wide range of methods exists for the determination of the CEC. The effective CEC in this work was determined with the cobalt(III) hexamine (cohex) method as described in the standardised protocol ISO 23470 (2018) with adapted mass and volume of extractant.. The cobalt (Co) complex is a stable trivalent cation that replaces the exchangeable cations on the negatively charged surfaces, i.e. the planar sites. This allows a one-step extraction with a 0.0166 M cobalt(III) hexamine chloride solution (Cohex) $[Co[NH_3]_6]Cl_3$. Measuring the CEC on natural glauconite samples is more complicated than in standard soils or clays. The pellet size implies that not all cation exchange sites might be (instantly) accessible for the large Co-complex. However, increasing the contact time might allow the $Co^{3+}$ to exchange some of the structural $Fe^{3+}$ (more on this in Annex1:Cation exchange capacity). Therefore all samples were milled and the effective CEC can be referred to as the potential CEC. The effective CEC was determined by measuring the remaining $Co^{3+}$ concentration in solution after one hour of contact time by inductively coupled plasma mass spectrometry (Agilent Technologies 7700 Series ICP-MS).

*Major element analysis*

The major elements were determined in the pore water samples, glauconite sands and glauconite fractions. Fresh in-situ pore water samples were measured with ICP-MS (Agilent Technologies 7700 Series). The solid samples were prepared in duplicate with the lithium(Li)-metaborate fusion method of

Vassilieva modified from Suhr et al. (1966) and Cremer et al. (1976). Samples were measured with the inductively coupled plasma optical emission spectroscopy (ICP-OES – Varian 720ES). A set of reference samples were chosen for data quality control, depending on the expected concentration of the major elements in the solution and additional elements of interest. In this case six reference samples were prepared with Li-metaborate and added to the batch for analysis (BCR-2, MRG-1, BCS-267, BCS-269, NIST-610, GA).

*$Fe^{2+}$ - $Fe^{3+}$ speciation*

The phenantroline method (Fritz and Popp, 1985; Shapiro, 1960) was used to determine the Fe speciation in the glauconite fraction (performed in triplicate). In this method samples are dissolved in a HF and $H_2SO_4$ solution in the presence of 1.10-phenantroline. The phenantroline forms a bright orange complex with $Fe^{2+}$ and prevents further oxidation. To determine the $Fe^{2+}$ content, the absorbance of the supernatants was measured at 555 nm using a Varian Model 635 UV-Visible Spectrometer. The total Fe content of the supernatants was determined by Atomic Absorption Spectroscopy (AAS) at 248 nm using a Thermo Electron Corporation S series AAS. The $Fe^{2+}$ and $Fe_{tot}$ mass percentages are calculated through a calibration curve obtained from geological Standard Reference Materials (SRM). A series of seven SRM's were selected based on the expected $Fe^{2+}$ and $Fe_{tot}$ content (NIM-G, GA, SY-3, DR-N, MRG1, BCR1 and NIM-D).

**Batch sorption studies**

The sorption is described by the distribution coefficient $K_D$ (L $kg^{-1}$), i.e. the ratio of adsorbed to solution $^{137}Cs$ concentration, the former calculated from the difference in radiocaesium concentration in solution between initial and final samples. Due to the strong competition with $K^+$, $^{137}Cs$ sorption is often expressed as the radiocaesium interception potential (RIP or $K_D.m_K$) or the distribution coefficient independent of the $K^+$ concentration (de Preter, 1990; Wauters and Cremers, 1996). The inverse linear relation between the $K_D$ and the $K^+$ concentration ($m_K$) makes it possible to recalculate sorption potential values to the in-situ $K_D$.

The $^{137}Cs$ sorption potential on glauconite sands was studied in a batch sorption test with a K-Ca background solution following the experimental procedure adapted from (Wauters et al., 1996b). The samples were prepared in duplicate and equilibrated in a background solution of 100 mM $CaCl_2$ and 0.5 mM KCl with a solid/liquid ratio of 1 g to 30 mL or 0.5 g to 80 mL. The relatively high $Ca^{2+}$ concentrations are used to saturate the planar sites in order to study $Cs^+$ sorption only at the specific sorption sites. Since the samples were pre-equilibrated in the K-Ca background solution, only the $^{137}Cs^+$ and $K^+$ can participate in ion exchange reaction on the FES. Sorption experiments were performed at neutral pH in a non-buffered system. The $Cs^+$ sorption on glauconite at trace concentration levels is not pH dependent (Poinssot et al., 1999a). Compared to standard batch sorption tests with illite (Comans et

al., 1991; Voronina et al., 2015a), the solid/liquid ratios in these batch sorption experiments are higher. Due to the large glauconite grains in the sand, larger solid sample sizes were required to have a representative sample.

The samples were weighed in dialysis bags (standard RC tubing, MWCO 6-8 kDa) and filled with 5 mL of background solution. Thereafter, they were transferred in 50 or 100 mL polypropylene (PP) tubes or bottles filled with 25 or 75 mL outer solution to obtain a solid/liquid ratio of 1 g to 30 mL or 0.5 g to 80 mL. This dialysis tubing does not affect the sorption kinetics (Poinssot et al. 1999). The tubes were shaken on an orbital bench shaker (0.42 $s^{-1}$). After establishing equilibrium between sample and background solution (the outer solution is renewed four times with 8 to 16 hour time intervals), the solution was labelled with radiocaesium. The initial $^{137}Cs$ activity in the solution was 1.5 kBq $mL^{-1}$ containing 0.01 µg $mL^{-1}$ CsCl carrier and agitation continued. The evolution of the $^{137}Cs$ activity concentration in solution was measured (TriCarb 2100TR, Perkin Elmer Ins.) at different time intervals from 8 hours up to 8.5 months after initial spiking, thereby identifying kinetics in these large pellets. At each sampling point 1 mL of the supernatans (outer solution) was sampled and replaced by an equal volume of 0.5 mM K, 0.1 M Ca solution. In the calculation of the $K_D$, this dilution effect was taken into account. The equilibrium $K^+$ concentrations were regularly measured by ICP-MS and were all within 6% of the nominal concentration of 0.5 mM.

An adsorption-desorption experiment was performed on a on a set of 10 complete glauconite sands and a subset of 4 milled samples. The samples were prepared with the same procedure as the batch sorption experiments. After 3 months of batch sorption, the membrane bags containing 1 g of soil and 5 mL of solution were placed in 25 mL $^{137}Cs$ free background solutions (0.5 mM $K^+$, 100 mM $Ca^{2+}$). The $^{137}Cs$ activity concentrations in the outer solution were measured up to 7 days and activity data were corrected for the dilution with the inner solution.

## 3. Results and discussion

### Glauconite sand and glauconite pellet properties

The glauconite sands are optically and mineralogically very different in terms of composition, grain size and grain morphology. The Diest Formation sands are coarse grained, contain 18-44 % glauconite and have very little to no other clays present. The range of globular to rounded glauconite pellets in these sands are associated with iron oxides on the outer rim and in the cracks of the grain. A crosscut of the grains shows a more oxidised outer rim (Figure 2.2) (Annex 1: Optical microscopy). Pyrite is present in the inner part and in the cracks of some of the grains. The combination of oxidation rim and pyrite can

be explained by formation in (locally) reducing conditions followed by a oxidation phase, probably during redeposition, and anoxic conditions after redeposition. The redox conditions of the environment are strongly influenced by the presence of organic matter. In the lower Berchem and Voort Fm samples the visible signs of weathering (iron oxide rim, oxidised outer rim) are no longer present. These changes in mineralogy can be of importance as they can influence the sorption sites. Due to weathering, $K^+$ is leached from the interlayer and more edges open up. This can imply an increase in the amount of FES (type I) or it could lead to more FES being transformed to type II or planar sites.

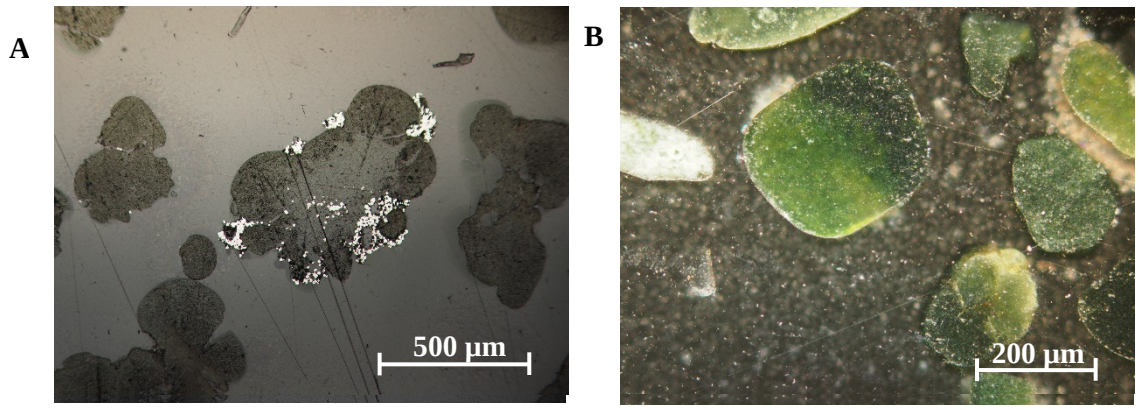


Figure 2.2 Optical microscopy image of a) crosscut of a globular glauconite pellet containing pyrite (white spots) both in the center and in the cracks (B2). And b) of the gradual colour changes indicative of differences in $K^+$ content in a rounded glauconite grain (D3).

The glauconite mineralogy is studied by three proxies: the $K^+$ content, the Fe content and the cation exchange capacity (CEC) (Table 2.2). In theory, high $K^+$ content implies mature glauconite (confer mature glauconite according to Odin (1988) > 8 wt% $K_2O$) with low weathering grade. During weathering the structural $Fe^{2+}$ can be oxidised to $Fe^{3+}$ and the total Fe content in the glauconite can decrease due to Fe leaching from the structure, mostly combined with the formation of Fe-oxy-hydroxides. The complexity in these proxies is their relation to each other. Releasing $K^+$ from the interlayer decreases the attraction of the interlayers and increases the accessible interlayer space, an effect visible in the CEC. All investigated glauconite fractions in the Neogene-Paleogene glauconite sands can be considered evolved to mature glauconite with a $K_2O$ wt% of 5.8 – 8.3. For both the Fe content and CEC the inter and intra formation variation is similar. The Fe contents are between 25.6 -152 mg $g^{-1}$ for the complete sands and 85-195 mg $g^{-1}$ for the glauconite fractions. The CEC ranges between 8.20 – 17.4 $cmol_c$ $kg^{-1}$. Most of the investigated properties of complete glauconite sands are correlated, it is rather obvious that such structural properties are inherently interrelated (Table 2.4). Glauconite is the main Fe-K-Mg containing component in the sand, therefore the content of these elements in the sand depends on the glauconite content. Based on these data the formations cannot be distinguished. Sample B1 is an outlier in the dataset by the very high glauconite content (89 wt%).

Table 2.2 The range, mean values (arithmetic mean) and standard deviation (SD) of a series of analysis parameters for the glauconite sands described in Table 2.1.

| | Qz | GL | total clay | $\frac{Fe^{2+}}{Fe_{tot}}$ | sands Fe | sands K | sands Mg | glauconite Fe | glauconite K | glauconite Mg | CEC sand | CEC GL |
|---|---|---|---|---|---|---|---|---|---|---|---|---|
| | % | | | | mg $g^{-1}$ | | | mg $g^{-1}$ | | | $cmol_c$ $kg^{-1}$ | |
| Min | 8.0 | 8.0 | 26 | 0.125 | 25.6 | 14.2 | 4.4 | 85 | 28.6 | 10.8 | 8.20 | 26.8 |
| Max | 64 | 89 | 89 | 0.247 | 152 | 59.1 | 19.6 | 195 | 69.7 | 23.4 | 17.4 | 33.3 |
| Mean | 53 | 31 | 36 | 0.187 | 57.8 | 26.9 | 7.9 | 155 | 53.7 | 20.1 | 11.2 | 27.9 |
| SD | 15.4 | 22 | 19 | 0.035 | 36.8 | 11.9 | 4.2 | 31 | 11.2 | 3.67 | 2.46 | 2.91 |
| D1 | 59 | 34 | 34 | 0.185 | 79.3 | 25.2 | 7.5 | 189 | 54.1 | 19.1 | 10.7 | 26.9 |
| D2 | 60 | 27 | 31 | 0.125 | 58.8 | 23.2 | 6.9 | 155 | 47.9 | 18.4 | 8.20 | 24.2 |
| D3 | 64 | 24 | 27 | 0.227 | 52.1 | 23.1 | 6.2 | 85 | 28.6 | 10.8 | 9.43 | 28.8 |
| D4 | 64 | 23 | 26 | 0.247 | 43.2 | 23.2 | 6.1 | 141 | 53.6 | 20.3 | 9.52 | |
| D5 | 57 | 30 | 33 | 0.183 | 26.6 | 14.2 | 4.4 | 148 | 58.3 | 23.4 | 12.0 | 30.1 |
| B1 | 8.0 | 89 | 89 | 0.184 | 152 | 59.1 | 19.6 | 174 | 65.8 | 21.9 | 17.4 | 24.8 |
| B2 | 56 | 27 | 32 | 0.216 | 49.2 | 28.5 | 7.3 | 195 | 69.7 | 23.0 | 11.3 | 33.3 |
| V1 | 55 | 17 | 29 | 0.143 | 33.8 | 23.3 | 6.3 | 158 | 56.6 | 22.8 | 11.1 | |
| V2 | 54 | 8.0 | 27 | 0.188 | 25.6 | 22.6 | 6.4 | 147 | 48.4 | 20.9 | 11.3 | |
| V3 | 51 | 17 | 33 | 0.169 | | | | | | | 13.8 | 27.5 |

**Cs sorption on glauconite sands**

A preliminary test showed that the $^{137}Cs$ continued to react beyond the standard times used in the protocols of de Preter (1990) and Wauters et al. (1996), but that equilibrium was near completeness after about one month. Therefore, $K_D$ data are first given for the apparent equilibrium at one month of interaction time. The log $K_D$ values (L $kg^{-1}$) of the complete glauconite sands range from 3.36 to 4.25 at 0.5 mM K (Table 2.3). Surprisingly these values are in the same range as the value for the Boom Clay Formation (3.54). The $K_D$‘s are significantly different among sands and formations. The factor 5.7 difference in $K_D$’s among sands is, however, small relative to that in surveys of corresponding studies in various soils where the $K_D$’s range often beyond factor 200 (Waegeneers et al. 1999, Uematsu et al. 2015). In soil studies the illite content often determines the $K_D$ value. The sand sample B1 with the highest glauconite content had also the highest $K_D$, in the range of the $K_D$ of illite (reference sample Illite du Puy, Table 2.3).

Table 2.3 The log $K_D$ (L $kg^{-1}$) values of the complete glauconite sands after 35 days, means ± standard deviation of two replicates with Illite du Puy and Boom Clay sample as internal references in the experiment.

| Formation | Sample | log $K_D$ (L $kg^{-1}$) complete sand | Log $K_D$ (L $kg^{-1}$) glauconite fraction |
|---|---|---|---|
| Diest Fm | D1 | 3.46 ± 0.02 | 4.14 ± 0.03 |
| | D2 | 3.42 ± 0.03 | 4.16 ± 0.03 |
| | D3 | 3.36 ± 0.01 | |
| | D4 | 3.53 ± 0.01 | 4.12 ± 0.03 |
| | D5 | 3.75 ± 0.03 | |
| Berchem Fm | B1 | 4.25 ± 0.05 | 4.27 ± 0.01 |
| | B2 | 3.59 ± 0.01 | |
| | W14 | | 4.09 ± 0.02 |
| Voort Fm | V1 | 3.59 ± 0.02 | |
| | V2 | 3.57 ± 0.03 | |
| | V3 | 3.86 ± 0.01 | 4.26 ± 0.01 |
| Illite du Puy | Ref | 4.39 ± 0.05 | |
| Boom Clay | Ref | 3.54 ± 0.03 | |

Regression analysis is often used to link the sorption potential to soil properties. We aim to study the effect of mineralogical variations on the $K_D$ and to evaluate if any of these parameters can be used to predict the sorption potential.

Table 2.4 The correlation coefficients among the properties (GL=glauconite content, total clay content, ratio $Fe^{2+}$ to $Fe_{tot}$ and wt% Fe, K and Mg) of complete glauconite sands and their glauconite fractions and with the distribution coefficient $K_D$ (L/kg) of the complete sand: *** p<0.001; ** p<0.01 and * p<0.05.

| | | | | | | Complete sand | | | Glauconite fraction | | | |
|---|---|---|---|---|---|---|---|---|---|---|---|---|
| | | $K_D$ | GL | total clay | $\frac{Fe^{2+}}{Fe_{tot}}$ | Fe | K | Mg | Fe | K | Mg | CEC |
| | $K_D$ | 1 | **0.82**** | **0.88**** | -0.81 | 0.64 | **0.74*** | **0.78*** | 0.33 | 0.62 | 0.53 | **0.95***** |
| | GL% | | 1 | **0.97***** | -0.63 | **0.95***** | **0.90**** | **0.93***** | 0.30 | 0.42 | 0.14 | **0.82**** |
| | total clay | | | 1 | -0.63 | **0.92***** | **0.94***** | **0.97***** | 0.31 | 0.45 | 0.23 | **0.90***** |
| | $\frac{Fe^{2+}}{Fe_{tot}}$ | | | | 1 | -0.42 | -0.37 | -0.46 | -0.37 | -0.44 | -0.46 | -0.77 |
| | Fe | | | | | 1 | **0.93***** | **0.95***** | 0.31 | 0.30 | -0.02 | **0.71*** |
| sand | K | | | | | | 1 | **0.99***** | 0.32 | 0.41 | 0.13 | **0.81**** |
| | Mg | | | | | | | 1 | 0.31 | 0.39 | 0.14 | **0.84**** |
| | Fe | | | | | | | | 1 | **0.87**** | **0.74*** | 0.36 |
| GL | K | | | | | | | | | 1 | **0.89**** | 0.57 |
| | Mg | | | | | | | | | | 1 | 0.44 |
| | CEC | | | | | | | | | | | 1 |

The interesting parameters are the CEC, the Fe and $K^+$ content as they reflect the weathering state of the glauconite (Table 2.4). In the previous section we explained that the intra and inter formation variation for these parameters have a similar range. In the complete glauconite sands the glauconite wt%, Fe, $K^+$ and $Mg^{2+}$ content are strongly correlated ( $p < 0.001$). Iron is mainly present in the sand as part of the glauconite, Fe-oxyhydroxides and pyrite. The variation in Fe content is limited over the different formations and solely linked to the glauconite content. There is no correlation between the $Fe^{2+}$ /$Fe_{tot}$ ratio and any of the studied parameters. The $Fe^{2+}/Fe_{tot}$ ratio is sensitive to oxidation or reduction. Over all samples the ratio ranges between 1/5 – 1/6, though oxidation after sampling could have occurred giving all samples a similar value. The correlations found in the complete sand reflect mostly the glauconite content. No conclusions can be made on the influence of the weathering state of the

glauconite as there is no correlation between the glauconite fraction $K^+$, Fe and $Mg^{2+}$ and any of the other investigated parameters.

The relevant correlations for the $K_D$ are the glauconite content, the total clay (mineral) content, the $K^+$ and $Mg^{2+}$ content of the complete sand and the CEC. The correlation between the $Cs^+$ $K_D$ and total $K^+$ in the complete sands is significant and positive (r=0.74), but not between the $K_D$ and the $K^+$ of the glauconite fraction. Several studies found strong positive associations between total K of clay fractions or soils and the $K_D$ (de Preter 1990, Waegeneers et al. 1999, Uematsu 2017). In sand-clay mixtures and soils, the total $K^+$ content will often relate to the illite content. Compared to mica and kaolinite, illite has both higher interlayer $K^+$ and more FES, resulting in higher $Cs^+$ $K_D$ values. In pure illite-like clays, e.g. glauconite, the amount of interlayer $K^+$ is much higher than the amount of exchangeable $K^+$ explaining the absence of correlation to the $K_D$. Not surprisingly, $K_D$ values also rise with increasing XRD detected clay (r= 0.90) and increasing glauconite content (r=0.82). The CEC is here a good predictor of the sorption potential (r=0.95), even though the frayed edges sites, constitute only a small fraction of the total CEC (~ 0.25 % (Bradbury & Baeyens, 2000)). If more smectite and mica type clays would be present, the ratio FES to CEC would decrease. In that case the CEC is a less accurate predictor of the radiocaesium interception potential.

The regression analysis suggests that the $K_D$ of the glauconite sand can be predicted based on the glauconite content of the sand (r=0.82, p<0.01). Therefore a small test was set up. For four samples the $K_D$ was determined for the complete sand and its glauconite fraction (Table 5). Based on the glauconite content and the $K_D$ of the isolated glauconite fraction, the $K_D$ of the complete sand can be estimated. This assumes that glauconite is the main sorbing component. In samples where glauconite makes up almost the complete clay mineral fraction, this assumption is valid. In the Voort Formation V3 sample, the true clay size fractions increases towards the Boom Clay Formation. In these samples a prediction based on the glauconite underestimates the $K_D$ of the complete sand showing that the glauconite is not the only reactive clay in the intact sand. The other reactive minerals in the Voort samples are smectite, illite-smectite mixed layer, kaolinite and muscovite. The ratio glauconite to total clay is > 0.84 for all samples of the Diest and Berchem Formation. In the Voort Fm the glauconite to total clay ratio is 0.48-0.59. The hypothesis is that for the Voort Fm samples the smectite and illite-smectite will sorb a significant part of the $Cs^+$.

**Effect of the K concentration in the pore water – In-situ $K_D$**

The Neogene-Paleogene glauconite sands were deposited in marine and estuarine environments in which average $K^+$ concentrations were about 10 mM upon deposition (Millero et al., 2008). Over time, the salt concentration in the sands evolved due to exchange between the pore water and the groundwater. The

concentration of $K^+$ in current groundwater ranges between 0.14 – 0.37 mM, lower than the 0.5 mM $K^+$ used in the batch sorption experiments. The aquifer solutions have $K^+$ concentrations at the high end of the range for standard groundwater, though still in the normal range for pore waters. The in-situ $K_d$ can be approximated by using the $K_d.m_K$ relation and the $K^+$ concentration of the pore water at the corresponding depth and formation. The log $K_d$ range of 3.4 – 3.9 L $kg^{-1}$ at 0.5 mM $K^+$ translates in values ranging from 3.7 to 4.2 L $kg^{-1}$ at in-situ concentrations. The lower competition effect implies that the in-situ sorption is expected to be higher than the sorption in the batch experiments at 0.5 mM $K^+$. The major element composition of the pore water extracts is given in Annex 1 (Pore water).

**Sorption kinetics of Cs in glauconite sands and pellets**

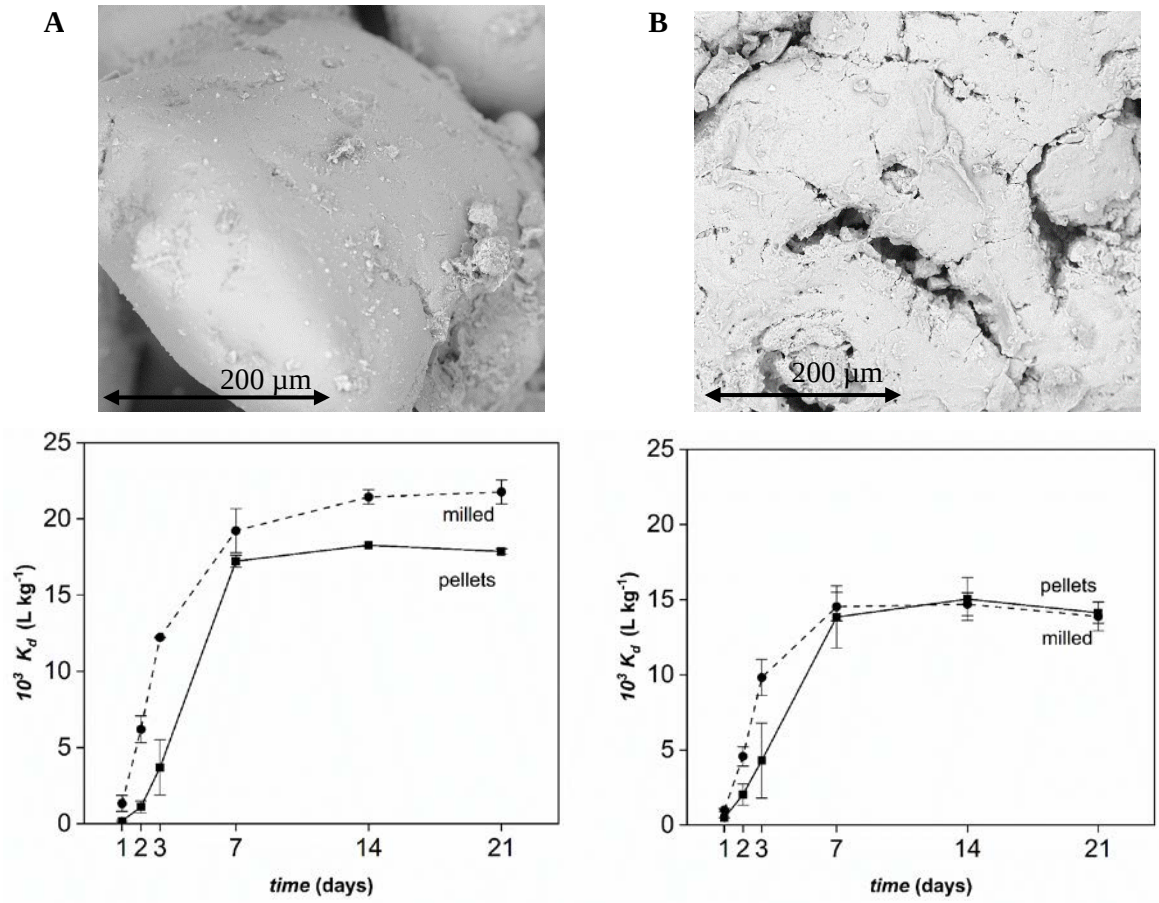


Figure 2.3 SEM images of the surface of glauconite grains and the evolution of the $K_D$ over time for milled and unmilled glauconite pellets. A) B1 - unweathered Berchem Fm sample B) B6 - strongly weathered surface sample (Berchem Fm).

The sorption kinetics were followed up for D1, B2, V1 and BC for 253 days (~ 8.5 months) on six replicates. The short-term $K_D$ evolutions are shown in Figure 2.3A for milled and un-milled glauconite pellets. After 48h, $^{137}Cs$ sorption is already rather strong (log $K_D$ 2.6-3.0), followed by slower sorption, the $K_D$ increases factors 6-8 between 48h and 1 month, with minor changes beyond 1 month. The experiment was repeated for all samples in duplicate (up to 9.5 months) and showed the same trends as the initial experiment. Hence, the 4-5 days needed for reaching equilibrium in illite suspensions

(Poinssot et al., 1999a) are far exceeded in these samples. Interestingly, the Boom Clay sample shows the same trend.

For $^{137}Cs$ sorption on illite, sorption on the FES is considered fast, though slower sorption takes place over months and explains the long-term ageing reactions of $^{137}Cs$ in soil, also denoted with ecological half-lives (e.g. 3.5 – 5.6 years (Merz et al., 2016)). This slower sorption process is described as interlayer migration (Fuller et al. 2015). The $K_D$ (at 0.5 mM $K^+$) did not significantly rise between 1-2 months, however a rise is detected after 8.5 months: the $K_D$ increased between 1 and 8.5 months by factor 1.7 (D1), 1.8 (B2), 1.6 (V1) and 1.8 (BC) (Figure 2.4).

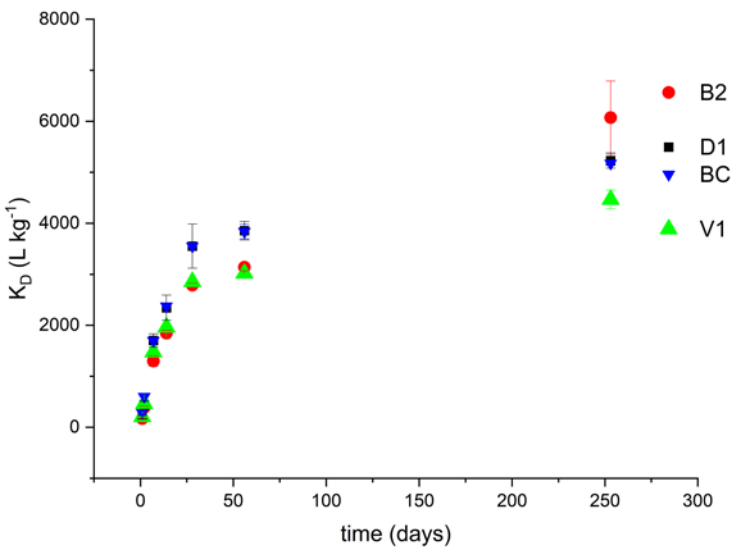


Figure 2.4 Evolution of the $K_D$ (L kg$^{-1}$) up to 253 days for sample D1, B2, V1 and BC reference sample.

For the more extended data (up to 9.5 months) of a set of nine glauconite sands the correlation between the $K^+$ content in the glauconite sand and the change in $^{137}Cs$ $K_D$ at several time frames is given (Table 2.5). On the short-term sorption reactions there is no significant effect of $K^+$ content. However, the factor change in $^{137}Cs$ $K_D$ (> 1 month) is positively correlated with the $K^+$ content of the sand i.e. there are more slow reactions as the total $K^+$ over the sands increases. This can be explained by the fact that part of the $K^+$ that is bound in the interlayer, can be exchanged by $Cs^+$ over longer time frames.

Table 2.5 Correlation coefficients r between the potassium content of the glauconite sand and the factor change in $^{137}Cs$ $K_D$ within various timeframes (for nine glauconite sands).

| Time frame | r | p-value |
|---|---|---|
| 48h/9.5m | -0.56 | 0.12 |
| 16d/9.5m | -0.64 | 0.06 |
| 1m/9.5m | -0.71 | 0.03* |
| 2m/9.5m | -0.70 | 0.03* |

The glauconite in the Neogene-Paleogene sands occurs mainly as pellets of, on average, ~150 µm. The size and density of the pellets can restrict the access of $^{137}Cs$ to the FES at the interior of the pellet. The sorption on the pellets is obviously most environmentally relevant. However, due to weathering, fractures can form in the pellet surface or the pellets can disintegrate to clay particles. A comparison of the sorption kinetics between milled (grain size > 2 µm) and unmilled pellets was made in a batch sorption experiment on five glauconite sands and two glauconite fractions.

Milled samples sorb $^{137}Cs$ faster and more $Cs^+$ compared to the equivalent unmilled sample ( Table 2.6). In the first 48 hours, the milled samples reacted faster than the glauconite pellets indicating reduced access to the sorption sites. The ratio milled to unmilled glauconite fraction $K_D$ stabilised after 7 days. Beyond 7 days the $K_D$ is 1.1-1.6 times larger for milled than for unmilled samples. This means that part of the inner sorption sites of the pellets remain inaccessible for $^{137}Cs$ sorption. Our set contains one exception, B6-GL, a heavily weathered Diest Formation sample. Though the milled fraction responded faster than the pellets, the equilibrium $K_D$ is the same (Figure 2.3). In the weathered sample, the glauconite grain surface is cracked and highly porous as shown in the SEM picture. We assume that the inner pellet sorption sites become accessible for Cs due to the cracks in the outer surface.

**Adsorption-desorption of $^{137}Cs$ in glauconite sands**

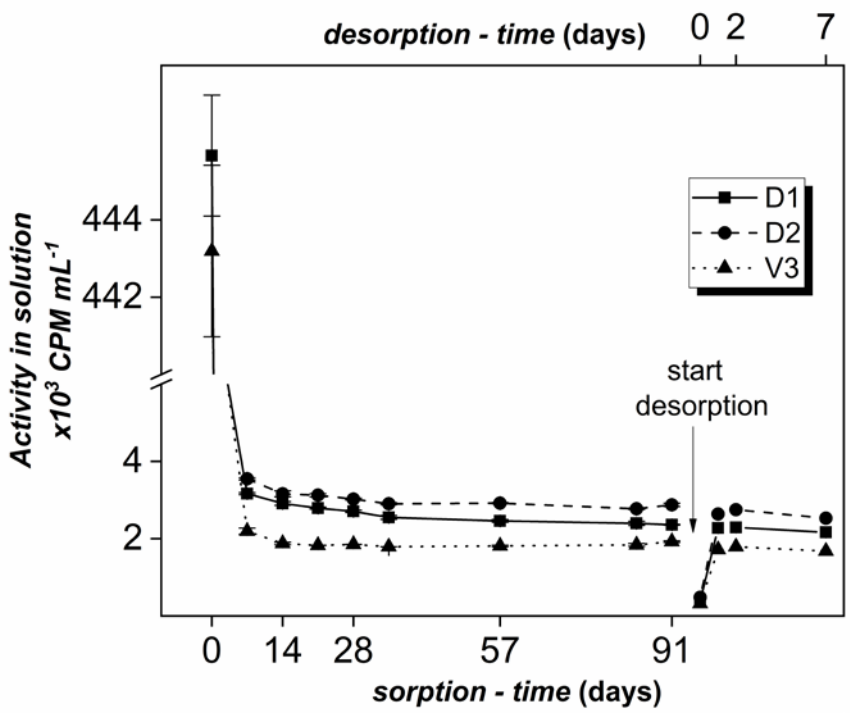


Figure 2.5 The activity in solution (CPM $mL^{-1}$) versus time for sorption and desorption. Desorption reaches equilibrium after 2 days. The activity in solution after desorption is only 0.87-0.92 of the corresponding activity in solution after adsorption at 91 days.

Adsorption-desorption experiments were performed to test reversibility of sorption. The desorption phase used the same concentration of $K^+$ and $Ca^{2+}$ as in the adsorption phase, i.e. mimicking the release of $Cs^+$ under natural pore water concentrations. In Figure 2.5 the activity in solution is plotted during sorption and desorption for three complete glauconite sands (D1, D2 and V3). The complete glauconite sands reach desorption equilibrium after 2 days, in the milled samples only one day is required. If the sorption is fully reversible, the activity concentration in solution at desorption equilibrium, corrected for dilution, is identical to that of sorption at sorption equilibrium. For example, for sample D2 the activity in the adsorption solution after 3 months was 2873 ± 44 CPM $mL^{-1}$. After correcting for the activity removed from solution a new solution activity concentration of 2869 CPM $mL^{-1}$ was calculated. The activity concentration at desorption equilibrium was 2529 ± 9 CPM $mL^{-1}$, i.e. a fraction 0.88 of the corresponding value after adsorption. This indicates some sorption irreversibility within the time limit of the investigations (7 days). For all investigated glauconite sands, these fractions ranged 0.73-0.95 depending on the sample (Table 2.6). Additionally, this fraction is smaller (higher retention) in milled than in unmilled glauconite sands. This implies that milling the sample does not only increase the sorption potential of the glauconite sand, but also the sorption retention.

Table 2.6 The activity in solution ($A_s$) at equilibrium (CPM mL-1), 3 months for sorption, 7 days for desorption. Several fractions were used in the experiment: complete glauconite sand (C), milled glauconite sand (M), glauconite fraction (GL), milled glauconite fraction (GLM) and Illite du Puy (IdP) as internal reference sample. The ratio is calculated by dividing the $A_s$ at desorption equilibrium by the $A_s$ at sorption equilibrium. A value of 0.99 would indicate reversible Cs sorption, everything below indicates Cs retention.

| Sample | Fraction | Sorption CPM $mL^{-1}$ | Desorption CPM $mL^{-1}$ | Ratio |
|---|---|---|---|---|
| B2 | C | 1581 ± 142 | 1499 ± 37 | 0.95 |
| | M | 1441 ± 65 | 1289 ± 13 | 0.89 |
| D1 | C | 2360 ± 10 | 2167 ± 43 | 0.92 |
| | M | 1773 ± 102 | 1560 ± 19 | 0.88 |
| V1 | C | 2044 ± 261 | 1774 ± 30 | 0.87 |
| D2 | C | 2873 ± 44 | 2529 ± 9 | 0.88 |
| | M | 2598 ± 387 | 2023 ± 81 | 0.78 |
| V2 | C | 2563 ± 168 | 2418 ± 8 | 0.94 |
| D3 | C | 3180 ± 409 | 2941 ± 24 | 0.92 |
| D4 | C | 2710 ±58 | 2426 ± 18 | 0.89 |
| D5 | C | 1373 ± 70 | 1158 ±3 | 0.84 |
| B1 | C | 740 ± 50 | 713 ± 5 | 0.96 |
| | GL | 729 ± 65 | 622 ± 3 | 0.85 |
| | M | 745 ± 12 | 611 ± 8 | 0.82 |
| V3 | C | 1923 ± 19 | 1678 ± 25 | 0.87 |
| | M | 1425 ± 74 | 1220 ± 19 | 0.86 |
| | GL | 758 ± 12 | 670 ± 17 | 0.88 |
| W14 | GL | 1540 ± 9 | 1126 ± 1 | 0.73 |
| IDP | | 851 ± 12 | 807 ± 6 | 0.77 |

## 4. Conclusion

This study showed that glauconite sands have strong radiocaesium sorption potential, the log $K_D$ (L $kg^{-1}$) at 0.5 mM $K^+$ ranged 3.4 – 4.3 with a limited variation in the sorption potentials among the investigated sands despite the natural diversity of the sand. The in-situ radiocaesium sorption can be expected to be even higher (3.7 – 4.2 log $K_D$) due to lower $K^+$ concentrations in the aquifer solutions (less competition effect). The sorption potential of a glauconite sand can be estimated from its percentage glauconite content, in case that the fraction of other clays is low. Comparing milled versus unmilled glauconite sorption data indicate that part of the inner pellet is not accessible for $^{137}Cs$. This effect is not present in weathered glauconite grains as cracks in the grain surface open up allowing access for $^{137}Cs$. In the unweathered samples, the grain size effects (assessed by the comparison of milled versus unmilled samples) are still limited with respect to the range of sorption potentials over all sands. $Cs^+$ sorption is not fully reversible on the glauconite sands in natural pore water concentrations. In addition, $^{137}Cs$ sorption kinetics on glauconite sands showed slower reaction than that estimated earlier in soils or clay fractions. We speculate that these slow reactions are likely important for reactive transport of $Cs^+$ sorption in the high permeable sands where the local non-equilibrium may induce early breakthrough. Such requires further column transport studies.

# Chapter 3. Characterisation of the highly selective caesium sorption on glauconite sands

Adapted from Bruneel et al. (2021a).


## Abstract

The Neogene-Paleogene glauconite sands are investigated in the framework of the Belgian radioactive waste disposal as material for an additional sorption sink. Glauconite is an Fe-rich phyllosilicate that is mainly present as 125-250 µm sized pellets in the sand. Recent studies have shown a surprisingly strong sorption of radiocaesium ($^{137}Cs$) on these sands, despite the coarse sized pellet structure. This study was set up to characterise the selective $^{137}Cs^+$ sorption sites on glauconite that are likely Frayed Edge Sites (FES) as in illite. First, the $NH_4$/K selectivity on the FES was determined as a fingerprint for the highly selective FES. The $NH_4$/K selectivity coefficient on the FES for three different sand formation ranged between 3.8-5.0, well in line with the range (4-7) that has been reported for illite clay and clay formations. Second, the $Cs^+$ sorption isotherms were determined on three sand formations in a background solution of 0.5 mM $K^+$, 100 mM $Ca^+$ and $10^{-8}$-$10^{-4}$ M $Cs^+$; isotherms were fitted with an optimised three-site model adapted after the illite model of Bradbury & Baeyens (2000). The optimised model fitted the data adequately. The FES capacities of the sands ranged from 0.04-0.06 % of the CEC which is significantly below that of illite (0.25 %). Similarly, a strong decrease in the FES - type II site capacities was observed (1.7-2.2 % of the CEC vs 20 % for illite). The lower fractions of FES - type I and FES - type II sites detected in glauconite sand are related to higher fractions of smectites (XRD confirmed) that do not have specific $Cs^+$ sorption sites. Taken together, this study suggests that the glauconite sands have highly selective sites that bind $^{137}Cs^+$ with similar properties as in illite, however the fractions of these sites in the total CEC pool are about a factor 5 lower than in pure illite.

## 1. Introduction

Radiocaesium ($^{137}Cs$) is a major component of high-level nuclear waste. The combination of a long half-life ($t_{1/2}$ 30 years) and the high solubility of the $Cs^+$ cation under all redox ($E_h$) and pH conditions makes it an element of concern in radioactive waste repositories. The mobility of $Cs^+$ in the environment is mainly controlled by the sorption onto mineral surfaces (Fuller et al., 2015; Sawhiney, 1972; Takeno, 2005). Especially the illitic type of clay minerals retain $Cs^+$ due to the selective sorption at the frayed edge sites (FES) (Sawhiney, 1972; Valcke, 1993).

The $^{137}Cs^+$ sorption of the Neogene glauconite sands is being investigated in the framework of the Belgian radioactive waste disposal program. The glauconite sands are not considered to be a suitable host formation for the geological disposal of high-level and/or long-lived radioactive because of its high permeability. However, depending on the choice of primary host formation, the sands might become part of the natural barrier surrounding the host. Glauconite sands are enclosing both the Boom Clay and Ypresian clays. A secondary purpose for the glauconite sands could be as an extra embankment below a surface disposal for short-lived and low-level waste. In the Neogene and Paleogene glauconite sands (Diest, Berchem and Voort Fm), a surprisingly strong $^{137}Cs^+$ sorption has been observed. The radiocaesium ($^{137}Cs$) distribution coefficients (log $K_D$, $K_D$ in L $kg^{-1}$) range between 3.4 and 4.3 after 30 days of reaction with 0.5 mM $K^+$ as competing cation (Bruneel et al., 2020) (Chapter 2). These $K_D$ values are very close to those of Boom Clay samples under the same conditions (3.5 log units). The main sorbent in the sands is the glauconite fraction. The $^{137}Cs^+$ $K_D$ values on pure glauconite fractions (4.0-4.3 log units at 0.5 mM potassium ($K^+$)) are within the range of corresponding values on illite (4.1-4.3). The difference in $^{137}Cs^+$ $K_D$ of glauconite fractions among the different formations remain below a factor 2.

The Diest and Berchem Formation contain 35-40 weight percent (wt %) glauconite pellets, locally up to > 85 wt% (Adriaens, 2015; Adriaens et al., 2014). The glauconite pellets are coarse sized (125-250 µm). Glauconite $(K,Na)(Fe^{3+}Fe^{2+},Al,Mg)_2(Si,Al)_4O_{10}(OH)_2$ has two end-members, an illitic or micaceous form, and a more smectitic form. The form present in the sediment depends on the maturity and weathering state. In the illitic form, potassium ($K^+$) is the main interlayer cation (Meunier and El Albani, 2007; Odin, 1988), while in the smectitic form part of the interlayer cations were leached out and replaced by hydrated exchangeable cations. Glauconite mostly occurs as a mixed form between the illitic and smectitic end-member (Courbe et al., 1981; Meunier and El Albani, 2007; Van Ranst and De Coninck, 1983).

The structure of the clay minerals affects the $Cs^+$ sorption. Three sorption sites are distinguished in illitic clays: planar sites, frayed edge type I and type II sites (Bradbury and Baeyens, 2000; Fuller et al., 2015; Poinssot et al., 1999a, b). The planar sites are characterised by high capacity and low selectivities for $Cs^+$ over the main other competing ions such as $K^+$ and $Ca^{2+}$. The sorption sites of interest for $Cs^+$

sorption are the frayed edge sites (FES) type I and, to a lower extent, the FES type II sites (Bradbury and Baeyens, 2000). The FES type I and type II are localised at the edges of the interlayers or in transition zone between the interlayer and hydrated interlayer, with the width of the FES between 1.0 and 1.4 nm (Nakao et al., 2008). The FES are only accessible to small cations with low hydration energies such as $Cs^+$, $K^+$ and $NH_4^+$ (Fuller et al., 2015; Sawhiney, 1972). Due to the high $Cs^+$ selectivities of these low capacity sorption sites, $Cs^+$ is strongly retained at low, but environmentally relevant concentrations. The FES type I and type II are distinguished based on experimental sorption isotherm data (Brouwer et al., 1983). In more recent characterisation studies, no clear structural differences were observed between type I and type II sites (Nakao et al., 2008; Okumura et al., 2018). Therefore, the FES can be described as Cs selective sites with a continuum of selectivity rather than distinct types of sites. In this study the term 'FES' is used to refer to the FES type I sites and 'type II' to the FES – type II sites.

In literature, selectivity coefficients ($K_c$) for Cs/K in the FES range between log 2.2 and 9.4 (Bradbury and Baeyens, 2000; Brouwer et al., 1982; de Preter, 1990; Poinssot et al., 1999b). The $NH_4^+$ over $K^+$ selectivity coefficient in the FES is about 4-7 (de Preter, 1990) and this is often used as the fingerprint to demonstrate the consistence of FES properties across different environments, e.g. soil, sediments and suspended matter (Wauters et al., 1996b). At high $Cs^+$ concentrations, the sorption to the less selective planar sites becomes important. The replacement of $K^+$ by hydrated exchangeable cations during weathering increases the interlayer width. This leads to an increase in the fraction of planar sites and a decrease in FES capacity. Therefore, the binding strength of $Cs^+$ to glauconite will be related to the ratio of illitic and smectitic layers (Fuller et al., 2015; Missana et al., 2014b).

In general, two types of ion exchange models are used to describe equilibrium $Cs^+$ sorption on clay and clay minerals under variable conditions (De Koning et al., 2007). A first group of models aims to accurately predict the $Cs^+$ sorption at trace $Cs^+$ concentrations (Cremers et al., 1988; de Preter, 1990). In this single-site approach, only the high affinity sites are assessed by the radiocaesium interception potential (RIP) or the $K_D.m_K$. The description of the sorption of $Cs^+$ as the solid:liquid distribution $K_D$ (L $kg^{-1}$) reads:

$$K_D \cdot m_K = K_c \ (Cs/K) \cdot [FES] \qquad \text{Eq 3.1}$$

With $m_K$ the $K^+$ concentration in solution (mmol $L^{-1}$); $K_c$ (Cs/K) the $Cs^+$ over $K^+$ selectivity coefficient in the FES and [FES] the capacity of the FES sites (mmol $kg^{-1}$). The RIP concept is theoretically valid in the 5-10 mmol $L^{-1}$ $K^+$ concentration range; at lower $K^+$ concentrations the RIP decreases (de Preter, 1990). In the lower $K^+$ concentration domain the RIP is underestimated (Hisashi et al., 2013) (Wauters et al., 1996b). The RIP at trace $Cs^+$ loadings is the product of the high affinity site capacity and its selectivity, with the assumptions that i) the amount of intercepted $Cs^+$ in the FES is only representing a very small fraction of the total FES capacity, ii) $K^+$ is the only competing cation, present in known concentration, and iii) the $Ca^{2+}$ background concentration prevents $Cs^+$ sorption on the planar sites.

The second type of models, the multi-site cation exchange models, allows the prediction of $Cs^+$ concentration dependent sorption for concentrations ranging between trace and high levels (Bradbury and Baeyens, 2000; Brouwer et al., 1982; De Koning et al., 2007; Missana et al., 2014b). The three-site model by Bradbury and Baeyens (2000) assumes that $Cs^+$ sorption in argillaceous systems is dominated by cation exchange reactions on the illite mineral component and that the uptake takes place on three sites, each with different site capacities and affinities. The total capacity of the sorption sites is described by the cation exchange capacity (CEC). The site capacity and affinity ($K_c$) for each site are linked. Table 3.1 summarises the selectivity and capacity data for four different three-site models based on illite. The FES capacities for illitic clays range between 0.05 – 6.5 % of the CEC (Bradbury and Baeyens, 2000; Brouwer et al., 1983; de Preter, 1990; Poinssot et al., 1999b). The variation mainly depends on the definition of the sorption sites. For mixed layer illite-smectite, FES capacities can be up to 10 times smaller (de Preter, 1990).

Table 3.1 Selectivity coefficients and individual sorption site capacity data for Illite du Puy in a three-site model (Bradbury and Baeyens, 2000; Brouwer et al., 1982; Fuller et al., 2014; Missana et al., 2014b).

| | Selectivity log $K_c$ (Cs/K) | | | Capacity % of the CEC | | |
|---|---|---|---|---|---|---|
| | *FES* | *type II* sites | *Planar* sites | *FES* | *type II* sites | *Planar* sites |
| Brouwer et al. (1982) | 4.1 | 1.4 | 0.65 | 0.25 | 2.5 | 97.25 |
| Bradbury & Baeyens (2000) | 4.6 | 1.5 | 0.50 | 0.25 | 20 | 80 |
| Fuller et al. (2014) | 5.5 | 3.0 | 1.1 | 0.05 | 2 | 97.95 |
| Missana et al. (2014) | 4.2 | 2.0 | 1.2 | 0.24 | 19.95 | 79.81 |

This study aimed to characterise the highly selective $Cs^+$ sorption on a range of natural glauconite sands and to relate sorption parameters with the mineralogy. Previous studies showed good sorption of $Cs^+$ on glauconite. It is unclear how to explain differences in $^{137}Cs$ sorption between a pure glauconite and a pure illite. Glauconite is described as an illite where part of the aluminium ($Al^{3+}$) has been replaced by $Fe^{2+}$ and with $K^+$ as the dominant interlayer cation (Bailey, 1980; Meunier, 2005). The capacity and affinity for $Cs^+$ on the different sorption sites is unknown for glauconite. In addition, the $K_D$ is lower for granular glauconite compared to milled glauconite. This could imply a different distribution of the site capacities among the accessible sites in granular versus milled glauconite. Here, the sorption isotherms of $Cs^+$ were measured in a wide range of $Cs^+$ concentrations to identify the sites capacities and corresponding selectivities. The isotherms were modelled to infer these sorption parameters. By combining the X-ray diffraction data with the modelled site capacities and selectivities, mineralogical indications for the variation between the sand and to illite can be found. The $NH_4$/K selectivity coefficient on the FES was measured and used as a fingerprint of the highly selective sorption sites.

## 2. Material and methods

### Sample selection

A set of three natural glauconite sands was selected for the experiments (Figure 3.1, Table 3.2). More details on these samples on the $^{137}Cs^{+}$ interception potential and kinetics were presented in Chapter 2. The samples are part of the Neogene glauconite sands and are known to have high glauconite and total clay mineral content. Sample D1 and B2 originate from the excavation of the second shaft to the HADES research lab of ONDRAF/NIRAS and SCK CEN in Mol. Sample D2 is part of the ON-Dessel5 drilling core. A purified Na-conditioned Illite du Puy reference sample was included. The samples were stored in vacuum sealed bags since sampling. Before use, the samples were oven-dried at 60°C.

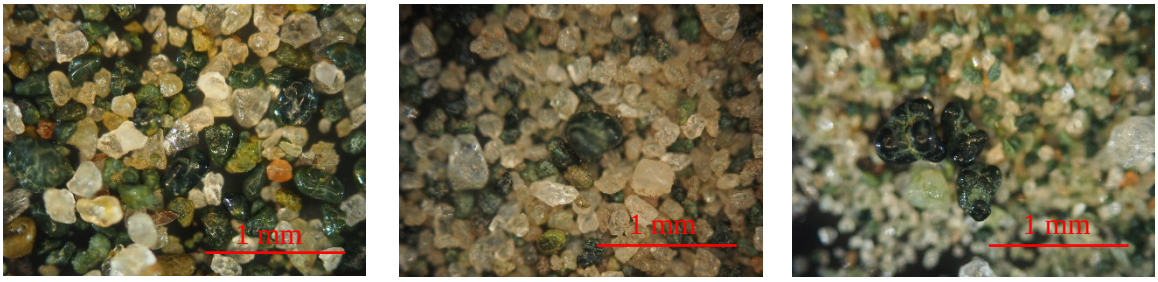


Figure 3.1 Optical microscopy images of the complete glauconite sands D1, D2 and B2.

Table 3.2 Characteristics of the selected glauconite rich sands; the $^{137}Cs^{+}$ log $K_D$ (L $kg^{-1}$) values were obtained after 35 days reaction with 0.5 mM K as competing ions. The properties were determined as described Chapter 2. The data is presented as mean ± standard deviation of two replicates.

| | Formation | Depth mTAW[$] | GL wt% | Total clay wt% | Quartz wt% | CEC[$$] $cmol_c$ $kg^{-1}$ | log $K_D$ L $kg^{-1}$ |
|---|---|---|---|---|---|---|---|
| D1 | Diest Fm | 72.8 | 34 | 34 | 59 | 10.7 ± 0.22 | 3.46 ± 0.02 |
| D2 | Diest Fm | 90.7 | 27 | 31 | 60 | 8.2 ± 0.83 | 3.42 ± 0.03 |
| B2 | Berchem Fm | 134.1 | 27 | 32 | 56 | 11.3 ± 0.01 | 3.59 ± 0.01 |
| IdP | Na-Illite du Puy | | | | | 20.4[*] | 4.59 ± 0.05 |

[$]The sampling depth is expressed in mTAW, or the reference level in Belgium (Tweede Algemene Waterpassing)

[$$]Cobalt hexamine method (Ciesielski et al., 1997).

[*]A value of 20 $cmol_c$ $kg^{-1}$ was reported by Bradbury and Baeyens (2000).

### Batch sorption studies

The sorption is described by the distribution coefficient $K_D$ (L $kg^{-1}$), i.e. the ratio of adsorbed to solution $^{137}Cs^{+}$ concentration. Two sets of batch experiments were performed, a $NH_4^{+}$-$K^{+}$ selectivity experiment and a sorption isotherm test. In both experiments the samples were prepared in duplicate in a solid/liquid ratio of 1 g to 30 mL. An internal reference sample (Na saturated Illite du Puy) was added to each of the batch experiments but was only used at zero $NH_4^{+}$ addition and zero stable $Cs^{+}$ addition, i.e. it allowed

referencing the $K_D$ values for one given ionic scenario. The samples were pre-equilibrated with the background solution 5 mM $K^+$, 100 mM $Ca^{2+}$ and 0-5 mM $NH_4^+$ for the selectivity experiment and 0.5 mM $K^+$ and 100 mM $Ca^{2+}$ in the sorption isotherm experiment. To prevent sample loss during liquid change in the pre-equilibration stage, the samples were weighed in dialysis bags (standard RC tubing, MWCO 6– 8 kDa) and filled with 5 mL of background solution. Thereafter, they were transferred in 50 mL polypropylene (PP) tubes filled with an additional 25 mL outer solution. During the pre-equilibration the supernatant was changed three times every 8-16 hours. Sorption experiments were performed at neutral pH in a non-buffered system. At trace concentration $Cs^+$ the $K_D$ is not pH dependent (Poinssot et al., 1999a, b). At higher $Cs^+$ concentrations (> $10^{-4}$ M) competition with $H^+$ lowers the $Cs^+$ $K_D$ at strongly acidic pH (between 2-5) (Fuller et al., 2014). The $^{137}Cs^+$ activity concentration in solution was measured with liquid scintillation counting (TriCarb 2100TR, Perkin Elmer Ins.). The concentration of stable $^{133}Cs^+$ in solution was measured by Inductively Coupled Plasma Mass Spectrometry (Agilent Technologies 7700 Series ICP-MS).

*$NH_4^+$-$K^+$ selectivity on the FES*

Competing cations $Cs^+$, $K^+$, $NH_4^+$ have similar ion properties and comparable selectivity for the planar exchange sites. On the FES, the differences become more pronounced, due to the specific size of the selective sorption sites. By adding radiocaesium and variable concentration of $NH_4^+$ the selectivity of $NH_4^+$ to $K^+$ can be determined.

The $^{137}Cs^+$ sorption on glauconite sands was studied in batch sorption using the experimental procedure adapted from Wauters et al. (1996b). The method is based on masking the regular exchange sites with $Ca^{2+}$ to ensure that only the FES take part in $Cs^+$ exchange. The experiment was performed in a background solution with 5 mM $K^+$, 100 mM $Ca^{2+}$ and $NH_4^+$ in five different concentrations between 0 and 5 mM (0, 1, 2, 2.5 and 5 mM). Working at lower $K^+$ concentrations is not relevant as the linear $K_D.m_K$ relationship is not strictly valid for $K^+$ concentrations below 1 mM. In the lower $K^+$ concentration domain the RIP is underestimated (de Preter, 1990; Hisashi et al., 2013; Wauters et al., 1996b).

On day zero the supernatant was spiked with 1.5 kBq $^{137}Cs^+$ $g^{-1}$ sand, containing $3.2 \times 10^{-8}$ M CsCl carrier. After 48 hours the $^{137}Cs^+$ activity concentration in solution was measured and the $K_D$ determined from the difference in $^{137}Cs^+$ activity concentrations between blank (no sand) and samples, the solution volume and the sand weight. From the start of the pre-equilibration phase the tubes were shaken on an orbital bench shaker (0.42 $s^{-1}$). The $NH_4^+$ concentrations in solutions at the start, after pre-equilibration and after 48 hours were confirmed with a colorimetric method.

Comparing the two-ion system (K-Ca) with the three-ion system (K-Ca-$NH_4$) allows the determination of the $NH_4^+$ to $K^+$ selectivity coefficient on the FES. The quantitative description has been derived before (Wauters et al., 1996b). Briefly, the $K_D$ value of $^{137}Cs^+$ in the FES sites in the two-ion system is termed the $K_D$ (K-Ca) and is described by Eqn. (3.1) that can rearranged to

$$K_D(K-Ca) = \frac{[FES].K_c^{FES}(Cs/K)}{mK} \qquad \text{Eq. 3.2}$$

With $K_c^{FES}$ (Cs/K) the selectivity to $Cs^+$ over $K^+$ on the FES and mK the $K^+$ concentration in solution (mM). It is assumed that trace levels of $Cs^+$, i.e. $^{137}Cs^+$, only bind to the FES and not to the other sites and equations *(3.1)* and *(3.2)* assume that the FES sites are close to 100% occupied by $K^+$. In the three-ion system, $NH_4^+$ also occupies the FES and the $K_D$ value of $^{137}Cs^+$ in that system is termed the $K_D$ (K – Ca – $NH_4$) for which it can be shown (Wauters et al., 1996b) that

$$K_D(K-Ca-NH_4) = \frac{[FES].K_c^{FES}(Cs/K)}{mK+K_c^{FES}(NH_4/K).mNH_4} \qquad \text{Eq. 3.3}$$

With $K_c^{FES}$ ($NH_4$/K) the selectivity to $NH_4^+$ over $K^+$ on the FES and $mNH_4$ the $NH_4^+$ concentration in solution (mM). The assumptions for equation 3.3 are similar to equation 3.2; valid at trace levels of $^{137}Cs^+$ and $Cs^+$ sorption limited to the FES sites. With the exception that the FES are occupied close to 100% by $K^+$ and $NH_4^+$ with a ratio depending on the $NH_4$/K-selectivity coefficient in the FES. $NH_4^+$ is generally a factor 4 to 7 more competitive than $K^+$ in the FES (de Preter, 1990; Wauters et al., 1996a).

Combining equations *(3.2)* and *(3.3)* yields:

$$\frac{K_D(K-Ca)}{K_D(K-Ca-NH_4)} = 1 + K_c^{FES}(NH_4/K).\frac{mNH_4}{mK} \qquad \text{Eq. 3.4}$$

Plotting the ratio of the $K_D$ of $^{137}Cs^+$ with or without $NH_4^+$ to the concentration ratio $mNH_4$ to mK yields a linear trend and the slope of that line equals the $K_c^{FES}$ ($NH_4$/K). A similar concept for the determination of the $K_c$ (K/Na) has been described by de Preter et al. (1991).

*Sorption isotherm*

Radiocaesium batch sorption experiments were performed on samples D1, D2 and B2. The experiment was performed in a 0.5 mM $K^+$ (KCl) and 100 mM $Ca^{2+}$ ($CaCl_2.2H_2O$) background solution. The lower background $K^+$ concentrations, compared to the selectivity experiment, were chosen to reproduce more realistic in-situ conditions. Freshly sampled aquifer solutions from the Diest and Berchem Formation contain 0.14-0.37 mM $K^+$, $Ca^{2+}$ concentrations range from 0.4-1.7 mM.

The procedure of the sorption isotherm experiment is similar to that of the selectivity experiment. The samples were pre-equilibrated in the background solution. At day zero the samples were spiked with $^{137}Cs^+$ (1.8 MBq $g^{-1}$ containing 8 x $10^{-8}$ M CsCl carrier). At the same time a stable $Cs^+$ solution was made from a calibrated CsCl stock solution that was added in a concentration range of $10^{-8}$ M to $10^{-4}$ M. To one set of duplicates no stable CsCl was added, these samples contain the lowest dose 8 x $10^{-8}$ M $Cs^+$. The supernatant was sampled and $^{137}Cs^+$ and total dissolved stable $Cs^+$ concentrations were measured at different time points (48 hours, 7 days, 28 days, 53 days and 90 days). The samples were placed on an end-over-end shaker (30 RPM) for the entire duration of the experiment. The adsorption $K_D$ values of

$^{137}Cs^+$ were derived from the radioactivity based concentrations, the volumes and sand weight as described above.

All samples had been pre-equilibrated with the background solution without added stable $Cs^+$, however natural $Cs^+$ is present at trace levels in the samples. At very low added $Cs^+$ concentrations in solution, this natural $Cs^+$ can be desorbed from the sample and this increases the total stable $Cs^+$ concentration in solution. The $Cs^+$ in solution detected by ICP-MS consists of the fraction of added stable $Cs^+$ that is not sorbed on the glauconite plus the desorbed natural $Cs^+$. The stable $Cs^+$ concentration can be measured at low concentrations by ICP-MS (limit of detection (LOD) 0.002 µg $^{133}Cs^+$ $L^{-1}$, equivalent to $1.5\times10^{-8}$ M) (Annex 1. Caesium-137 versus caesium-133 data).

The adsorbed [$Cs^+$] (mol $kg^{-1}$ sand) at equilibrium is preferably derived from the $^{137}Cs^+$ activity based $K_D$ by the following equation.

$$Cs_s = [^{133}Cs].K_D^{137Cs} \qquad \text{Eq. 3.5}$$

with $Cs_s$ the sorbed stable $Cs^+$ concentration in mol $kg^{-1}$, $[^{133}Cs^+]$ the solution concentration of stable $Cs^+$ in mol $L^{-1}$ and the $K_D$ of $^{137}Cs^+$ in L $kg^{-1}$. The data of $Cs_s$ were plotted to the measured stable $^{133}Cs^+$ concentrations to obtain the isotherms.

**Modelling**

The three-site model (Bradbury and Baeyens, 2000) was described for Illite du Puy in the PHREEQC geochemical code (Parkhurst and Appelo, 1999). PhreeqC allows the adjustment of the model parameters and constants, however, direct optimisation of the parameters is not possible. We used the PHREEQC version embedded in HP1 that allows for a straightforward optimisation of the parameters by coupling to the UCODE_2014 code (Poeter, Hill et al. 2014). The parameters can be iteratively optimised using least squares fitting to improve the fit between the experimental and modelled data points. Each of the parameters is defined by upper and lower constraints in a realistic range, based on known illite parameters from literature. UCODE makes it possible to calculate parameter statistics.

**X-ray diffraction (XRD) analysis**

The glauconite content of the complete glauconite sands 'bulk' was determined by quantitative powder X-ray diffraction (XRD) measurements. The complete sample was milled to produce a fine random powder (using the McCrone micronizing mill). Zincite was used as internal standard in a 10 wt% ratio. The samples were loaded using the side loading technique. In addition to the bulk measurement, oriented clay slides were made for detailed clay analysis. The samples were subjected to the Jackson treatment (modified after (Jackson, 1975), (Zeelmaekers, 2011)) before XRD analysis. In several steps the aggregates were broken up, the carbonates, organic matter (OM) and Fe-(oxy)hydroxides were removed. The carbonates were removed by a acetic acid-sodium acetate ($CH_3COOH$-$CH_3COONa$) buffer with a pH of 5. Hydrogen peroxide ($H_2O_2$) was used to remove the OM. And the Fe-(oxy)hydroxides are

removed by small amounts of sodium dithionite ($Na_2S_2O_4$). To ensure homogeneous swelling of the smectite phases the clay was Ca-saturated and oven-dried at 60°C.

The X-ray diffraction scans were measured using a Phillips PW1830 diffractometer with CuKα radiation at 30 mA and 45 kV using a graphite monochromator and a scintillation detector. The diffractometer scans were recorded in Bragg-Brentano geometry, 5 to 65 º for bulk measurements and 2 to 47 º for clay measurements, each time with a step size of 0.02 º and 2 s counting time per step. The oriented clay slides were measured under air-dry and glycolated (Ethylene glycol) conditions.

## 3. Results and discussion

**The $K_D$ of $^{137}Cs^+$ at trace levels of glauconite sand relative to that in illite**

At the lowest $Cs^+$ concentration, i.e. no carrier $Cs^+$ added except for that added through the $^{137}Cs^+$ spike, the sorption strength of $^{137}Cs^+$ is largest, corresponding to a log $K_D$ value of 3.64 (D1), 3.56 (D2) and 3.78 (B2) in the presence of 0.5 mM $K^+$ as the only competing cation (Table 3.3). The illite $Cs^+$ $K_D$ values are a factor 7.5 to 5.2 higher than those glauconite sands. The difference in $K_D$ can only partially be explained by the glauconite content: the $^{137}Cs^+$ $K_d$ is still a factor 1.8 to 2.0 higher for illite has than for pure glauconite. The difference in $K_D$ is also only partially explained by the CEC (Table 3.3). This is the first indication that the glauconite sands contain a smaller fraction of FES than the pure illite.

Table 3.3 The $K_D$ of $^{137}Cs^+$ at 0.5 mM K and at trace levels of stable $Cs^+$ for the glauconite sands and for illite as a reference (Illite du Puy).

| Sample | $K_D$ L $kg^{-1}$ | CEC $cmol_c$ $kg^{-1}$ | $K_D.m_K$ per unit of CEC (mol $cmol_c^{-1}$ ) |
|---|---|---|---|
| D1 | 4340 | 10.7 | 0.26 |
| D2 | 3530 | 8.2 | 0.16 |
| B2 | 5350 | 11.3 | 0.25 |
| IdP | 38 900 | 20.4 | 0.95 |

**The $NH_4^+$ to $K^+$ selectivity coefficients in the FES**

The selectivity of $NH_4^+$ ions for the FES was tested in a batch experiment. The $K^+$ and $NH_4^+$ ions have similar ion properties and comparable selectivity for planar exchange sites (Bruggenwert and Kamphorst, 1979). The dependence of the ratio $K_D$ ($K^+$) to $K_D$ ($NH_4^+$ + $K^+$) versus the $NH_4$/K plots for all three samples are shown in Figure 3.2. The resulting selectivity coefficients are summarised in Table 3.4.

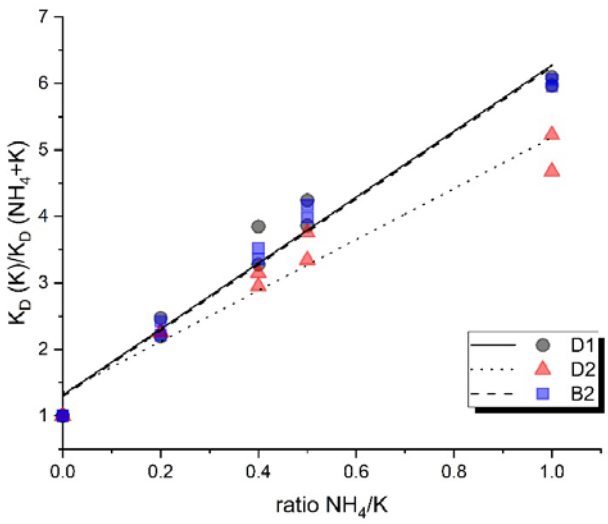


Figure 3.2 Dependence of the $K_D$ ($K^+$)/ $K_D$ ($NH_4^+ + K^+$) on the molar $NH_4^+/K^+$ ratio, in the liquid phase for sample D1, D2 and B2. The $K^+$ and $Ca^{2+}$ concentrations are kept constant at respectively 5 and 10 mM.

Table 3.4 Selectivity coefficients for $NH_4$/K on the FES obtained from the batch experiments with glauconite sand samples (D1, D2 and B2) performed in duplicate. The slope of the linear fit of the experimental data (Figure 3.2) gives the selectivity coefficient. The error on the selectivity coefficients of $NH_4$/K represent the error on linear fit.

| | $K_c^{FES}$ $(NH_4/K)$ |
|---|---|
| D1 | 4.96 ± 0.31 |
| D2 | 3.84 ± 0.31 |
| B2 | 4.96 ± 0.25 |

The $K_c^{FES}$ ($NH_4$/K) values on the FES (Table 3.4) are in good correspondence to results reported by de Preter (1990) and Wauters et al. (1994) showing that $NH_4^+$ ions bind 4 to 7 times more selective then $K^+$ ions on the FES. More specifically, de Preter (1990) reported $K_c$ ($NH_4$/K) values for the FES on clay minerals (ilite 5.85, Boom Clay 5.50 and illite-smectite 7.50), while Wauters et al. (1994) reported data for different soil types (sandy 3.5, sandy loam 5.7, loam, 6.5 and clay 6.4). The consistency of these data indicate that the FES sites in the glauconite rich sands are structurally not different from those in illite clays. This will be taken forward for isotherm fitting where we will assume that $K_c$ (Cs/K) is identical to that in illite as a starting point in the non-linear curve fitting procedure. The implication of the $NH_4$/K selectivity coefficient is that $^{137}Cs^+$ can be remobilised by ammonium in anoxic sediments.

**Sorption isotherm: effect of the $Cs^+$ concentration in solution on sorption**

The experimental sorption isotherm data of the natural glauconite sands are similar for all three samples (Figure 3.3). A strong decrease in $K_D$ is observed at increasing $Cs^+$ concentration. The shape of the log-log plot of the isotherm indicates non-linear sorption due to the site heterogeneity.

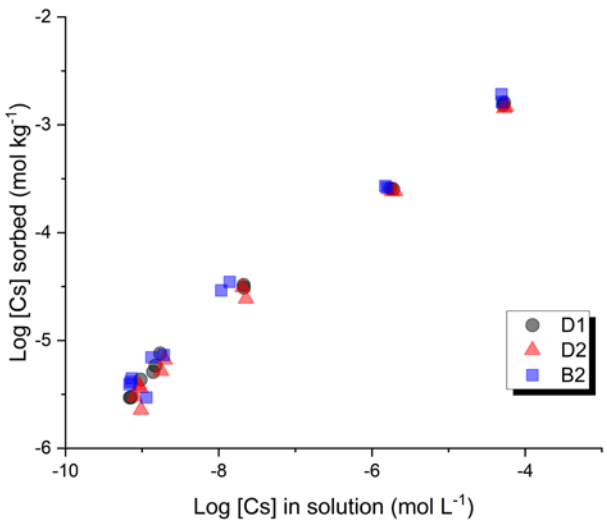


Figure 3.3 Experimental sorption isotherm data for three complete glauconite sands in a $Cs^+$ concentration range of $10^{-8}$ M to $10^{-4}$ M after 48 hours set against a background solution of 0.5 mM $K^+$ and 100 mM $Ca^{2+}$.

To fit the experimental data of the sorption isotherm, the three-site illite model of Bradbury & Baeyens (2000) was chosen as the starting point. For each site the product of the selectivity and capacity needs to be optimised. That model has six adjustable parameters: three site capacities and three selectivity coefficients of Cs-K for each type of sorption site. The capacities of the different sites are linked through the experimentally determined cation exchange capacity.

$$[\text{planar sites}] = \text{CEC} - [\text{FES}] - [\text{typeII}] \qquad \text{Eq. 3.6}$$

| | | |
|---|---|---|
| with | [planar sites] | the capacity of the planar sites (cmolc/kg) |
| | [FES] | the capacity of the FES (type I) sites (cmolc/kg) |
| | [typeII] | the capacity of the (FES) type II sites (cmolc/kg) |

This leaves five parameters to be optimised because the CEC is the experimentally determined value (Table 3.1). The illite model was plotted on the experimental data of sample D1, using the experimentally determined CEC value for sample D1, i.e. assuming equal selectivity coefficients and assuming that the fractions of FES, type II and planar sites in the total CEC are identical as in illite. The illite model in PHREEQC uses sorption constants between free sites and occupied sites, a value for each ion separately. The selectivity coefficients between two ions is, by definition, the ratio of sorption constants and it is that ratio which was used as a starting point in the isotherm fitting. For example, the sorption constants of $K^+$ on the FES is $10^{2.4}$, that for $Cs^+$ is $10^{7.0}$ and, hence, the $K_c$ (Cs/K) = $10^{(7.0-2.4)}$ = $10^{4.6}$.

The model fit sensitivity was analysed for all five parameters. First, the isotherm fitting is insensitive to the parameter $K_c$ (Cs/K) on the planar sites (Annex 1. Model fit sensitivity). The effect of the planar $K_c$

is beyond the investigated concentration range and only at high $Cs^+$ loadings, the planar sites and divalent competing cations will become relevant. Therefore, this parameter was fixed to the illite reference value in all other further optimisation. A refinement of the selectivity coefficients only or the capacities can both lead to a good optimisation of the model to the experimental data. Hence, fitting all parameters simultaneously in an optimisation will most probably give several optimised error minima and there is a covariance in optimised site capacities and selectivities (Bradbury and Baeyens, 2000). Therefore, a choice need to be made. The selectivity can be determined in batch sorption with the competing cations. The similarities of the FES of glauconite with those of illite was described above, hence it was selected to use the Cs-K selectivities of illite on FES, type II and planar sites as the starting point.

The unadjusted illite model overestimated the sorption isotherms of glauconite by factors 4.5 – 5.9 at the lower $Cs^+$ concentration range, i.e. the environmentally relevant range (Annex 1. Evaluation of the model in the lower concentration domain). The fractions of the type II and FES were optimised within boundaries, respectively 5 - 30 % and 0.02 - 0.30 % of the CEC (Table 3.5). The optimised model fitted the data of all three glauconite sands fairly well in a wide range of $Cs^+$ concentrations (Figure 3.4). The results of the optimisation are given in Table 3.5. The model predicts the experimental data quite well. In the trace $Cs^+$ concentration domain the model differs from the experimental data within factors 0.9 - 1.1, i.e. an excellent fit. The main difference between the illite model and the optimised model are the much lower FES capacities (D1 0.042 ± 0.009, D2 0.055 ± 0.005, B2 0.049 ± 0.016 % of the CEC), the error on the FES capacities refer to the 95 % confidence interval of the parameter.

Table 3.5 Results of the optimisation of the three-site model. The selectivity coefficients values were taken from the illite model (Bradbury and Baeyens, 2000) (log $K_c$ (Cs/K) FES 4.6, log $K_c$ (Cs/K) type II 1.5, log $K_c$ (Cs/K) planar sites 0.5). The represented capacities are the optimised values with the error on the site capacities representing the 95% confidence interval and the RMSE (Residual Mean Squared Error) of the log [$Cs_s$].

| | | D1 | D2 | B2 | Illite du Puy B&B model |
|---|---|---|---|---|---|
| Capacity *FES* | %CEC | 0.042 ± 0.009 | 0.055 ± 0.005 | 0.049 ± 0.016 | 0.25 |
| Capacity *type II* | %CEC | 1.70 ± 0.93 | 2.22 ± 0.56 | 1.87 ± 1.38 | 20 |
| RMSE | | 0.15 | 0.030 | 0.31 | |

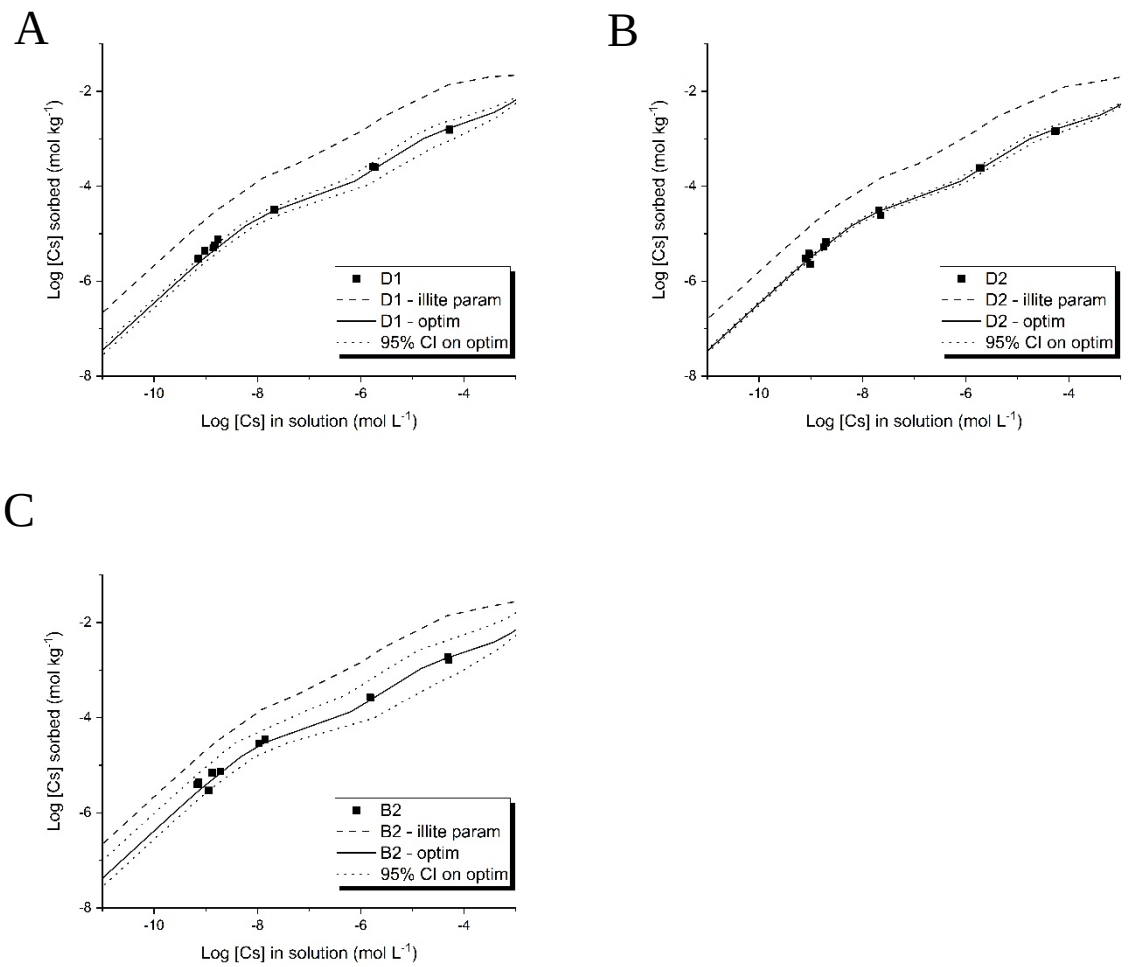


Figure 3.4 Optimisation results for each of the three samples (A) sample D1, B) sample D2, C) sample B2). The selectivity coefficients values were taken from the illite model (Bradbury and Baeyens, 2000). The plots contain the model to the experimental data using the original illite parameters (with CEC values of the glauconite sands) (dashed line) and the optimised model (full line) including the 95% confidence interval on the optimisation (dotted line).

Compared to the original illite model, the capacity of the type II is markedly smaller. The type II sites have much lower selectivity for $Cs^+$ than the FES. At trace concentration $Cs^+$ the lower capacities of the type II sites have no importance. However, there will be an impact on the sorption isotherm in the concentration range $10^{-7.5}$ to $10^{-4}$ M [$Cs^+$] in solution. The capacity of the sorption sites was determined on the experimental sorption isotherm after 48 hours. The increase in the $Cs^+$ sorption potential at trace $Cs^+$ concentration (Chapter 2) over time suggests that the accessible capacity of the selective sorption sites will increase over time. At equilibrium, after 1-2 months, the capacity of the FES and type II sites will be higher (Annex 1. Evolution of the sorption site availability over time).

**Alternative determinations of the FES capacity**

Direct measurement of FES capacity is rarely correct, due to very small capacity of the sites (De Koning et al., 2007; de Preter, 1990). Often the corrections for non-specific $Cs^+$ sorption are larger than the FES capacity. The determination of the FES capacity through the isotherm fitting is likely most correct, however several other approximate methods exist. A first method was applied by Wauters et al. (1996b): in a system with known ionic composition, the FES capacity can be calculated based on the sorption potential and the selectivity of the ions in the system. At trace concentration $Cs^+$ (no carrier $Cs^+$ added except for the radiotracer), the fraction $K^+$ on the FES ($Z_K$) is ~ 1 (Eq. 3.1). The illite $K_c$ (Cs/K) (log 4.6) is used to calculate the FES capacity for the glauconite sands. The sorption potential values are based on the equilibrium $K_D$ (48 hours). The FES capacities determined by the method of Wauters range between 4.43 and 6.71 $10^{-8}$ eq $g^{-1}$ for the glauconite sands, about one order of magnitude below estimates for Illite du Puy (4.89 $10^{-7}$ eq $g^{-1}$) (Table 3.6).

Table 3.6 Estimated FES capacity for all three samples (complete sand) calculated with the method of Wauters (Wauters et al., 1996b), with a log $K_c$ Cs/K of 4.6 and with the method of Bradbury & Baeyens (Bradbury and Baeyens, 2000) using equilibrium $K_D$ values measured in batch sorption (after 48 hours).

| Sample | FES capacity – RIP, Method of Wauters (1996b) | | FES capacity – break in the isotherm, Method of Bradbury and Baeyens (2000) | |
|---|---|---|---|---|
| | % CEC | eq $g^{-1}$ | % CEC | eq $g^{-1}$ |
| D1 | 0.05 | 5.45 E-8 | 0.06 ± 0.02 | 6.53 ± 2.03 E-8 |
| D2 | 0.05 | 4.43 E-8 | 0.12 ± 0.01 | 9.42 ± 0.96 E-8 |
| B2 | 0.06 | 6.71 E-8 | 0.07 ± 0.01 | 7.34 ± 1.22 E-8 |
| Illite Du Puy | 0.24 | 4.89 E-7 | | |

A second method for FES capacity approximation is based on the break in the sorption isotherm (Bradbury and Baeyens, 2000). The break indicates the saturation of the FES and the transition to sorption on the less selective type II sites. The intersection of the two linear fits on the two sections of the sorption isotherm represents the FES capacity (Figure 3.5 –D1, Annex 1. Determination of the FES capacity). With this dataset the position of the break cannot be determined with good accuracy due to the limited amount of data points in the log $10^{-9}$ to $10^{-7.5}$ M [$Cs^+$] in solution. Instead, the two outermost breakpoints were determined to give a FES capacity range (Table 3.6).

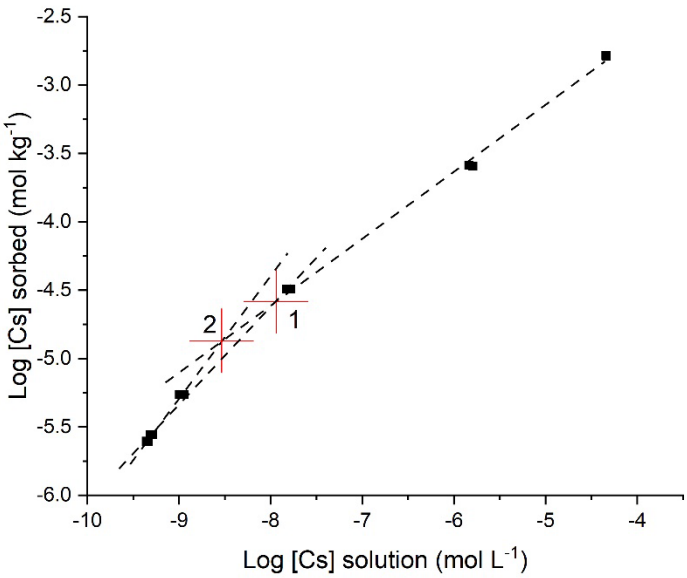


Figure 3.5 FES capacity estimate based on the break in the sorption isotherm for sample D1. The limited number of data points in the log $10^{-9}$ to $10^{-7.5}$ M [$Cs^+$] in solution does not allow an exact determination of the break point. Based on the linear fit of separate sections of the sorption isotherm two break points were determined.

The three different models to determine the FES capacities denote similar trends that its fraction of the CEC is a factor 5 lower than that of illite. The average FES fractions among the three glauconite samples are 0.05 % (isotherm method), 0.05 % (Wauters et al. (1996) method) and 0.08 % (Bradbury and Baeyens (2000) 'break in the isotherm' - method).

Variations in mineralogy, induced by weathering for example, are expected to have a strong effect on the capacity of the FES. Weathering of glauconite is described by $K^+$ leaching from the interlayer, isomorphic substitutions in the octahedral ($Fe^{2+}$ and $Mg^{2+}$ for $Al^{3+}$) and tetrahedral sheet ($Si^{4+}$ for $Al^{3+}$) and is associated with a decrease in layer charge (Meunier, 2013; Pugliese Andrade et al., 2014). The glauconite evolves to smectite via an I/S type mixed layer. $K^+$ content is inversely correlated with the smectite content (Meunier, 2005). Removal of the $K^+$ ions from the interlayer will cause an increase of the interlayer width, what has on its turn an effect on the sorption site capacities. During smectitisation the fraction of FES of the total CEC will decrease, while the total CEC can increase. Although the FES are only representing an extremely small fraction of the CEC, its capacity will determine the sorption potential at trace $Cs^+$ concentration. A secondary effect of the mineralogical variations concerns the selectivity coefficients. The strength of the selectivity for a certain cation depends on the size and charge of the cation and on the size and charge of the site. Isomorphic substitutions in the structure changing the layer charge will therefore have an effect on the $K_c$ values. However, the effect on the $K_c$ values is estimated to be smaller than the effect on the capacity of the FES.

**Lower FES capacity of glauconite evidenced by the mineralogy**

The implication of the lower FES (type I) and type II capacity on the structure has to be found in the mineralogical analysis. In Table 3.7 the mineralogical composition of the samples is given. The quantification of the glauconite content in QUANTA is based on the 060 peak positions. Due to the proximity of the $d_{060}$ values the minerals glauconite, nontronite, illite, illite-smectite and Fe-smectite are grouped together. The position of the $d_{060}$ peak depends on the size of the cations and isomorphic substitutions in the octahedral layer. The strong differences in Fe content between illite and glauconite allow clear identification based on the $d_{060}$ value (illite 1.499 Å versus glauconite >1,510 Å (Bailey, 1980)). The samples have a broad $d_{060}$ reflection and can be identified as glauconite. The $d_{060}$ values shift slightly towards lower values from D1 to B2 (Figure 3.6), indicating a change in the composition of the octahedral layer. Isomorphic substitutions in the octahedral ($Fe^{2+}$ and $Mg^{2+}$ for $Al^{3+}$) and tetrahedral sheet ($Si^{4+}$ by $Al^{3+}$) increase the interlayer width (Meunier, 2013; Pugliese Andrade et al., 2014). Small increases in the width of the FES can decrease the selectivity of the FES.

Smectite has in general higher CEC values than illite due to the accessible interlayer (e.g. ferruginous smectite ref. SWa-1 90 $cmol_c\ kg^{-1}$ (Favre et al., 2006) vs 20 $cmol_c\ kg^{-1}$ for Illite du Puy). Illite is defined as pure endmember with a smectite content < 10 wt % (Clay Mineral Society). Glauconite fractions have smectite contents of 20-27 wt%, corresponding to higher CEC values for the glauconite fraction (24.2 to 33.3 $cmol_c\ kg^{-1}$). In the smectite component, the FES and type II site capacity is ~ 0. The combination of these two effects decreases the FES fraction of the total CEC drastically. In the case of a mixture of 80-20 illite-smectite, the CEC of the mixture is expected to be 34 $cmol_c\ kg^{-1}$. Assuming that the FES and type II capacity in the illite component are resp. 0.25 and 20% of the CEC, the capacities of the fractions in the mixture will be resp. 0.12 and 9.4%. The calculated FES capacity of the CEC slightly overestimates the optimised values. The FES capacity is the most important value as this fraction will determine the $K_D$ at trace $Cs^+$ loadings.

Table 3.7 Mineralogical composition of the complete sample in wt%. The category 'other' groups the carbonate and feldspar mineral phases (n.p. not present). Other parameters given are the CEC of the glauconite fraction, the $K^+$ content of the glauconite fraction as determined by major element analysis, the smectite content (S%) in the clay fraction (e.g. for D1 20% of 34%, or 6.8% of the complete sample) and the position of the $d_{060}$ peak for the glauconite samples. The CEC was measured using the cobalthexamine method.

| | Quartz wt% | GL wt% | Other clays wt% | Fe-oxide wt% | other wt% | CEC $cmol_c\ kg^{-1}$ | $K^+$ mg $g^{-1}$ | %S in GL/S wt% | %S in bulk wt% | $d_{060}$ Å |
|---|---|---|---|---|---|---|---|---|---|---|
| D1 | 59 | 34 | < 0.1 | 0.6 | 6.4 | 26.9 | 54.1 | 20 | 6.0 | 1,5166 |
| D2 | 60 | 27 | 4.0 | 0.9 | 8.2 | 24.2 | 47.9 | 27 | 8.1 | 1,5162 |
| B2 | 56 | 27 | 5.0 | n.p. | 12 | 33.3 | 69.7 | 25 | 6.5 | 1,5153 |

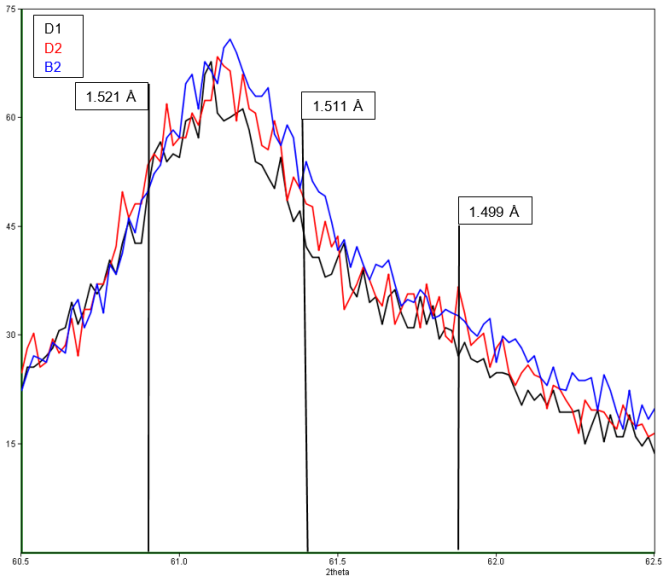


Figure 3.6 The d060 peak position in the 60.5 to 62.5 2Θ region for samples D1, D2 and B2 in comparison to illite (1.499 Å), theoretical glauconite (>1.511 Å) and nontronite (1.521 Å). The broadened shoulder indicates the presence of illite.

## 4. Conclusion

The sorption of caesium in a range of $10^{-8}$ to $10^{-4}$ M CsCl on natural glauconite sands is non-linear and requires a multi-site ion exchange model to fit the experimental data. The sorption isotherms denote lower $Cs^+$ sorption for the FES and type II sites than Illite du Puy, however glauconite sands have a uniquely larger radiocaesium interception potential than most sand substrates due to the larger fraction of clay minerals present in the glauconite pellets. The sorption per unit CEC is lower than for illite because of a lower capacity of the FES compared to illite (0.04-0.06 % of the CEC vs 0.25% for Illite du Puy) combined with a lower type II site capacity (1.6-2.2 % vs 20%). The presence of mixed layer illite-smectite and smectite in the glauconite pellets can account for part of this observation. The $NH_4^+$ to $K^+$ selectivity studies in the glauconite indicate that the ion binding characteristics are highly similar as in illite. Hence, lower sorption of $Cs^+$ on glauconite than in illite is likely reflecting the lower FES site capacities. Glauconites contain smectite that increase the CEC, however, the fraction of FES to the total CEC decreases. The $K_D$ at trace $Cs^+$ occupation is the product of the FES selectivity and its capacity. If the capacity is significantly lower, the $K_D$ will also be lower. The optimised model for glauconite is able to represent $Cs^+$ sorption data qualitatively and quantitatively in a wide range of $Cs^+$ concentrations. Determining the selectivity coefficients for additional competing cations (e.g. $Na^+$ and $Rb^+$) can fine-tune the model for more complex chemical conditions.

# Chapter 4. Glauconite sands as caesium barriers at environmentally relevant water flow rates


## Abstract

Glauconite has a radiocaesium interception potential that is comparable to illite, suggesting that glauconite containing sands may be an effective geological barrier for radiocaesium. However, glauconite is present as coarse pellets (125-250 µm diameter) and considerable sorption non-equilibrium may occur during reactive transport in these permeable sands. Here, we analysed trace caesium (Cs) sorption kinetics in agitated batch suspensions to forward predict reactive transport at variable flow rate in glauconite containing sands. Caesium sorption isotherms showed that sorption $K_D$ values in agitated suspension of glauconite sand of the Diest Fm (Dessel Member) increased factors 6-8 between 48 h and 94 days at trace $Cs^+$ concentration (~$10^{-9}$ M), a faster reaction was found at higher concentrations. A breakthrough (BT) experiment was set up with 13 packed columns of the same Fm during 154 days that were leached with $10^{-6}$ M $Cs^+$ at variable flow rates equivalent to water residence times 0.07-3.4 days. The BT was observed in treatments with the higher flow rates after 890-1170 pore volumes. The breakthrough to pore volume plot revealed earlier breakthrough at only the highest flow rate, indicating chemical non-equilibrium in that treatment. The BT curves were modelled with HP1 (Hydrus-PhreeqC), thereby relying on batch data obtained at 90 days and assuming local reaction equilibrium. The BT curves were well predicted with this model, corroborating local equilibrium unless at the highest flow rates. It is concluded that $Cs^+$ sorption on highly permeable glauconite sands is sufficiently fast to delay breakthrough in flow rates below 2.4 m $d^{-1}$. Only in high flow rate, unrealistic for the Neogene and Paleogene formations, early breakthrough could occur.

## 1. Introduction

In Belgium, deep geological disposal is proposed for high-level and/or long-lived radioactive waste, the Boom Clay or Ypresian clays are among the proposed hosts. Both clay formations are enclosed in glauconite-rich sands or silts. In the Neogene and Paleogene marine sands, glauconite is very abundant. Glauconite is a phyllosilicate, classified as a clay mineral, but mostly present as course grains or pellets sizing 125-250 µm that are present in the sand-silt fractions, only minor amounts are found in the clay fraction (< 2µm). We previously showed that the $^{137}Cs$ interception potential of glauconite sands is almost as high as that of the Boom Clay, the distribution coefficient ($K_D$, in L $kg^{-1}$, expressed as $log_{10}$ units) of $^{137}Cs$ ranges between 3.4-3.9 at 0.5 mM KCl after two months, indicating sorption similar to $^{137}Cs$ $K_D$ values in the Boom Clay (log $K_D$ 3.5 ) (Chapter 2). However, a significant reaction time is needed to reach sorption equilibrium with the $K_D$ increasing factor 6-8 between 48 h and 35 days (at trace concentration $Cs^+$ and 0.5 mM $K^+$). These slow reactions are partly related to the size of the pellets, their limited porosity reduces sorption reaction rates as demonstrated by a faster reaction in milled than in unmilled pellets. After 48 h the $K_D$ of the milled pellets is a factor 2.0-5.6 higher than in unmilled pellets. Beyond the 7 days the $K_D$ of the milled pellets is only a factor 1.1 to 1.6 higher, indicating that a part of the inner sorption sites remain inaccessible.

Contrary to the poorly indurated clays, e.g. the Boom Clay, the Neogene sands are highly permeable and groundwater velocities can be orders of magnitude higher in the sands than in the clays. High groundwater velocities increase the likelihood of physical and chemical non-equilibrium. This becomes critical for glauconite sand because adsorption of $^{137}Cs$ with the intact pellets is slow, even in stirred batch systems as given above. Hence, glauconite sands may not act as effective geological barrier because the reactive sites can be bypassed at the high flow rates. Several groundwater models exist for the Neogene aquifers and formations, mean flow rates are 0.81 ± 0.87 m $d^{-1}$ (Diest Fm) and 0.12 ± 0.43 m $d^{-1}$ (Berchem and Voort Fm). The Diest Fm has large ranges in flow rate due to the combination of proximity to the surface (< 1 m depth at some locations, with maximal flow rates of 30.6 m $d^{-1}$) and clay sections/lenses with extremely low flow rates numerically close to Boom Clay (flow rate $4.23 \times 10^{-19}$ m $d^{-1}$) (Deckers et al. (2019); Rogiers et al. (2015); Casillas-Trasvina et al. (in prep)).

Reactive transport models have been made to infer the conditions under which the reaction of the solute with the substrate (soil, aquifer material) is at equilibrium or not. The deviations of the Local Equilibrium Assumption (LEA) become apparent at the effluent side of a column: if the reactive solute is given as a pulse, then the solute exhibits earlier breakthrough followed by more tailing after the peak compared to the pulse expected with the LEA. Deviations from the LEA logically increases as reaction times increase and the residence times decrease. Valocchi (1985) numerically analysed the departures of the LEA as a function of dimensionless variable: for linear sorption (as for trace $Cs^+$ quantities in

soil), non-equilibrium in a column increases as the ratio of reaction time (reciprocal of reverse sorption rate constant) to the residence time of the water in the column increases, as the equilibrium retardation coefficient decreases and as the Peclet number increases. The Peclet number is the product of flow rate and column length divided by the dispersion coefficient. For $^{137}Cs$, the retardation factors are extremely large, based on the $K_D$ values on glauconite sand, R values exceed $10^4$, suggesting small effects on slow reactions. However, the residence time of water in such sands surrounding waste can be less than a day which, again, suggests that LEA is maybe invalid. There are surprisingly few studies who have tested the LEA for $^{137}Cs$ in soils or groundwater at different flow rates. Most studies compare the LEA prediction to the experimental results at one constant flow rate. In the case of non-ideal behaviour, seen as discrepancies between the modelled and experimental results, chemical non-equilibrium or non-linear sorption reactions are assumed.

The reactive transport models cannot grasp the complexity of the local physical environment surrounding the binding sites, for example because sorption kinetics in and around pellets in a column is different from that in batch as even batch kinetics may be affected by diffusion processes in immobile water. Hence, experimental evidence is still warranted to test LEA. Against this background, we have set up column experiments to identify if $Cs^+$ sorption is sufficiently fast to delay $Cs^+$ breakthrough under realistic flow conditions and if chemical equilibrium flow is still valid at extreme flow rates. This required a two-step approach: (1) experimentally determining $Cs^+$ breakthrough curves (BTC) in columns subjected to a range of flow rates; (2) use batch sorption kinetics to forward predict the experimental results. Breakthrough curves were obtained with a step inflow of stable $Cs^+$ and ICP-MS detection of $Cs^+$ rather than trace $^{137}Cs$ because of the high doses required before reaching breakthrough. The sorption isotherms on glauconite sand have shown that sorption is still in the linear range at the trace solution concentrations used ($10^{-6}$ M), but a kinetic analysis was used for the concentration dependent sorption.

## 2. Material and methods

### Sample selection

The Neogene and Paleogene glauconite sands are very diverse sands in respect to the grain size, the glauconite content and total clay content. However, the $Cs^+$ sorption potentials are similar. The Diest sand formations have the highest permeability and flow rates. One glauconite sand of the Diest Fm, Dessel member, was chosen for the column experiment (Sample D5).

The sample D5 originates from the ONDRAF-NIRAS- Dessel-5 core (core 48, 138.45 m below surface). The sample was stored in vacuum sealed bags since sampling. Before use, the samples were oven-dried at 60°C. Data of this sample on the chemical and mineralogical composition and $Cs^+$ sorption potential are presented in Chapter 2. The geology, hydrogeology and hydrology of the ON-Dessel-5 core was studied in more detail in the context of the surface disposal site (Beerten et al., 2010). The specific core 48, used in this study, is not represented in that study. More extensive data is present on core 49, comparable to the D5 sample based on the available data (Table 4.1).

The commission of stratigraphy characterises the lower section of the Diest Formation (the Dessel Member) by fine dark green glauconite pellets, mica flakes and calcareous fragments (Figure 4.1). Sample D5 fits perfectly to this description. When separating the glauconite from the matrix, two main types of glauconite pellets can be distinguished: large rounded/globular pellets (~ 500 µm average diameter) and small angular pellets (~ 125 µm).

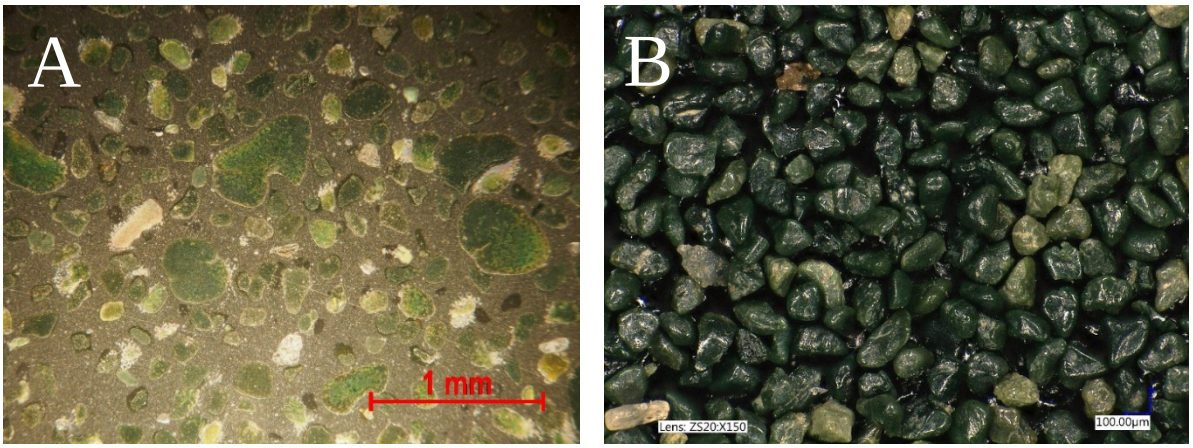


Figure 4.1 Sample D5 contains two types of glauconite distinctly different in size and shape (A). In the size fraction below 125 µm (B) the glauconite is relatively uniform in size, colour and shape.

Table 4.1 Available data on sample D5 used in this study and a sample from core 49 that has similar properties as D5.

| Parameter | Unit | Sample D5 | (Beerten et al., 2010) | |
|---|---|---|---|---|
| Core number | | ON-Dessel-5-48 | ON-Dessel-5-49 | |
| Depth | mTAW* | 113 | 114 | |
| Grain size | | N.A.** | Grain size (µm) | % |
| | | | < 2 µm | 0.7 |
| | | | < 10 | 1.2 |
| | | | < 20 | 1.7 |
| | | | < 50 | 2.5 |
| | | | < 100 | 7.4 |
| | | | < 200 | 92.3 |
| | | | < 500 | 99.7 |
| | | | < 1000 | 100 |
| CEC | $cmol_c\ kg^{-1}$ | 12 | 13 | |
| Glauconite content | wt % | 30 | 19.9 | |
| Bulk density | $g\ cm^{-3}$ | N.A. | 1.62 | |
| Porosity | | N.A. | 40.5 | |
| Hydraulic conductivity ($K_h$ horizontal and $K_v$ vertical) | $m\ d^{-1}$ | N.A. | $K_h$ 3.30<br>$K_v$ 1.81 | |
| Flow rate | $m\ d^{-1}$ | $3.6 \pm 0.7 \times 10^{-2}$ *** | | |

* The sampling depth is expressed in mTAW, or the reference level in Belgium (Tweede Algemene Waterpassing)
** N.A. not analysed or data not available
*** The flow rate of sample D5 is based on the groundwater discharge at -125 mTAW in the L-64a filter, representative for the in-situ conditions of the D5 sample Rogiers et al. (2015).

**Batch sorption studies**

Sorption of $^{137}Cs$ on glauconite was studied in batch experiments with a K-Ca background solution based on the experimental procedure adapted from Wauters et al. (1996b). The glauconite sands were pre-equilibrated with a background solution of 0.5 mM KCl and 100 mM $CaCl_2$ in a solid/liquid ratio of 1 g to 30 mL. The $Ca^{2+}$ in solution is added to saturate the planar sites and hence limit the $Cs^+$ sorption to the selective sorption sites (FES type I and type II). After pre-equilibration the solution was labelled with radiocaesium (1.5 kBq $mL^{-1}$ containing 0.01 µg $mL^{-1}$ CsCl carrier). The solution was sampled at several time points (2, 35, 64, 94, 287 days) and the activity in solution was measured with liquid scintillation counting (TriCarb 2100TR, Perkin Elmer Ins.). Sorption experiments were performed in a non-buffered system (pH ~ 7) and at a S/L of 1g to 30 mL. The choice for a higher S/L than typically used in standard batch sorption experiments with clay (S/L of 1 g $L^{-1}$), is required to have a representative sample size. The effect of the higher solid-liquid ratio on $^{137}Cs$ sorption and kinetics was evaluated in a small side experiment (Annex 2. Effect of the solid/liquid ratio).

**Column set-up**

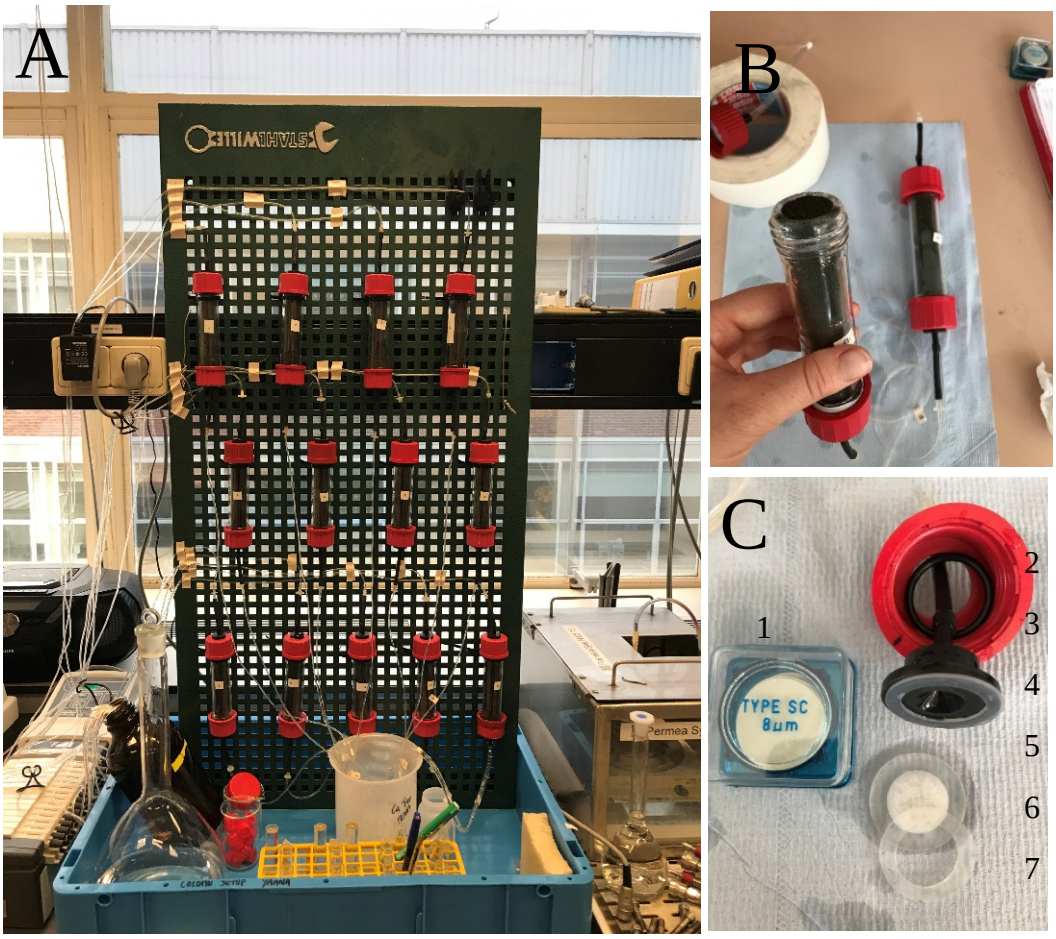


Figure 4.2 A) Set-up of the column experiment; B) filled column before mounting in the set-up. Teflon tape is added in the screw thread of the end-caps for sealing. C) 1- 8 µm Millipore membrane, 2,4- two part end cap, 3,5,7-o-rings for sealing, 6-fritted glass filter (P2, pore size 40-90 µm).

Vertical continuous flow column experiments were conducted to evaluate the sorption of $Cs^+$ at a concentration of $10^{-6}$ M onto glauconite sand at eight Darcy velocities between 0.079 and 3.5 m $d^{-1}$. The experiments were performed with stable $^{133}Cs^+$ (CsCl), since the amount of activity needed to obtain breakthrough in the effluent was unrealistically large to allow. The concentration of $10^{-6}$ M $^{133}Cs^+$ in the influent is high enough to be detectable in the effluent with ICP-MS (limit of detection (LOD) 0.002 µg $^{133}Cs$ $L^{-1}$, equivalent to $1.5 \times 10^{-11}$ M) and low enough to be within the environmental relevant ranges (see below for a discussion). The $K^+$ competition was increased by using a higher $K^+$ concentration of 1 mM, compared to 0.5 mM in batch sorption experiments, in order to decrease the breakthrough time. The concentration independent radiocaesium interception potential is expressed by the $K_D.m_K$ with $K_D$ the sorption potential and $m_K$ the concentration $K^+$ at which the $K_D$ was measured.

Glass columns of 2 cm internal diameter and 12 cm length were wet-packed with 51.5 g of glauconite sand to avoid air entrapment. Fritted glass filters (P2, pore size 40-90 µm) and a Millipore membrane (8 µm) were added to the end-caps to prevent sample loss and O-rings for sealing. Since the glauconite

sand contains a small clay-sized fraction, the glass filter could be clogged by the clay particles. By adding the Millipore membrane the loss of clay fraction with the effluent and blocking of the glass filter could be prevented. The glass columns, end-caps and glass filters were acid washed in 0.1 M HCl (Figure 4.2).

*Pre-equilibration*

The glauconite sand was pre-equilibrated with a 1 mM $K^+$, 10 mM $Ca^{2+}$ background solution by rinsing the columns for 50 pore volumes (PVs) over the course of six days. In the pre-equilibration stage with the $Cs^+$-free inlet solution the same flow rate was applied to all columns (1.2 m $d^{-1}$). At the last day the tubing was replaced with tubing of different bore diameters (see 2.7) and the flow rate was determined in all columns by measuring the volume of effluent over time.

Two additional columns were set up and flushed with a $Cs^+$-free background solution (< $4 \times 10^{-8}$ M) with a flow rate of 1.2 m $d^{-1}$ over a time of 21 days to determine the background concentration $Cs^+$ leached from the sand by the pre-equilibration solution.

*Bromide tracer test*

A tracer test with the inert tracer bromide ($Br^-$) was performed in three columns to obtain the physical transport parameters and to evaluate physical non-equilibrium conditions. Heterogeneities in the columns can cause non-equilibrium flow through preferential pathways. A pulse of 0.6 PVs of 0.1 mM $Br^-$ was injected and the effluent concentration was sampled periodically over 3 PVs and $Br^-$ detected by ICP-MS. The flow rate of the columns (3) subjected to the $Br^-$ tracer test was 1.2 ± 0.09 m $d^{-1}$.

*Column experiment*

The column experiment (13 columns in total) was run at eight different Darcy velocities between 0.079 and 3.5 m $d^{-1}$ (0.079, 0.17, 0.33, 0.54, 0.73, 1.2, 2.4, 3.5 m $d^{-1}$) (Figure 2). The columns are named based on the number of PVs per day (K29A-B, K20A-B, K10A-F, K6, K5, K4, K3, K1, K0.7). The combination of the bore diameter of the pump tubing, the pump velocity and the counter pressure in the column determines the actual flow rate. We assume the counter pressure in the column was the same for all columns. The effluent was collected and weighed to determine the flow rates over the entire duration of the column experiment. In some columns the flow rate decreased over time, mostly indicating wear or clogging of the tubing. The original flow rate could be restored by flushing or replacing the tubing. By tracking the flow rate, the exact number of pore volumes at every $Cs^+$ concentration measurement point could be calculated.

An inlet solution with 1 mM $K^+$, 10 mM $Ca^{2+}$ and $10^{-6}$ M $Cs^+$ was injected for 154 days (step), or until the glauconite sand was saturated (when the effluent concentration $Cs^+$ was ≥ 95 % of the inlet concentration). The effluent concentration $Cs^+$ was determined by ICP-MS (Agilent Technologies 7700 Series) in 2% $HNO_3$ acidified samples. Stop-flow was used to identify slow reactions: the flow was

stopped for 48 h to 1 week, a leachate sample was taken before the stop event and immediately after the flow was resumed and both concentrations were compared.

*Modelling*

The software STANMOD is used to obtain the column dispersion coefficient (D). An inverse equilibrium CDE (convection-dispersion equation) can be optimised with the experimental data of the $Br^-$ tracer test to determine the dispersion coefficient D (inverse CXTFIT program).

Forward modelling of the experimental $Cs^+$ breakthrough results based on the local equilibrium assumption (LEA) can be done both in STANMOD or HYDRUS-1D. Both programs simulate one-dimensional movement of water, heat and multiple solutes in the unsaturated, partially saturated porous media (Šimůnek et al., 2005). In HYDRUS the Richards equation is used for simulating variably-saturated water flow and advection-dispersion type equations for heat and solute transport. STANMOD simulates the solute transport in saturated columns with the CDE model (CHAIN program). In both programs the one-dimensional advection-dispersion equation for solute transport prediction is as follows:

$$R \cdot \frac{\delta c}{\delta t} = D \frac{\delta^2 C}{\delta x^2} - v \frac{\delta C}{\delta x} \qquad \text{Eq. 4.1}$$

where R is the retardation coefficient (-), *C* the solute concentration in the liquid phase (mg $L^{-1}$), *t* is the time (d), D is the dispersion coefficient ($m^2$ $d^{-1}$), *x* the vertical coordinate in the column (m) and *v* the linear water velocity (m $d^{-1}$). The R describes the effects of interactions between a solute and the surrounding porous matrix, on the transport of the solute. For inert tracers R is 1. In the case of linear sorption R can be written as:

$$R = 1 + \frac{\rho}{\theta} K_D \qquad \text{Eq. 4.2}$$

with ρ the bulk density of the porous medium (g $m^{-3}$), θ the porosity of the porous medium (-) and $K_D$ the distribution coefficient (L $kg^{-1}$) determined in batch sorption experiments.

HYDRUS and STANMOD allow interaction of solutes with the solid phase with linear sorption (constant $K_D$ values) only and no competition. These models are not suitable for the situation here: (1) at variable $Cs^+$ concentration (e.g. between natural background $Cs^+$ vs $10^{-6}$ M Cs), sorption is not linear and the linear sorption–transport model will not be able to predict $Cs^+$ retention. The highly selective sites with high $K_D$ values have very low capacities leading to much lower $K_D$ values at higher $Cs^+$ concentrations; (2) the interaction and competition effects among the solutes in solution cannot be taken into account. The capacity and selectivity of different types of sites can be taken into account by extending the transport model with a geochemical model. The HP1 code couples transport modelling in HYDRUS with the PHREEQC biogeochemical code (Jacques and Šimůnek, 2000). The HYDRUS component still uses the Richards equation for simulating variably-saturated water flow and advection-

dispersion type equations for heat and solute transport. The PHREEQC component adds interactions with minerals, gases, exchangers and sorption surfaces based on thermodynamic equilibrium, kinetic, or mixed equilibrium-kinetic reactions. The Cs sorption isotherms on glauconite sands between $10^{-9}$ and $10^{-4}$ M Cs have be calibrated with PHREEQC based on a three-site model (Chapter 3). This model was used to predict Cs transport in the columns.

## 3. Results & discussion

**Batch Cs sorption experiments**

The sample D5 was part of the data presented in Chapter 2. The equilibrium $K_D$ (± standard deviation of two replicates) of $Cs^+$ in sample D5 is 5350 ± 320 L $kg^{-1}$ after 35 days in a 0.5 mM and 100 mM Ca background solution. The $Cs^+$ sorption increases with a factor 2 between 48 hours and 1 month and with a factor 1.6 to 1.8 between 1 and 8.5 months at trace $Cs^+$ concentration (Chapter 3) (Figure 4.3).

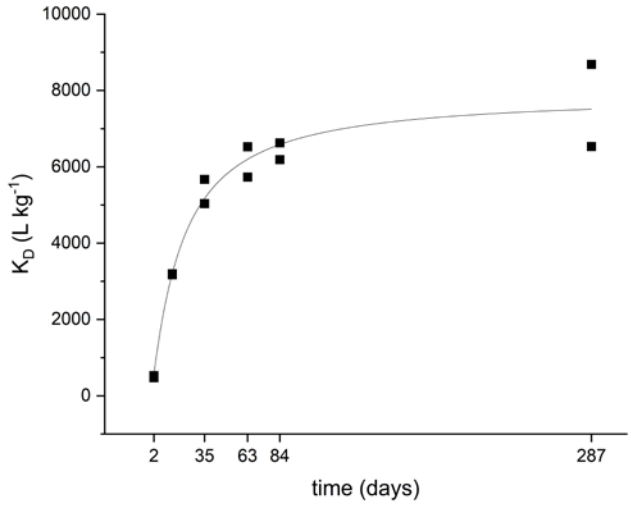


Figure 4.3 Experimental data and empirical fit of the evolution of the $K_D$ (L $kg^{-1}$) of $Cs^+$ with time for sample D5 determined in batch experiment (in duplicate) in a background solution of 0.5 mM K, 100 mM Ca at trace concentration $Cs^+$ ($<10^{-8}$ M).

Two aspects should be taken into account to translate the batch sorption data of Figure 4.3 to sorption in the column. First is concentration and composition of the solution and second is the sorption kinetics. The columns were leached with a solution containing higher Cs and K concentration than in that batch study. The higher $K^+$ and $Cs^+$ concentration will reduce the $Cs^+$ $K_D$. Under the column experiment conditions (1 mM $K^+$, 0.01 M $Ca^{2+}$ and $10^{-6}$ M $Cs^+$), an equilibrium $K_D$ of 145 L $kg^{-1}$ can be predicted for reasons explained in the next paragraph. That equilibrium $K_D$ is equivalent to R=423 according to Eqn. (4.2).

The concentration and time dependent sorption of Cs was not measured for sample D5, however it was measured for very similar samples D1 and D2 and shown in Figure 4.4. At the lowest Cs concentration, i.e. where $^{137}Cs$ was added without carrier, the $K_D$ values increased factors 6-8 between 2 and 94 days. At and around Cs concentration at the column influent ($10^{-6}$ M), $Cs^+$ sorption $K_D$ increases factor 1.4-3.2 between 2 days and 94 days. Above $10^{-5}$ M [Cs] in solution, the effect of kinetics is negligible. The increase in $K_D$ with time (2 days versus 94 days) can be modelled for samples D1 and D2 in PHREEQC as an increase in accessible FES sites (type I) from 0.05 to 0.09 % of the CEC and from 1.9 to 2.9 % of the CEC for the type II sites. The sorption isotherm on sample D5 was modelled with this concept, thereby changing the CEC to that of the D5 sample and by adjusting $K^+$ concentration (1 mM), thereby keeping the selectivity coefficients unmodified (after (Bradbury and Baeyens, 2000) (Table 4.2 and Figure 4.5).

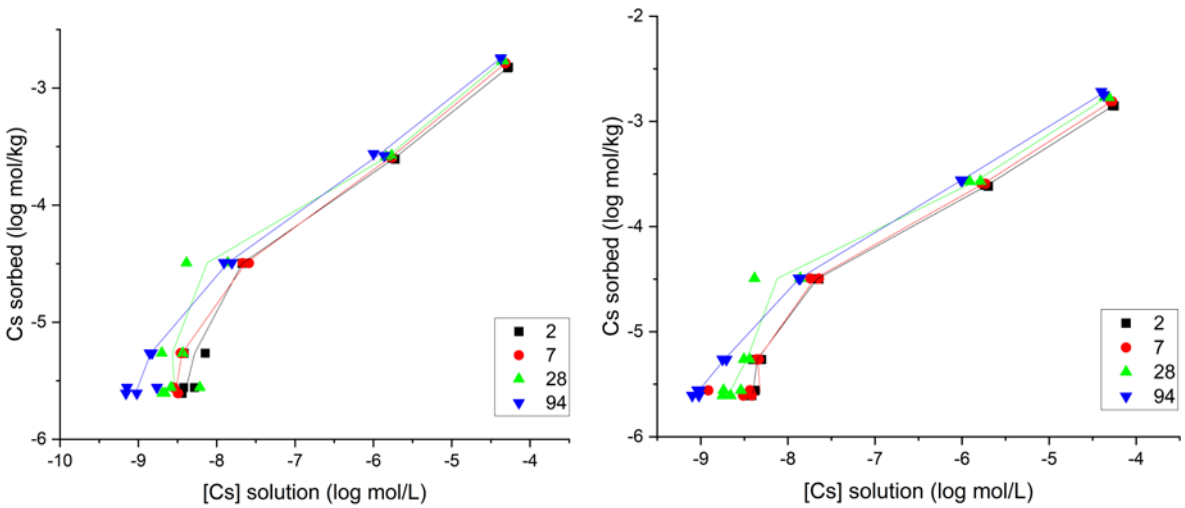


Figure 4.4 The sorption isotherm for $Cs^+$ at different time points between 2 and 94 days for sample D1 (A) and D2 (B), comparable to sample D5, in a background solution of 0.5 mM $K^+$ and 100 mM $Ca^{2+}$. At $10^{-6}$ M $Cs^+$ in solution, the $K_D$ increases with a factor 1.2, 1.3 and 1.9 between 2 days and, respectively, 7, 28 and 94 days.

Table 4.2 Model parameters for a three-site sorption model at 2 days and 94 days interaction time for sample D5 (CEC 12 $cmol_c$ $kg^{-1}$) under the experimental conditions of the column set-up (1 mM KCl, 10 mM $CaCl_2$).

| | 2 days sorption isotherm | 94 days sorption isotherm |
|---|---|---|
| | % of the CEC | % of the CEC |
| FES | 0.05 | 0.09 |
| type II | 1.9 | 2.9 |
| planar | 98 | 97 |

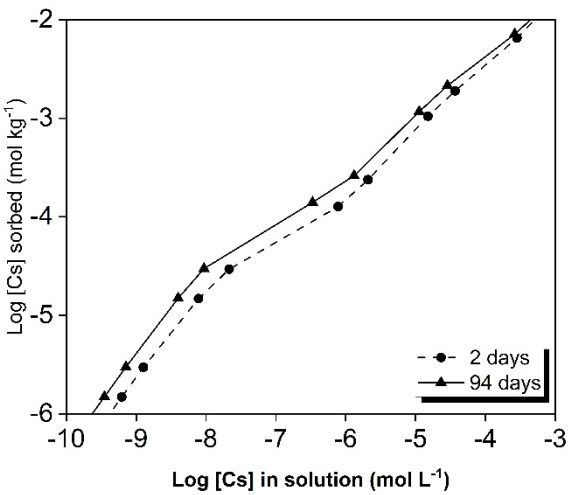


Figure 4.5 Modelled $Cs^+$ sorption isotherm for sample D5 for 2 and 94 days in a background solution of 1 mM $K^+$ and 10 mM$Ca^{2+}$ (PHREEQC).

## Column experiments

*Column characterisation: Pore volume, bulk density and water content*

The total column volume of each column is 37.7 $cm^3$. A particle density ($\rho_p$) of 2.65 g $cm^{-3}$ was assumed. In each column the equivalent weight of 51.5 g dry glauconite sand ($M_{dry}$) was added. The bulk density ($\rho_b$) (Eq. 4.4) in the column is 1.34-1.37 g $cm^{-3}$. The porosity ($\Theta$) calculated by Eq. 4.5 equals 0.483. The pore volume ($PV$) is calculated based on the porosity (Eq. 4.6) and equals 18.3 ± 0.1 $cm^3$ .

$$\rho_b = \frac{M_{dry}}{V_{tot}} \qquad Eq.\ 4.4$$

$$\theta = \left[1 - \frac{\rho_b}{\rho_p}\right] \cdot 100 \qquad Eq.\ 4.5$$

$$PV = \theta \cdot V_{tot} \qquad Eq.\ 4.6$$

The time to peak ($t_p$) can be calculated by Eq. 4.7. An inert tracer is expected to break through the column after 140 minutes in three replicate columns with a flow rate of 1.17 ± 0.09 m $d^{-1}$.

$$t_p = \frac{A \cdot \theta \cdot L}{Q} \qquad Eq.4.7$$

With A the surface area of the column (1.57 × $10^{-4}$ $m^2$), L the length of the column (0.12 m) and Q the volumetric flow rate [$m^3$ $d^{-1}$]. The breakthrough curve peak was reached after 150 minutes (Figure 4.6) confirming the calculated porosity results (by Eq. 4.6).

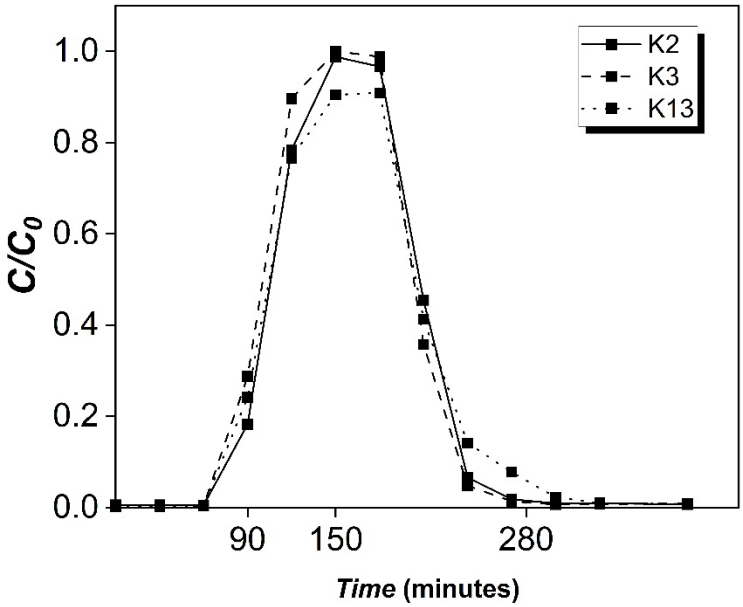


Figure 4.6 $Br^-$ breakthrough curves for three columns (K10D, K10B and K10A). The peak $Br^-$ concentration is reached at about 150 minutes, at a flow rate of 1.2 ± 0.1 m $d^{-1}$, with a pulse of 0.1 mM $Br^-$ for 0.6 PVs.

The $Br^-$ breakthrough curves were fitted in STANMOD to the one-dimensional equilibrium CDE model to obtain the dispersion coefficient (D) in the column (Simunek et al., 1999) (Table 4.3) (Annex 2. The dispersion coefficient). Bromide breakthrough curves were symmetrical and exhibited a small tailing. The equilibrium CDE corresponds relatively well to the measured breakthrough points ($r^2$ =0.77-0.97), indicating water flow occurred at physical equilibrium. Any deviations of the $Cs^+$ transport in the model to the equilibrium model must therefore be related to chemical non-equilibrium. The longitudinal dispersivity (λ) calculated by the ratio between D and the flow rate (*v*) is 3.8 ± 0.9 × $10^{-3}$ m.

Table 4.3 Dispersion coefficient (D) based on the least-squares fit to the equilibrium convection-dispersion model (CDE) in STANMOD. Dispersivity (λ) is calculated by dividing D by the Darcy velocity v.

| Column | *v* m $d^{-1}$ | D × $10^{-3}$ $m^2$ $d^{-1}$ | λ × $10^{-3}$ m | $R^2$ - |
|---|---|---|---|---|
| K10A | 1.25 | 6.36 | 5.1 | 0.97 |
| K10B | 1.24 | 3.84 | 3.1 | 0.86 |
| K10D | 1.06 | 3.29 | 3.1 | 0.77 |

*Flow rates*

A range of eight different flow rates were applied to the columns (0.079 and 3.5 m $d^{-1}$) (Table 4.4). The flow rates remained stable over time with a maximum of 2.7 to 16.3 % deviation (Figure 4.7). The corresponding water residence times are 0.83-36 hours. In long-term column experiments it is a challenge to keep the columns running at constant conditions. For example, in column K5, the flow rate strongly decreased between 28 and 37 days. By changing the tubing, the flow rate in the column could

be restored to the originally flow rate (0.56 m $d^{-1}$). In the columns K29A and K20B, the flow rate could not be restored and the columns were stopped (Table 4.4).

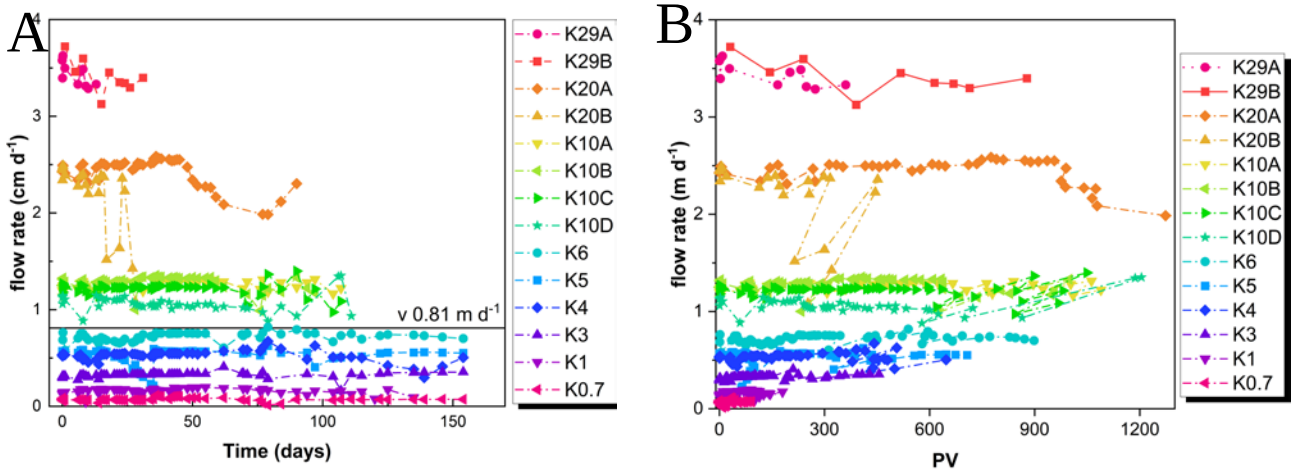


Figure 4.7 Evolution of the flow rate with time (A) and pore volume (B) for all columns with a running time of 154 days or shorter, if breakthrough was achieved. The average flow rate in the Diest Fm sands is 0.81 m $d^{-1}$ (corresponding to 6.8 PV $d^{-1}$ in the columns).

Table 4.4 Flow rate (in PV $d^{-1}$ and m $d^{-1}$), running time (d) and total number of pore volumes in the running time for all column and ranked from highest to lowest flow rate. The column names refer to the flow rate in pore volumes per day. Column K29A and K20B (grey italics) were stopped early due to problems (leaking, blocked tubing). A new column with the same flow rate as K29B was started to try to obtain breakthrough in the highest flow rate column. In columns K10E and K10F a Cs-free inlet solution was used and after 21 days the flow was stopped.

| Column name | Pore volumes per day<br>PV $d^{-1}$ | Flow rate<br>m $d^{-1}$ | Running time<br>d | Total number of pore volumes<br>$PV_{tot}$ |
|---|---|---|---|---|
| *K29A* | *29* | *3.46* | *20* | *440* |
| K29B | 29 | 3.48 | 32 | 910 |
| K20A | 20 | 2.42 | 62 | 1260 |
| *K20B* | *20* | *2.35* | *28* | *450* |
| K10A | 10 | 1.25 | 111 | 1120 |
| K10B | 10 | 1.24 | 111 | 990 |
| K10C | 10 | *1.22* | 111 | 1080 |
| K10D | 10 | 1.06 | 111 | 950 |
| K10E | 10 | 1.24 | 21 | 220 |
| K10F | 10 | 1.10 | 21 | 190 |
| K6 | 6 | 0.725 | 154 | 920 |
| K5 | 5 | 0.559 | 154 | 670 |
| K4 | 4 | 0.538 | 154 | 670 |
| K3 | 3 | 0.329 | 154 | 410 |
| K1 | 1 | 0.170 | 135 | 180 |
| K0.7 | 0.7 | 0.0792 | 154 | 97 |

*Breakthrough*

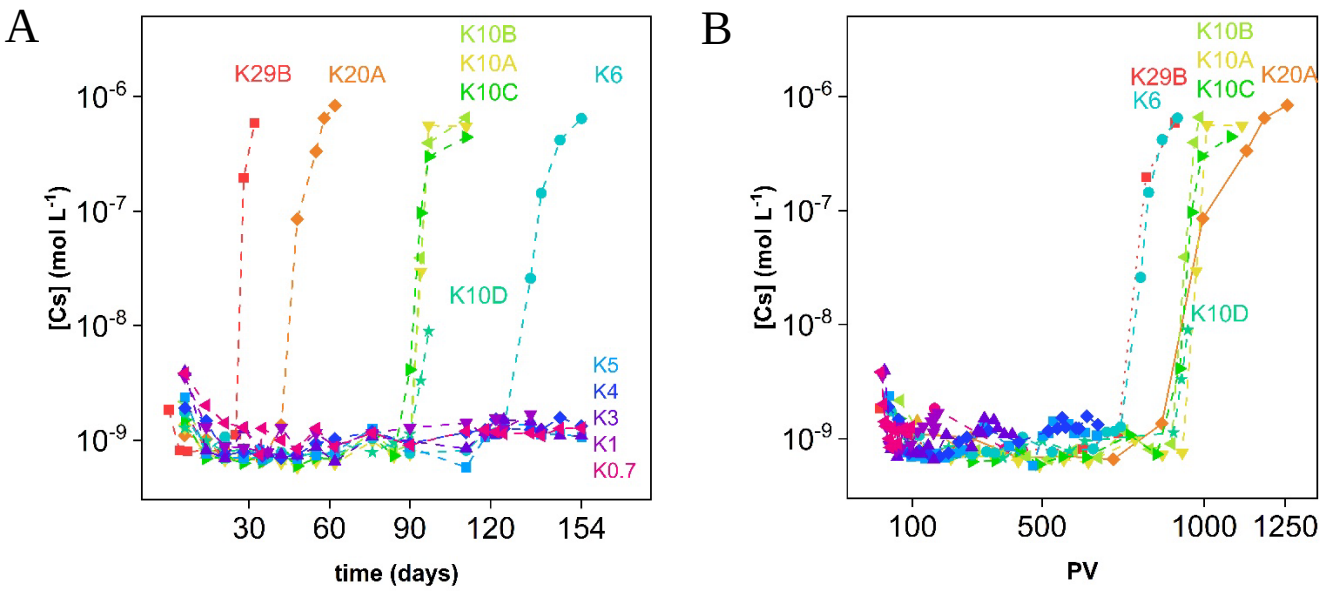


Figure 4.8 Semi-log plot of the Cs concentration in the effluent as a function of the time (A) and number of pore volumes (B). Breakthrough was reached in seven columns: in column K29B and K6 after about 900 PVs, in K10D, K10B, K10C and K10A after 1000 PVs and in K20A after about 1200 PVs.

In the seven columns with the highest flow rate, $Cs^+$ breakthrough was reached within the time span of 154 days (Figure 4.8A) following the order of flow rates. Column K29A and K20B were stopped before breakthrough was reached because of blockages in the tubing. A new column (K29B) was set up during the experiment with the same flow rate (3.5 m $d^{-1}$). The K10D reaches breakthrough slightly later than K10B, K10C and K10A (despite similar flow rate) due to a short flow stop. The BTC plotted to the number of pore volumes is measured at about 890 PVs (K29B and K6) and breakthrough is reached after 1000 PVs for K10D, K10B, K10C and K10A and in K20A after about 1170 PVs. The $Cs^+$ sorption capacity of the glauconite sand equals 3.23-3.59 × $10^{-4}$ mmol $g^{-1}$ and is estimated by the number of PVs to breakthrough ($PV_{BT}$), the pore volume of the filled column ($V_c$), the glauconite sand mass in the column ($M_c$ ) and the $Cs^+$ concentration in solution (Eq. 4.8).

$$Cs^+\ capacity = PV_{BT} \times \frac{V_C}{M_C} \times [Cs^+] \qquad Eq\ 4.8$$

The columns K29B and K6 reach breakthrough much faster with a rise in concentration starting at 740 PVs and reaching inlet solution concentration at about 900 PVs. The early breakthrough in K29B (highest flow rate) is likely related to disequilibrium flow due to the high flow rate. The only way to test this hypothesis is by stop flow. Due to practical problems stop flow could not be performed on K29B. Column K6 with a much lower flow rate was possibly not perfectly loaded, so physical non-equilibrium flow could occur. This hypothesis could have been tested by an inert tracer test. In the K20A column the $Cs^+$ increases above background after 900 PVs, however, breakthrough is delayed to about 1200 PVs.

On column K20A, K10A, K10B and K10D the flow was suspended (stop flow event; Annex 2. Stop flow). The Cs concentrations in the effluent after the stop flow did not decrease when flow resumed, i.e. there were no indications of chemical disequilibrium. However, due to the delay between sampling and measurements of the effluent, the stop flow events were performed either too early or when the column was already saturated and not in the rising limb of the BTC where sorption reaction rate can be most critically detected.

*Initial leachate concentrations reflecting native Cs desorption from the sand*

The columns were rinsed with the background solution (1 mM $K^+$, 10 mM $Ca^{2+}$) for six days to pre-equilibrate the columns. During the pre-equilibration, all columns were flushed with equal flow rates (1.2 m $d^{-1}$). The first measurement of the $Cs^+$ concentrations was made after seven days of running the $10^{-6}$ M Cs-inlet solution (and 1 mM $K^+$, 10 mM $Ca^{2+}$) at the final flow rates. The first leachates contained detectable $Cs^+$ that generally decreased over time (Figure 4.9). The highest $Cs^+$ concentrations were measured in the columns with the lowest flow rates. The effluent $Cs^+$ concentrations do not decrease to the level of the Cs-free inlet solution (<0.4 $\times 10^{-9}$ M), but stabilise at about 0.7 $\times 10^{-9}$ M. That level is reached faster in the columns with higher flow rate.

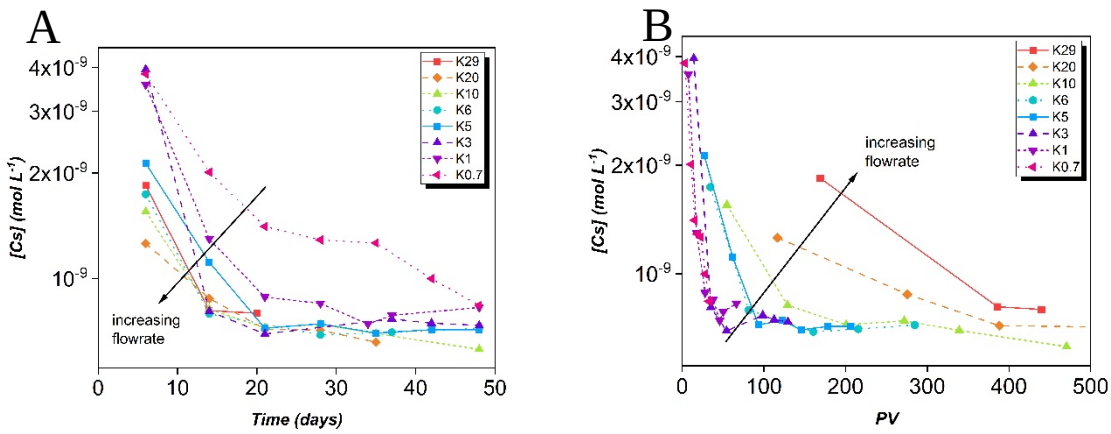


Figure 4.9 Evolution of the $Cs^+$ concentration measured in the effluent versus the time (days) (A) and the pore volumes (PV) (B). The columns are ranked from high to low flow rates.

To better understand the flow dependent $Cs^+$ concentrations at the start, two new columns were set up and flushed with a $Cs^+$-free background solution (<0.4 × $10^{-9}$ M). At a flow rate of 1.2 m $d^{-1}$, 50 pore volumes were needed to reach the same steady state Cs concentration (0.7 × $10^{-9}$ M) as in the columns leached with $10^{-6}$ M (Figure 4.10). This illustrates that the initial $Cs^+$ concentrations in the effluent are related to natural Cd desorption from the sand and, also, that resident pore water $Cs^+$ concentrations are higher than the steady state value. It is, hence, logical that the steady state is reached faster in time as the flow rate increases (Figure 4.9A), that may be the result of the combination of more removal of soluble stable $Cs^+$ by increased cumulative leaching volume and, probably, of the role of non-equilibrium for $Cs^+$ desorption. However, the latter hypothesis is counteracted when plotting the graph

of the columns leached with $10^{-6}$ M to the PVs: less PVs are needed to reach the $Cs^+$ plateau as the flow rate decreases (Figure 4.9B). The detailed plot is lacking for the high flow rate columns but the higher stable $Cs^+$ concentration at higher flow, but equal PVs leached, may already be affected by incomplete sorption of influent Cs by preferential flow of the influent to the effluent, i.e. departures from the LEA as better indicated by the early BTC at the highest flow rate (see above for K29).

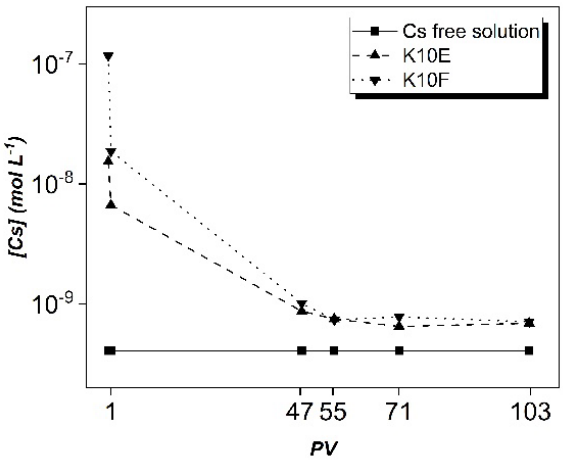


Figure 4.10 Cs concentration measured in the effluent over time (expressed in PV) in two additional columns (K10E and K10F) leached with a Cs-free background solution (<0.4 × $10^{-9}$ M).

**Forward modelling of experimental results - Local equilibrium assumption (LEA)**

The $Cs^+$ breakthrough was modelled under the LEA with the three-site sorption model in HP1. The optimised sorption model (Table 4.2), either fitted to the 2 days or 94 days batch sorption data, was used to predict breakthrough. We recall that the breakthrough times for the fast flowing columns ranged 30-120 days and that non-equilibrium reactions (factor change in $K_D$) are pronounced between 2-94 days at low $Cs^+$ concentrations (near $10^{-9}$ M), but are less than factor 2 at $10^{-6}$ M[3] (Chapter 3). The model is based on LEA, implying that the predicted breakthrough in terms of PVs will be the same for all columns, except for effect of flow rate on dispersion (Figure 4.11). Under the conditions of the column experiment, the point of breakthrough, here defined as that where effluent $Cs^+$ is half of the influent (the so-called $C/C_0$=0.5, found at PV=R (Van Genuchten et al., 2012)), is predicted after 640 PVs for the '2 days' model and 980 PVs for the '94 days' model. The model based on the 94 days isotherm accurately predicts the breakthrough of the column K10C with equilibrium flow. The slope of the breakthrough curve is comparable to the experimental data. In the column K29B and K6, both exhibiting non-equilibrium flow, the equilibrium model (94 days) overestimates $Cs^+$ retention. In this case the '2 days' model provides a better breakthrough prediction.

[3] In batch experiments (trace concentration $Cs^+$, 0.5 mM $K^+$ and 100 mM $Ca^{2+}$) the $K_D$ increases with a factor 6-8 between 48h and 3 months (Chapter 2). In the sorption isotherm experiment the $K_D$ increase is 1.4-3.9 ($10^{-8}$ M $Cs^+$), 1.2-2.0 ($10^{-6}$ M $Cs^+$) and 1.2-1.6 ($10^{-4}$ M $Cs^+$) in a background of 1 mM $K^+$, 10 mM $Ca^{2+}$ (Chapter 3).

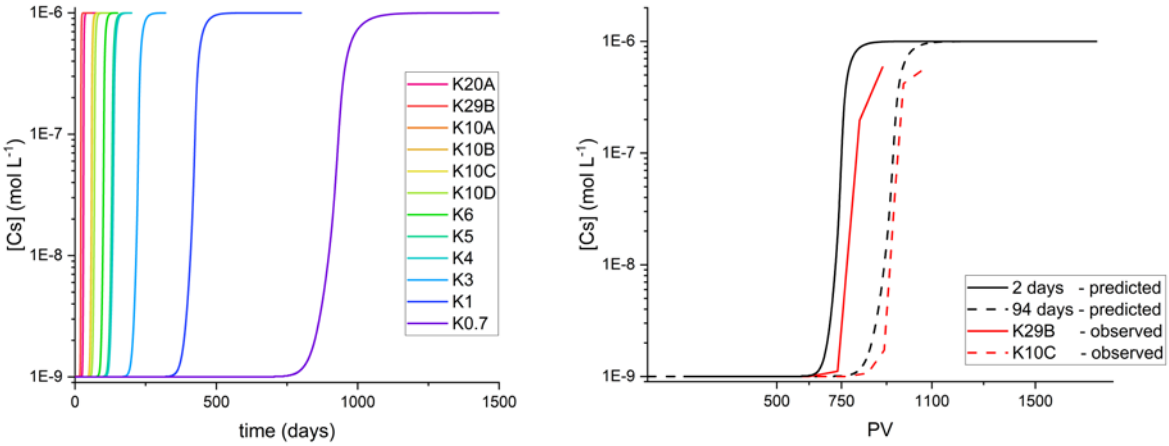


Figure 4.11 Breakthrough prediction (HP1) for all columns versus time using the '2 days' sorption isotherm model (A) and versus PVs for the '2 days' and '94 days' isotherm model (B). The red lines on the right are the observed values, the black are predicted ones.

In Table 4.5 a comparison is made between the modelled breakthrough and the experimental data in days. This, again, confirms that the LEA assumption is valid up to a flow rate of that in the column K20 and that departures of LEA (early breakthrough) is found at the highest flow rate (K29B). Modelling with the 2 days isotherm provides a good fit for K29B, but is unlikely proving the LEA, because the breakthrough time is 22 days, well beyond the 2 days.

Table 4.5 Breakthrough prediction (in days) by forward modelling with HYDRUS-HP1 based on the sorption isotherm models fitted to batch data after 2 or 94 days of reaction and compared to the experimental results.

| | Modelled breakthrough (HP1) | | Experimental breakthrough | conclusion on LEA? |
|---|---|---|---|---|
| | 2 d Days | 94 d Days | Days | |
| K29B | 22 | 34 | 30 | not valid |
| K20A | 32 | 49 | 57 | valid |
| K10B | 65 | 130 | 110 | valid |
| K6 | 110 | 160 | 150 | valid |
| K5 | 140 | 210 | >153 | valid |
| K4 | 150 | 220 | >153 | valid |
| K3 | 230 | 360 | >153 | valid |
| K1 | 440 | 690 | >153 | valid |
| K0.7 | 970 | 1490 | >153 | valid |

## 4. Environmental consequences

Caesium sorption in batch studies on glauconite sands requires >1 month to reach equilibrium, because not all of the sorption sites in the pellets are instantly accessible. There is a considerable concentration dependency, slow reactions are much more pronounced at low than at high concentrations, thereby defining the slow reactions as the factor change in the $K_D$. In the column experiments higher $Cs^+$ concentrations than ambient were used ($10^{-6}$ M compared to $10^{-8}$ M) for practical reasons, i.e. radiation hazard, but also to obtain realistic breakthrough times. At trace levels the $K_D$ values are factor 10 higher and breakthrough is expected in several years after spiking only. Even at the worst case high flow scenario, beyond the relevant range, glauconite sands effectively removed $Cs^+$ from the influent, however an early breakthrough was found. At all flow rates that are environmentally relevant (< 0.8 m $d^{-1}$, see Figure 4.7), the LEA is valid. There was one exception, the earlier breakthrough in K6 is most likely attributed to preferential flow in the column.

The key environmental question is if the LEA is equally valid at low (trace) $Cs^+$ concentrations reflecting the $^{137}Cs$ contamination scenario. The validity of the LEA depends on all system parameters including the form of the assumed non-equilibrium model (Valocchi, 1985). On the one hand, slow reactions are far more pronounced at trace concentrations compared to $10^{-6}$ M (Figure 4.4), suggesting that early breakthrough may be expected. On the other hand, the equilibrium retardation of trace $^{137}Cs$ on glauconite sand is 9300, more than factor 10 larger than at $10^{-6}$ M Cs (R=800, details not shown) and, with higher retardation, the time for reaction also increases, thereby decreasing the likelihood to detect early breakthrough. Theory predicts that both factors (R and reaction rate) counteract each other. Long-term experimental work with isotopically labelled $Cs^+$ is required to identify this. It is also suggested that advanced modelling with batch sorption kinetics should be initiated to identify mechanisms. HP1 allows to include adsorption reaction kinetics and all data are available to set up such modelling. That modelling may also reveal the time and PVs dependent stable $Cs^+$ trends at the initial phase of the experiment that are not fully explained.

At least, this study showed no early breakthrough at flow rates relevant to the field in packed columns. It speaks for itself that undisturbed heterogeneous sand formations will invariably lead to preferential fingering of contaminant plumes through zones of low glauconite content, the visual evidence on the glauconite cores readily witness such zones based on the colour. Caesium transport in the glauconite sands was tested under saturated conditions. If the water content decreases, the $K_D$ is known to decrease as competing ion concentrations increase (Szenknect et al., 2003). In the case of contamination at the surface or the application of glauconite sand as a sorption sink below the surface disposal the water content should be taken into account for accurate breakthrough predictions.

Hence, in conclusion, $Cs^+$ sorption on highly permeable glauconite sands is sufficiently fast to delay breakthrough. Only at high flow rate, unrealistic for the Neogene and Paleogene formations, early breakthrough occurs.

# Chapter 5. Radiostrontium sorption on natural glauconite sands

Adapted from Bruneel et al. (2021b).


## Abstract

The Neogene-Paleogene glauconite sands are investigated for radionuclide sorption in the framework of the Belgian radioactive waste disposal program. This study was set up to measure the adsorption of radiostrontium ($^{85}Sr$) on the sands and on glauconite fractions to identify factors explaining variable sorption among different formations. Batch $^{85}Sr$ sorption experiments were set up with 45 different glauconite sands and glauconite fractions (125-250 µm) in a background solution of 1 mM $CaCl_2.H_2O$ and 0.5 mM KCl. The distribution coefficients ($K_D$) for $^{85}Sr^{2+}$ ranged 23-65 L $kg^{-1}$ for the intact sands and ranged 50-144 L $kg^{-1}$ for the glauconite fractions. The $K_D$ values strongly correlated with the CEC ($R^2$ =0.62 for sands and 0.82 for glauconite fractions) and corresponded well with CEC based predictions based on two existing models calibrated to soils. The $K_D$ on the complete sand is proportional to the glauconite content and the $K_D$ of the glauconite fraction if no other clay minerals are present in significant amounts. Sorption equilibrium was reached within 48 hours in the complete sands, in milled complete sands, in glauconite fractions and in milled glauconite fractions, suggesting no diffusive boundaries in the glauconite pellets. It is concluded that glauconite sands have a suitably high retention of radiostrontium and the sorption strength is in line with that of other geological barriers when judged from the CEC.


## 1. Introduction

Safe storage of radioactive waste for hundreds to hundreds of thousands of years is one of the basic requirements of radioactive waste disposal. To assess the long-term safety of disposal sites, a good understanding of the processes and mechanisms controlling the radionuclide (RN) transport in the various system components is essential. Due to the long residence time of radioactive waste in the disposal site, a natural barrier will need to take over the role of the engineered barrier. In Belgium the Neogene glauconite sands have been considered as an extra embankment below the surface disposal for the short-lived and low-level waste. For the high-level and/or long-lived radioactive waste a geological disposal is proposed. Depending on the chosen host rock, glauconite sand can be present next to the natural barrier, as is the case for the Boom Clay and Ypresian clays.

The glauconite content of the Neogene Diest and Berchem Formation (Fm) varies between 35-40 %, with locally up to 89 % glauconite (e.g. Berchem Fm). The glauconite occurs in the glauconite sands mostly as sand-sized pellets. This strongly affects the properties of the sands that logically have high porosities and permeabilities. Glauconite is an iron (Fe) -rich dioctahedral mica, though it can be compared to an Fe-rich illite structure-wise with potassium ($K^+$) the dominant interlayer cation. The mineral glauconite is defined as $K\ (R^{3+}_{1.33}\ R^{2+}_{0.67})\ (Si_{3.67}\ Al_{0.33})\ O_{10}(OH)_2$ with $Fe^{3+}$ >> aluminium ($Al^{3+}$) and magnesium ($Mg^{2+}$) > $Fe^{2+}$ (Adriaens et al., 2014; Meunier and El Albani, 2007). The diverse

composition of glauconite pellets, even in similar formations, stems from both the formation and weathering history. Glauconite is a redox sensitive mineral due to the presence of both $Fe^{3+}$ and $Fe^{2+}$. Weathering affects the structural cation occupancy and interlayer composition. Iron and $Mg^{2+}$ are removed or substituted in the structure and $K^{+}$ is leached from the interlayer (Courbe et al., 1981; Van Ranst and De Coninck, 1983).

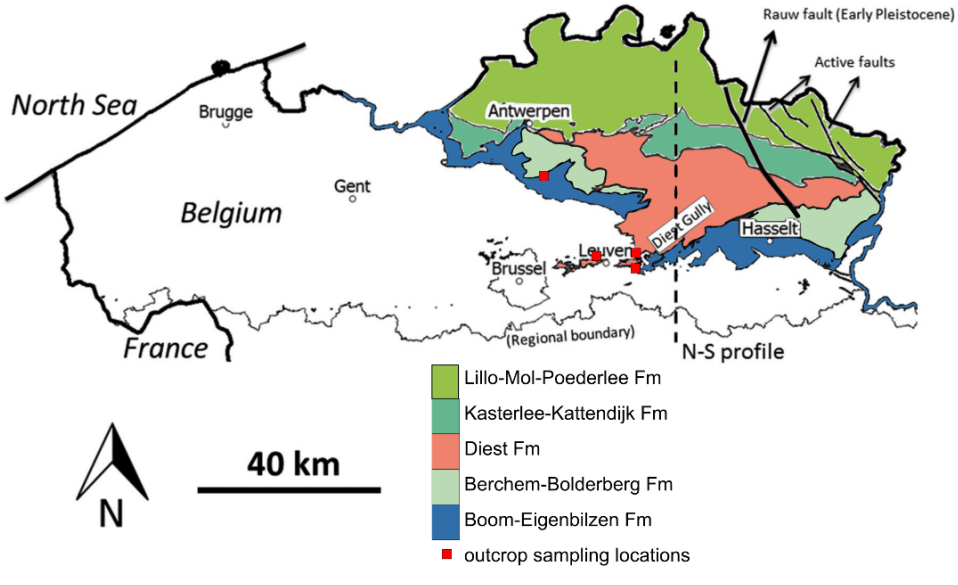


Figure 5.1 Outcrop of the Neogene formations in Belgium with indicated sampling locations of the surface sands. Map modified after ALBON (2009).

Radiostrontium ($^{90}Sr$) is as a fission product of uranium and plutonium present in nuclear waste and in sites contaminated by nuclear accidents. The radionuclide (RN) has a half-life of 28.78 years and is highly soluble under all $E_h$ and pH conditions occurring as the divalent cation $Sr^{2+}$. Strontium sorption depends on the cation exchange capacity (CEC) of the solid phase, the ionic strength and the pH (Bradbury and Baeyens, 2005; Wallace et al., 2012). The solid-liquid distribution coefficient ($K_D$) of $^{90}Sr$ is well below that of $^{137}Cs$. The $Sr^{2+}$ log $K_D$ on illite is 1.9 ± 0.3 with the $K_D$ expressed in L $kg^{-1}$ at 0.1 M ionic strength and pH 7 (Altmann et al., 2014; Poinssot et al., 1999b). As the ionic strength decreases to 0.01 M, the log $K_D$ increases with 1 to 1.5 units (Altmann et al., 2014) or even 2 units (Poinssot et al., 1999b) in the pH range 5.5 to 8.3. For pure glauconite, log $K_D$ for Sr is 1.9 ± 0.2 L $kg^{-1}$ in tap water with pH 7.8 at 0.1 mM $K^{+}$, 1.1 mM $Na^{+}$, 1 mM $Ca^{2+}$, 0.3 mM $Mg^{2+}$ (Voronina et al., 2015b).

The uptake of $Sr^{2+}$ on glauconite is expected to be dominated by cation exchange processes similar to $Sr^{2+}$ sorption on illite. Strontium is predominantly bound by outer sphere bonding on the planar sorption sites, making it vulnerable to exchange by cations with higher charge density. The capacity of the planar sites is reflected in the effective CEC, i.e. the CEC valid at the pH at which the sorption is measured. For illite a large variation in the capacity of the planar sites is found in literature, ranging from 80 to 98% of the CEC (Bradbury and Baeyens, 2000; Brouwer et al., 1983; Fuller et al., 2014; Missana et al.,

2014a). In smectite minerals the fraction of planar sites increases to nearly 100 % of the CEC. Contrary to illite, the interlayer is accessible to (hydrated exchangeable) cations in smectite like minerals. Glauconite occurs mostly as a mixed layer mineral of illite-like and smectite-like end members (Meunier and El Albani, 2007). The CEC of illite ranges 20-40 $cmol_c$ $kg^{-1}$, that of smectite 80-120 $cmol_c$ $kg^{-1}$ (Meunier, 2005). Available data for glauconite indicate an intermediate CEC suggesting that the $K_D$ of $Sr^{2+}$ is between that of illite and that of smectite. The $Sr^{2+}$ $K_D$ (in L $kg^{-1}$) can be modelled (Eqn. 5.1) using the selectivity coefficient $K_c$ (Sr/Ca) and the measured effective CEC (eCEC, in mol $kg^{-1}$), with the assumption that the $Ca^{2+}$ concentration in solution is known and the sorption sites are fully occupied with $Ca^{2+}$ (Konoplev et al., 1992; Valcke et al., 1998):

$$K_D = \frac{K_c(Sr/Ca) \cdot CEC \cdot Z_{Ca}}{2\, m_{Ca}} \qquad \text{Eq. 5.1}$$

With $Z_{Ca}$ the fractional loading of $Ca^{2+}$ on the sorption sites and $m_{Ca}$ the concentration of $Ca^{2+}$ in solution in mol $L^{-1}$. The selectivity coefficient for Sr/Ca can be calculated based on equation 5.1 with the assumption that $z_{ca}$, the fractional occupation by $Ca^{2+}$, approaches 1.

$$K_c\ (Sr/Ca) = \frac{K_D \times 2m_{Ca}}{CEC} \qquad Eq.\ 5.2$$

The $K_c$ (Sr/Ca) typically ranges around 0.7 for humic acids, between 0.8-1 in Ca-soils and between 1- 2 for clay minerals (Valcke et al., 1998).

A high ionic strength is measured at many nuclear legacy sites, versus low ionic strength in the natural pore waters of the potential glauconite sand to RN interaction. At neutral pH, $Ca^{2+}$ and $Mg^{2+}$ in solution will compete with $Sr^{2+}$ and the distribution ratios in the background electrolyte will determine the sorption of each cation (Poinssot et al., 1999b). In acid environments the permanently negatively charged surfaces will become protonated and hydrogen ($H^+$) will compete with the cations in solution for the sorption sites. However, at low pH the clay can start to dissolve, releasing cations in solution and giving rise to secondary precipitation. Below pH 5.5 Poinssot et al. (1999b) observed a decrease in $Sr^{2+}$ sorption combined with an increase of cations in solution due to partial dissolution of the clay. In the pH range 5.5 to 8.5 the sorption remains relatively stable, above pH 8.5 an increase in $Sr^{2+}$ sorption can be observed possibly due to surface complexation reactions similar to $Ca^{2+}$ sorption on Na-montmorillonite (Baeyens and Bradbury, 1995; Poinssot et al., 1999b).

This study aimed to assess the sorption of radiostrontium on natural glauconite sands from the Neogene-Paleogene formations in Belgium and to identify the factors explaining the variation in $Sr^{2+}$ sorption among the samples (n=45 sand samples). The effect of glauconite weathering on $Sr^{2+}$ sorption was evaluated by comparing a range of naturally weathered glauconite sands with subsurface samples. The role of sorption kinetics and of diffusion within glauconite pellets was addressed by measuring adsorption kinetics on glauconite fractions that were either or not milled before the adsorption tests. Caesium sorption on equivalent substrates identified such diffusive boundaries (Chapter 2).

## 2. Materials and methods

**Natural glauconite sands**

Natural glauconite sands occur in the Neogene and Paleogene formations mainly situated in the North and North-East of Belgium. For the surface disposal the Neogene Berchem and Diest Formation are of importance, though the Paleogene Voort and Eigenbilzen Formation can give additional information on the additional natural barrier for a possible repository in the Boom Clay. The glauconite in the investigated formations is very diverse in grain size, morphology and colour (Annex 3. Optical microscopy).

*Voort Fm*

The Voort Formation is Paleogene in age (Chattian 28.1 – 23 Ma) and forms the transition to the Neogene sands from the Eigenbilzen and Boom Clay Formation. The Voort Formation is a fine grained and clay rich sand characterised by a high glauconite content. Disperse clay layers are present reducing the permeability of the formation. The transition to lower Eigenbilzen Fm and Berchem Fm below are gradual (Adriaens et al., 2014).

*Berchem Fm*

The Berchem Formation consists of three members, Edegem, Kiel and Antwerp, separated by hiatal intervals as the result of deposition in marginal marine environments with fluctuating sea levels (Adriaens et al., 2014; Vandenberghe, 2004). The lithology is characterised by highly glauconitic sands with frequent clay intercalations. The three members are fine- to medium-grained sand units and distinction among them is made based on the calcareous fossils, dinoflagellate biozonations and glauconite content (Louwye, 1999; Louwye et al., 2006). Due to the marginal marine conditions not all members of the Berchem Formation have been deposited over the total Campine area. In the region of Mol – Dessel only the Antwerp Member is present. It is characterised by a high glauconite content of about 46 % with local units enriched in glauconite up to 70-80 %. The glauconite pellets are described as smectite rich high expandable glauconite-smectite. Towards the underlying Voort Formation the Antwerp Member becomes more clay rich and more fine grained. The mineralogy of the disperse clay layers in the Antwerp Member were characterised by Adriaens (2015) and contains no glauconite pellets. However, glauconite is present in the clay fraction of these clay layers.

*Diest Fm*

Sedimentation only restarted after an important phase of erosion known as the Mid-Miocene unconformity. Due to the erosion phase the Diest Fm has a highly irregular base with gully structures to go up to the Boom Clay Formation in some locations. The Diest Fm itself is characterised by poorly sorted, coarse glauconitic sands with low clay fraction content. The Diest Formation was deposited over a larger region giving rise to lateral variation (Adriaens et al., 2014; Louwye, 1999; Louwye and De

Schepper, 2010; Louwye et al., 2006). The lower Diest formation is defined as the Dessel member in the Dessel-Mol region. This lower member has 26 % glauconite described as smectite rich high-expandable glauconite smectite. The upper Diest Formation is more coarse and has glauconite contents of about 38 % characterised as glauconite-smectite low-expandable (Adriaens et al., 2014).

*Naturally weathered glauconite sands*

Due to a dip to the east, the Neogene formations have outcrops at the surface (Figure 5.1). For this study a set of subsurface samples (from drilling cores) and surface samples (collected in quarries and outcrops) was selected (Table 5.1). The subsurface samples represent the glauconite sands in its current state. Subsurface samples were selected from the Kasterlee Fm, Diest Fm, Berchem Fm and Voort Fm. The surface samples are subjected to the elements in natural outcrops and quarries. These naturally weathered samples were selected to test the effect of weathering of the glauconite sands on the sorption of Sr. Samples of the weathered Diest Formation sands were collected in Wezemaal, at the Wijngaardberg and Beniksberg, and in Lubbeek in the Zavelstraat. At the Wienerberger quarry in Rumst samples were taken from the green sands above the Boom Clay, part of the Berchem Formation.

Table 5.1 Inventory of the selected glauconite sand samples from the Neogene-Paleogene formations for this study. Subsurface samples are indicated with K, D, B or V (indicating the formation Kasterlee, Diest, Berchem or Voort) and originate from the collection of NIRAS/ONDRAF (ON-Mol1 31W237, ON-Dessel3 31W354, ON-Dessel5 31W370 borehole). The samples indicated with shaft excavation originate from the excavation of the second shaft to the underground lab HADES in Mol. Surface samples were collected in Wezemaal, at the Wijngaard or Beniksberg, in Lubbeek in the Zavelstraat and in Rumst at the Wienerberger Boom Clay quarry. The Boom Clay sample is a sample from a recent sampling campaign at HADES level.

| Sample name | Formation | Origin | Depth m TAW$ | Sample fractions | | | |
|---|---|---|---|---|---|---|---|
| | | | | Intact | | Milled | |
| | | | | Sand | GL | Sand | GL |
| K1 | Kasterlee | ON-Dessel 3-20 | 3.6 | X | | | |
| D1 | Diest | Shaft excavation | -73 | X | X | X | X |
| D2 | Diest | Shaft excavation | -91 | X | X | | |
| D3 | Diest | ON-Dessel 5-30 | -95 | X | X | X | |
| D4 | Diest | ON-Dessel 5-44 | -109 | X | X | X | X |
| D5 | Diest | ON-Dessel 5-48 | -113 | X | X | X | X |
| D6 | Diest | Shaft excavation | -78 | X | X | X | |
| D7 | Diest | Shaft excavation | -83 | X | | | |
| D8 | Diest | ON-Dessel 5-20 | -85 | | X | | X |
| D9 | Diest | Shaft excavation | -101 | X | X | | |
| D10 | Diest | ON-Dessel 5-44 | -109 | | X | | |
| D11 | Diest | Boring Put 8_PIDPA | -48 | | X | | X |
| D12 | Diest | Boring Put 8_PIDPA | -52 | | X | | |
| D13 | Diest | Boring Put 8_PIDPA | -60 | | X | | |

| Sample name | Formation | Origin | Depth m TAW$ | Sample fractions | | | |
|---|---|---|---|---|---|---|---|
| | | | | Intact | | Milled | |
| | | | | Sand | GL | Sand | GL |
| D14 | Diest | Boring Put 8_PIDPA | -96 | | X | | X |
| D15 | Diest | Boring Put 8_PIDPA | -104 | | X | | |
| D16 | Diest | Boring Put 8_PIDPA | -108 | | X | | |
| B1 | Berchem | ON-Dessel 5-63 | -126 | X | X | X | X |
| B2 | Berchem | Shaft excavation | -134 | X | X | X | X |
| B3 | Berchem | ON-Mol 1-14 | -134 | X | | | |
| B4 | Berchem | ON-Dessel 5-77 | -140 | | X | | |
| V1 | Voort | Shaft excavation | -144 | X | X | X | X |
| V2 | Voort | Shaft excavation | -152 | X | | | |
| V3 | Voort | Shaft excavation | -140 | X | X | | |
| V4 | Voort | ON-Mol 1-24 | -144 | X | | | |
| V5 | Voort | Shaft excavation | -141 | X | | | |
| V6 | Voort | Shaft excavation | -147 | | X | | |
| W1 | Diest | Wijngaardberg, | 55 | X | X | | |
| W2 | Diest | Wijngaardberg, | 55 | X | X | | |
| W3 | Diest | Wijngaardberg, | 51 | X | | | |
| W4 | Diest | Wijngaardberg, | 51 | X | X | | |
| W5 | Diest | Beniksberg | 44 | X | X | | |
| W6 | Diest | Beniksberg, | 44 | X | X | | |
| W7 | Diest | Beniksberg | 45 | X | X | | |
| W8 | Diest | Beniksberg | 45 | X | X | | |
| W9 | Diest | Beniksberg | 45 | X | X | X | |
| W10 | Diest | Zavelstraat | 56 | X | X | | |
| W11 | Diest | Zavelstraat | 56 | X | X | X | |
| W12 | Berchem | BC quary | 26 | X | X | | |
| W13 | Berchem | BC quary | 26 | X | X | | |
| W14 | Berchem | BC quary | 31 | X | X | | |
| W15 | Berchem | BC quary | 27 | X | X | | |
| W16 | Berchem | BC quary | 27 | X | X | | |
| W17 | Berchem | BC quary | 26 | X | X | | |
| W18 | Berchem | BC quary | 28 | X | X | | |
| I | Na-illite du Puy | Reference material | | X | | | |
| BC | Boom Clay | HADES sampling campaign 2017 | -197 | X | | | |

$The sampling depth is expressed in mTAW, or the reference level in Belgium (Tweede Algemene Waterpassing).

**Sample preparation**

For analysis and batch sorption studies, four different fractions of the glauconite sands were prepared, i.e. the complete sand, the glauconite fraction, the milled complete sand and the milled glauconite fraction. For a selection of the samples (selected from the collection of R. Adriaens), only the glauconite fractions were available (D8, D10-16 and B4). These four fractions were prepared for several reasons. The glauconite content is variable over the glauconite sand formations. By separating the glauconite fraction from the matrix the effect of the mineralogical and chemical variability of the glauconite on $Sr^{2+}$ sorption can be tested. Radiocaesium sorption on the glauconite sands revealed a strong effect of the grain (full grains versus milled grains < 2 µm) on the sorption kinetics and restricted access to the sorption sites at the centre of the grain (Chapter 2). To make all sorption sites accessible for comparison, milled complete glauconite sands and milled glauconite fractions were prepared.

The complete sands required only drying (oven drying at 60 °C). To separate the glauconite fraction, the complete sands were wet sieved to obtain the 125-250 µm size fraction. This is the dominant size fraction in the sands and has sufficiently large glauconite grains to allow good separation of the glauconite fraction from the quartz phases by magnetic separation. The oven dried (60 °C) glauconite fraction was separated using a Frantz isodynamic magnetic separator. The milled fractions were produced with a McCrone Micronizing mill using zirconium grinding elements. The samples were wet milled with ethanol to avoid amorphisation of the crystal structure.

**Sample analysis**

A smaller set of samples was analysed in more detail to relate $Sr^{2+}$ sorption to mineral or chemical parameters of the glauconite sands and fractions.

Powder X-ray diffraction (XRD) analysis was used to determine the glauconite content, the total clay content and position of the $d_{060}$ reflection and was applied to 29 samples. The X-ray diffraction scans were measured using a Phillips PW1830 diffractometer with CuKα radiation at 30 mA and 45 kV using a graphite monochromator and a scintillation detector. The diffractometer scans were recorded in Bragg-Brentano geometry, 5 to 65 º for bulk measurements and 2 to 47 º for clay measurements, each time with a step size of 0.02 º and 2 s counting time per step. The glauconite sands were milled (McCrone) with zincite as internal standard (for quantification 10 wt % zincite, for $d_{060}$ determination 5 wt % zincite) to reduce the offset error. To avoid preferred orientation, the samples were side loaded in the sample holders. Data interpretation and quantitative data analysis was done using QUANTA (© Chevron ETC). The $d_{060}$ reflection allows the distinction between dioctahedral and trioctahedral clay minerals and is sensitive to weathering. The reflection depends on the size of the cations and the cation occupancy in the octahedral layer (Moore and Reynolds, 1997). The accuracy of the quantification can be assumed < 1% for non-clay minerals and 3-4 % for clay minerals. The position of the $d_{060}$ peak is calibrated with the internal reference standard (ZnO). The data point with the highest intensity in the $d_{060}$ region was

chosen to determine the position. Therefore, the error on the position is 1-2 data points (stepsize 0.02° 2Θ or 0.0005 Å).

The cation exchange capacity (CEC) at the pH of the substrate was determined using a cobalt (III) hexamine chloride cation exchange (standardised protocol ISO 23470 (2007)). All samples were milled before CEC determination. The glauconite grains or pellets are relatively large (125-250 µm average) and not all of the internal cation exchange sites are instantly accessible to the large cobalt(III) hexamine cation. The standard protocol for the CEC determination uses one hour equilibration time, therefore milling was used. Using longer equilibration times might overcome diffusion limitation in the kinetics of the cation exchange reaction. On a subset of samples, both milled and un-milled, the cobalt (III) hexamine chloride cation exchange was extended to 14 days with regular samples. In addition, CEC was also determined on five non-milled samples.

The elemental composition was determined on nine complete glauconite sands and glauconite fractions. To the batch, a set of six reference samples were added (BCR-2, MRG-1, BCS-267, BCS-269, NIST-610, GA). The samples were prepared in duplicate with the lithium(Li)-metaborate fusion method of Vassilieva modified from Suhr and Ingamells (1966) and Cremer and Schlocker (1976). The samples were measured with Inductively Coupled Plasma Optical Emission Spectroscopy (ICP-OES – Varian 720ES).

The speciation of $Fe^{2+}$ to $Fe^{3+}$ in the glauconite fraction was determined on 31 samples using the 1.10-phenantroline method (Fritz and Popp, 1985; Shapiro, 1960). The phenantroline forms a bright orange complex with $Fe^{2+}$ and prevents further oxidation. The $Fe^{2+}$ content can be determined based on the UV-VIS absorbance in the supernatants at 555 nm (Varian Model 635 UV-Visible Spectrometer). The total Fe content of the supernatants was determined at 248 nm by Atomic Absorption Spectroscopy (AAS) (Thermo Electron Corporation S series AAS). The $Fe^{2+}$ and $Fe_{tot}$ mass percentages are calculated through a calibration curve obtained from geological Standard Reference Materials (SRM). A set of seven SRM's with similar $Fe^{2+}$ and $Fe_{tot}$ contents to the glauconite fraction were added to the batch (NIM-G, GA, SY-3, DR-N, MRG1, BCR1 and NIM-D), all analyses were performed in triplicate.

**Batch sorption studies**

The $^{85}Sr$ batch sorption experiment was performed in a background solution of 1 mM $CaCl_2.H_2O$ and 0.5 mM KCl (I=0.002 M) with a solid liquid ratio of 1 g to 30 mL. The background concentration was chosen to be representative of the in-situ pore water in the Neogene-Paleogene formations (0.14-0.37 mM $K^+$ and 0.3-1.7 mM $Ca^{2+}$). The experiment was performed in duplicate and with $^{85}Sr$ as an analogue for $^{90}Sr$. To ensure equilibrium between the sample and the background solution, the background solution was changed four times over the course of three days prior to $Sr^{2+}$ addition. A dialysis membrane (MWCO 6-8 kD) was used to contain the sample and 5 mL solution and prevented loss of the fine fraction during solution changes. After equilibration, the supernatant was spiked with

$^{85}Sr$ (carrier free, radionuclidepurity > 99 %) and initial activities in all samples were 305 ± 4 Bq $mL^{-1}$ (mean ± standard deviation). The suspensions were equilibrated in an end-over-end shaker (0.42 $s^{-1}$) at 25°C and the solution was sampled after 48 hours, 7 days, 14 days, 28 days and 56 days. The $^{85}Sr$ activity in solution was analysed using a gamma counter (Canberrra Packard Cobra type 5003). The system uses a single 3-inch NaI through-hole crystal detector and operates at a 2000 KeV energy range. The activity measurements were decay corrected. The distribution coefficient of $^{85}Sr$ ($K_D$) between the sorbed activity and activity in solution is used to express the sorption of radiostrontium on glauconite (sands).

$$K_D = \frac{A_{ini} - A_{eq}}{A_{eq}} \cdot \frac{V}{m} \qquad Eq.\ 5.3$$

with $A_{ini}$ and $A_{eq}$ the initial and equilibrium activity in solution, with $V$ the solution volume (L) and $m$ the sample mass (kg).

## 3. Results

**Radiostrontium sorption on glauconite sands**

The adsorption kinetics showed that the $K_D$ values beyond 48 h and up 56 days ranged factors 0.85-1.1 of the corresponding values at 48 h, illustrating that sorption equilibrium was reached after 48 h in all fractions data not shown). The complete sand and glauconite fraction were milled to test the accessibility of the sorption sites in the glauconite pellets. After 48 h, the $K_D$ of the milled and intact complete sands were almost identical, the ratio of the $K_D$ of the milled to that of the intact complete sand ranged 0.97 to 1.13. Similar ratios are observed between the milled glauconite fraction and the intact glauconite (0.88 to 1.50). Taken together, these data shows that slow reactions related to micropore diffusion in the pellets are negligibly small.

The distribution coefficients of $Sr^{2+}$ sorption after 48 h on the four different fractions of the glauconite sands are summarised in Table 5.2. The measurement error between two replicates, expressed as standard deviation/mean was 7.4 % on average, illustrating a rather high precision. The $K_D$ values for the Neogene and Paleogene glauconite sands range between 23 and 86 L $kg^{-1}$ for CEC values ranging between 8.3 and 15.4 $cmol_C$ $kg^{-1}$. The sample B1 has a $Sr^{2+}$ $K_D$ of 86 L $kg^{-1}$ for the compete sand due to the very high glauconite content (89 wt%). The CEC values for the glauconite fractions range between 20.7 and 33.6 $cmol_c$ $kg^{-1}$, higher than reported for the Illite du Puy references (20 $cmol_c$ $kg^{-1}$) (Bradbury and Baeyens, 2000). For the internal reference sample Illite du Puy, a $K_D$ of 132 L $kg^{-1}$ was measured, while the $K_D$ values range between 50 and 144 L $kg^{-1}$. This means that lower $K_D$ values per unit of CEC are observed for the glauconite sands (2.3-5.0, mean 3.8 L $kg^{-1}$/($cmol_c$ $kg^{-1}$)) than for illite (6.1 L $kg^{-1}$/($cmol_c$ $kg^{-1}$)). The $Sr^{2+}$ sorption in the complete sand is proportional to the glauconite content of the sand, since the CEC of the sands is defined almost completely by the glauconite. The Sr/Ca $K_c$ was calculated (Eq. 5.2) for the CEC of the complete sand and gives a range of 0.33-1.0 for the glauconite sands (Table 5.2).

Table 5.2 Distribution coefficients of Sr ($K_D$ L $kg^{-1}$) after 48 hours (in a 0.5 mM KCl and 1 mM $CaCl_2.H_2O$ background solution) for the four different fractions of the glauconite sands: the complete sand, the glauconite fraction (GL), the milled complete sand and the milled glauconite fraction. The $K_D$ values are given as means ± standard deviation of two replicates. The average $K_D$ of the complete glauconite sand in each formation was added. The sorption data are complemented by the glauconite content, total clay content, the cation exchange capacity (CEC) of the complete sand and the glauconite fraction ($cmol_c$ $kg^{-1}$) and the calculated selectivity coefficient ($K_c$ (Sr/Ca)) through Eq 5.1. The CEC is given as mean ± the standard deviation of two replicates.* The measured CEC value for Na-illite du Puy, within the expected range compared to literature references (20 cmolc $kg^{-1}$ reported by Bradbury and Baeyens (2000)).

| Sample name | $K_D$ (L $kg^{-1}$) | | | | | GL content | Total Clay | CEC Sand | CEC GL | $K_c$ (Sr/Ca) |
|---|---|---|---|---|---|---|---|---|---|---|
| | Sand | Fm average | Milled sand | GL | Milled GL | wt % | wt % | $cmol_c$ $kg^{-1}$ | | |
| K1 | 6 ± 1 | | | | | 3 | 5 | 3.6 ± 0.5 | | 0.33 |
| D1 | 51 ± 2 | 42 ± 10 | 53 ± 1 | 116 ± 1 | 130 ± 1 | 34 | 34 | 10.7 ± 0.2 | 26.9 ± 2.1 | 0.95 |
| D2 | 37 ± 11 | | | 89 ± 1 | | 27 | 31 | 8.2 ± 0.8 | 24.2 ± 0.1 | 0.90 |
| D3 | 35 ± 4 | | 41 ± 1 | 121 ± 1 | | 24 | 27 | 9.4 ± 0.5 | 28.8 ± 0.1 | 0.74 |
| D4 | 35 ± 1 | | 39 ± 1 | 131 ± 1 | 154 ± 1 | 23 | 25 | 9.5 ± 0.3 | | 0.74 |
| D5 | 58 ± 1 | | 56 ± 1 | 144 ± 4 | 177 ± 3 | 30 | 34 | 12.0 ± 0.1 | 30.1 ± 2.3 | 0.97 |
| D6 | 33 ± 14 | | 54 ± 1 | 121 ± 1 | | 33 | 37 | 12.5 ± 0.1 | | 0.52 |
| D7 | 53 ± 1 | | | | | 30 | 32 | 13.1 ± 0.2 | | 0.81 |
| D8 | | | | 113 ± 1 | 120 ± 3 | 23 | | | | |
| D9 | 33 ± 1 | | | 136 ± 1 | | 18 | 19 | 10.4 ± 0.4 | 33.1 ± 1.0 | 0.82 |
| D10 | | | | 132 ± 1 | | 31 | | | 33.6 ± 0.4 | 0.78 |
| D11 | | | | 50 ± 1 | 75 ± 2 | 43 | | | 20.7 ± 1.5 | 0.48 |
| D12 | | | | 71 ± 1 | | 40 | | | 21.9 ± 0.6 | 0.64 |
| D13 | | | | 81 ± 1 | | 41 | | | 23.9 ± 0.1 | 0.68 |
| D14 | | | | 107 ± 1 | 130 ± 27 | 44 | | | | |
| D15 | | | | 91 ± 1 | | 43 | | | 26.0 ± 0.3 | 0.70 |
| D16 | | | | 101 ± 1 | | 40 | | | 26.0 ± 0.3 | 0.78 |
| B1 | 86 ± 2 | 55.8 ± 22 | 85 ± 1 | 100 ± 3 | 106 ± 1 | 89 | 89 | 17.4 ± 0.2 | 24.8 ± 0.4 | 0.99 |
| B2 | 48 ± 4 | | 49 ± 1 | 139 ± 1 | 123 ± 1 | 27 | 32 | 11.3 ± 0.0 | 33.3 ± 0.3 | 0.85 |
| B3 | 33 ± 14 | | | | | 15 | 31 | 11.0 ± 0.1 | | 0.61 |
| B4 | | | | 135 ± 2 | | 45 | | | 33.1 ± 1.0 | 0.81 |

| Sample name | $K_D$ (L kg$^{-1}$) | | | | GL content | Total Clay | CEC Sand | CEC GL | $K_c$ (Sr/Ca) |
|---|---|---|---|---|---|---|---|---|---|
| V1 | 37 ± 8 | 50.1 ± 9 | 42 ± 1 | 126 ± 1 | 17 | 29 | 11.3 ± 0.1 | | 0.67 |
| V2 | 47 ± 1 | | | | 8 | 27 | 11.3 ± 0.1 | | 0.84 |
| V3 | 50 ± 1 | | | 141 ± 1 | 17 | 33 | 13.8 ± 0.0 | | 0.73 |
| V4 | 65 ± 3 | | | | 37 | 43 | 12.9 ± 0.2 | | 1.00 |
| V5 | 51 ± 1 | | | | 16 | 33 | 15.4 ± 0.7 | | 0.66 |
| V6 | | | | 143 ± 2 | 16 | 27 | | | |
| W1 | 49 ± 3 | 43.6 ± 10 | | 112 ± 1 | 45 | 47 | 11.3 ± 0.3 | | 0.87 |
| W2 | 31 ± 1 | | | 64 ± 1 | 33 | 36 | 9.1 ± 0.9 | 24.1 ± 1.9 | 0.69 |
| W3 | 56 ± 4 | | | | 47 | 49 | 12.0 ± 0.2 | | 0.94 |
| W4 | 51 ± 1 | | | 119 ± 4 | 37 | 39 | 11.2 ± 0.1 | | 0.92 |
| W5 | 39 ± 1 | | | 86 ± 1 | 40 | 40 | 10.4 ± 0.1 | | 0.75 |
| W6 | 36 ± 1 | | | 108 ± 5 | 29 | 29 | 8.1 ± 4.0 | | 0.58 |
| W7 | 44 ± 1 | | | 114 ± 2 | 35 | 35 | 11.5 ± 0.5 | | 0.77 |
| W8 | 40 ± 1 | | | 80 ± 1 | 40 | 40 | 10.9 ± 0.7 | | 0.74 |
| W9 | 36 ± 1 | | 40 ± 1 | 78 ± 2 | 39 | 39 | 14.1 ± 2.2 | | 0.51 |
| W10 | 55 ± 1 | | | 99 ± 3 | 49 | 51 | 13.8 ± 0.3 | | 0.80 |
| W11 | 49 ± 1 | | 52 ± 1 | 81 ± 1 | 43 | 43 | 12.3 ± 3.8 | | 0.80 |
| W12 | 33 ± 1 | | | 84 ± 1 | | | 9.7 ± 0.2 | | 0.68 |
| W13 | 56 ± 5 | | | 118 ± 1 | | | 15.3 ± 0.6 | | 0.73 |
| W14 | 52 ± 5 | | | 120 ± 1 | | | 10.0 ± 5.1 | | 0.70 |
| W15 | 32 ± 14 | | | 73 ± 1 | | | 9.0 ± 0.7 | 28.6 ± 0.9 | 0.71 |
| W16 | 23 ± 4 | | | 70 ± 1 | | | 10.2 ± 0.4 | | 0.46 |
| W17 | 57 ± 1 | | | 129 ± 15 | | | 13.1 ± 1.3 | | 0.87 |
| W18 | 45 ± 1 | | | 124 ± 1 | | | 13.1 ± 0.4 | | 0.68 |
| I | 132 ± 3 | | | | | | 20.4 ± 0.4* | | 1.22 |
| BC | 70 ± 2 | | | | | | 24.0 ± 0.3 | | 0.58 |

**Properties affecting the $Sr^{2+}$ sorption**

The Neogene-Paleogene glauconite sands are very diverse in glauconite content, grain size of the glauconite, morphology and the grade of exterior weathering (Adriaens, 2015). The diversity is assessed by the major element composition, content of the bulk composition (XRD) and the iron speciation. Glauconite has both $Fe^{2+}$ and $Fe^{3+}$ in the structure and is redox sensitive. It is expected that this ratio will change during weathering. The major element content of the complete sands and the glauconite fraction and the iron speciation in the glauconite fraction are given in Tables 5.2 and 5.3. The XRD patterns of a set of complete glauconite sands (5-65°), clay slides of the glauconite fraction (2-47°) and glauconite fractions in the $d_{060}$ region (55-65°) including clay fraction quantification results are given in the supplementary information (Annex 3. XRD patterns).

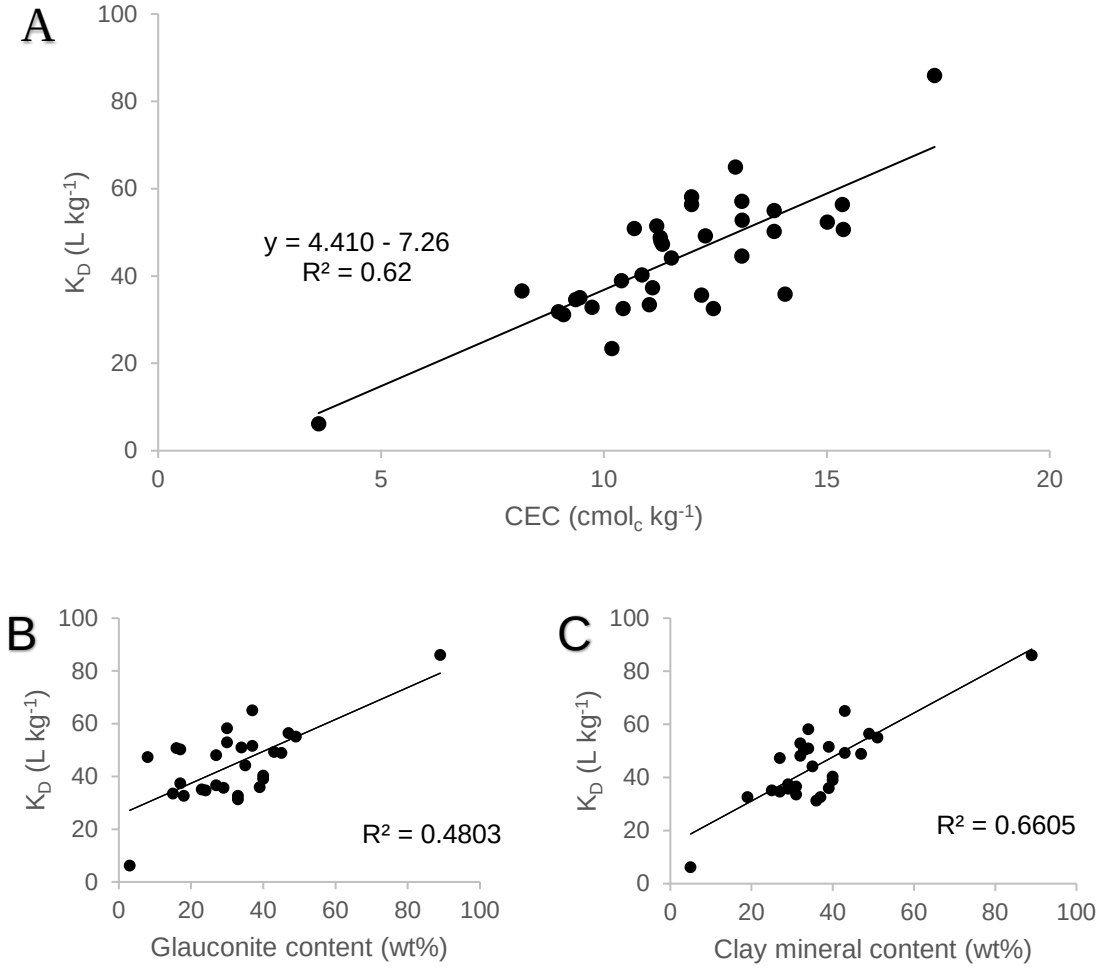


Figure 5.2 Linear relationship between the Sr distribution coefficient $K_D$ (L $kg^{-1}$) and the A) cation exchange capacity (CEC – $cmol_c$ $kg^{-1}$), n = 35, complete sands); B) the glauconite content (wt%) (n=28); and C) the total clay (mineral) content of the complete sand (wt%) (n=28). The glauconite content by itself gives a rather poor relation to the $K_D$ of the complete sand ($R^2$ = 0.48).

Table 5.3 Major element analysis in the complete glauconite sands and glauconite fraction and iron speciation ($Fe^{2+}/Fe_{tot}$) of the subsurface and surface sands.

| | | Complete sand | Glauconite fraction |
|---|---|---|---|
| Major elements (wt %) | Si | 25-39 | 22-27 |
| | Al | 2.2-4.6 | 3.6-5.2 |
| | Fe | 2.6-15.2 | 14.1-19.5 |
| | K | 2.3-5.9 | 4.8-7.0 |
| | Na | 0.05-0.42 | 0.02-0.08 |
| | Mg | 0.60-2.0 | 1.8-2.3 |
| Iron speciation | | | |
| $Fe^{2+/}Fe_{tot}$ | | Subsurface sands | 0.10-0.29 |
| | | Surface sands | 0.02-0.17 |

The correlation analysis (Table 5.4) suggests that several parameters are indicative for the $Sr^{2+}$ sorption $K_D$ (after 48 h) in the complete glauconite sands; the CEC ($r = 0.95$, $p < 0.001$), the glauconite content ($r = 0.69$, $p < 0.001$) and the total clay content ($r = 0.81$, $p < 0.001$). The CEC provides the best prediction of $K_D$ values (Figure 5.2). Glauconite is the major cation exchanging component in the sand and the most important component of the clay fraction. Only in the Voort Fm samples, the content of other clays (smectite, illite, chlorite) increases and the glauconite fraction alone provides an underestimate of the $K_D$ value of the complete sand (Table 5.2).

The subsurface samples were compared with the weathered surface samples (Annex 3. Welch test). Clear signs of weathering are the lower $Fe^{2+}/Fe_{tot}$ ratios combined with higher total Fe content in the glauconite fraction, due to iron oxides formation. The mean $Fe^{2+}/Fe_{tot}$ of weathered samples was 0.053 and differed significantly with the subsurface samples (0.14) ($p<0.001$, two sided t-test). The differences in total Fe (16.3 wt% versus 13.3 wt% for weathered versus subsurface) were smaller and less pronounced ($p<0.01$). The increase in total Fe content cannot be explained by weathering of glauconite. It is much more likely iron rich pore water evaporated and an iron coating was deposited on the grains. Weathered intact sand samples had similar CEC and lower $^{85}Sr$ $K_D$ values than corresponding values for the subsurface sands: the ratio of means were only 1.03 (CEC) and 0.84 ($K_D$). However, slight differences in glauconite content between both groups explained these differences, since multivariate analysis showed no differences ($p>0.05$) in either CEC and $^{85}Sr$ $K_D$ values between weathered and subsurface samples after correcting for % glauconite in a linear model.

Table 5.4 The correlation coefficients (r) among the properties of the complete sands and their glauconite fractions. (Significant correlations in bold, ***p <0.001, ** p <0.01, * p <0.05). The correlation given for the CEC of the complete sand.

| | | | | | | Complete sand | | | | Glauconite fraction | | | | | |
|---|---|---|---|---|---|---|---|---|---|---|---|---|---|---|---|
| $K_{D-GL}$ | $CEC_{GL}$ | GL % | Clay % | $d_{060}$ | $Fe^{2+}$ $Fe_{tot}$ | Al | Fe | K | Mg | Al | Fe | K | Mg | | |
| 1 | **0.94*** ** | **0.69** ** | **0.81*** ** | -0.18 | 0.12 | 0.03 | 0.12 | 0.15 | 0.14 | -0.02 | 0.01 | 0.20 | 0.17 | $K_D$ | |
| | 1 | 0.56 | **0.72*** ** | -0.03 | 0.17 | 0.11 | 0.23 | 0.24 | 0.23 | -0.19 | 0.29 | 0.36 | 0.22 | CEC | |
| | | 1 | **0.94*** ** | 0.27 | -0.43 | 0.23 | **0.99*** ** | **0.96*** ** | **0.96*** ** | -0.24 | 0.33 | 0.53 | 0.07 | GL% | |
| | | | 1 | 0.09 | -0.29 | 0.46 | **0.94*** ** | **0.99*** ** | **0.99*** ** | -0.15 | 0.26 | 0.50 | 0.14 | Clay% | |
| | | | | 1 | 0.04 | **-0.68** ** | 0.36 | 0.03 | 0.09 | -0.18 | 0.28 | -0.34 | **-0.84*** ** | $d_{060}$ | |
| | | | | | 1 | -0.15 | -0.22 | -0.39 | -0.38 | 0.13 | 0.30 | -0.37 | -0.43 | $Fe^{2+}$ $Fe_{tot}$ | |
| | | | | | | 1 | 0.40 | **0.66** ** | **0.62** ** | -0.10 | 0.12 | **0.56* ** | **0.53* ** | Al | Sand |
| | | | | | | | 1 | **0.93*** ** | **0.95*** ** | -0.14 | 0.32 | 0.39 | -0.07 | Fe | |
| | | | | | | | | 1 | **0.99*** ** | -0.14 | 0.22 | **0.57* ** | 0.23 | K | |
| | | | | | | | | | 1 | -0.06 | 0.17 | **0.49* ** | 0.19 | Mg | |
| | | | | | | | | | | 1 | **-0.65** ** | **-0.52* ** | 0.10 | Al | GL |
| | | | | | | | | | | | 1 | **0.59* ** | 0.03 | Fe | |
| | | | | | | | | | | | | 1 | **0.69** ** | K | |
| | | | | | | | | | | | | | 1 | Mg | |

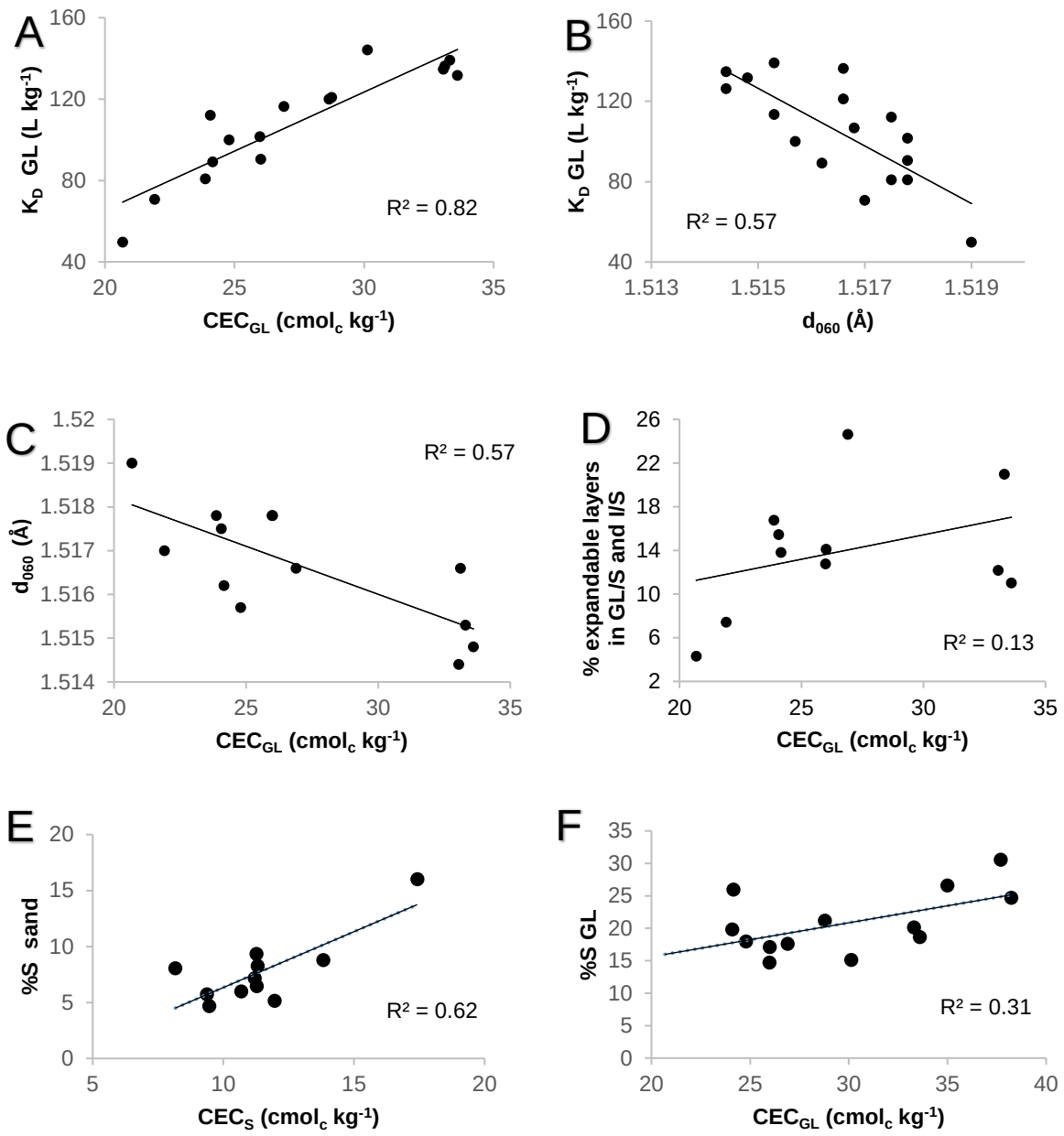


Figure 5.3 (A and B) Linear relationships between the distribution coefficient $K_D$ (L kg$^{-1}$) of the glauconite fraction and A) the CEC of the glauconite fraction ($CEC_{GL}$) and B) the $d_{060}$ reflection of the clay phase in the XRD pattern (C to F) Correlations between the $CEC_{GL}$ and C) the $d_{060}$ reflection of the glauconite fraction (n = 13), D) the expandable layers (% smectite) in glauconite-smectite and illite-smectite (n = 11); E) the total smectite content of the sand (%S sand) to the $CEC_S$ (CEC of the complete glauconite sand) (n=11) and F) the total smectite content of the glauconite fraction (%S GL) to the $CEC_{GL}$ (n=13).

Focussing on isolated glauconite from the subsurface samples, a linear relation can be found between the $K_D$ of the glauconite fraction (after 48 h) and the $CEC_{GL}$ (of the glauconite fraction) ($R^2$ = 0.82) (Figure 5.3A). In addition, a markedly strong negative relationship was observed between the $K_D$ and the position of the $d_{060}$ reflection ($R^2$ = 0.57) (Figure 5.3B). A negative correlation is found between the Mg content and the $d_{060}$ position ($R^2$ = 0.71). With increasing Mg content the $d_{060}$ position shifts to lower peak positions. The $CEC_{GL}$ and $d_{060}$ reflection are negatively correlated ($R^2$ = 0.57) (Figure 5.3C). There

is no significant correlation between the $CEC_{GL}$ and the expandable layer content (smectite content in the GL-S en I-S phases) ($R^2$ = 0.13) (Figure 5.3D. The $CEC_{GL}$ and the total smectite content of the glauconite fraction correlate stronger with an $R^2$ of 0.31 (Figure 5.3F). The correlation with the smectite content is the strongest with the CEC of the complete sand ($CEC_S$). The $CEC_S$ positively correlates to the total smectite content of the sand (Figure 5.3E) ($R^2$ = 0.62). Table A3.4 (Annex 3) gives the $d_{060}$ values and corresponding expandable layer content. The iron speciation, expected to be linked with the weathering grade, had no correlation to the subsurface glauconite sand and glauconite fraction parameters.

The glauconite phases in the investigated sands have $d_{060}$ reflections between 1.5144 and 1.5190 Å. This range of reflections clearly distinguished the glauconite from illite (1.499 Å) and nontronite (1.521 Å) and less clearly from montmorillonite (1.50-1.52 Å for respectively dioctahedral and trioctahedral montmorillonite) (Emmerich et al., 2009; Moore and Reynolds, 1997). When $K^+$ is leached from glauconite (e.g. during weathering), the interlayer space increases and becomes accessible to larger (hydrated) cations. This is reflected in the $d_{001}$ reflection, at 15 Å for smectite and 10 Å for illite and glauconite. By weathering the $d_{00l}$ reflection broadens and shifts to the smectite position. The transition of an illitic to smectitic end member goes along with an increase in the planar sites and an increase in the total cation exchange capacity. Glauconite weathering hence increases the sorption of $Sr^{2+}$.

However, the expected correlation between the CEC of the glauconite and the expandable layer content was not present in this dataset. The trend observed in the glauconite fraction of the subsurface sands is opposite to the comparison of the subsurface versus the weathered surface samples, where lower CEC and lower $K_D$ values were observed for the weathered samples. That may be related to differences in glauconite content as well and it is of note that the differences in CEC and $K_D$ between surface and subsurface samples were relatively small. Indeed, multivariate analysis showed that there was no significant difference in either CEC or $K_D$ between weathered surface and subsurface samples after correcting for glauconite content (details not shown).

## 4. Discussion

There is a close resemblance in mineralogy between glauconite and (Fe-)illite, apart from the pelletal form in which glauconite mainly occurs. Radiocaesium sorption on the glauconite fraction is similar but slightly lower compared to illite (Chapter 2). For $Sr^{2+}$, however, the glauconite fractions have mostly lower $K_D$ values compared to the Illite du Puy reference (50 -144 L $kg^{-1}$ versus 132 L $kg^{-1}$) despite the generally higher CEC values (20.7-33.6 $cmol_C$ $kg^{-1}$ versus 20.4 $cmol_C$ $kg^{-1}$). Hence, $Sr^{2+}$ $K_D$ values per unit of CEC in glauconite are lower compared to illite. The higher CEC can be attributed to the smectitic glauconite layers. Compared to its illitic counterpart, the interlayer space is more accessible for hydrated exchangeable cations, including $Ca^{2+}$ and $Sr^{2+}$. The combination of an increase in the total capacity of

sorption sites and a lower $Sr^{2+}$ $K_D$ suggests lower selectivity of $Sr^{2+}$ to $Ca^{2+}$ as well. During weathering of glauconite the number of smectitic layers increases (associated with an increase in CEC and a decrease in $d_{060}$ value). In the subsurface glauconite samples the increase in CEC is associated with an increase in $Sr^{2+}$ $K_D$.

With regard to adsorption rates it was observed that radiocaesium sorption on glauconite sand required more time to reach equilibrium than corresponding sorption on illite (one month versus 48 hours) (Chapter 2). The sorption sites at the centre of the grain proved to be inaccessible for $Cs^+$. This delay in reaching sorption equilibrium was not observed for $Sr^{2+}$, despite the cation being much larger equilibrium is reached within 48 h. At trace concentration $Cs^+$ sorption will be limited to the FES, while $Sr^{2+}$ sorbs on the planar sites. Caesium can migrate from the FES to the interlayer and exchange for the interlayer $K^+$. This process is much slower, explaining the large differences between the $Cs^+$ and $Sr^{2+}$ sorption kinetics (Annex 3. Comparison caesium and strontium sorption).

The $Sr^{2+}$ $K_D$ values (Table 5.2) obtained here might be compared with existing models/equations. One way is based on the CEC and the $Ca^{2+}$ concentration in solution (Eq. 5.1). At trace concentration $Sr^{2+}$, the product of the selectivity coefficient and the fractional $Ca^{2+}$ loading ($K_c$ (Sr/Ca).$Z_{Ca}$) approaches one (Konoplev et al., 1992). Therefore equation 5.1 can be converted to:

$$K_D \approx \frac{CEC}{2\, m_{Ca}} \qquad \text{Eq. 5.3}$$

with units as determined in Eq. 5.1. Several other researchers have determined the correlation between the CEC and $Sr^{2+}$ $K_D$ values. In Table 5.5 the experimental data are compared to the calculated $K_D$ values with the method of Konoplev et al. (1992) (Eq. 5.1) and Valcke et al. (1998). The model of Valcke et al. (1998) uses the linear relation of the CEC tot $K_D$ determined on soils at 4.47 mM $Ca^{2+}$ ($K_D$ = 0.47 + 1.12 × CEC) with the $K_D$ (L $kg^{-1}$) and the CEC ($cmol_c$ $kg^{-1}$). The calculated $K_D$ values fit markedly strong ($R^2$=0.78) within factors 0.94-1.6 to the experimentally determined values.

The calculated $K_D$ values, largely based on soil data, slightly overestimate the experimental results; mean ratio of predicted/observed is 1.25 (model Konoplev) or 1.42 (model Valcke and Cremers). The main factors determining the $Sr^{2+}$ $K_D$ are the selectivity coefficient (Sr/Ca) and the $Ca^{2+}$ concentration in solution. Based on Eq. 5.1 and the slope of the $K_D$/CEC correlation, the $K_c$ (Sr/Ca) is 0.87.

A note should be made on the CEC analysis as the CEC might be slightly overestimated due to the milling procedure adopted for CEC determination, not for the $Sr^{2+}$ adsorption. The $Cs^+$ sorption on glauconite sands proved that the internal surface is available for sorption, though it requires longer equilibrium times (Chapter 2). As the cobalt (III) hexamine cation complex is much larger than $Ca^{2+}$ and $Sr^{2+}$, we speculated that it is not able to reach all sorption sites that are accessible to $Sr^{2+}$. The CEC values of milled samples (complete sands) are 1.03-2.9 times (mean: 1.7, n=5) higher compared to the corresponding unmilled form data not shown). Milling will open up the mesopores (2-50 nm) and larger

pores breaking up the glauconite pellet to a clay sized fraction. The nanopores (< 2 nm) in the particles should remain unaffected. A kinetic experiment showed that the CEC, based on $Co^{3+}$ adsorption, did not reach equilibrium in 14 days when adopted to the unmilled pellets; the CEC increased with a factor 1.4-2.8 (mean 1.7, n = 7) between one hour and 14 days (Annex 1: Cation exchange capacity), well in contrast with $Sr^{2+}$ that obtained equilibrium after 48h. Both additional tests suggest that the 1h determined CEC values on the milled samples are probably overestimating the CEC accessible for the $Sr^{2+}$ exchange on the un-milled samples. With smaller CEC values adopted in the existing models described above, the $K_D$ values would be less overestimated.

Table 5.5 Comparison of measured and calculated (two ways) $Sr^{2+}$ $K_D$ data for a subset of complete glauconite sands. The $K_D$'s were calculated with Equation 3 with the method of Konoplev et al. (1992) and the one of Valcke et al. (1998). Uncertainty of measured $K_D$ is expressed by the standard deviation of the duplicates.

| Formation | Sample | Measured $K_D$ L kg$^{-1}$ | Calculated $K_D$$ Konoplev et al. (1992)$ L kg$^{-1}$ | Calculated $K_D$$$ Valcke et al. (1998)$$ L kg$^{-1}$ |
|---|---|---|---|---|
| Diest Fm | D1 | 51 ± 2 | 53 | 56 |
| | D2 | 37 ± 11 | 41 | 43 |
| | D3 | 35 ± 4 | 47 | 49 |
| | D4 | 35 ± 1 | 47 | 49 |
| | D5 | 58 ± 1 | 60 | 62 |
| Berchem Fm | B1 | 86 ± 2 | 87 | 89 |
| | B2 | 48 ± 4 | 56 | 59 |
| | B3 | 33 ± 14 | 55 | 57 |
| Voort Fm | V1 | 37 ± 8 | 56 | 58 |
| | V2 | 47 ± 1 | 57 | 59 |
| | V3 | 50 ± 1 | 69 | 71 |
| Illite du Puy | Ref | 132 ± 3 | 108 | 111 |

$ Calculated by equation 5.3 with the assumption $K_c = 1$.
$$ Linear relation CEC ($cmol_C$ kg$^{-1}$) to $K_D$ (L kg$^{-1}$) determined on soils ($K_D = 0.47 + 1.12$ CEC), valid at 4.47 mM $Ca^{2+}$. The $K_D$ value at 1 mM $Ca^{2+}$ (experimental condition) is obtained by $K_D = (0.47 + 1.12 \text{ CEC}) \times 4.47$.

## 5. Conclusion

The $K_D$ values of $Sr^{2+}$ in the Neogene-Paleogene glauconite sands range from 23 to 65 L $kg^{-1}$ in a 0.5 mM KCl and 1 mM $CaCl_2.H_2O$ background solution. Equilibrium is reached within 48 hours in all fractions (complete glauconite sand, glauconite fraction, milled complete sand and milled glauconite fraction), which means that the glauconite grains do not limit $Sr^{2+}$ sorption. The internal sorption sites are accessible without time-lag in reaching sorption equilibrium. In the case of a radiostrontium contamination this is an important factor for RN transport, as the glauconite sands are highly permeable.

Pure glauconite fractions show higher sorption with $K_D$ values of 50 to 144 L $kg^{-1}$ in the range of $Sr^{2+}$ $K_D$ values for illite. The $Sr^{2+}$ sorption $K_D$ of the complete sand is positively correlated with the CEC of the complete sand ($R^2 = 0.62$) and can be predicted very good based on the CEC and $Ca^{2+}$ concentration. Further, correlation analysis indicated that in the subsurface glauconite sands, $Sr^{2+}$ sorption increases upon weathering due to the formation of more smectite-type layers and associated planar sites. In the investigated range of glauconite fractions, a factor 3 difference in $K_D$ was observed.

# Chapter 6. Accelerated weathering of glauconite sands and the effect on the radiocaesium sorption potential


## Abstract

The Neogene-Paleogene glauconite sands in Belgium have been investigated for caesium ($Cs^+$) retention in the framework of radioactive waste disposal. The glauconite grains, sizing 150-250 µm, are the main $Cs^+$ adsorbent. It is unclear how long-term weathering of glauconite can affect the radiocaesium ($^{137}Cs$) retention given that redox or pH dependent transformation may change the Fe speciation, leaching of $K^+$ and, hence, affect clay mineralogy. The objective of this study is to evaluate the effect of weathering on the radiocaesium interception potential (RIP). Three different glauconite sands collected from geological formations (< 70 m below sea level) were artificially weathered at ambient temperature during 27 months in four different scenarios: continuously purged with oxygen (oxidation), a cement water at pH =13 in the absence of oxygen, an acid solution of pH =4 and an anoxic set-up at pH =7 under $N_2$ atmosphere. The samples were sampled before, during and after weathering and characterised for their cation exchange capacity (CEC), contents of major elements, Fe speciation and RIP. The $Fe^{2+}$ to $Fe_{tot}$ ratio doubled under anoxic conditions and remained similar in the other treatments. The CEC increased by factors 1.1-1.2 under alkaline conditions whereas it decreased by similar factors under the oxic and acid conditions. The RIP enhanced by factor 1.1-1.3 under alkaline conditions consistent with the changes in CEC, however no decreases in RIP were detected in the oxic and acid samples. No effects of weathering on Si/Al or on Al/Fe ratio were found. Taken together, this study suggests that glauconite sands do not exhibit strong changes in these weathering conditions and that the effects on the radiocaesium sorption are marginal within the conditions used here.


## 1. Introduction

In the previous chapters we showed that glauconite is a strong sorbent for radiocaesium and radiostrontium with strong similarities to illite. The variations in sorption potential among different glauconite sands are limited and the glauconite pellet is the main adsorbent. An approximate sorption $K_D$ can be estimated for both $Cs^+$ and $Sr^{2+}$ from the cation exchange capacity (CEC) of the sample. Despite the longer equilibration times for $Cs^+$ sorption, sorption is sufficiently fast to prevent an early breakthrough even at high flow rates. All of this is important information in the evaluation of the glauconite sands as a potential sorption sink or barrier for radionuclides (RN). A suitable sorption sink or host formation must have a high RN retention potential and must be stable on the long-term, depending on the intended radioactive waste. A surface disposal must remain stable for several hundreds of years. In a geological disposal intended for cat B and C waste, the RN must be isolated from the biosphere during the entire decay time of the radioactive waste, several 100 000 years or even up to one million years. In most disposal concepts, clays and clay rocks are investigated because of their high

sorption potential. These clays can act as additional sorption sinks, e.g. bentonite layer below a surface disposal, or as host formation, such as the Boom Clay, Ypresian clays and several clay rocks (argillites and slate) that are being considered in Belgium. The long-term efficiency of these barriers must account for changes in the clay mineralogy that may occur due to weathering. Indeed, a number of scenario's can occur over the disposal time such as fluctuations of groundwater and associated redox changes, sea water intrusion, bacterial growth and interactions with the disposal facility, e.g. young cement water coming from the concrete encasing of the disposal facility.

Glauconite sands are unlikely primary hosts for radioactive waste disposal due to the high permeability. They can, however, be considered as a complementary sorption sink or embankment in surface disposal facilities or as an additional barrier if naturally present in the proximity of a primary host formation. An additional sorption barrier might never, or only in a later phase of the disposal, encounter RN.

In Chapter 2 it was shown that the Neogene and Paleogene glauconite sands have a strong radiocaesium ($^{137}Cs$) sorption potential, the log $K_D$ (L $kg^{-1}$) ranged 3.4 – 4.3 at 0.5 mM K. Isolated glauconite fractions exhibited similar $^{137}Cs$ sorption potentials compared to illite (log $K_D$ 4.1-4.3 vs 4.4 for Illite du Puy). The strong $^{137}Cs$ sorption potential is attributed to the sorption on the highly selective frayed edge sites (FES) type I and to a lesser extent FES type II (Chapter 3). The FES sites in the glauconite sands are structurally not different from those in illite. However, the sorption per unit CEC is lower than for illite due to a lower capacity of the FES (0.04-0.06 % of the CEC vs 0.25% for Illite du Puy) combined with a lower type II site capacity (1.6-2.2 % vs 20%). The question is whether the sorption potential, or selective sorption site capacity, changes when the glauconite has been weathered.

Due to weathering, the structure of glauconite can be altered. The most sensitive changes are the $K_2O$ content (6-9 wt%), the ratio of $Al^{3+}$ to $Fe^{2+}$ in the octahedral positions and the number of expandable layers (Meunier, 2005). These factors are interlinked. The $Al^{3+}$ to $Fe^{2+}$ ratio decreases by weathering, causing a decrease in the CEC. The ratio of $Al^{3+}$ to $Fe^{2+}$ will influence the total negative layer charge and strength of the interlayer $K^+$ bound. Leaching K from the interlayer increases the interlayer width and, thereby, introduces FES (width of 1.0 -1.4 nm) (Nakao et al., 2008). However, continued leaching can alter the FES to a hydrated interlayer by introducing expandable layers (Figure 6.1). The basal distance or width of the expandable layer increases according to the number of water molecules linked to the hydrated cation (Ferrage et al., 2005) (Table 6.1). A $Ca^{2+}$ saturated smectite has a 1.4-1.5 nm basal spacing. Despite the effects of weathering on both the $K^+$ and Fe content, Meunier and El Albani (2007) found no correlation between either $K^+$ or Fe content and the weathering stage in glauconite.

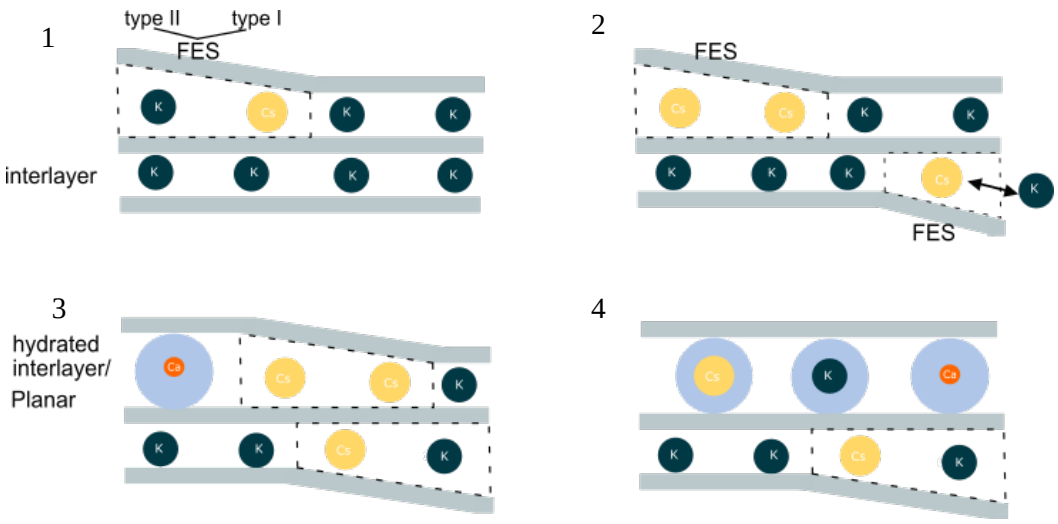


Figure 6.1 Evolution of an illite or glauconite structure during weathering. 1) Leaching of $K^+$ from the interlayer leads to the formation of FES. 2) Continued leaching of $K^+$ can both lead to the formation of more FES sites or 3) the transformation of FES to hydrated interlayer sites. In the hydrated interlayer sites or planar sites the $Cs^+$ selectivity is a factor $10^4$ lower compared to the FES type I sites. 4) If weathering continues FES are transformed to hydrated interlayers and expandable layers are introduced.

Table 6.1 Basal distances in illite and smectite with variable interlayer cations. In the case of a hydrated monolayer only water molecules, no interlayer cations are present. The hydrated interlayer – water bilayer, is the most frequent form for a Ca saturated smectite mineral. The interlayer width increases with increasing hydration radius and or larger cations.

| | | Basal distance (nm) |
|---|---|---|
| Illite interlayer | with $K^+$ | 1.0 (0.99-1.02) [(1)] |
| | with $Cs^+$ | 1.07 (1.06-1.11) [(1)] |
| FES | | 1.0-1.4 [(1)] |
| Hydrated interlayer | water monolayer | 1.26 [(2)] |
| | water bilayer | 1.4-1.5 [(2)] |
| | water trilayer | 1.9 [(2)] |

[(1)] (Nakao et al., 2012; Nakao et al., 2008; Ogasawara et al., 2013)
[(2)] (Ferrage et al., 2005)

The presence of structural Fe in both $Fe^{2+}$ and $Fe^{3+}$ state makes glauconite a redox sensitive mineral. The redox state has an effect on the physicochemical properties as was observed in smectite (Gorski et al., 2012). In smectite a reduction of structural $Fe^{3+}$ to $Fe^{2+}$ increases the CEC (Khaled and Stucki, 1991) by a change in the expandability (swelling) (Stucki et al., 1984; Wu et al., 1989). A distinction between partially and fully expanded layers should be made. With an increase in the $Fe^{2+}$ to $Fe_{tot}$ ratio only the amount of partially expanded layers increases, the amount of fully expanded layers remains the same (Wu et al., 1989). In contrast, in oxic environments a decrease in the total Fe and $K^+$ content and an increase in expandable layers can be expected (Pestitschek et al., 2012). The oxidation of $Fe^{2+}$ to $Fe^{3+}$ and leaching of interlayer $K^+$ leads to a net decrease in the negative layer charge and an increase in expandable layers and, thereby, to a lower sorption of $Cs^+$ (Voronina et al., 2015a). Beside the possible internal changes in glauconite, weathering can cause zonation in the grain (Figure 6.2) and precipitation

of iron oxide (limonite $FeO(OH).nH_2O$) or phosphate, depending on the environment, on the outer rim of the grain (Chorover et al. 2008). The precipitate can be crystalline or amorphous in the form of iron coatings or films on the glauconite grains. The presence of Fe coatings decrease $Cs^+$ sorption (Kobets et al., 2014). The pyrite present in some of the glauconite sand can cause acidification of the environment when the pyrite is oxidised to sulphate.

In the previous chapters, only small difference in Fe speciation among different subsurface samples have been found. However, in naturally weathered glauconite sands collected at the surface, the $Fe^{2+}$ /$Fe_{total}$ content is significantly lower than that in the subsurface (0.053 versus 0.14, Chapter 5). The variation in the Fe speciation did not significantly impact the CEC, weathered glauconite sands have CEC values in the same range as subsurface sands and thereby, no differences were found for the $^{85}Sr$ $K_D$ of the surface versus subsurface samples. That observation already suggests that weathering is unlikely to change the sorption of $^{85}Sr$ or $^{137}Cs$.

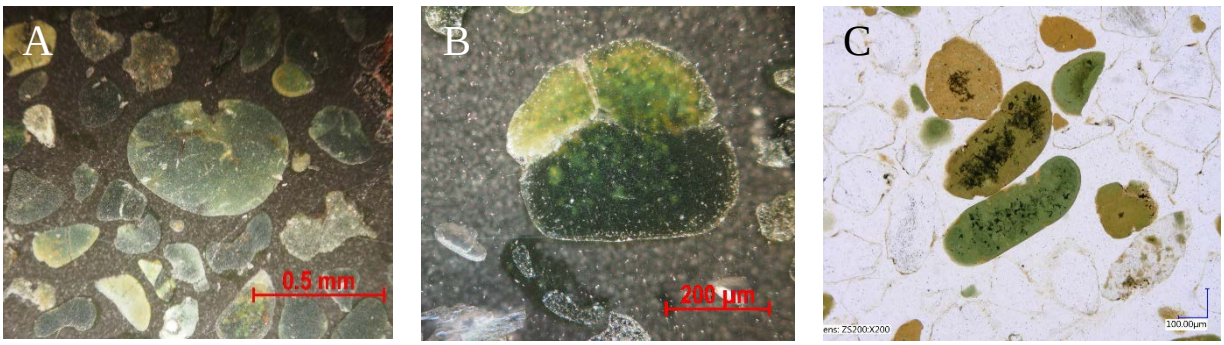


Figure 6.2 Thin section of glauconite grains showing the diversity in weathering state in the grains. From cracking and deposition of iron oxides in the cracks without change in grain colour (A – D2) to zonation within one grain delineated by the cracks in the grain (B – D5) and variable weathering states of glauconite grains in one sample (C-D2-162_Vito).

The Paleogene-Neogene glauconite sands in Belgium are currently present at a depth between -73 to - 152 mTAW in the Campine region and are present under anoxic conditions. A considerable part of the Diest Formation has been reworked from older Miocene deposits (Vandenberghe, 2014). During reworking the glauconite grains can be exposed to changing pore water conditions, leaching, oxygen, sorting and the grains can disintegrate into clay-sized fragments. Evidence of weathering is found in the presence of clay-sized glauconite that is often more expandable than the pelletal glauconite (Adriaens and Vandenberghe, 2020).

The most important scenarios in the surface disposal are interactions with cementitious pore water and oxidation-reduction due to fluctuations in the groundwater level or erosion. Cement will be omnipresent in the radioactive waste facilities from seals and buffer material to general construction (Mann et al.,

2019). The interaction of the cementitious pore water with the surrounding geological barrier or sorption sink can affect the RN retention of the barrier.

The effect of the acid and alkaline environment on illite is relatively well studied. In strongly acid and alkaline solutions the structure starts to dissolve and $Al^{3+}$ and $Si^{4+}$ and interlayer $K^{+}$ is released into the solution (Liu et al., 1999). The presence of carbonate shells strongly buffers the effect of acid solutions (e.g. in the Antwerp Member of the Berchem Fm). The strong alkaline environment induced by young cement water (pH =13.5) is characterised by a high ionic strength. The $Ca^{2+}$ (2 mM ) in solution is known to 'weather' illite. In the presence of high $Ca^{2+}$ concentrations, the $Ca^{2+}$ exchanges part of the interlayer $K^{+}$ at the edge sections, introducing both FES and hydrated interlayer sites. At the same time the solution contains high $K^{+}$ concentrations (0.2 M) that may induce a collapse of the hydrated interlayer. The effects of alkaline environments on the structure of glauconite were reported for a regolith profile (Kisiel et al., 2018). In the weathered glauconite, part of the $Fe^{2+}$ is oxidised and leached out together with $Si^{4+}$ and $Mg^{2+}$. The $Fe^{3+}$ recrystallised in situ as goethite. In addition, the weathering induced a higher amount of expandable layers.

The aim is to study the changes of the glauconite properties and RIP upon artificial weathering, thereby relying on extreme conditions that may be encountered. A set of samples were subjected to artificial weathering in four different environments (oxic, anoxic, acid and alkaline) over 27 months and changes in glauconite composition and their RIPs were analysed.

## 2. Materials and methods

### Sample selection

A set of three natural glauconite sands (complete) was selected for the experiments (Table 6.2). More details on these samples on the $^{137}Cs$ interception potential and kinetics were presented in Chapter 2. In Chapter 3 the sorption isotherm was presented for sample D1 and B2. Several cores of the Dessel 5 core showed signs of oxidation (Annex 4. Oxidation during storage).

Table 6.2 Selected glauconite sand samples for the artificial weathering set-up. These samples were part of the earlier presented results on the batch sorption (Chapter 2, D1,D5 and B2), sorption isotherm (Chapter 3, D1 and B2), column experiment (Chapter 4, D5) and Sr sorption (chapter 5, D1, D5 and B2).

| Sample | Origin | Depth (mTAW$) | Formation | Ionic strength of the pore water$$ |
|---|---|---|---|---|
| D1 | Excavation second shaft | -73 | Diest Fm | 7.5 mM |
| D5 | Dessel 5 core | -113 | Diest Fm | 21.2 mM |
| B2 | Excavation second shaft | -134.1 | Berchem Fm | 53.3 mM |

$ The sampling depth is expressed in mTAW, or the reference level in Belgium (Tweede Algemene Waterpassing)
$$ Ionic strength calculated based on the major element content of the pore water extract from the sand samples

**Set-up of the weathering experiment**

To evoke weathering, the samples were subjected to four different environments: oxic, anoxic, alkaline and acid. A 1/1 solid-to-liquid ratio was consistently used for all set-ups, by mixing 200 g of glauconite sand with 200 mL deionised water. The glauconite sand mass had to be sufficient to take subsamples every 6 months over the entire duration of the experiment (about 2 years). A larger reagent solution volume was used to ensure excess reagent, instead of using saturated water content for the in-situ glauconite sand (about 50% volumetric). The sand/water mixtures were stirred (oxic set-up) or shaken on a regular basis (every 2 to 4 weeks).

To mimic oxidation, a set-up was designed where compressed air was purged through a water saturated sample (Figure 6.3). An inox cylinder of 20 cm long and 10.1 cm Ø with a removable lid was fitted with an inox filter (10 µm pore size) as such that some space for an air pocket was kept at the bottom where air was purged into via tubing. During the course of the experiment the mixture of sand and water was stirred and the water level checked on a regular basis. In case that the water level was decreased due to evaporation, deionised water was added again to keep the S/L ratio constant.

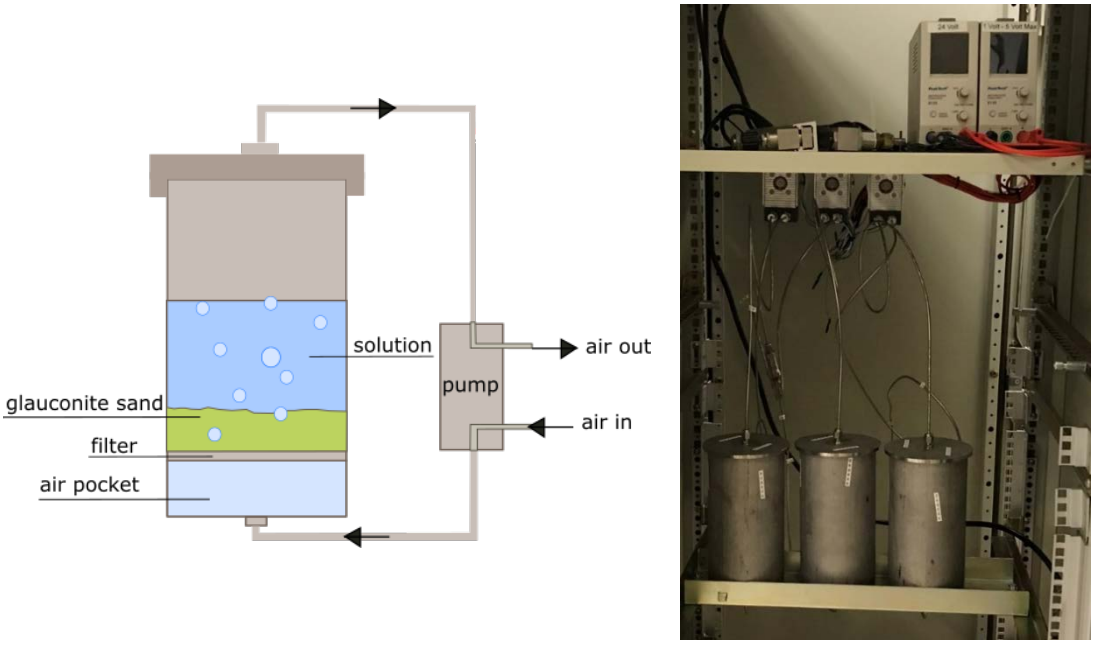


Figure 6.3 Schematic representation of the oxidation set-up. Air was purged continuously through the water saturated glauconite sand.

For the anoxic environment, similar inox vessels were made of the same dimensions. After adding the glauconite sand and the deionised water the lid was welded onto the vessel. The valve on the top of the vessel was used for flushing the system with nitrogen gas. After flushing the vessels three times for 5 min, with pause in between, to remove the oxygen, the set-up remained closed until the end of the experiment. The vessel was shaken once every 2 to 4 weeks.

The alkaline conditions were applied to mimic the conditions of leaching cement water. In the current disposal concepts there are many different types of cement mixtures under consideration (different compositions and hydration ratio's). Each of these cement types will lead to different leaching solutions. For the purpose of this experiment, the theoretical 'young cement water' (0.17 M KOH, 0.047 M NaOH, 0.002 M $Ca(OH)_2$ – pH ~13.5) was chosen. Compared to evolved cement water (0.028 M $Ca(OH)_2$ – pH ~12.5)., the young cement water is more aggressive and represents a more fresh cement water. The young cement water is relevant during the initial phases of disposal, in the case glauconite is used as an additional sorption sink. Over time the alkalinity will decrease and the composition of the solution will change. In this experiment the 'worst case' scenario was tested, the young cement water, to be able to evaluate the more extreme interaction between the glauconite sand and the alkaline solution. The alkaline set-up was placed in a nitrogen glovebox, where also the young cement water was prepared. The mixtures of glauconite sand and young cement water were stored in 1 L polypropylene bottles and shaken every 2-4 weeks. Subsamples collected at intermediate intervals were left in the glovebox to dry before taking them out into the lab for analysis. The clay fraction was left to settle for 1 day before the supernatant was pipetted of.

The acid environmental conditions were mimicked by mixing glauconite sand with HCl (pH =4 – prepared from concentrated HCl (37 %)), stored in glass bottles under ambient conditions. The bottles were closed and only opened to sample. Since the carbonate content of the sample (shell fragments etc.) allows some buffering of the pH, the pH was adjusted with concentrated HCl until pH =4 was maintained.

Representative subsamples were collected from the four environments at different time points. For the oxic conditions samples were taken after about 6, 12, 18 and 27 months, for the alkaline conditions after 6, 12, 18 and 26 months, for the acid conditions after 6, 12 and 24 months and for the anoxic only after 27 months. The subsamples (~ 20 g) were air dried in the laboratory, except the samples of the alkaline and anoxic set-up that were dried in the $N_2$ glovebox. The samples were washed with deionised water before drying.

**Glauconite analysis**

The mineralogy of the glauconite sands was studied by three proxies: the contents of major elements, the cation exchange capacity (CEC) and the Fe speciation, similar to the mineralogy approximation in Chapter 2. To avoid matrix effects, the analysis was performed on the magnetically separated glauconite fraction, more specifically the 125-250 µm grain size fraction. The analyses of samples D1, D5 and B2 were performed in 2017 and 2019. In the intermediate time the (un-milled) sample was stored dry in a ziplock bag. The data of the initial analyses in 2017 are used as untreated reference points. For the analysis of 2019 a new subsample of the glauconite fraction was milled.

The samples for major element analysis were prepared in duplicate with the lithium(Li)-metaborate fusion method (Vassilieva modified from Suhr and Ingamells (1966) and Cremer and Schlocker (1976)). The major element composition was measured by ICP-OES (Varian 720ES). The CEC was determined on the milled glauconite fraction (McCrone micronizing mill) with the cobalt(III) hexamine chloride-method (standardised protocol ISO 23470 (2018)) (duplicate, 1h of equilibration). The remaining Co concentrations in solution were determined by ICP-MS (Agilent Technologies 7700 Series). The Fe speciation was determined using the phenantroline method (Fritz and Popp, 1985; Shapiro, 1960). The combination of UV-Vis (Varian Model 635) and AAS (Thermo Electron Corporation S series) was used to determine the $Fe^{2+}$ and $Fe_{tot}$ content respectively (triplicate).

The artificially weathered samples (complete sands) were used in a $^{137}Cs$ batch sorption test. Detailed sample preparation and analysis are described in Chapter 2. The procedure of the batch $^{137}Cs$ sorption experiment was adapted from Wauters et al. (1996b). The samples were equilibrated in a 100 mM $CaCl_2$ and 0.5 mM KCl background solution and that solution was replaced 4 times, every 8 to 16 hours, to remove any salts that may have been added upon weathering, e.g. $K^+$ in the alkaline conditions. The experiment was performed in duplicate using a solid:liquid ratio of 1 g to 30 mL. The $^{137}Cs$ activity in solution was determined by liquid scintillation counting after 24h, 48h, 7d, 14d, 28d and 85d.

**Statistical analysis**

The changes in mean glauconite properties (CEC, $K_D$, major element composition and Fe speciation) due to weathering are analysed per sample and treatment and analysed relative to the untreated sample with a Dunnett's test, thereby using the sampling replicates as treatment replicates. In addition, the relative changes in these properties are analysed by calculating the ratio of the property of the weathered to corresponding unweathered (untreated) sample. These relative changes are subsequently averaged for all three glauconite samples and are analysed with the Dunnett's test, thereby indicating if weathering generally changes glauconite properties across different glauconite samples.

## 3. Results

**The effects of artificial weathering on elemental composition, CEC and Fe speciation**

Optically there were no clear differences between the glauconite sand before and after weathering for all set-ups and time points. The glauconite sands had not visibly changed colour, dissolved or disintegrated with time. No visible Fe-oxide coatings were formed in the oxic set-up, despite the assumption of the high oxidation sensitivity of glauconite and the presence of iron crusts in naturally weathered glauconite sand (Figure 6.4). To find differences induced by the artificial weathering, the composition of the glauconite fraction is studied by the CEC, major element composition and Fe-speciation. The starting point is the unaltered glauconite sand (analysed at the start of the artificial weathering experiment). To eliminate matrix effects, only the glauconite fraction is analysed. The data of these initial analyses are used as reference measurement.

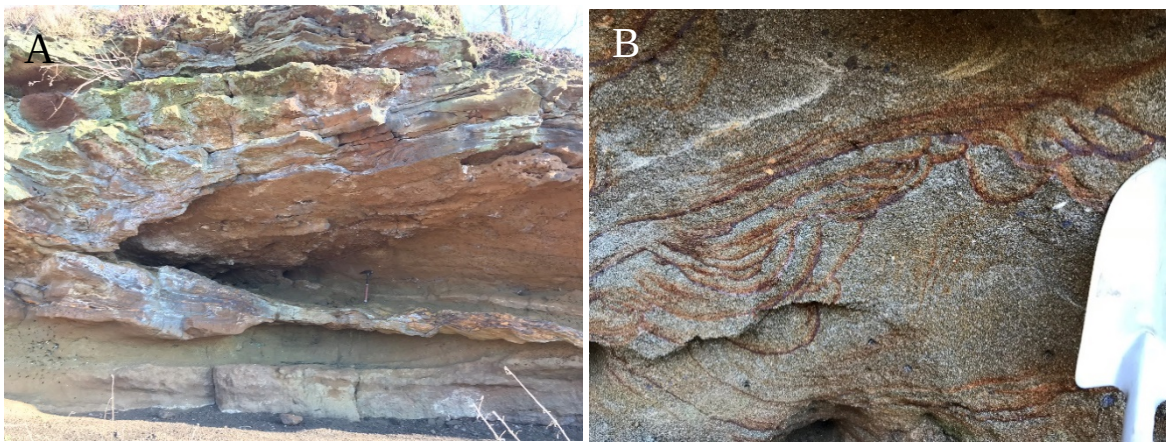


Figure 6.4 A) Iron concretions and iron sandstone in the Wijngaardberg intercalated by unconsolidated glauconite sands. B) Iron deposition in the glauconite sands at the Zavelstraat, Lubbeek.

The changes in the major element compositions of the different conditions are shown in Figure A4.3 (Annex 4: Accelerated weathering). The Al and Fe content (wt %) of the glauconite fraction remain unchanged over the different treatments. The largest changes are observed in the $Na^+$ and $K^+$ concentrations. Under the alkaline conditions (after 18 months), the concentrations logically increased with 0.22-0.34 wt % ($Na^+$) and 0.42-2.2 wt % ($K^+$) (Figure 6.5). This increase in the $Na^+$ and $K^+$ content was to be expected due to the composition of the young cement water (0.17 M KOH, 0.047 M NaOH, 2 mM $Ca(OH)_2$). The $Ca^{2+}$ concentration is much lower and only induced a small increase of 0.034-0.53 wt %. A larger $K^+$ concentration in solution is known to increase the interlayer $K^+$ occupation. However, in this case the increase is most probably attributed to deposition of the salts when drying in the samples, rather than changes in the structural composition. Due to practical constraints[4] the glauconite sands in

[4] The most optimal procedure would have been to add deionised water, centrifuge the sample and remove the supernatant before drying. However, the nitrogen glovebox was standing in a radioactive lab without centrifuge. Moving the sample in and out of the radioactive lab for centrifugation in a different lab was not allowed. Performing the washing and drying out of the glovebox could have allowed oxidation of the sample.

the alkaline set-up could not be washed after drying to remove the salts. Drying a sample of 20 g of (dry) glauconite sand that was immersed in 20 mL of young cement water, can add about 0.3 wt % $Na^+$ and 2.2 wt % K to the glauconite fraction, which is in correspondence with the observed increases of $Na^+$ and $K^+$ content.

None of the treatments significantly affected the $Ca^{2+}$, $Fe_{tot}$ and $Al^{3+}$ concentrations when analysed as relative changes (treated/untreated ratio). In contrast, weathering treatments significantly reduced the $Si^{4+}$ (mean factor change 0.94 ± 0.01) and $Mg^{2+}$ (0.87 ± 0.01) irrespective of the treatments. The $Si^{4+}$ to Al and Al to Fe ratio are often used as parameters to describe mineralogical variation in glauconite and illite minerals (Meunier and El Albani, 2007; Voronina et al., 2015a). The $Si^{4+}$ to $Al^{3+}$ ratio remained unchanged, just as the $Al^{3+}$ to Fe ratio, with exception of sample B2, where the $Si^{4+}$ to $Al^{3+}$ ratio is much higher in the untreated sample and the Al to Fe ratio is lower. Finding a significant decrease in the $Si^{4+}$ content after treatment and no significant effect in the $Si^{4+}$ to $Al^{3+}$ ratio is counter intuitive. There is a small decrease in $Al^{3+}$ content and $Si^{4+}$ to $Al^{3+}$ ratio after treatment. However, the large variation in the ratio probably does not allow detection of a significant trend. The inverse correlation found by Meunier between the $K^+$ content and $Al^{3+}$ to $Fe_{tot}$ ratio was not found in the glauconite samples (Annex 4. Major element analysis).

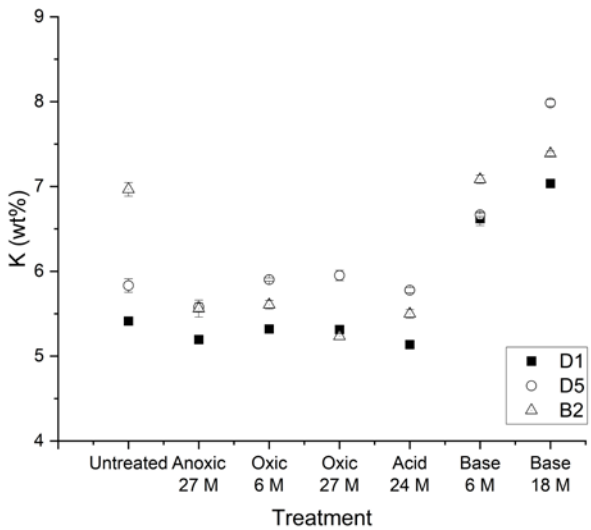


Figure 6.5 Effect of the different conditions (oxic, anoxic, alkaline, acid) on the K content of the glauconite fraction after different exposure times. The K content increased under alkaline conditions (of young cement water), but are most probably attributed to drying in of the cement water. Points are mean values and error bars represent the variation between the replicates, the statistical tests of changes are given in the text.

Weathering affected CEC significantly ($p<0.05$) but only slightly: it increased factors 1.1-1.2 under alkaline conditions (after 18 months) and decreased to, on average among the three samples, factors 0.8-0.9 (acid and oxic) relative to the untreated samples (Figure 6.6,Table 6.3).

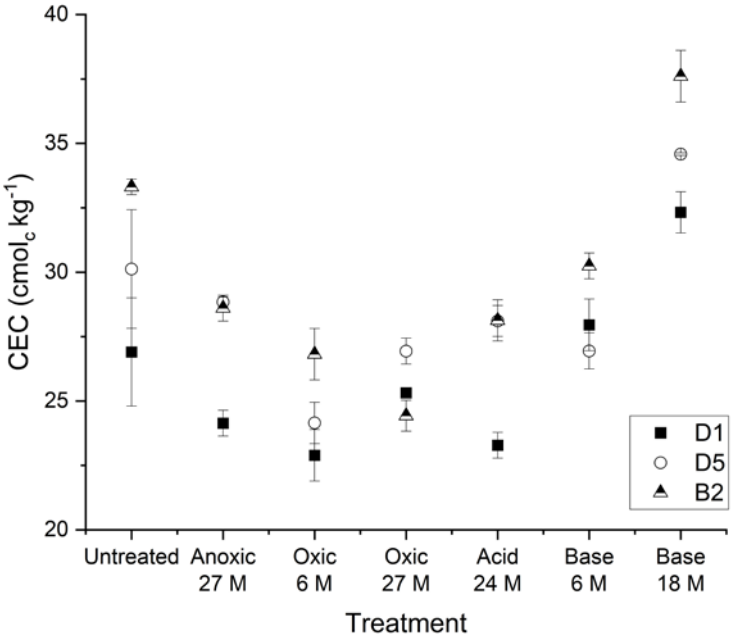


Figure 6.6 Effect of the different environmental conditions (oxic, anoxic, alkaline, acid) on the cation exchange capacity after different exposure times.

Table 6.3 The factor change in the CEC (cmol$_c$ kg$^{-1}$) relative to the CEC of the untreated presented as mean of all three samples. Mean factor changes followed by * are significantly different at $p<0.05$ compared to the untreated samples (Dunnett's test).

| Treatment | Factor change in CEC relative to Untreated (mean of three samples) | |
|---|---|---|
| | Average | Range |
| Untreated | 1.00 | |
| Anoxic 27 M | 0.90 | 0.86-0.96 |
| Oxic 6 M | 0.82* | 0.80-0.85 |
| Oxic 27 M | 0.86* | 0.73-0.94 |
| Acid 24 M | 0.89* | 0.82-0.93 |
| Base 6 M | 0.93 | 0.87-1.04 |
| Base 18 M | 1.16* | 1.13-1.20 |

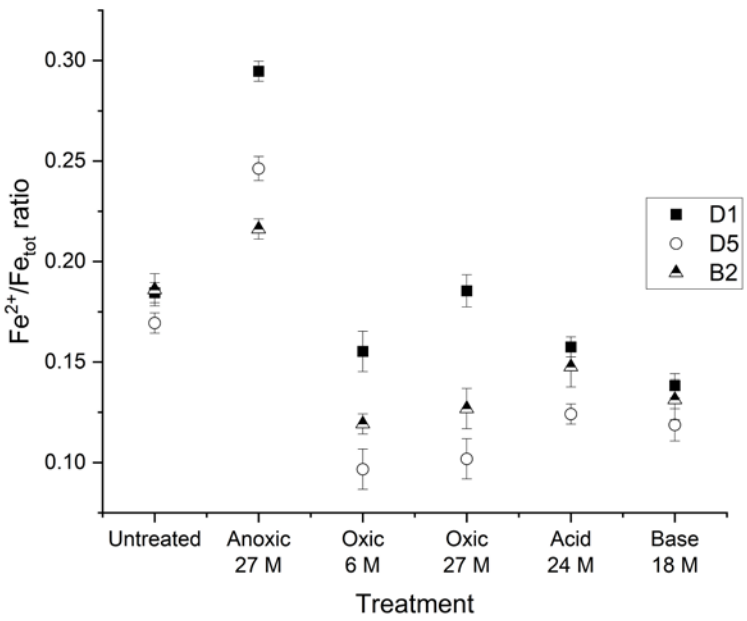


Figure 6.7 Fe speciation ($Fe^{2+}/Fe_{tot}$ ratio) in the glauconite fraction after exposure to different environmental conditions (oxic, anoxic, alkaline, acid) for different times. Sample D5 and B2 were measured in 2017 and 2019 (D1 only in 2019). The glauconite fraction (un-milled) was stored dry in a zip lock bag in the intermediate time. For the analysis of 2019 a new subsample of the glauconite fraction was milled.

The average total Fe content in the glauconite fraction of the (un-weathered) subsurface sands is 13.4 ± 1.8 m% (n= 21) with an average $Fe^{2+}$ to $Fe_{tot}$ ratio of 0.14 ± 0.04 (standard deviation, data presented in Chapter 5). The naturally weathered glauconite fraction discussed in Chapter 5 has a slightly higher average total Fe content (15.9 ± 3.3 m%, n= 9) and a much lower average $Fe^{2+}$ to $Fe_{tot}$ ratio (0.051 ± 0.040, n= 9).

The accelerated weathering reduced the $Fe^{2+}$ to $Fe_{tot}$ ratio (i.e. oxidation took place) in all treatments except the anoxic environment (Table 6.4). The changes in $Fe^{2+}/Fe$ ratio must be treated with caution: the untreated glauconite fractions of sample D5 and B2 were analysed in 2017 and 2019 with dry storage in a zip lock bag between both analyses. The $Fe^{2+}$ content decreased between the two measurement points (Figure 6.7). The same trend was observed in an additional set of glauconite fractions that were measured in both batches, with an average decrease of the $Fe^{2+}$ to $Fe_{tot}$ ratio with 31% (n=8) (Annex 4. Major element analysis), illustrating that oxidation takes place during laboratory storage, even in frozen or vacuum conditions. The accelerated weathering did not yield significant oxidation when referenced to the 2019 untreated sample. However, the reduction under anoxic conditions was highly significant and large (Table 6.4).

Table 6.4 Factor change in $Fe^{2+}/Fe_{tot}$-relative to untreated sample (mean of three samples), * are significantly different from the untreated (original) sample (Dunnett's test). Results of the Dunnett's test on the individual samples is given in Annex 4. Dunnett's test of individual samples.

| | Factor change in $Fe^{2+}/Fe_{tot}$ (mean of three samples) | | | |
|---|---|---|---|---|
| Treatment | To untreated 2017 | | To untreated 2019 | |
| | Average | Range | Average | Range |
| Untreated 2017 | 1.0 | | | |
| Untreated 2019 | 0.60* | 0.57-0.63 | 1.0 | |
| Anoxic 27 M | 1.18 | 1.00-1.35 | 1.84* | 1.61-2.26 |
| Oxic 6 M | 0.54* | 0.53-0.55 | 0.90 | 0.89-0.91 |
| Oxic 27 M | 0.57* | 0.56-0.59 | 0.97 | 0.93-1.01 |
| Acid 24 M | 0.68* | x | 0.98 | 0.79-1.14 |
| Base 18 M | 0.63* | 0.61-0.65 | 0.95 | 0.75-1.09 |

**Radiocaesium sorption on artificially weathered glauconite sand**

The sorption kinetics follow the same trend for all artificially weathered glauconite sands (Figure 6.8). Equilibrium is reached after about 28 days. The distribution coefficients after 28 days are given in Table 6.5. The alkaline conditions (after 18 months) yielded the highest $^{137}Cs$ $K_D$ values and anoxic conditions the lowest values. The effect of the treatment is very similar for all samples at 28 days, with the $^{137}Cs$ $K_D$ of base > oxic > untreated ≈ acid > anoxic. The differences in the $K_D$ values due to weathering are below a factor 1.5 for all treatments (Table 6.5). This is much smaller than the spatial variability effect, for example the $K_D$ varies with a factor 8 in subsurface samples due to large differences in glauconite content (Chapter 2).

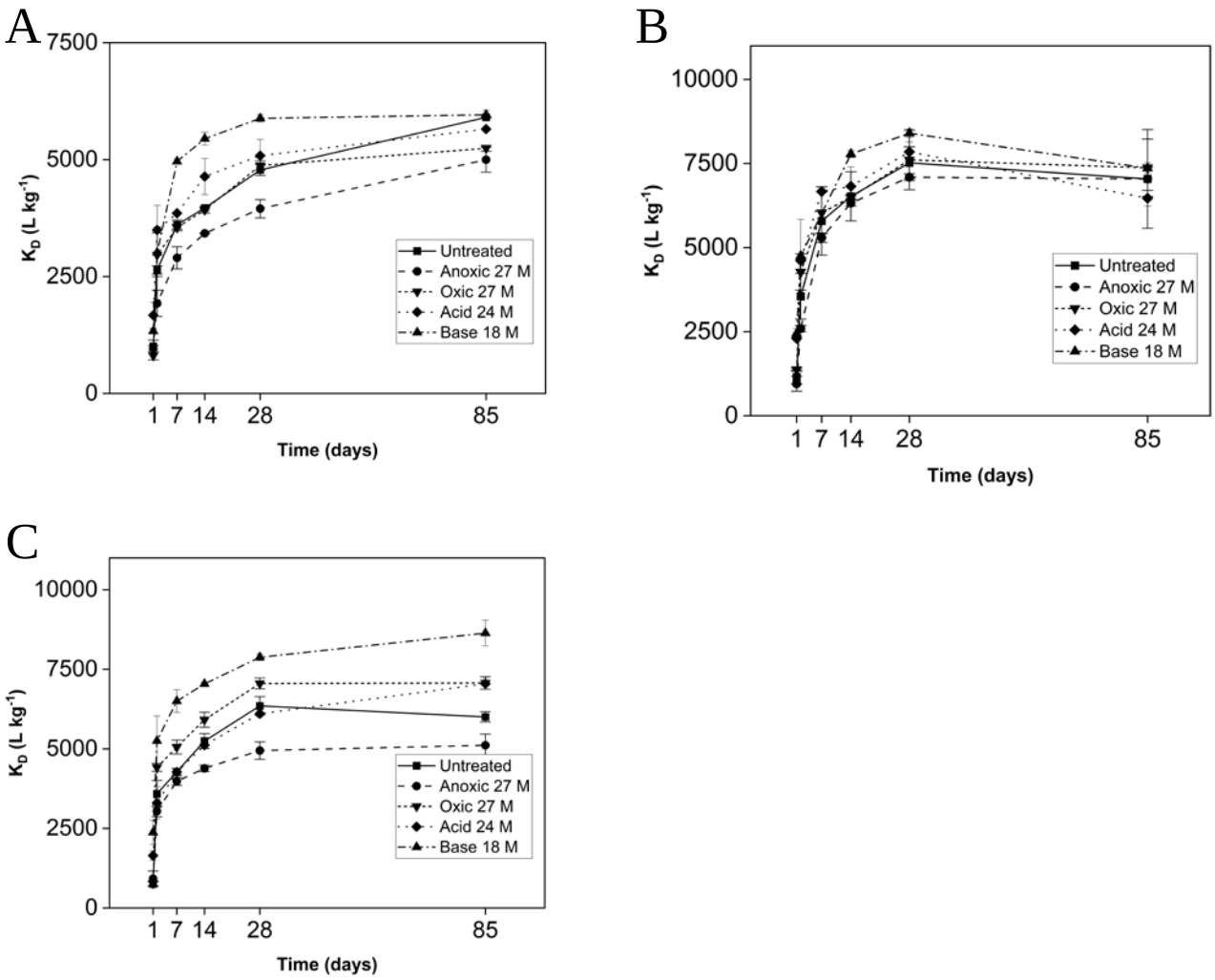


Figure 6.8 The evolution of the $^{137}Cs$ $K_D$ (L kg$^{-1}$) in time (days) for the three artificially weathered glauconite sands D1 (A), D5 (B) and B2(C) under four different conditions: anoxic (27 months), oxic (27 months), acid (24 months) and alkaline (18 months).

The relative change in $K_D$ was plotted with respect to the relative change in CEC (Figure 6.9). The CEC increase in the alkaline glauconite sands (18 months) is in line with the increase of the $K_D$. Less outspoken is the trend for the anoxic glauconite sands, where both the CEC and $K_D$ decreased with respect to the untreated sample. The decrease in the CEC of the oxic glauconite sand (both 6 and 27 months) is not accompanied by a decrease in $K_D$.

Table 6.5 The $^{137}Cs$ distribution coefficients at 0.5 mM $K^+$ (mean ± SD between replicates) in L $kg^{-1}$ after 28 days for all three samples and all treatments. Means followed by * are significantly different at $p<0.05$ from the untreated (original) sample (Dunnett's test).

| Treatment | D1 | D5 | B2 | Factor change in $K_D$ relative to untreated (mean of three samples) | |
|---|---|---|---|---|---|
| | | $K_D$ (L $kg^{-1}$) | | Average | Range |
| Untreated | 4780 ± 120 | 7520 ± 480 | 6350 ± 290 | 1.00 | |
| Anoxic 27 M | 3950 ± 200 | 7100 ± 100 | 4950 ± 280 | 0.85 | 0.74-0.96 |
| Oxic 6 M | 4880 ± 100 | 7610 ± 890 | 7050 ± 170 | 1.05 | 0.89-1.14 |
| Oxic 27 M | 5090 ± 350 | 7850 ± 290 | 6100 ± 110 | 1.02 | 0.91-1.14 |
| Acid 24 M | 4300 ± 170 | 9310 ± 230 | 5150 ± 320 | 0.98 | 0.76-1.27 |
| Base 6 M | 6260* ± 520 | 5190 ±190 | 8640 ± 40 | 1.12* | 0.67-1.42 |
| Base 18 M | 5880* ± 80 | 8400 ± 130 | 7880 ± 100 | 1.20* | 1.10-1.26 |

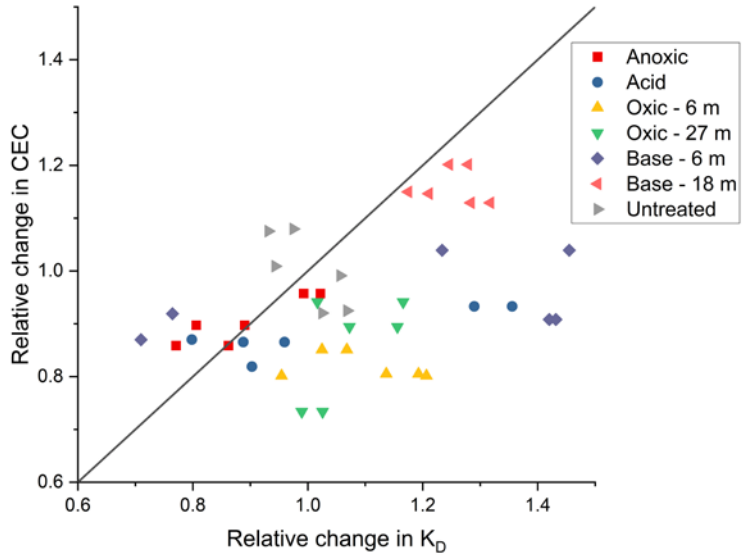


Figure 6.9 The relative change in $K_D$ to the relative change in CEC upon accelerated weathering with respect to the untreated sample. The values for the untreated sample are not all at 1.0 because the replicates are shown, their means are logically 1.0 on X and Y axes.

## 4. Discussion

The anoxic set-up was initially intended as a neutral reference point for the artificial weathering. The glauconite sand was mixed with deionised water under neutral pH (7) and stored under $N_2$ gas. However, compared to the untreated sample (the sample analysed at the start of the experiment) several differences stand out: the glauconites equilibrated under anoxic conditions had a factor 2 increase in the $Fe^{2+}$ to $Fe_{tot}$ ratios compared to the untreated sample of 2019. Compared to the sample of 2017, the $Fe^{2+}/Fe_{tot}$ ratio is not significantly higher. Additionally, the $Si^{4+}$ and $Mg^{2+}$ content are lower in the anoxic samples than in the untreated sample. This trend is present in all weathered samples. This can be an effect of weathering or, more likely, from traces of quartz present in the sample that have been dissolved and removed with the solution. The anoxic weathering had no effect on the $^{137}Cs$ $K_D$. It was, however, expected that the reduction of structural $Fe^{3+}$ to $Fe^{2+}$ would increase the FES because of an increase in the partially expanded layers (Wu et al., 1989).

The oxidation set-up had little to no effect on the major element composition and on the $Cs^+$ sorption potential of the samples. Oxidation slightly lowered the CEC. Under prolonged or more extreme conditions, the oxidation of $Fe^{2+}$ to $Fe^{3+}$ decreases the charge defect and, hence, lowers the CEC. The changes in charge defect decrease the attraction to the interlayer cations and thereby increase the interlayer space. If this happens to a small extent the FES capacity increases and the $Cs^+$ sorption increases. This probably explains the higher $K_D$/CEC ratio of the oxidised samples compared to the unweathered samples. If the oxidation continues, hydrated interlayer sites are formed leading to a decrease of the sorption potential for $Cs^+$. In addition, the iron precipitates often occur as amorphous films or coatings on the grains. The higher total Fe content in the naturally weathered (surface) glauconite compared to subsurface sands indicates that the Fe-coating does not only originate from weathering of the glauconite grain or leaching of structural Fe but that it is likely derived from an external source, e.g. Fe-rich ground water. The coating can decrease the accessibility of the sorption sites thus decreasing $Cs^+$ sorption. However, if iron films are formed after $Cs^+$ sorption the $Cs^+$ is 'trapped' in the grain and $Cs^+$ desorption decreases. No such trends have been identified here, the oxidation did neither affect the kinetics of $^{137}Cs$ sorption nor its final $K_D$. There are some effects that are present in-situ but that the oxidation set-up does not take into account i.e. groundwater movement, mechanical weathering, drying/wetting, freezing.

The alkaline environment with the young cement water has the strongest effect on the $^{137}Cs$ $K_D$ of the glauconite. The $K_D$ increased in all glauconite samples with a factor 1.1-1.3 in comparison to the untreated sample. Calcium can promote weathering of illite in high $Ca^{2+}$ environments, $K^+$ is exchanged at the edges of the interlayer and hydrated interlayer sites are formed. At the same time the high $K^+$ concentration can alter hydrated interlayer sites to FES (type II or type I) or collapsed interlayer sites. This can coincide with an increase in the FES site capacity. This hypothesis is confirmed by the increase

in the CEC with a factor 1.1-1.2. Changes in structural $K^+$ were undetected, though, they were likely masked by the presence of $K^+$ derived from the alkaline solution (0.17 M $K^+$).

The acid environment caused only small changes to the glauconite such as the decrease in the CEC with, on average, factor 1.1. The first signs of acid weathering would be dissolution and $Al^{3+}$ and $K^+$ release into the solution (Liu et al., 1999). Changes in the major element composition were, however, not observed.

One of the more striking observations is that the subsurface samples are sensitive to oxidation during storage as witnessed by decreasing $Fe^{2+}/Fe_{tot}$ ratio, even when stored dried or frozen. During the storage in the core library oxidation is observed in the glauconite in the outer rim. These samples were stored for about 20 years before this speciation analysis was performed. It is unclear if the glauconite at the interior of the core remained un-oxidised. The glauconite sands that were prepared in 2017 and re-measured in 2019 have a lower $Fe^{2+}$ content after storage. This leads to questions about the reliability of the storage conditions preceding the Fe speciation analysis. Further, the preparation methods before the analysis could alter the Fe speciation as well. In a standard preparation the sample is washed and sieved before magnetic separation and (wet) milling and drying under oxic conditions (air or 60° C oven dried). This preparation opens up the glauconite grains and facilitates oxidation.

## 5. Conclusion

Previous studies have suggested that weathering can both increase and decrease the $Cs^+$ sorption potential. On the one hand, weathering can enhance the $Cs^+$ sorption by increasing the FES capacity. On the other hand, prolonged weathering can alter the FES to hydrated interlayer sites or cause a dissolution of the glauconite and thereby decrease the FES capacity and, hence, the $^{137}Cs$ sorption potential. These effects can be expected both in alkaline and oxic conditions.

The artificial weathering had a limited effect on the glauconite sands. Among the different treatments very small differences were observed in the parameters evaluated (CEC, major elements, Fe speciation) and the $^{137}Cs$ $K_D$ does not factor more than factor 1.5. Under the alkaline conditions of young cement water, the $^{137}Cs$ $K_D$ increased in all samples. Oxidation had no significant change on the $^{137}Cs$ $K_D$ of the samples. We can conclude that these glauconite sands are not highly sensitive to weathering. Over the time span of the experiment (up to 27 months) the glauconite did not dissolve or disintegrate. Longer and more extreme conditions of artificial weathering might be required to evoke stronger effects on the glauconite. Natural analogues from soil profiles or surface samples might provide a good alternative to evaluate the effect on sorption capacity.

# Chapter 7. General conclusions and future prospects

This study has been set up to provide a quantification and a mechanistic understanding of the sorption of radiocaesium and radiostrontium onto diverse natural glauconite (sands) from the Cenozoic (Paleogene and Neogene) formations. It was hypothesised that glauconite is a strong sorbent for $Cs^+$ and $Sr^{2+}$ based on its mineralogical similarities to illite, suggesting that selective sorption of $Cs^+$ sorption is possible. However, in contrast to illite, glauconite occurs mostly as large grains, sizing 125-250 µm. The density and size of the grains were expected to reduce the sorption potential and reaction rate as they do not allow direct contact between the reactive surfaces and the mobile pore water. Hence, it was speculated that reaction kinetics may be importantly affecting the sands as geological barriers. In case of local non-equilibrium sorption, early breakthrough could be induced, making the glauconite sands unsuitable as a barrier in a radioactive waste disposal system. Finally, the effects of glauconite weathering on the sorption potential was unclear. An assessment of the weathering susceptibility of glauconite was required to warrant the long-term efficacy as a barrier in a radioactive waste disposal system.

This last chapter evaluates the initial objectives and hypotheses against the results and gives an outlook on the practical implications of the results of this study.

## To assess the sorption of trace concentration $^{137}Cs$ on natural glauconite sands from the Cenozoic formations in Belgium.

The sorption potential of trace concentration $^{137}Cs$ on natural glauconite sands was assessed in batch sorption experiments in a background solution of 0.5 mM $K^+$ and 100 mM $Ca^{2+}$. Several fractions of the sand were prepared to evaluate the effect of the pellet size on the sorption of the trace element by comparing milled vs unmilled samples, and the contribution of the glauconite was identified by comparing complete sand with the glauconite fraction. The sorption data were compared to three mineralogical proxies: the $K^+$ content, the Fe content and the cation exchange capacity (CEC).

The experiments revealed that the glauconite sands have a strong radiocaesium sorption potential, the log $K_D$ (L $kg^{-1}$) at 0.5 mM K ranged between 3.4 – 4.3 with a limited variation in the sorption potentials among the investigated sands, despite the natural diversity of the sand. In the isolated glauconite fraction the log $K_D$ (L $kg^{-1}$) ranges between 4.1 – 4.3, comparable to pure illite (Illite du Puy 4.4). The sorption potential of a glauconite sand can be estimated from its percentage glauconite content, in case that the fraction of other clays is low, indicating that glauconite is the main sorbing component of the sand. Potassium concentrations in the aquifer solution range from 0.14-0.37 mM, suggesting that even higher $Cs^+$ $K_D$ values (3.7 – 4.2 log $K_D$) can be expected in-situ. The $^{137}Cs$ sorption correlates better to the CEC (r = 0.95) than to the $K^+$ content or the Fe content.

The $^{137}Cs$ sorption rate on glauconite sands, i.e. time to reach equilibrium, was slower than estimated earlier in soils or in clay fractions. In illite sorption tests, equilibrium is reached within 24 hours to 7 days (Poinssot et al., 1999a). Sorption equilibrium in the glauconite sands and fractions was almost complete within 1 month and was followed by a small additional slow reaction, i.e. the $K_D$ increases about factor 1.6-1.8 between 1 month and 8.5 months. In the milled grains sorption occurred faster in the first 7 days, suggesting that the pellet restricts the sorption rate. The slow long-term reactions might be related to $Cs^+$ migration into the interlayer space. We speculate that these slow reactions are important for reactive transport of $Cs^+$ sorption in the high permeable sands where the local non-equilibrium may induce early breakthrough.

The pellet also has an effect on the total sorption potential at equilibrium. Indeed, the equilibrium $Cs^+$ $K_D$ for milled glauconite is a factor 1.1-1.5 higher compared to the $K_D$ of the respective pelletal glauconite. This finding suggests that the inner part of the glauconite pellet is not accessible to $^{137}Cs$. In strongly weathered grains, however, the milled glauconite and pelletal glauconite have the same $K_D$ at equilibrium. The SEM images (Figure 7.1) show cracks in the grains that can explain higher accessibility of the inner part of the pellet. Overall, the grain size effect is limited in comparison to the range of $K_D$ values measured among different glauconite sands.

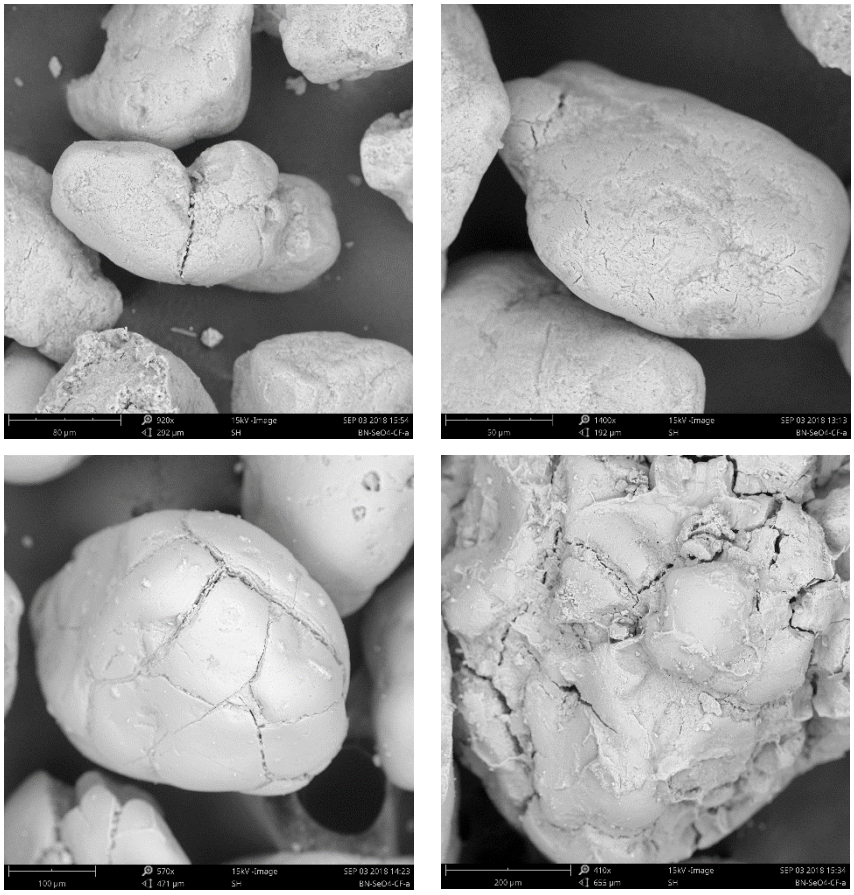

Figure 7.1 SEM images of glauconite pellets of the Voort Fm (A), Berchem Fm (B), Diest Fm (C) and naturally weathered Diest Fm (D) respectively sample V1, B2, D1 and W11.

**To characterise and model the concentration-dependent selective $Cs^+$ sorption on a range of glauconite sands and relate the sorption parameters to the mineralogy.**

Competing cations $Cs^+$, $K^+$, $NH_4^+$ have similar ion properties and comparable selectivity for the planar exchange sites. On the FES, the differences become more pronounced, due to the specific size of the selective sorption sites. The $NH_4$/K selectivity on the FES was determined as a fingerprint for the highly selective FES on glauconite. In addition, the $Cs^+$ sorption isotherm was determined in batch in a background solution of 0.5 mM $K^+$, 100 mM $Ca^{2+}$ and the $Cs^+$ concentration ranging between $10^{-8}$ and $10^{-4}$ M. The experimental sorption isotherm data were fitted with an optimised three-site model adapted after the illite model of Bradbury & Baeyens (2000).

The $NH_4^+$ to $K^+$ selectivity studies in the glauconite indicated that the ion binding characteristics are highly similar to illite, i.e. similar selectivity coefficients. The lower sorption of $Cs^+$ on glauconite than in illite as observed in the initial batch sorption experiments, log $K_D$ (L $kg^{-1}$) 4.1 – 4.3 in the glauconite fraction versus 4.4 for Illite du Puy, is, hence, likely reflecting the lower FES site capacities of the glauconite.

The sorption data on natural glauconite sands, with an initial concentration of $10^{-8}$ to $10^{-4}$ M CsCl, showed that caesium sorption is non-linear and requires a multi-site ion exchange model to fit the experimental data. The optimised sorption isotherm (Figure 7.2) suggests a lower sorption per unit CEC than for illite. This is reflected in a lower capacity of the FES (type I) compared to illite (0.04-0.06 % of the CEC vs 0.25% for Illite du Puy) combined with a lower (FES) type II site capacity (1.6-2.2 % vs 20%). The presence of mixed layer illite-smectite and smectite in the glauconite pellets can account for part of this observation. The smectite content strongly increases the CEC (90-100 $cmol_c$ $kg^{-1}$ vs 20 $cmol_c$ $kg^{-1}$ for illite). However, the fraction of FES to CEC in smectite is nearly zero. The introduction of smectite interlayers hence strongly decrease the fraction of FES to total CEC. The $K_D$ at trace $Cs^+$ occupation is the product of the FES selectivity and its capacity. If the capacity is significantly lower, the $K_D$ is consequently lower.

The effect of the reaction kinetics was similarly observed in the sorption isotherm as in the batch experiment at trace $^{137}Cs$ levels. The increase in $K_D$ between 48 hours and 94 days is modelled as an increase in the accessible FES (type I) and type II sites, resp. 0.04-0.06 to 0.08-0.1 % of the CEC and 1.7-2.2 to 2.3-3.7 % of the CEC; the capacity of the long-term accessible FES sites is still lower than that reported for illite.

The optimised model for glauconite was able to represent $Cs^+$ sorption data qualitatively and quantitatively in a wide range of $Cs^+$ concentrations. Determining the selectivity coefficients for additional competing cations (e.g. $Na^+$ and $Rb^+$ ) could fine-tune the model for more complex chemical conditions.

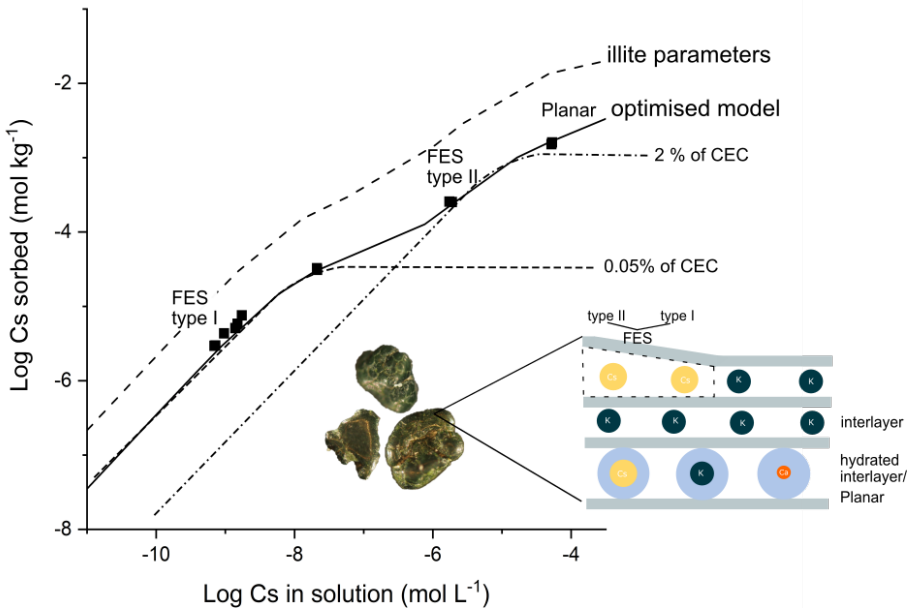


Figure 7.2 Three-site sorption model for glauconite optimised based on the experimental sorption isotherm indicating non-linear sorption.

In the more recent characterisation studies of the FES (Nakao et al., 2012; Nakao et al., 2008; Ogasawara et al., 2013) no distinction is made between type I and type II sorption sites. Both are considered part of the FES with a interlayer width of 1.0-1.4 nm. The experimental sorption isotherm on glauconite can, however, not be adequately explained by a two-site only (i.e. selective-non selective) model. This observation was also the base for the three-site model as proposed by Bradbury and Baeyens (2000). More work will be needed to understand structural differences between type I and type II sites in order to evaluate if the three-site model is structurally grounded or, alternatively, if a model with a continuous distribution of selectivities rather than discrete sites, is not more applicable. Such models, often termed Sips adsorption models (Sips, 1948), have only limited number of parameters and are widely used for heterogeneous organic matter but are much less used for trace elements on clay minerals.

**To evaluate the validity of chemical equilibrium for $Cs^+$ sorption during transport in glauconite sand at a range of different realistic flow rates.**

The relatively slow sorption of $Cs^+$ on glauconite raised questions on the validity of chemical equilibrium during transport in the glauconite sands. The current groundwater models suggest mean flow rates of 0.81 ± 0.87 m $d^{-1}$ (Diest Fm) and 0.12 ± 0.43 m $d^{-1}$ (Berchem and Voort Fm). A column experiment with a range of realistic flow rates between 0.079 and 3.5 m $d^{-1}$ was set up to test the validity of the local equilibrium assumption (LEA).

The breakthrough to pore volume plot revealed earlier breakthrough only for the highest flow rate, indicating chemical non-equilibrium in flow rates above 2.4 m $d^{-1}$. Still, in the worst case high flow scenario, beyond the relevant range, glauconite sands effectively removed $Cs^+$ from the influent. The

HP1 model predicted the breakthrough curves well for the columns with flow rates below 2.4 m $d^{-1}$, confirming the local equilibrium assumption. It should be kept in mind that the columns were set up under ideal conditions, i.e. small, homogeneous, saturated columns. In undisturbed heterogeneous sand formations preferential fingering of contaminant plumes through zones of low glauconite content can be expected (Figure 7.3). If the water content decreases (i.e. partly saturated), the $K_D$ of $^{137}Cs$ will decrease, as competing ion concentrations increase (Szenknect et al., 2003).

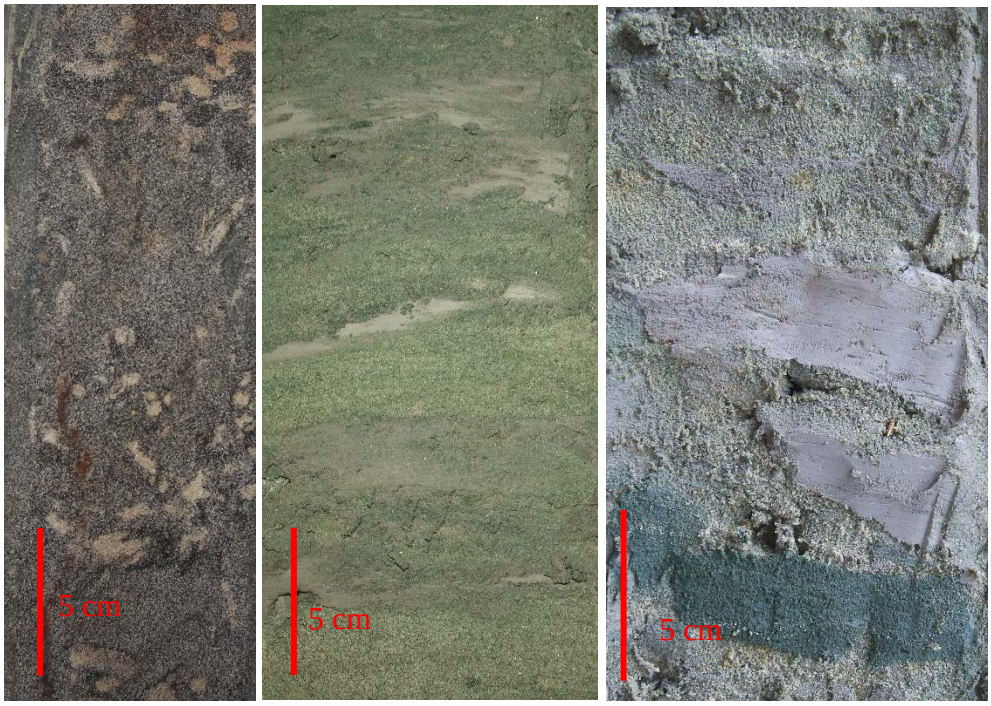


Figure 7.3 Core sections showing the heterogeneity of the glauconite sands A) Strong bioturbations in the Beerse URS borehole (128-129 m), B) clay intercalations in glauconite sand in the ON-Dessel-3 core (30.4-30.7) and C) dark green glauconite rich band in the ON-Dessel-2 core, (32 -32.2 m) (Pictures Rieko Adriaens).

In the column experiments $10^{-6}$ M CsCl (stable) was used instead of trace concentrations radiocaesium (< $10^{-8}$ M) to obtain realistic breakthrough times. In a realistic $^{137}Cs$ contamination scenario low (trace) $Cs^+$ concentrations can be expected. Therefore, the question is if the LEA is also valid under trace $Cs^+$ conditions. At trace concentrations, the slow reactions are more pronounced than at higher concentrations suggesting early breakthrough. However, the equilibrium retardation of trace $^{137}Cs$ on glauconite sand is more than a factor 10 larger than at $10^{-6}$ M $Cs^+$. The retardation and reaction rate counteract each other. At higher retardation the time for reaction increases and early breakthrough is less likely. To confirm this hypothesis, long-term experimental work with isotopically labelled $Cs^+$ is required.

Hence, in conclusion, $Cs^+$ sorption on highly permeable glauconite sands is sufficiently fast to delay breakthrough. Only at high flow rate, unrealistic for the Neogene and Paleogene formations, early breakthrough could occur. The heterogeneities of glauconite distribution in undisturbed formation require attention as that factor might logically cause preferential fingering.

**To assess the strength and kinetics of radiostrontium sorption on the natural (subsurface) and weathered (surface) glauconite sands**

The sorption potential of trace concentration $^{85}Sr$ on natural glauconite sands, both un-weathered subsurface sands and weathered surface sands, was assessed in batch sorption experiments in a background solution of 0.5 mM $K^+$ and 1 mM $Ca^{2+}$. In total 45 different glauconite sands and fractions of the sand were prepared to evaluate the effect of the pellet size on the sorption of the trace element by comparing milled vs unmilled samples, and the contribution of the glauconite was identified by comparing complete sand with the glauconite fractions. The sorption data were compared to four mineralogical proxies: major element composition, the Fe-speciation, mineralogical composition (the glauconite and clay content) and the cation exchange capacity (CEC).

The $K_D$ values of $Sr^{2+}$ in the glauconite sands ranged from 23 to 65 L $kg^{-1}$. Equilibrium was reached within 48 hours in all fractions (complete glauconite sand, glauconite fraction, milled complete sand and milled glauconite fraction). Contrary to $Cs^+$ sorption, there was no difference in the $K_D$ and the kinetics between milled and pelletal glauconite. This implies that the internal sorption sites are accessible without time-lag in reaching sorption equilibrium, important for predicting $Sr^{2+}$ transport in the glauconite sands. Pure glauconite fractions show higher sorption with $K_D$ values of 50 to 144 L $kg^{-1}$, in the range of $Sr^{2+}$ $K_D$ values for illite (132 ± 3.2 L $kg^{-1}$). Just as for $Cs^+$ sorption, glauconite is the main $Sr^{2+}$ sorbing component in the sand. The $K_D$ on the complete sand is proportional to the glauconite content and the $K_D$ of the glauconite fraction if no other clay minerals are present in significant amounts. The $K_D$ values can be calculated based on two existing models calibrated to soils, with CEC and $Ca^{2+}$ concentration as input parameters. Both models gave a good prediction with a factor 0.94-1.6 deviation between calculated and experimentally determined $K_D$ values.

Further, the study revealed that the $Sr^{2+}$ sorption $K_D$ of the complete sand positively correlates with the CEC of the complete sand ($R^2$=0.62) and the glauconite fraction ($R^2$=0.82). Within the investigated mineralogical proxies no clear distinction could be made between the natural (subsurface) and weathered (surface) sands. Among all samples, there is a negative correlation between the CEC and $d_{060}$ reflection ($R^2$ = 0.57) and between the $K_D$ and the $d_{060}$ reflection ($R^2$ = 0.57). The $d_{060}$ represents the b cell dimension of a crystal. A crystal is described in three-dimensions by a, b and c (length) and the angles α, β, γ in between. The a and b cell dimension are affected by isomorphic substitutions in both the octahedral and tetrahedral layer. The $d_{060}$ reflection is mainly sensitive to the size of the cations and the cation occupancy in the octahedral layer. Changes in the interlayer occupancy or interlayer width influence the c dimension (d00l reflection). The $d_{060}$ reflection broadens and shifts to lower d-values in case of more weathered samples due to a decrease in the Fe content in the octahedral layer. With weathering the interlayer $K^+$ content is expected to decrease combined with an increase in the expandable layer, or smectite layer, content. This leads to an increase in the interlayer width and increasing CEC. The $d_{060}$ peak is often used as diagnostic peak for clay mineral identification with a

peak at 1.499 Å for illite, >1.511 for (pure) glauconite and 1.50-1.52 Å for montmorillonite. However, the $d_{060}$ reflection is sensitive to the size of the cations and the cation occupancy in the octahedral layer and not to the interlayer width or basal spacing. Hence, a correlation with the expandable layer content would be expected rather than a correlation with the $d_{060}$ peak. However, the expected correlation between the CEC and the expandable layer content was not present in this dataset.

**To assess the effects of accelerated weathering of glauconite on RN sorption in order to evaluate the evolution of the sorption potential and retention over the time frame of radioactive waste disposal.**

Glauconites are redox sensitive minerals because both $Fe^{2+}$ and $Fe^{3+}$ are present in the structure. Based on the literature description of weathering on glauconite and illite, weathering can both increase and decrease $Cs^{+}$ and $Sr^{2+}$ sorption. On the one hand, the weathering can enhance the $Cs^{+}$ sorption by increasing the FES capacity, with little effect on $Sr^{2+}$ sorption. On the other hand, prolonged weathering can alter the FES to hydrated interlayer sites or planar sites, decreasing $Cs^{+}$ sorption and increasing $Sr^{2+}$ sorption. Further accelerated or extreme weathering can cause a (partial) dissolution of the glauconite and thereby decrease sorption of both $Cs^{+}$ and $Sr^{2+}$. Similar effects are described to varying extent in both in alkaline and oxic conditions.

A set-up was built to simulate weathering on glauconite sand in four different environments (oxic, anoxic, alkaline and acidic). The experiment with three glauconite sands from different formations ran up to 27 months and subsamples were collected at intermediate times. The results of the artificial weathering on the CEC, major element composition and Fe speciation were compared to ranges in the subsurface sands (unweathered) and surface sands (naturally weathered). In a final step the artificially weathered sands were used in a $Cs^{+}$ batch sorption experiment.

The artificial weathering had only a limited effect on the properties of the glauconite sands, i.e. on CEC, major elements concentration and Fe speciation. Oxidation of $Fe^{2+}$ to $Fe^{3+}$ decreases the negative layer charge. The CEC is expected to decrease with more $Fe^{3+}$ in the structure, possibly negatively affecting the $K_D$. The effect of the treatment on the $Cs^{+}$ sorption remained below a factor 1.5, which is much smaller than the effects of glauconite content or even type when comparing different formations or sand. The highest $K_D$ was measured in the glauconite sands after alkaline conditions, followed by the oxic conditions with similar $K_D$ values to the untreated samples. The acid and anoxic treatment resulted in lower $K_D$ values to the untreated samples, with the anoxic glauconite sands having the lowest $K_D$.

We can conclude that the studied glauconite sands are not highly sensitive to weathering. Over the time span of the experiment (up to 27 months) the glauconite did not dissolve or disintegrate. Longer and more extreme conditions of artificial weathering might be required to evoke stronger effects on the

glauconite. Natural analogues from soil profiles or surface samples might provide a good alternative to evaluate the effect on sorption capacity. This had been elaborated in this work by contrasting glauconite sands from outcrops from the Diest Fm in the Hageland region. These naturally weathered glauconite sands have lower $Fe^{2+}$ to $Fe_{tot}$ ratios combined with a higher total Fe content compared to subsurface sands. The changes in the Fe speciation did however not impact the CEC or $^{85}Sr$ $K_D$ values.

## Suggestions for future research

Taken together, glauconite exhibits strong sorption potential for radiocaesium and radiostrontium with strong similarities to illite. The $^{137}Cs$ sorption potential of a sand with 25-30% glauconite appeared surprisingly as high as that of Boom Clay with 30-60 % clay and which is one of the candidate hosts for category B and C waste. The variations in sorption potential among the glauconite sands are limited and can be estimated based on the CEC. Sorption is sufficiently fast to prevent an early breakthrough even at high flow rates. Accelerated weathering had little effect, suggesting that glauconite will remain relatively stable over the time of the disposal. From the research work performed in this PhD, we could conclude that glauconite can act as an additional sorption sink for $Cs^{+}$ and $Sr^{2+}$. However, before glauconite can be applied as a barrier in a disposal system several factors require further research.

First, at the scale of the mineral structure, this work had not clearly revealed the structural difference between the type I and type II FES in glauconite. The presence of the type II sites has been experimentally determined in sorption isotherms. In the more recent structural analysis with HRTEM no distinction between the selective sites is made. Further research is needed to solve the question if the type I and type II sites are clearly discretised or if they are rather a continuum of selective sites. The answer to this question might change the way we model sorption on illite and glauconite.

Second, at the scale of a formation, there are uncertainties on transport phenomena that can take place in the environment. The current column set-up used a simplification of the system with uniform small columns with one type of glauconite sand that was washed, homogenised and packed. The glauconite sands are known for strong spatial variability with high and low glauconite enriched zones, clay lenses, variable grain sizes, etc. Undisturbed larger columns should be studied to evaluate the effect of the spatial variability. The current model in HP1, a combination of a geochemical and transport model, allows to increase the complexity of the system. The composition of the background solution can be varied and the column can be described in more layers with different sorption capacities. Changes in the composition of the aqueous phase are very relevant, considering the pore water composition might evolve due to climate change e.g. sea water intrusion. In addition, the experimental sorption data of the different formations can be combined with the groundwater model of the Neogene sands to account for the variation in the flow rates.

Third, the accelerated weathering showed very little effect, possibly due to the limited time span of the experiment. It is the problem of every scientist studying processes that take place over longer times than a PhD. An alternative can be to study natural analogues e.g. soil weathering profiles or to subject the samples to more extreme conditions (higher temperatures, higher flow rates, leaching experiments).

Fourth, radiocaesium and radiostrontium will not be the only radionuclides of interest. Especially in the case of the geological disposal actinide sorption needs to be studied. Glauconite sands are highly reactive because of the high clay content, presence of (amorphous) iron oxy-hydroxides and limited presence of organic matter. Therefore, it is possible the glauconite sands and associated Fe-oxides will be susceptible to the sorption of actinide-organic matter complexes.

Finally, the loose nature of the sands gives the possibility to create a custom barrier based on glauconite, for example as embankment in the surface disposal of category A waste. At several locations the glauconite sands can be mined. The magnetic susceptibility of the glauconite allows separation of the glauconite fraction from the matrix. A mixture can be made with glauconite and quartz to create the optimal permeability and desired sorption potential. Additional components can be added, e.g. iron oxides, to immobilise other radionuclides.

## References


Adriaens, R., 2015. Neogene and Quaternary clay minerals in the southern North Sea. Leuven : KU Leuven. Science, engineering & Technologie.

Adriaens, R., Vandenberghe, N., 2020. Quantitative clay mineralogy as a tool for lithostratigraphy of Neogene Formations in Belgium: a reconnaissance study. Geologica Belgica.

Adriaens, R., Vandenberghe, N., Elsen, J., 2014. Natural Clay-Sized Glauconite in the Neogene Deposits of the Campine Basin (Belgium). Clays and Clay Minerals 62, 35-52.

Akar, D., Shahwan, T., Eroğlu, A.E., 2005. Kinetic and thermodynamic investigations of strontium ions retention by natural kaolinite and clinoptilolite minerals. Radiochemica Acta 93, 477-485.

ALBON, 2009. Afdeling Land en Bodembescherming, Ondergrond & Natuurlijke rijkdommen, Tertiair Geologische kaart Vlaanderen. Vlaamse Overheid, Departemend LNE.

Altmann, S., Aertsens, M., Appelo, T., Bruggeman, C., Gaboreau, S., Glaus, M., Jacquier, P., Kupcik, T., Maes, N., Montoya, V., 2014. Processes of cation migration in clayrocks (CATCLAY), in: Altmann, S., Van Laer, L. (Eds.). Final Scientific Report.

Baetsle, L., 2003. Application of partitioning/transmutation of radioactive materials in radioactive waste management.

Baeyens, B., Bradbury, M.H., 1995. A Quantitative Mechanistic Description of Ni, Zn and Ca Sorption on Na-Montmorillonite: Part II: Sorption Measurements. Paul Scherrer Insitut (PSI), Würenlingen/Villigen.

Bailey, S., 1980. Summary of recommendations of AIPEA nomenclature committee on clay minerals. American Mineralogist 65, 1-7.

Baldermann, A., Dietzel, M., Mavromatis, V., Mittermayr, F., Warr, L.N., Wemmer, K., 2017. The role of Fe on the formation and diagenesis of interstratified glauconite-smectite and illite-smectite: A case study of Upper Cretaceous shallow-water carbonates. Chemical Geology 453, 21-34.

Beerten, K., Wemaere, I., Gedeon, M., Labat, S., Rogiers, B., Mallants, D., Salah, S., Leterme, B., 2010. Geological, hydrogeological and hydrological data for the Dessel disposal site, Project near surface disposal of category A waste at Dessel, Version. SCK CEN Studiecentrum voor Kernenergie, Mol, p. 273.

Belousov, P., Semenkova, A., Egorova, T., Romanchuk, A., Zakusin, S., Dorzhieva, O., Tyupina, E., Izosimova, Y., Tolpeshta, I., Chernov, M., Krupskaya, V., 2019. Cesium Sorption and Desorption on Glauconite, Bentonite, Zeolite, and Diatomite. Minerals 9.

Bradbury, M.H., Baeyens, B., 2000. A generalised sorption model for the concentration dependent uptake of caesium by argillaceous rocks. Journal of Contaminant Hydrology 42, 141-163.

Bradbury, M.H., Baeyens, B., 2005. Experimental and Modelling Investigations on Na-Illite: Acid-Base Behaviour and the Sorption of Strontium, Nickel, Europium and Uranyl. Paul Scherrer Institut (PSI), Villigen.

Bradbury, M.H.B., B., 2005. Modelling titration data and the sorption of Sr (II), Ni (II), Eu (III) and U (VI) on Na-illite. Paul Scherrer Institut (PSI), Villigen.

Brouwer, Baeyens, Maes, A., Cremers, A., 1983. Cesium and rubidium ion equilibriums in illite clay. Journal of Physical Chemistry 87, 1213-1219.

Brouwer, E., Baeyens, B., Maes, A., Cremers, A., 1982. Cesium ion equilibria in illite clay, Abstracts of papers of the American Chemical Society. American Chemical Society, p. 97.

Bruggeman, C., Maes, N., 2016. Radionuclide migration and retention in Boom Clay. SCK•CEN, Institute for Environment, Health and Safety, Expert group Waste and Disposal, Unit R&D Disposal.

Bruggenwert, M., Kamphorst, A., 1979. Survey of experimental information on cation exchange in soil systems, Developments in Soil Science. Elsevier, pp. 141-203.

Bruneel, Y., 2016. Quantification of complex mineral phases using PONKCS-assisted Rietveld refinement. Leuven : KU Leuven. Faculteit Wetenschappen.

Bruneel, Y., Van Laer, L., Brassinnes, S., Smolders, E., 2020. Radiocaesium sorption on natural glauconite sands is unexpectedly as strong as on Boom Clay. Science of the Total Environment 720, 137392.

Bruneel, Y., Van Laer, L., Brassinnes, S., Smolders, E., 2021a. Characterisation of the highly selective caesium sorption on glauconite rich sands of contrasting geological formations. Applied Geochemistry 128, 104926.

Bruneel, Y., Van Laer, L., Brassinnes, S., Smolders, E., 2021b. Radiostrontium sorption on natural glauconite sands of the Neogene-Paleogene formations in Belgium. Journal of Environmental Radioactivity 233, 106588.

Chan, C.Y., 1992. Radioactive waste management: an international perspective. IAEA Bulletin 34, 7-15.

Ciesielski, H., Sterckeman, T., Santerne, M., Willery, J.P., 1997. Determination of cation exchange capacity and exchangeable cations in soils by means of cobalt hexamine trichloride. Effects of experimental conditions. Agronomie 17, 1-7.

Comans, R.N., Haller, M., De Preter, P., 1991. Sorption of cesium on illite: non-equilibrium behaviour and reversibility. Geochimica et Cosmochimica Acta 55, 433-440.

Comans, R.N., Hockley, D.E., 1992. Kinetics of cesium sorption on illite. Geochimica et Cosmochimica Acta 56, 1157-1164.

Courbe, C., Velde, B., Meunier, A., 1981. Weathering of glauconites: reversal of the glauconitization process in a soil profile in western France. Clay Minerals 16, 231-243.

Cremer, M., Schlocker, J., 1976. Lithium borate decomposition of rocks, minerals, and ores. American Mineralogist 61, 318-321.

Cremers, A., Elsen, A., Preter, P.D., Maes, A., 1988. Quantitative analysis of radiocaesium retention in soils. Nature 335, 247.

de Koning, A., Comans, R.N.J., 2004. Reversibility of radiocaesium sorption on illite. Geochimica et Cosmochimica Acta 68, 2815-2823.

De Koning, A., Konoplev, A., Comans, R., 2007. Measuring the specific caesium sorption capacity of soils, sediments and clay minerals. Applied geochemistry 22, 219-229.

De Pourcq, K., Ayora, C., García-Gutiérrez, M., Missana, T., Carrera, J., 2015. A clay permeable reactive barrier to remove Cs-137 from groundwater: column experiments. Journal of Environmental Radioactivity 149, 36-42.

de Preter, P., 1990. Radiocesium retention in the aquatic, terrestrial and urban environment: a quantitative and unifying analysis, Faculteit Landbouwwetenschappen. KULeuven, Leuven, p. 93.

de Preter, P., Vanloon, L., Maes, A., Cremers, A., 1991. Solid Liquid Distribution of Radiocesium in Boom Clay - A Quantitative Interpretation. Radiochimica Acta 52-3, 299-302.

Deckers, J., De Koninck, R., Bos, S., Broothaers, M., Dirix, K., Hambsch, L., Lagrou, D., Lanckacker, T., Matthijs, J., Rombaut, B., 2019. Geologisch (G3Dv3) en hydrogeologisch (H3D) 3D-lagenmodel van Vlaanderen.

Dohrmann, R., Kaufhold, S., 2009. Three new, quick CEC methods for determining the amounts of exchangeable calcium cations in calcareous clays. Clays and Clay Minerals 57, 338-352.

Drits, V., Sakharov, B., Lindgreen, H., Salyn, A., 1997. Sequential structure transformation of illite-smectite-vermiculite during diagenesis of Upper Jurassic shales from the North Sea and Denmark. Clay Minerals 32, 351-371.

Drits, V.A., Zviagina, B.B., McCarty, D.K., Salyn, A.L., 2010. Factors responsible for crystal-chemical variations in the solid solutions from illite to aluminoceladonite and from glauconite to celadonite. American Mineralogist 95, 348-361.

Durrant, B.C., Begg, J., Kersting, A., Zavarin, M., 2017. Cesium sorption reversibility and kinetics on illite, montmorillonite, and kaolinite. Science of the total environment 610-611, 511-520.

Dusar, M., Vandenberghe, N., 2020. Upper Oligocene lithostratigraphic units and the transition to the Miocene in North Belgium. Geologica Belgica.

Eberl, D.D., 1980. Alkali cation selectivity and fixation by clay minerals. Clays and Clay Minerals 28, 161-172.

Emmerich, K., Wolters, F., Kahr, G., Lagaly, G., 2009. Clay profiling: The classification of montmorillonites. Clays and Clay Minerals 57, 104-114.

Essa, M.A., Ahmed, E.A., Kurzweil, H., 2016. Genesis, maturity and weathering of some Upper Cretaceous Egyptian glauconites: Mineralogical and geochemical implications. Journal of African Earth Sciences 124, 427-446.

FANC, 2019. Oppervlakteberging in Dessel.

Favre, F., Bogdal, C., Gavillet, S., Stucki, J.W., 2006. Changes in the CEC of a soil smectite–kaolinite clay fraction as induced by structural iron reduction and iron coatings dissolution. Applied Clay Science 34, 95-104.

Ferrage, E., Lanson, B., Malikova, N., Plançon, A., Sakharov, B.A., Drits, V.A., 2005. New Insights on the Distribution of Interlayer Water in Bi-Hydrated Smectite from X-ray Diffraction Profile Modeling of 00l Reflections. Chemistry of Materials 17, 3499-3512.

Frederickx, L., 2020. An advanced mineralogical study of the clay mineral fraction of the Boom Clay, in: Leuven, K. (Ed.), Leuven.

Fritz, S.F., Popp, R.K., 1985. A single-dissolution technique for determining FeO and Fe 2 O 3 in rock and mineral samples. American Mineralogist 70, 961-968.

Fuller, A.J., Shaw, S., Peacock, C.L., Trivedi, D., Small, J.S., Abrahamsen, L.G., Burke, I.T., 2014. Ionic strength and pH dependent multi-site sorption of Cs onto a micaceous aquifer sediment. Applied Geochemistry 40, 32-42.

Fuller, A.J., Shaw, S., Ward, M.B., Haigh, S.J., Mosselmans, J.F.W., Peacock, C.L., Stackhouse, S., Dent, A.J., Trivedi, D., Burke, I.T., 2015. Caesium incorporation and retention in illite interlayers. Applied Clay Science 108, 128-134.

Gaudin, A., Buatier, M. D., Beaufort, D., Petit, S., Grauby, O., & Decarreau, A., 2005. Characterization and origin of Fe3+-montmorillonite in deep-water calcareous sediments (Pacific Ocean, Costa Rica margin). Clays and Clay Minerals 53.5, 452-465.

Goolaerts, S., De Ceuster, J., Mollen, F.H., Gijsen, B., Bosselaers, M., Lambert, O., Uchman, A., Van Herck, M., Adriaens, R., Houthuys, R., Louwye, S., BRUNEEL, Y., ELSEN, J., Hoedemakers, K., 2020. The upper Miocene Deurne Member of the Diest Formation revisited: unexpected results from the study of a large temporary outcrop near Antwerp International Airport, Belgium. Geologica Belgica 23 (2020).

Gorski, C.A., Aeschbacher, M., Soltermann, D., Voegelin, A., Baeyens, B., Marques Fernandes, M., Hofstetter, T.B., Sander, M., 2012. Redox properties of structural Fe in clay minerals. 1. Electrochemical quantification of electron-donating and-accepting capacities of smectites. Environmental science & technology 46, 9360-9368.

Hisashi, M., Kohei, S., Masato, I., Daigo, Y., Kazuki, I., 2013. Characterization of radiocaesium retention in Japanese soils. SCK-CEN; KULeuven, p. 17.

Huggett, J.M., McCarty, D. K., Calvert, C. C., Gale, A. S., & Kirk, C., 2006. Serpentine-nontronite-vermiculite mixed-layer clay from the Weches formation, Claiborne group, middle Eocene, northeast Texas. Clays and Clay Minerals 54.1, 101-115.

IAEA, 2009. Classification of Radioactive Waste. INTERNATIONAL ATOMIC ENERGY AGENCY, Vienna.

IAEA, 2011. Disposal of Radioactive Waste. INTERNATIONAL ATOMIC ENERGY AGENCY, Vienna.

IAEA, 2020. Development of a Common Framework for Addressing Climate and Environmental Change in Post-closure Radiological Assessment of Solid Radioactive Waste Disposal. INTERNATIONAL ATOMIC ENERGY AGENCY, Vienna.

Ishiwatari, N., Nagai, H., 1981. Release of xenon-137 and iodine-137 from UO2 pellet by pulse neutron irradiation at NSRR. Nippon Genshiryoku Gakkai-Shi 23, 843-850.

Ivanovskaya, T.A., Zviagina, B.B., Sakharov, B.A., Zaitseva, T.S., Pokrovskaya, E.V., Dorzhieva, O.V., 2015. Globular layer silicates of the glauconite–illite composition in Upper Proterozoic and Lower Cambrian rocks. Lithology and Mineral Resources 50, 452-477.

Jackson, M.L., 1975. Soil chemical analysis: Advanced course. UW-Madison Libraries Parallel Press.

Kelly, J.C., Webb, J.A., 1999. The genesis of glaucony in the Oligo–Miocene Torquay Group, southeastern Australia: petrographic and geochemical evidence. Sedimentary Geology 125, 99-114.

Khaled, E.M., Stucki, J.W., 1991. Iron oxidation state effects on cation fixation in smectites. Soil Science Society of America Journal 55, 550-554.

Kisiel, M., Skiba, M., Skoneczna, M., Maj-Szeliga, K., Błachowski, A., 2018. Weathering of glauconite in an alkaline environment — A case study from Krakow area, Poland. CATENA 171, 541-551.

Kobets, S.A., Fedorova, V.M., Pshinko, G.N., Kosorukov, A.A., Demchenko, V.Y., 2014. Effect of humic acids and iron hydroxides deposited on the surface of clay minerals on the 137Cs immobilization. Radiochemistry 56, 325-331.

Koning, A., Forrest, R., Kellett, M., Mills, R., Henriksson, H., Rugama, Y., Bersillon, O., Bouland, O., Courcelle, A., Duijvestijn, M., 2006. The jeff-3.1 nuclear data library-jeff report 21. Organisation for Economic Co-operation and Development.

Konoplev, A., Bulgakov, A., Popov, V., Bobovnikova, T.I., 1992. Behaviour of long-lived Chernobyl radionuclides in a soil–water system. Royal Society of Chemistry 117, 1041-1047.

Lee, J., Park, S.-M., Jeon, E.-K., Baek, K., 2017. Selective and irreversible adsorption mechanism of cesium on illite. Applied Geochemistry 85, 188-193.

Liu, C., Zachara, J.M., Smith, S.C., McKinley, J.P., Ainsworth, C.C., 2003. Desorption kinetics of radiocesium from subsurface sediments at Hanford Site, USA. Geochimica et Cosmochimica Acta 67, 2893-2912.

Liu, W., Sun, Z., Forsling, W., Du, Q., Tang, H., 1999. A Comparative Study of Surface Acid–Base Characteristics of Natural Illites from Different Origins. Journal of Colloid and Interface Science 219, 48-61.

Louwye, S., De Coninck, J., & Verniers, J. , 1999. Dinoflagellate cyst stratigraphy and depositional history of Miocene and Lower Pliocene formations in northern Belgium (southern North Sea Basin). Geologie en Mijnbouw 78.1, 31-46.

Louwye, S., De Schepper, S., 2010. The Miocene–Pliocene hiatus in the southern North Sea Basin (northern Belgium) revealed by dinoflagellate cysts. Geological Magazine 147, 760-776.

Louwye, S., De Schepper, S., Laga, P., Vandenberghe, N., 2006. The Upper Miocene of the southern North Sea Basin (northern Belgium): a palaeoenvironmental and stratigraphical reconstruction using dinoflagellate cysts. Geological Magazine 144, 33.

Madruga, M.J.B., 1993. Adsorption-desorption behaviour of radiocaesium and radiostrontium in sediments. KU Leuven.

Maes, N., Salah, S., Bruggeman, C., Aertsens, M., Martens, E., Van Laer, L., 2017. Strontium retention and migration behaviour in Boom Clay. SCK-CEN Studiecentrum voor Kernenergie.

Mann, C., Ferrand, K., Liu, S., Eskelsen, J.R., Pierce, E., Lemmens, K., Corkhill, C., 2019. Influence of young cement water on the corrosion of the International Simple Glass. npj Materials Degradation 3, 5.

Marcus, Y., 1994. A simple empirical model describing the thermodynamics of hydration of ions of widely varying charges, sizes, and shapes. Biophysical Chemistry 51, 111-127.

Mathieu, A., Kajino, M., Korsakissok, I., Périllat, R., Quélo, D., Quérel, A., Saunier, O., Sekiyama, T.T., Igarashi, Y., Didier, D., 2018. Fukushima Daiichi–derived radionuclides in the atmosphere, transport and deposition in Japan: A review. Applied Geochemistry 91, 122-139.

McCarty, D.K., Drits, V.A., Sakharov, B., Zviagina, B.B., Ruffell, A., Wach, G., 2004. Heterogeneous mixed-layer clays from the Cretaceous Greensand, Isle of Wight, southern England. Clays and Clay Minerals 52, 552-575.

Meier, L., Kahr, G., Lorenz, P., 1999. Determination of the cation exchange capacity (CEC) of clay minerals using the complexes of copper (II) ion with triethylenetetramine and tetraethylenepentamine. Clays and clay minerals 47, 386-388.

Merdun, H., 2012. Effects of Different Factors on Water Flow and Solute Transport Investigated by Time Domain Reflectometry in Sandy Clay Loam Field Soil. Water, Air & Soil Pollution 223, 4905-4923.

Merz, S., Shozugawa, K., Steinhauser, G., 2016. Effective and ecological half-lives of 90Sr and 137Cs observed in wheat and rice in Japan. Journal of Radioanalytical and Nuclear Chemistry 307, 1807-1810.

Meunier, A., 2005. Clays. Springer Science & Business Media.

Meunier, A., and Bruce D. Velde, 2013. Illite: Origins, evolution and metamorphism. Springer Science & Business Media.

Meunier, A., El Albani, A., 2007. The glauconite?Fe-illite?Fe-smectite problem: a critical review. Terra Nova 19, 95-104.

Millero, F.J., Feistel, R., Wright, D.G., McDougall, T.J., 2008. The composition of Standard Seawater and the definition of the Reference-Composition Salinity Scale. Deep Sea Research Part I: Oceanographic Research Papers 55, 50-72.

Missana, T., Benedicto, A., García-Gutiérrez, M., Alonso, U., 2014a. Modeling cesium retention onto Na-, K- and Ca-smectite: Effects of ionic strength, exchange and competing cations on the determination of selectivity coefficients. Geochimica et Cosmochimica Acta 128, 266-277.

Missana, T., Garcia-Gutierrez, M., Alonso, U., 2008. Sorption of strontium onto illite/smectite mixed clays. Physics and Chemistry of the Earth 33, S156-S162.

Missana, T., García-Gutiérrez, M., Benedicto, A., Ayora, C., De-Pourcq, K., 2014b. Modelling of Cs sorption in natural mixed-clays and the effects of ion competition. Applied Geochemistry 49, 95-102.

Moore, D.M., Reynolds, R.C., 1997. X-ray diffraction and the identification and analysis of clay minerals, 2nd ed. ed. Oxford : Oxford university press.

Nakao, A., Funakawa, S., Tsukada, H., Kosaki, T., 2012. The fate of caesium-137 in a soil environment controlled by immobilization on clay minerals. SANSAI: An Environmental Journal for the Global Community 6, 17-29.

Nakao, A., Thiry, Y., Funakawa, S., Kosaki, T., 2008. Characterization of the frayed edge site of micaceous minerals in soil clays influenced by different pedogenetic conditions in Japan and northern Thailand. Soil Science and Plant Nutrition 54, 479-489.

NIRAS, 2010. Het cAt-project in Dessel: Een langetermijnoplossing voor het Belgische categorie A-afval.

NIRAS, 2019a. Hoofdstuk 4 - Karakteristieken van de site en haar omgeving, Veiligheidsrapport voor de oppervlaktebergingsinrichting van categorie A-afval in Dessel, Brussel.

NIRAS, 2019b. Hoofdstuk 6 - Afval, Veiligheidsrapport voor de oppervlaktebergingsinrichting van categorie A-afval in Dessel, Brussel.

Odin, G., 1988. Green marine clays. Developments in Sedimentology 45, 1-444.

Odin, G.S., & Gale, N. H., 1982. Some fundamental considerations in the dating of glauconies: a comment on "A test of the reliability of RbSr dates for selected glauconite morphologies of the upper cretaceous (Navesink formation) of New Jersey", by RL Montag and DE Seidemann. Earth and Planetary Science Letters 58.3, 443-445.

Odin, G.S., and Albert Matter, 1981. De glauconiarum origine. Sedimentology 28.5, 611-641.

Ogasawara, S., Nakao, A., Yanai, J., 2013. Radiocesium interception potential (RIP) of smectite and kaolin reference minerals containing illite (micaceous mineral) as impurity. Soil Science and Plant Nutrition 59, 852-857.

Okumura, M., Kerisit, S., Bourg, I.C., Lammers, L.N., Ikeda, T., Sassi, M., Rosso, K.M., Machida, M., 2018. Radiocesium interaction with clay minerals: Theory and simulation advances Post–Fukushima. Journal of Environmental Radioactivity 189, 135-145.

ONDRAF/NIRAS, 2020. Milieueffectenrapport (Strategic Environmental Assessment–SEA) voor het voorontwerp van koninklijk besluit tot vaststellingvan het goedkeuringsproces voor de nationale beleidsmaatregelenmet betrekking tot het langetermijnbeheer van geconditioneerd hoogradioactief en/of langlevend afval en tot bepalingvan de beheeroplossing op lange termijn voor dit afval. Nationale instelling voor radioactief afval en verrijkte splijtstoffen.

Parkhurst, D.L., Appelo, C., 1999. User's guide to PHREEQC (Version 2): A computer program for speciation, batch-reaction, one-dimensional transport, and inverse geochemical calculations. Water Resources Investigations Report 99, 312.

Pestitschek, B., Gier, S., Essa, M., Kurzweil, H., 2012. Effects of weathering on glauconite: Evidence from the Abu Tartur plateau, Egypt. Clays and Clay Minerals 60, 76-88.

Poinssot, C., Baeyens, B., Bradbury, M.H., 1999a. Experimental and modelling studies of caesium sorption on illite. Geochimica et Cosmochimica Acta 63, 3217-3227.

Poinssot, C., Baeyens, B., Bradbury, M.H., 1999b. Experimental Studies of Cs, Sr, Ni and Eu Sorption on Na-illite and the Modelling of Cs Sorption. Paul Scherrer Institut (PSI), Villigen.

Programma, C.v.h.N., 2015. Nationaal programma voor het beheer van verbruikte splijtstoffen en radioactief afval, in: FOD Economie, M.e.E.N.S. (Ed.), Brussel.

Pugliese Andrade, G.R., de Azevedo, A.C., Cuadros, J., Souza Jr., V.S., Correia Furquim, S.A., Kiyohara, P.K., Vidal-Torrado, P., 2014. Transformation of Kaolinite into Smectite and Iron-Illite in Brazilian Mangrove Soils. Soil Science Society of America Journal 78, 655-672.

Rogiers, B., Labat, S., Gedeon, M., 2015. An assessment of dilution tests and ambient temperature logging for quantifying groundwater flow in the Neogene aquifer. SCK-CEN Studiecentrum voor Kernenergie.

Sawhiney, B., 1972. Selective sorption and fixation of cations by clay minerals: a review. Clays and Clay Minerals
20.

Sawhney, B., 1972. Selective sorption and fixation of cations by clay minerals: a review. Clays and Clay Minerals 20.

Sawhney, B.L., 1970. Potassium and Cesium Ion Selectivity in Relation to Clay Mineral Structure. Clays and Clay Minerals 18, 47-52.

Semenishchev, V.S., Ryabukhina, V.G., Voronina, A.V., Mashkovtsev, M.A., Nikiforov, A.F., 2016. The study of selectivity of caesium sorption by a natural and surface-modified glauconite in presence of potassium and ammonium ions. Journal of Radioanalytical and Nuclear Chemistry 309, 583-588.

Shapiro, L., 1960. A spectrophotometric method for the determination of FeO in rocks. US Geological Survey Professional Papers 400, 496-497.

Šimůnek, J., Van Genuchten, M.T., Sejna, M., 2005. The HYDRUS-1D software package for simulating the one-dimensional movement of water, heat, and multiple solutes in variably-saturated media. University of California-Riverside Research Reports 3, 1-240.

Simunek, J., Van Genuchten, M.T., Sejna, M., Toride, N., Leij, F., 1999. The STANMOD computer software for evaluating solute transport in porous media using analytical solutions of convection-dispersion equation. Versions 1.0 and 2.0. US Salinity Laboratory, USDA ARS: Riverside, CA, USA.

Sips, R., 1948. On the structure of a catalyst surface. Journal of Chemical Physics 16, 490-495.

Środoń, J., Drits, V.A., McCarty, D.K., Hsieh, J.C., Eberl, D.D., 2001 Quantitative X-ray diffraction analysis of clay-bearing rocks from random preparations. Clays and Clay Minerals 49, 514-528.

Staunton, S., Roubaud, M., 1997. Adsorption of Cs-137 on montmorillonite and illite: Effect of charge compensating cation, ionic strength, concentration of Cs, K and fulvic acid. Clays and Clay Minerals 45, 251-260.

Stucki, J.W., Low, P.F., Roth, C.B., Golden, D., 1984. Effects of oxidation state of octahedral iron on clay swelling. Clays and Clay Minerals 32, 357-362.

Stumm, W., Morgan, J.J., Drever, J.I., 1996. Aquatic chemistry. Journal of Environmental Quality 25, 1162.

Suhr, N.H., Ingamells, C.O., 1966. Solution Technique for the Analysis of Silicates. Analytical Chemistry 38, 730-734.

Szenknect, S., Gaudet, J., Dewiere, L., 2003. Evaluation of distribution coefficients for the prediction of strontium and cesium migration in a natural sand at different water contents, Journal de Physique IV (Proceedings). EDP sciences, pp. 1279-1282.

Takeno, N., 2005. Atlas of Eh-pH diagrams. Geological survey of Japan open file report 419, 102.

Tansel, B., 2012. Significance of thermodynamic and physical characteristics on permeation of ions during membrane separation: Hydrated radius, hydration free energy and viscous effects. Separation and Purification Technology 86, 119-126.

Valcke, E., 1993. the behaviour dynamics of radiocesium and radiostrontium in soils rich in organic matter, Faculteit landbouwkundige en toegepaste biologische wetenschappen. KULeuven, Leuven, p. 135.

Valcke, E., Cremers, A., Moskaltchuk, L., 1998. The use of sapropels as amendments in radiocaesium and radiostrontium contaminated soils. Applied Geochemistry 13, 155-164.

Valocchi, A.J., 1985. Validity of the local equilibrium assumption for modeling sorbing solute transport through homogeneous soils. Water Resources Research 21, 808-820.

Van Genuchten, M.T., Šimunek, J., Leij, F., Toride, N., Šejna, M., 2012. STANMOD: Model use, calibration, and validation. Transactions of the ASABE 55, 1355-1366.

Van Ranst, E., De Coninck, F., 1983. Evolution of glauconite in imperfectly drained sandy soils of the Belgian Campine. Journal of Plant Nutrition and Soil Science 146, 415-426.

Vandenberghe, N., De Craen, M., Beerten, K., 2014. Geological framework of the Campine Basin. Geological setting, tectonics, sedimentary sequences. SCK•CEN - Studiecentrum voor Kernenergie/Centre d'Etude de l'Energie Nucléaire.

Vandenberghe, N., et al., 2014. The implications of K-Ar glauconite dating of the Diest Formation on the paleogeography of the Upper Miocene in Belgium. Geologica Belgica 17.2, 161-174.

Vandenberghe, N., Van Simaeys, S., Steurbaut, E., Jagt, J. W. M., & Felder, P. J., 2004. Stratigraphic architecture of the Upper Cretaceous and Cenozoic along the southern border of the North Sea Basin in Belgium. Netherlands Journal of Geosciences 83, 155-171.

Vandenberghe, N.L., P., 1996. De aarde als fundament. Een inleiding tot de geologie van de ingenieurs.

Voronina, A.V., Blinova, M.O., Kulyaeva, I.O., Sanin, P.Y., Semenishchev, V.S., Afonin, Y.D., 2015a. Sorption of cesium radionuclides from aqueous solutions onto natural and modified aluminosilicates. Radiochemistry 57, 522-529.

Voronina, A.V., Blinova, M.O., Semenishchev, V.S., Gupta, D.K., 2015b. Returning land contaminated as a result of radiation accidents to farming use. Journal of Environmental Radioactivity 144, 103-112.

Voronina, A.V., Semenishchev, V.S., Bykov, A.A., Savchenko, M.O., Kutergin, A.S., Nedobuh, T.A., 2013. Approaches to rehabilitation of radioactive contaminated territories. Journal of Chemical Technology & Biotechnology 88, 1606-1611.

Wallace, S.H., Shaw, S., Morris, K., Small, J.S., Fuller, A.J., Burke, I.T., 2012. Effect of groundwater pH and ionic strength on strontium sorption in aquifer sediments: Implications for 90Sr mobility at contaminated nuclear sites. Applied Geochemistry 27, 1482-1491.

Wang, T.-H., Li, M.-H., Teng, S.-P., 2009. Bridging the gap between batch and column experiments: A case study of Cs adsorption on granite. Journal of Hazardous Materials 161, 409-415.

Wauters, J., Cremers, A., 1996. Effect of particle concentration and fixation on radiocesium sorption. Environmental Science & Technology 30, 2892.

Wauters, J., Elsen, A., Cremers, A., Konoplev, A., Bulgakov, A., Comans, R., 1996a. Prediction of solid/liquid distribution coefficients of radiocaesium in soils and sediments. Part one: a simplified procedure for the solid phase characterisation. Applied Geochemistry 11, 589-594.

Wauters, J., Sweeck, L., Valcke, E., Elsen, A., Cremers, A., 1994. Availability of radiocaesium in soils: a new methodology. Science of the Total Environment 157, 239-248.

Wauters, J., Vidal, M., Elsen, A., Cremers, A., 1996b. Prediction of solid/liquid distribution coefficients of radiocaesium in soils and sediments. Part two: a new procedure for solid phase speciation of radiocaesium. Applied geochemistry 11, 595-599.

Wu, J., Low, P., Roth, C., 1989. Effects of octahedral-iron reduction and swelling pressure on interlayer distances in Na-nontronite. Clays and Clay Minerals 37, 211-218.

Zeelmaekers, E., 2011. Computerized qualitative and quantitative clay mineralogy: introduction and application to known geological cases. Leuven : K.U.Leuven. Faculteit Wetenschappen.

# Annex

# A1. Glauconite sand characterisation

## Sample selection

For this study a set of subsurface samples (from drilling cores) and surface samples (collected in quarries and outcrops) was selected. All of the collected samples are unconsolidated glauconite sands with variable glauconite contents. The subsurface samples represent the glauconite sands in its current state. Subsurface samples were selected from the Kasterlee Fm, Diest Fm, Berchem Fm and Voort Fm (Table A1.1).

Table A1.1 Subsurface glauconite sands used in this work. The glauconite sands originate from several cores (ON-Dessel-3, ON-Dessel-5, ON-Mol-1) and from the excavation of the second shaft to the underground research lab Hades.

| Sample | Formation | Sample origin | Core nr | Depth in core | Depth mTAW |
|---|---|---|---|---|---|
| K1 | kasterlee | ON-Dessel-3 | 20 | -20.0 | 3.6 |
| D1 | diest | Hades Shaft | X | -98.7 | -72.8 |
| D6 | diest | Hades Shaft | X | -104.0 | -78.1 |
| D7 | diest | Hades Shaft | X | -109.0 | -83.1 |
| D2 | diest | Hades Shaft | X | -116.6 | -90.7 |
| D3 | diest | ON-Dessel-5 | 30 | -117.0 | -91.8 |
| D9 | diest | Hades Shaft | X | -127.0 | -101.1 |
| D4 | dessel | ON-Dessel-5 | 44 | -134.0 | -108.8 |
| D5 | dessel | ON-Dessel-5 | 48 | -138.0 | -112.8 |
| B1 | berchem | ON-Dessel-5 | 63 | -151.0 | -125.8 |
| B3 | berchem | ON-Mol-1 | 14 | -163.3 | -133.6 |
| B2 | berchem | Hades Shaft | X | -160.0 | -134.1 |
| V7 | voort | Hades Shaft | X | -163.6 | -137.7 |
| V3 | voort | Hades Shaft | X | -166.0 | -140.1 |
| V5 | voort | Hades Shaft | X | -167.0 | -141.1 |
| V4 | voort | ON-Mol-1 | 24 | -173.6 | -143.9 |
| V1 | voort | Hades Shaft | X | -170.0 | -144.1 |
| V8 | voort | Hades Shaft | X | -171.0 | -145.1 |
| V6 | voort | Hades Shaft | X | -173.0 | -147.1 |
| V9 | voort | Hades Shaft | X | -174.3 | -148.4 |
| V2 | voort | Hades Shaft | X | -178.0 | -152.1 |

Due to a dip to the east, the Neogene formations have outcrops at the surface. The surface samples are subjected to the elements in natural outcrops and quarries (Table A1.2). These naturally weathered samples were selected to test the effect of weathering of the glauconite sands. Samples of the Diest Fm sands were collected in Wezemaal, at the Wijngaardberg and Beniksberg, and in Lubbeek in the Zavelstraat (Figure A1.1). At the Wienerberger quarry in Rumst samples were taken from the green sands above the Boom Clay, part of the Berchem Formation.

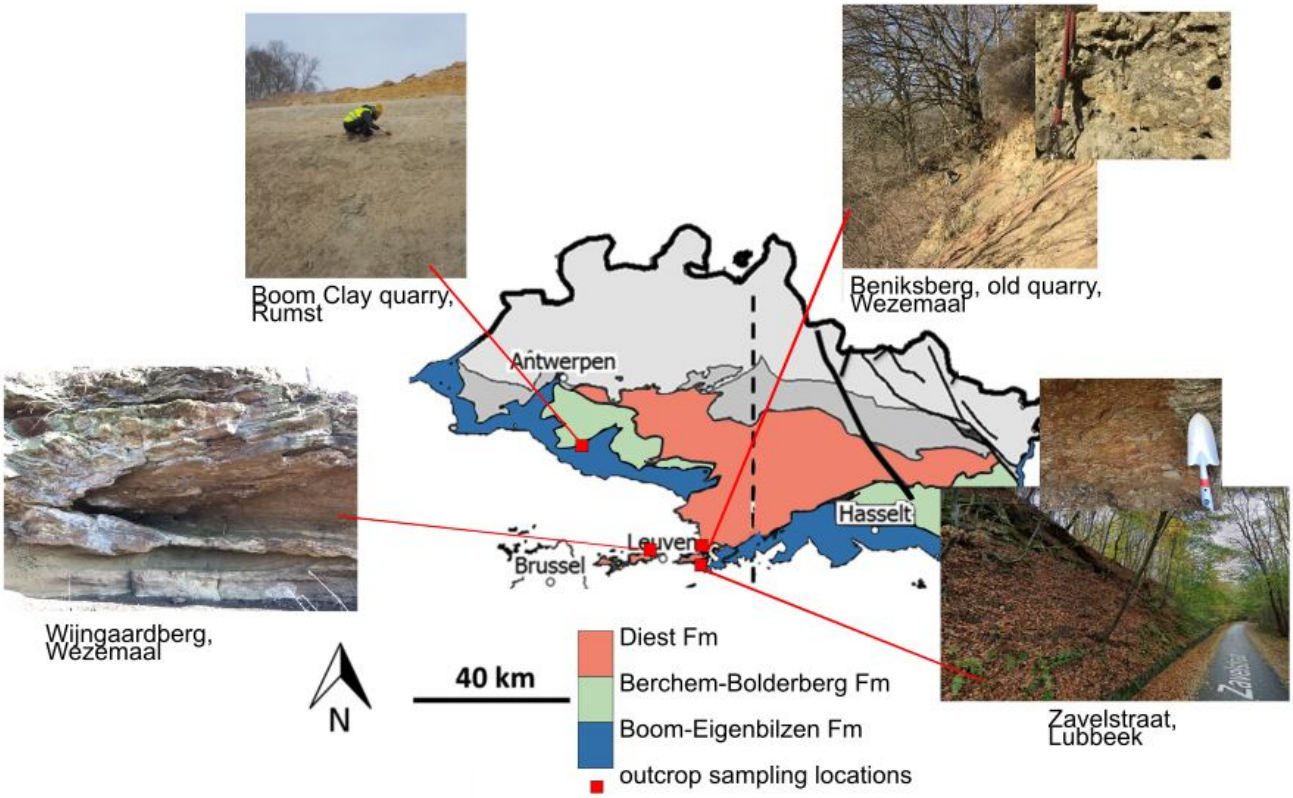


Figure A1.1 Sampling locations of the surface sands. Four sampling locations were selected based on the available outcrops of glauconite sands.

At the outcrop sites of the Wijngaardberg and Zavelstraat cemented iron sandstone bands alternated with unconsolidated glauconite sands. The glauconite sand is strongly oxidised at the surface. Removing the top cm reveals green glauconite sands. Samples were taken both from the top layer, most oxidised and from 10 cm below the surface, below the visible oxidation. The glauconite sand at the (unactive) quarry at the Beniksberg is strongly bioturbised and does not have any iron sandstone concretions. The signs of weathering are less outspoken at the last sampling location, the Boom Clay quarry of Wienerberger in Rumst. The green sand deposit on top of the Boom Clay Formation was sampled, most likely part of the Berchem Fm. The sand contains a lot of shells (molluscs) and the glauconite content decreases towards the top. At the top a fine gravel deposit with shark teeth is present.

Table A1.2 Surface sands collected in March and April 2018 in the region around Leuven (Wijngaardberg, Beniksberg and Zavelstraat) and from the Wienerberger quarry in Rumst.

| Sample | Formation | Location | Depth mTAW | Description |
|---|---|---|---|---|
| W1 | Diest | wijngaardberg, wezemaal | 55.0 | N-side of the Wijngaardberg, under the oxidised top layer |
| W2 | Diest | wijngaardberg, wezemaal | 55.0 | N-side of the Wijngaardberg, top glauconite sand |
| W3 | Diest | wijngaardberg, wezemaal | 51.0 | S-side, of the Wijngaardberg, top glauconite sand |
| W4 | Diest | wijngaardberg, wezemaal | 50.5 | S-side of the Wijngaardberg, under the oxidised top layer |
| W5 | Diest | beniksberg, Wezemaal | 44.0 | Old quarry |
| W6 | Diest | beniksberg, Wezemaal | 44.0 | Old quarry |
| W7 | Diest | beniksberg, Wezemaal | 44.5 | Old quarry |
| W8 | Diest | beniksberg, Wezemaal | 44.5 | Old quarry |
| W9 | Diest | beniksberg, Wezemaal | 45.0 | Old quarry |
| W10 | Diest | zavelstraat, Lubbeek | 56.0 | Hollow road |
| W11 | Diest | zavelstraat, Lubbeek | 56.0 | Hollow road |
| W12 | Berchem | Wienerberger, Rumst | 25.5 | Shell rich sand, dry material |
| W13 | Berchem | Wienerberger, Rumst | 25.5 | Shell rich sand, frozen block of sand |
| W14 | Berchem | Wienerberger, Rumst | 25.5 | Shell rich sand |
| W15 | Berchem | Wienerberger, Rumst | 27.0 | green sand, surface material |
| W16 | Berchem | Wienerberger, Rumst | 26.5 | green sand, below possibly oxidised layer (10 cm under surface) |
| W17 | Berchem | Wienerberger, Rumst | 26.0 | green-brown sand, W15 and W16 |
| W18 | Berchem | Wienerberger, Rumst | 28.0 | green sand, just below the gravel layer known for the presence of shark teeth. |

A smaller subset of samples came from the glauconite collection of R. Adriaens (Table A1.3). These samples originate mostly from the Diest Fm, except for B4 – Berchem Fm. The samples have been analysed (mineralogy) for the PhD of R. Adriaens (2015). Only the glauconite fractions of the samples were available.

Table A1.3 Glauconite fractions received from R. Adriaens from several Neogene formations. The samples were collected and analysed in the framework of the PhD of R. Adriaens (Adriaens, 2015).

| Sample | Sample nr PhD Adriaens | Formation | Sample origin | Depth in core (m) |
|---|---|---|---|---|
| D8 | RAT217 | Diest | ON-Dessel-5 | -110.3 |
| D10 | RAT219 | Diest | ON-Dessel-5 | -134.25 |
| B4 | RAT223 | Berchem | ON-Dessel-5 | -165.5 |
| D11 | RAT282 | Diest | Boring Put 8_PIDPA | 48-52 |
| D12 | RAT283 | Diest | Boring Put 8_PIDPA | 52-56 |
| D13 | RAT285 | Diest | Boring Put 8_PIDPA | 60-64 |
| D14 | RAT294 | Diest | Boring Put 8_PIDPA | 96-100 |
| D15 | RAT296 | Diest | Boring Put 8_PIDPA | 104-108 |
| D16 | RAT297 | Diest | Boring Put 8_PIDPA | 108-112 |

## Optical microscopy

The glauconite sands were studied under the microscope, both loose grains, and inbedded grains in the form of thin sections. Thin sections allow to study a grain inside and outside. Especially in the case of glauconite this is interesting, mainly because of weathering. Weathering can be visualised by the color of the pellets. High K glauconites have a dark green color. When the potassium content decreases, the color becomes lighter. Pellets that are coated in iron oxides have a more yellow to rusty appearance. Additionally, thin sections can be used to study the morphology and internal structure of the pellets; do they consist of several fragments, are they rounded/angular, etc. An important question is how the cracks run through the globular pellets and how they relate to the weathering. For these thin sections, separated glauconite fractions were used. The sands were washed with demineralised water and sieved into fractions > 250 µm, 250 – 150 µm, 150 – 32 µm and < 32 µm. After sieving the fractions were dried at 60°C overnight. Glauconite pellets, separated from the fraction by magnetic separation, were mixed with a polyurethane powder and pressed into pellets. Thin sections were made by Herman Nijs (KULeuven). The images were taken with a standard optical microscope with transmitted light and an optional polarizer. An extra light source was added to create strong reflections on the iron oxides allowing identification of pyrite (incident light).

There are some general trends that can be observed with increasing depth in the Neogene sediments.

- Grain size: There is a large scale coarsening upwards sequence over the Voort, Berchem to Diest formations. In the Diest formations nearly all pellets have an average diameter between 200-500 µm and a globular habitus. Towards the Berchem formation a smaller glauconite size fraction (< 200 µm, average 100 µm) appears with more angular habitus. Both fractions can be separarted by sieving. Globular glauconite is only present in the fractions >250 µm, the angular glauconite <200 µm. In the Voort formation the globular fraction has almost completely disappeared (Figure A1.2).
- Color: The color refers roughly to the potassium content in the pellets, the darker the grain, the higher the K content. In the Diest formation samples there is a larger color variation/range in the pellets. Towards the deeper formations the color becomes more uniform. The Berchem formation has the darkest green grains.
- Weathering: the indications of weathering change with increasing depth. Only in the Diest formation iron oxide coats and fully oxidised pellets are present. Below the Diest formation weathering is present as pitting and lighter colored grain rims (Figure A1.3).

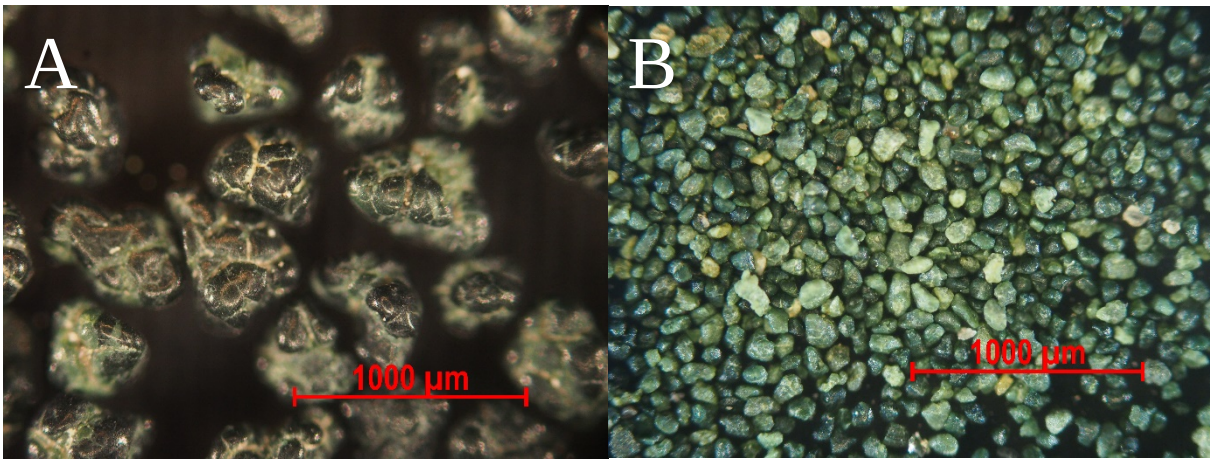


Figure A1.2 Microscopy images taken with incident light. A. the glauconite fraction > 500 µm of samples GLY001 (Berchem Fm) with a globular habitus and dark green colour. B. glauconite fraction of the GLY003 sample (Voort Fm). Fine lighter green pellets with a more (sub) angular habitus.

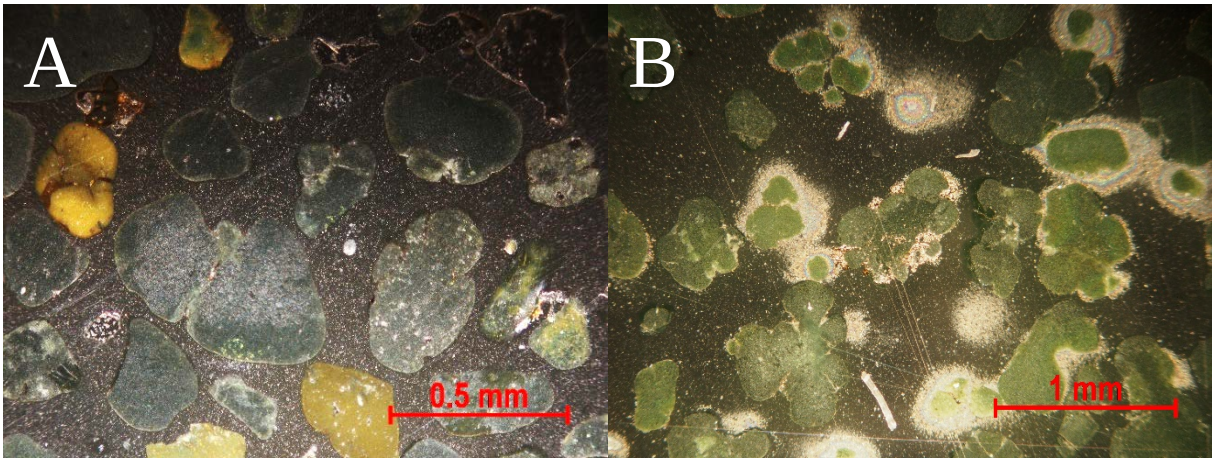


Figure A1.3 Microscopy images of thin sections (incident and transmitted light, with polarizer). A. GLY002 (Diest Fm) both oxidised and (optically) unweathered grains are present in the same sample. B. No oxidised grains in the GLY001 sample (Berchem Fm) instead framboidal pyrite and pyrite clusters are present.

## Pore water

The pore water composition was determined in order to understand the in-situ conditions for sorption of both $^{137}Cs$ and $^{90}Sr$ in the Paleogene and Neogene glauconite sands. The samples originating from the excavation of the second shaft to HADES have been vacuum packed and stored in the freezer since the sampling in 1998. The samples of the ON-Dessel-5, ON-Dessel-3 and ON-Mol-1 core have been stored vacuum packed in the core library of NIRAS. All vacuum packed samples still contain pore water that can be extracted. However, in the samples of the cores some of the pore water appears to have evaporated. The partial evaporation of the pore solution will cause an increase in the ionic strength. In addition to pore water extracts, water was collected in monitoring wells in the area of Mol (26$^{th}$ of April 2017). Seven wells were selected with filters at representative depth in each of the investigated formations (Mol, Kasterlee, Diest, Berchem and Voort Fm).

**Method**

Standard pore water extraction from clay formations is done by squeezing. For sand samples this has little success due to the lower compressibility. A double chamber centrifugation technique was used to extract pore water from the sands. Samples were centrifuged for 30 min on 3000 RCF and immediately acidified with 1% $HNO_3$. To ensure particle free pore water for ICP-MS measurement a chromafil Xtra PET 45/25 filter was used. For the extraction of the aquifer waters, the well volume was pumped three times out before collecting a sample to ensure the water was not affected by standing still in the well. To prevent oxidation the waters were acidified with 1% $HNO_3$ in the field and stored in the fridge.

**Results**

The major element composition of the pore water extracts and the aquifer solutions are given in respectively Table A1.4 and Table A1.5. The aquifers at shallow depths are more sensitive to anthropogenic influences. Most sensitive is the aquifer water in the Mol formation filter, positioned only 10 m below the surface (at +16 mTAW). One of the key elements implying anthropogenic influence is sodium (Na). However, in the waters of the Mol formation the concentration is in the range of average groundwater composition. The potassium content ranges from 0.14 to 0.37 mM, below the 0.5 mM concentration used in the $^{137}Cs$ sorption batch experiments. The total Fe and zinc (Zn) content are higher than expected. Concentrations in this range are not standard for groundwaters unless large amounts of iron oxides or iron rich minerals are present in the aquifer. Due to the reducing conditions in water saturated sediments and aquifers, $Fe^{3+}$ is reduced to the more soluble $Fe^{2+}$. In these systems the iron is dissolved from the sediment, from glauconite, and transported with the groundwater. Upon surfacing the iron oxidizes and precipitates on the river bedding (e.g. the Nete river, average 1-10 mg/l Fe in the streams, fed by groundwater containing up to 20 mg/l Fe ).

Table A1.4 Major element composition of the pore water extracts.

| Depth (mTAW) | Sample | Na | Mg | K | Ca | Sr | Al | Fe | Mn | Zn |
|---|---|---|---|---|---|---|---|---|---|---|
| | | mM | | | | µM | | | | |
| -73 | D1 | 0.36 | 0.60 | 1.2 | 2.3 | 3.4 | 3.1 | 5.2 | 0.05 | 0.08 |
| -91 | D2 | 0.55 | 8.4 | 5.2 | 16 | 45 | 1.1 | 0.55 | 0.75 | 0.06 |
| -95 | D3 | 0.69 | 8.5 | 5.4 | 16 | 64 | 0.97 | 0.59 | 0.99 | 0.07 |
| -109 | D4 | 3.2 | 14 | 10 | 14 | 77 | 1.2 | 0.99 | 3.3 | 15 |
| -113 | D5 | 3.6 | 3.1 | 3.9 | 3.7 | 21 | 2.4 | 1.3 | 0.26 | 0.10 |
| -126 | B1 | 18 | 13 | 8.9 | 14 | 83 | 2.1 | 1.6 | 0.10 | 0.38 |
| -134 | B2 | 21 | 6.7 | 6.5 | 6.2 | 41 | 3.0 | 1.2 | 0.21 | 0.43 |
| -144 | V1 | 29 | 11 | 6.5 | 12 | 71 | 5.1 | 1.5 | 0.94 | 0.24 |
| -152 | V2 | 41 | 11 | 6.8 | 15 | 85 | 8.2 | 2.0 | 1.4 | 0.97 |

The concentration of the major elements in the pore waters is significantly higher than the concentrations measured in the aquifer waters pumped out of the Berchem and Voort formation filters. The major element concentrations increase towards the Berchem formations and decrease towards the Voort

formation. The concentrations used in the batch sorption experiments (0.5 mM K, 100 mM Ca) are exceeded in all pore water samples, with a maximum concentration of 7.1 mM K reached in the Voort formation sample (GLY003, -144 mTAW). Subsample analysis of that Voort formation sample revealed concentrations in the same range (6.5 to 7.2 mM).

Table A1.5 Major element composition of the aquifer solutions.

| Depth (mTAW) | Sample | Na | Mg | K | Ca | Sr | Al | Fe | Mn | Zn |
|---|---|---|---|---|---|---|---|---|---|---|
| | | | | mM | | | | µM | | |
| 16 | Mol | 1.6 | 0.38 | 0.18 | 1.7 | 2.2 | 0.68 | 11 | 130 | 5.2 |
| 1 | Kasterlee | 0.94 | 0.13 | 0.37 | 1.2 | 2.1 | 2.8 | 59 | 53 | 5.6 |
| -43 | Diest 1 | 0.71 | 0.23 | 0.22 | 0.83 | 1.4 | 0.32 | 180 | 150 | 7.3 |
| -101 | Diest 2 | 0.48 | 0.46 | 0.28 | 0.75 | 2.3 | 0.47 | 29 | 32 | 5.2 |
| -128 | Berchem 1 | 2.4 | 0.18 | 0.26 | 0.35 | 0.89 | 0.63 | 7.8 | 41 | 5.2 |
| -154 | Berchem 2 | 2.2 | 0.24 | 0.34 | 0.30 | 1.1 | 0.72 | 4.8 | 53 | 5.2 |
| -294 | Voort | 0.64 | 0.14 | 0.14 | 0.97 | 1.3 | 0.57 | 160 | 500 | 5.4 |

## XRD analysis

Powder X-ray diffraction analysis was used to determine the glauconite content and the total clay content of the glauconite sand. For the identification of the clay minerals clay slides were made from the < 2 µm fraction. The X-ray diffraction scans were measured using a Phillips PW1830 diffractometer with Copper (Cu) Kα radiation at 30 mA and 45 kV using a graphite monochromator and a scintillation detector. The diffractometer scans were recorded in Bragg-Brentano geometry, 5 to 65 º for bulk measurements and 2 to 47 º for clay measurements, each time with a step size of 0.02 º and 2 s counting time per step.

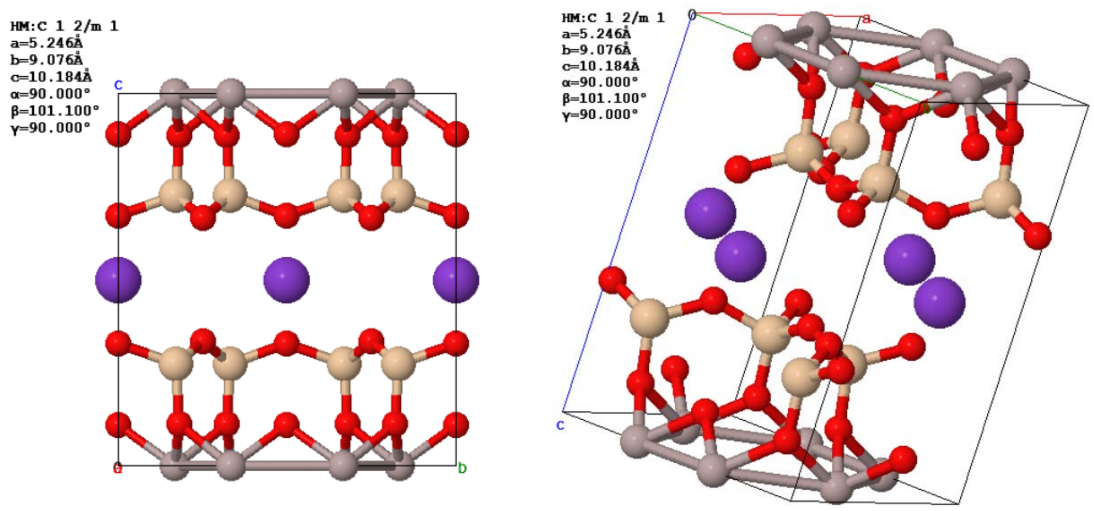


Figure A1.4 Prototype of the structure of glauconite based on the refined crystallographic data of a glauconite from the Baltic region, Russia, by Drits et al. (2010).

There are a lot of similarities between glauconite and illite also on a crystallographic level. A prototype of the glauconite structure is given in Figure A1.4. Glauconite and illite both have strong reflections at 10 Å (001) and 3.33 Å (003). The intensity ratio of the 001/003 is higher for glauconite, however, the strongest difference is in the weak 002 reflection at 5Å.

One of the components that can strongly influence the quality of the quantification is the amorphous content. Amorphous phases in mixtures are difficult to recognize below 15 wt%, especially if the mixture contains phases with high peak intensities (e.g. quartz). The tell-tale for the presence of amorphous material is a 'hump' or broad low intensity peak in the pattern. This hump was not observed in any of the patterns. The results of the mineralogical analyses of the Neogene glauconite by Adriaens (2020, 2014) also did not contain amorphous phases.

Originally we intended to do an extensive mineralogical analysis of the glauconite sands, fractions and clay mineralogy. However, due to the relatively small differences in sorption potential for $^{137}Cs$ and $^{90}Sr$ among the sands, only a limited mineralogical analysis was performed. The composition of the bulk, the complete glauconite sand, was determined for all glauconite sands in this study. The quantification of these sands resulted in the total glauconite content and total clay mineral content. A smaller subset of samples was prepared with the Jackson treatment for detailed clay mineral analysis (< 2 µm).

Table A1.6 Quantification results of the bulk XRD analysis of the (complete) glauconite sands. The pattern analysis was performed with Quanta.

| | | | | calcite, siderite, ankerite | | Di 1:1 kaolite dickite halloysite nacrite | Di 2:1 Smectite, bentonite, illite-smectite, montmorillonite | Illite, glauconite, nontronite, Fe-smectite | | Tri 2:1 Vermiculite, saponite, biotite, phlogopite, hectorite, talc | | |
|---|---|---|---|---|---|---|---|---|---|---|---|---|
| | Quartz | K-feldspar | Plagioclase | Carbonate | Pyrite | Kaolinite | 2:1 Al Clay | 2:1 Fe Clay | Fe-Chlorite | Tri 2:1 Clay | Muscovite | Total clay |
| K1 | 92 | 2 | 0 | 0 | 0 | 0 | 0 | 3 | 0 | 0 | 2 | 5 |
| D1 | 59 | 5 | 0 | 1 | 0 | 0 | 0 | 34 | 0 | 0 | 0 | 34 |
| D2 | 60 | 8 | 0 | 0 | 0.2 | 0.9 | 0 | 27 | 0 | 0 | 3 | 31 |
| D3 | 64 | 6 | 1 | 1 | 0 | 0.8 | 2 | 24 | 0 | 0 | 0 | 27 |
| D4 | 64 | 10 | 0.9 | 0 | 0.5 | 2 | 1 | 23 | 0 | 0 | 0 | 25 |
| D5 | 57 | 6 | 2 | 2 | 0.1 | 1 | 2 | 30 | 0 | 0 | 0 | 34 |
| D6 | 56 | 4 | 0 | 2 | 0.2 | 0.9 | 0 | 33 | 0 | 0 | 3 | 37 |
| D7 | 61 | 4 | 2 | 0 | 0.2 | 0 | 2 | 30 | 0 | 0 | 0 | 32 |
| D9 | 71 | 5 | 3 | 0 | 0 | 0 | 0 | 18 | 0 | 0 | 0.9 | 19 |
| B1 | 8 | 0 | 1 | 0 | 0.3 | 0 | 0 | 89 | 0 | 0 | 0 | 89 |
| B2 | 56 | 9 | 3 | 0.3 | 0.2 | 0 | 0 | 27 | 0 | 0 | 5 | 32 |
| B3 | 54 | 6 | 3 | 5 | 0.7 | 4 | 4 | 15 | 0 | 2 | 5 | 31 |
| V1 | 55 | 10 | 2 | 2 | 0.5 | 3 | 0 | 17 | 0 | 4 | 5 | 29 |
| V2 | 54 | 10 | 3 | 3 | 0.6 | 6 | 4 | 8 | 0 | 6 | 3 | 27 |
| V3 | 51 | 7 | 5 | 3 | 1 | 0 | 8 | 17 | 0 | 0 | 8 | 33 |
| V4 | 39 | 8 | 2 | 8 | 0.1 | 0 | 1 | 37 | 0 | 5 | 0 | 43 |
| V5 | 55 | 7 | 3 | 1 | 0.4 | 0 | 12 | 16 | 0 | 0 | 5 | 33 |
| V6 | 60 | 8 | 5 | 0 | 0.7 | 0 | 7 | 16 | 0 | 0 | 4 | 27 |
| W1 | 50 | 2 | 0 | 0 | 0 | 0 | 0 | 45 | 0 | 0 | 2 | 47 |
| W2 | 59 | 2 | 0 | 0 | 0 | 0 | 0 | 33 | 0 | 0 | 3 | 36 |
| W3 | 48 | 0.5 | 0 | 0 | 0 | 0 | 0 | 47 | 0 | 0.4 | 1 | 49 |
| W4 | 58 | 2 | 0 | 0 | 0 | 0 | 0 | 37 | 0 | 2 | 0 | 39 |
| W5 | 58 | 2 | 0 | 0 | 0 | 0 | 0 | 40 | 0 | 0 | 0 | 40 |
| W6 | 67 | 2 | 0 | 0 | 0 | 0 | 0 | 29 | 0 | 0 | 0.9 | 29 |
| W7 | 60 | 3 | 0 | 0 | 0 | 0 | 0 | 35 | 0 | 0 | 0.2 | 35 |
| W8 | 59 | 1 | 0 | 0 | 0 | 0 | 0 | 40 | 0 | 0 | 0 | 40 |
| W9 | 58 | 1 | 0 | 0 | 0 | 0 | 0 | 39 | 0 | 0 | 0 | 39 |
| W10 | 41 | 0 | 0 | 0 | 0 | 0 | 0 | 49 | 0 | 0 | 2 | 51 |
| W11 | 45 | 0 | 0 | 0 | 0 | 0 | 0 | 43 | 0 | 0 | 0 | 43 |

**Clay mineral identification through the $d_{060}$ peak position**

With the $d_{060}$ a distinction can be made between the dioctahedral and trioctahedral clay minerals because of the sensitivity of the b-cell dimension to the size of the cations and the cation occupancy in the octahedral layer. The position of the $d_{060}$ peak for the most common clay minerals is given in Table A1.7. By using an internal standard (zincite, quartz or corundum) the pattern is calibrated on a high intensity peak and the position of the $d_{060}$ reflection can be accurately determined. The $d_{020}$ cannot be used for identification due to the overlap of different clay minerals in this region ($d_{020}$ position for glauconite 4.54 Å, illite 4.51 Å, smectite 4.52-4.64 Å). In addition, close to the $d_{060}$ peak several other (high) intensity peaks can be present.

Table A1.7 Position of the d(060) and 2Θ data for micas and clay minerals (Bailey, 1980).

| Mineral | d(060) (Å) | 2Θ |
|---|---|---|
| Kaolinite | 1.490 | 62.31 |
| Montmorillonite | 1.492-1.5004 | 62.22-61.67 |
| Illite (muscovite) | 1.499 | 61.90 |
| Glauconite | 1.511 | 61.35 |
| Saponite | 1.520 | 60.95 |
| Nontronite | 1.521 | 60.91 |
| hectorite | 1.530 | 60.51 |
| Serpentines | 1.531-1.538 | 60.47-60.16 |
| Biotite | 1.538 | 60.16 |
| Chlorite | 1.538-1.549 | 60.16-59.69 |
| Sepiolite | 1.540-1.550 | 60.07-59.65 |
| Vermiculite | 1.541 | 60.03 |
| Berthierine | 1.555 | 59.44 |
| Palygorskite | 1.560 | 59.23 |

The clay mineral analysis in this work is limited. Clay slides were made and measured of a limited set of samples (Figure A1.5). Quantifying clay mineral mixtures is very challenging, as proven by the Reynoldscup. A detailed clay mineral analysis was performed on four samples by R. Adriaens from Qmineral (Table A1.8).

Table A1.8 Detailed clay analysis performed by R. Adriaens (Qmineral) on the < 2 µm fraction prepared by Jackson treatement and measured on clay slides.

| | D1 | D2 | B2 | V1 |
|---|---|---|---|---|
| Glauconite/Smectite | 87.5 | 69.7 | 62.4 | 28.8 |
| Illite/Smectite | 8.3 | 5.3 | 16.6 | 32.2 |
| Illite | 0.8 | 4.6 | 4.6 | 12.1 |
| Smectite | 2.4 | 15.8 | 11.9 | 17.2 |
| Kaolinite | 1.0 | 2.9 | 4.4 | 6.6 |
| Chlorite | | 1.6 | | 3.1 |
| % Illite in I/S | 71.0 | 71.0 | 71.0 | 71.0 |
| % Glauconite in G/S | 82.4 | 67.3 | 74.6 | 74.1 |

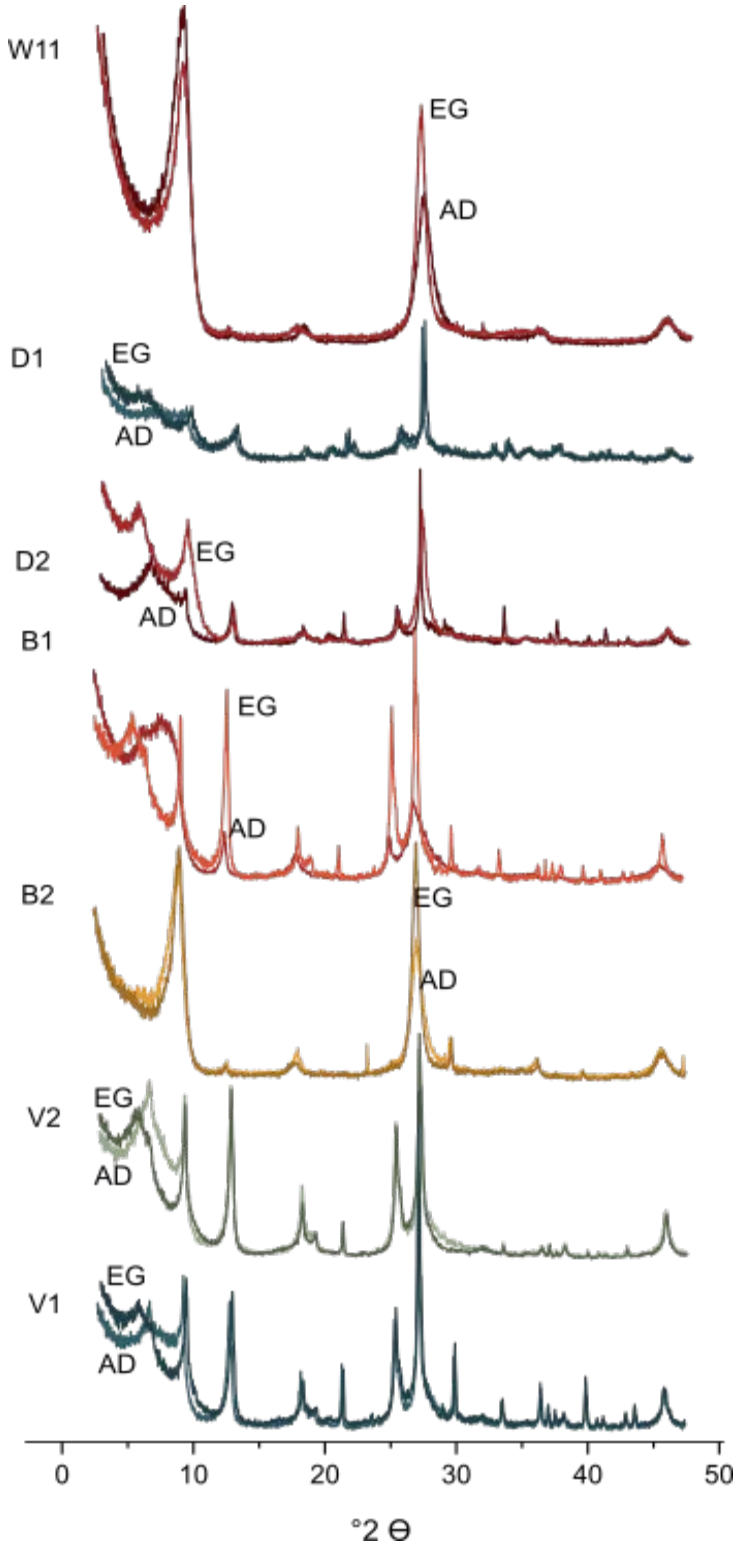


Figure A1.5 XRD patterns of air dried (AD) and ethylene glycolated (EG) clay slides made from the glauconite fraction of seven glauconite sands.

## Cation exchange capacity

The occurrence of glauconite as grains implies that not all cation exchange sites might be (instantly) accessible for the large Co-complex. In a standard CEC determination 1 hour of interaction time is allowed between the sorbent and the cobalt hexamine cation. An additional problem might arise in glauconite samples when exposed to cobalt hexamine for longer times. The increased contact time might allow the Co to exchange some of the Fe.

### Method

The CEC was determined through the cobalt(III) hexamine method on four different fractions; complete glauconite sand (C), the glauconite fraction (GL), the complete milled sand (CM) and the milled glauconite fraction (GLM). The cobalt (Co) complex is a stable trivalent cation that replaces the exchangeable cations on the negatively charged surfaces, i.e. the planar sites. Glauconite sand (1.25 g) was weighed in duplicate into acid-washed 50 mL centrifuge tubes. 25 ml of 0.0166M cobalt(III) hexamine was added to each tube, after which the tubes were placed in an end-over-end shaker. At several time points the samples were centrifuged at 3000 RPM and subsamples of 500 µl were taken from the supernatant. The subsamples were diluted 25 times and acidified with 1% $HNO_3$. The effective CEC is calculated by measuring the remaining concentration in solution after one hour of contact time by inductively coupled plasma spectrometry (Agilent Technologies 7700 Series ICP-MS).

For a subset of samples the CEC was also determined with the copper (II) triethylenetetramine-method (Cu-trien) as described by Dohrmann and Kaufhold (2009). The glauconite sand was weighed in duplicate (2 g) into acid-washed 50 mL centrifuge tubes. The tubes were placed in a horizontal shaker overnight followed by centrifugation. One subsample of the supernatant is measured by ICP analysis (Varian 720-ES ICP-OES, Agilent). A second sample of the supernatant is measured photometrically to determine the CEC by the concentration of the Cu complex in solution (577 nm).

### Results

*Effect of the size fraction*

Table A1.9 Cation exchange capacities (cmolc $kg^{-1}$) after 1h for complete sands (C), complete milled sands (CM), the glauconite fraction (GL) and the milled glauconite fraction (GLM). The error on the CEC is represents the difference between the replicates.* This sample was not performed in duplicate.

| Sample name | C<br>cmolc $kg^{-1}$ | CM<br>cmolc $kg^{-1}$ | GL<br>cmolc $kg^{-1}$ | GLM<br>cmolc $kg^{-1}$ |
|---|---|---|---|---|
| D4 | 6.14 ± 1.52 | 9.46 ± 0.30 | 23.4 ± 4.1 | 27.4 ± 0.23 |
| B1 | 16.9 ± 1.1 | 17.4 ± 0.18 | 15.4 ± 1.4 | 17.2 ± 1.9 |
| D6 | 8.04 * | 12.5 ± 0.13 | 13.7 ± 6.9 | 17.6 ± 1.4 |
| D9 | 3.55 ± 0.87 | 10.4 ± 0.45 | 12.4 ± 9.4 | 20.2* |
| V3 | 10.4 ± 0.63 | 13.8 ± 0.03 | 16.7 ± 5.7 | 26.9 ± 2.2 |
| TM2 | 5.66 ± 0.08 | | | |
| TM3 | 7.31 ± 0.18 | | | |

The results of the cation exchange experiment on the four different fractions for five samples are summarised in Table A1.9. The CEC values are a factor 1.3 to 2.9 higher in the milled complete sands versus the unmilled sample (except for sample B1). Similar ranges are observed for the ratio milled glauconite to unmilled glauconite (1.1 to 1.6).

*Evolution of the CEC in the time – complete sands*

There is clearly an effect of the grain, limiting the access of the cohex cation to the internal cation exchange sites. A second option is to use a longer interaction time between the sample and the cohex solution. In Figure A1.6 the evolution of the CEC with time is given for five samples and a soil reference, Ter Munck 3. Where the CEC does not reach equilibrium for the glauconite sands within 14 days, the CEC remains stable for the TM3 sample (Table A1.10). Leaving the reaction longer makes little sense as it is unclear if the glauconite structure will remain stable. The cohex cation is a large trivalent cation that can cause an expansion of the interlayer and in long term exposure alterations to the structure of glauconite. Using glauconite pellets for the determination of the CEC will give an underestimate. Especially in sorption experiments that run over several months the 1h CEC might not be representative. Therefore it was opted to use milled glauconite CEC data for this work.

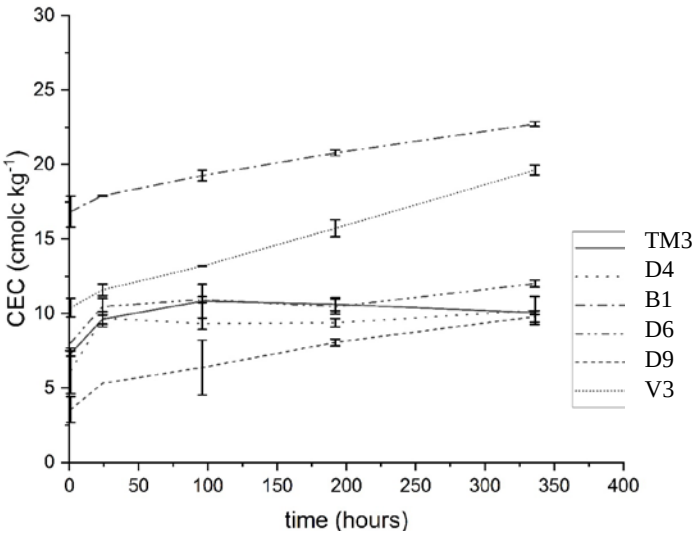


Figure A1.6 Complete glauconite sands (unmilled) versus time (cohex method) for five samples and the Ter Munck 3 reference sample.

Table A1.10 Cation exchange capacities (cmolc $kg^{-1}$) for complete glauconite sands (unmilled) after 1h and 336 hours of interaction with Cohex and the ratio's between the CEC values.

| Sample name | CEC – 1h cmolc $kg^{-1}$ | CEC – 336h cmolc $kg^{-1}$ | Ratio CEC 24/1h | Ratio CEC 336/1h |
|---|---|---|---|---|
| D4 | 6.14 ± 1.52 | 10.2 ± 0.95 | 1.58 | 1.66 |
| B1 | 16.9 ± 1.1 | 22.7 ± 0.15 | 1.06 | 1.35 |
| D6 | 8.04 | 12.0 ± 0.23 | 1.30 | 1.49 |
| D9 | 3.55 ± 0.87 | 9.79 ± 0.38 | 1.50 | 2.76 |
| V3 | 10.4 ± 0.63 | 19.6 ± 0.33 | 1.11 | 1.89 |
| TM2 | 5.66 ± 0.08 | 6.01 ± 0.19 | 1.46 | 1.06 |
| TM3 | 7.31 ± 0.18 | 10.1 ± 0.12 | 1.32 | 1.37 |

*Comparison of the Cu-trien and Co-hexamine method*

The CEC can be measured with several methods. Often each lab has a preferred method. In the lab of the Waste and Disposal group at SCK CEN the copper (II) triethylenetetramine-method is the method of choice ("Cu-trien" method; Meier et al. (1999)). In the lab of the soil and water management group at KU Leuven, the cobalt (III) hexamine method is preferred. The CEC has been determined at both labs. A set of milled complete glauconite sands was measured with both methods. The Co and Cu complexes both have amine groups that show high affinity for the negatively charged sites of the clay minerals. There is a difference in cation size and charge that might affect cation exchange. Recent studies suggest that the methods give comparable results (Frederickx, 2020). The glauconite sand data confirm this hypothesis.

Table A1.11 Comparison of the CEC determination with the Cutrien and Cohex method for a set of complete milled glauconite sands.

| | Cutrien $cmol_c\ kg^{-1}$ | Cohex $cmol_c\ kg^{-1}$ | Ratio Cu/Co |
|---|---|---|---|
| K1 | 2.00 ± 0.13 | 3.60 ± 0.50 | 0.56 |
| D1 | 11.8 ± 0.32 | 10.7 ± 0.22 | 1.10 |
| D3 | 9.50 ± 0.17 | 9.37 ± 0.47 | 1.01 |
| D4 | 9.50 ± 0.74 | 9.46 ± 0.30 | 1.00 |
| D5 | 12.9 ± 0.47 | 12.0 ± 0.13 | 1.08 |
| D6 | 11.9 ± 0.60 | 12.5 ± 0.13 | 0.96 |
| D9 | 8.20 ± 0.01 | 10.4 ± 0.45 | 0.79 |
| B1 | 18.7 ± 0.07 | 17.4 ± 0.18 | 1.07 |
| B2 | 12.3 ± 0.07 | 11.3 ± 0.01 | 1.09 |
| B3 | 12.2 ± 0.50 | 11.0 ± 0.14 | 1.11 |
| V1 | 11.0 ± 0.50 | 7.11 ± 0.70 | 1.55 |
| V3 | 13.8 ± 0.72 | 13.8 ± 0.03 | 1.00 |
| V4 | 13.4 ± 0.05 | 13.0 ± 0.22 | 1.03 |
| V5 | 14.8 ± 0.28 | 15.4 ± 0.71 | 0.96 |
| V6 | 12.9 ± 0.50 | 13.1 ± 0.23 | 0.98 |
| W1 | 13.6 ± 0.91 | 11.3 ± 0.35 | 1.21 |
| W2 | 11.5 ± 1.3 | 9.09 ± 0.90 | 1.26 |
| W4 | 11.9 ± 0.50 | 11.2 ± 0.11 | 1.06 |
| W5 | 11.4 ± 1.16 | 10.4 ± 0.10 | 1.10 |
| W6 | 10.2 ± 0.73 | 8.14 ± 0.05 | 1.25 |
| W7 | 11.1 ± 0.98 | 11.5 ± 0.49 | 0.96 |
| W8 | 9.40 ± 1.55 | 10.9 ± 0.66 | 0.87 |
| W9 | 11.6 ± 1.46 | 14.1 ± 2.20 | 0.82 |
| W10 | 17.2 ± 0.46 | 13.8 ± 0.30 | 1.24 |
| W11 | 13.6 ± 0.90 | 12.3 ± 0.50 | 1.11 |

## A2. Caesium sorption isotherm

### Model fit sensitivity

The model parameters each affect different parts of the sorption isotherm. To assess the sensitivity of the univariate parameters sensitivity an analysis was performed in PhreeqC (Figure A2.1). The modelled $Cs^+$ concentration in solution (equilibrium) is affected by the $K_C$ (Cs/K) for the FES in the region $< 10^{-6.5}$ mol $L^{-1}$, $K_C$ (Cs/K) for the type II between $10^{-8}$ – $10^{-3}$ mol $L^{-1}$ and $K_C$ (Cs/K) in the planar sites $> 10^{-3.5}$ mol $L^{-1}$. The selectivity of the planar sites is not relevant in the investigated concentration domain ($10^{-8}$ – $10^{-4}$ mol $L^{-1}$). Testing the effect of the individual sorption site capacity is more complicated due to the correlation of the fractions by the CEC (Eqn. 6). Five different runs were executed varying the FES (type I) between 0.05-0.25 % of the CEC and the (FES) type II sites between 10-20% of the CEC.

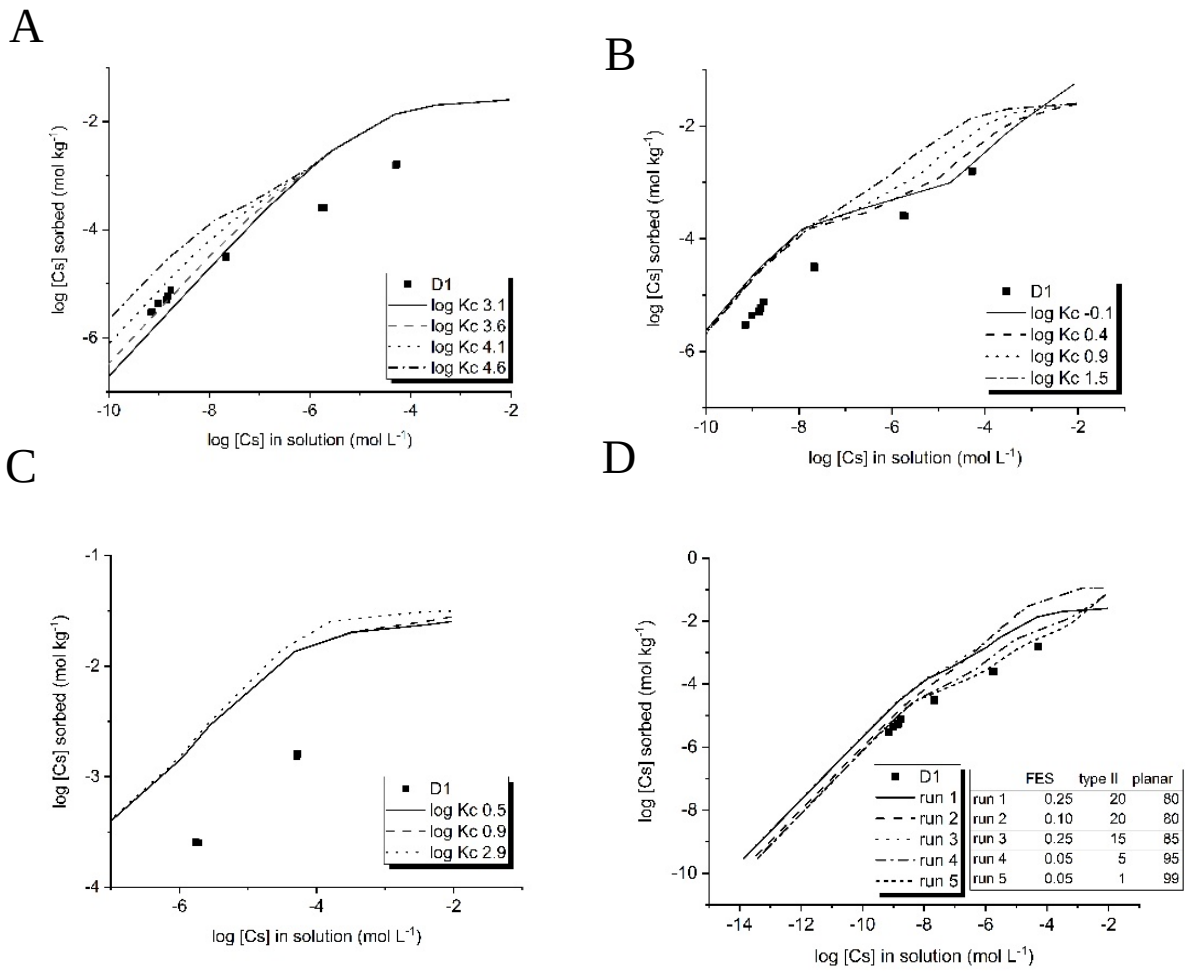


Figure A2.1 Univariate parameter sensitivity analyses of the three-site $Cs^+$ sorption model (Bradbury and Baeyens, 2000) on sample D1 for A) the effect of the Cs-K selectivity coefficient in the FES; (B) the effect of the Cs-K selectivity coefficient in the type II sites; C) the effect of the Cs-K selectivity coefficient in the planar sites; D) the effect of site capacities, i.e. as fractions of the CEC (%) for the FES and for the type II sites.

**Determination of the FES capacity**

The FES capacity can be estimated by the break in the linearity of the sorption isotherm by a method of Bradbury and Baeyens (2000). The break indicates the saturation of the FES-type I and the transition to sorption on the less selective FES-type II sites. The limited amount of data points in the log $10^{-9}$ to $10^{-7.5}$ M [$Cs^+$] in solution reduce the accuracy of the break point determination. Therefore, the two outermost breakpoints were determined to give a FES capacity range (Figure A1.2).

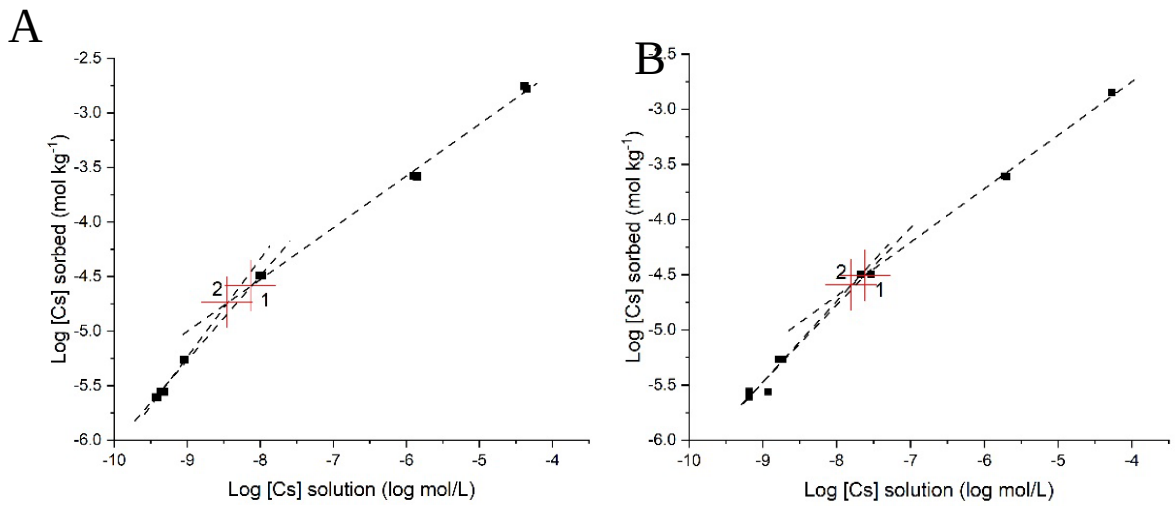


Figure A2.2 FES capacity estimate based on the break in the sorption isotherm for sample B2(A) and D2(B). The limited number of data points in the range of log $10^{-9}$ to $10^{-7.5}$ M [$Cs^+$] in solution doesn't allow an exact determination of the break point. Based on the linear fit of separate sections of the sorption isotherm two break points were determined.

**Caesium-137 versus caesium-133 data**

The $Cs^+$ concentration in solution can be measured by solution concentration of $^{133}Cs$ and $^{137}Cs$ - here done by ICP-MS and solution activity $^{137}Cs$ – here by beta counter. The $Cs^+$ concentration calculated by the activity in solution uses one measurement of the CsCl stock solution ($^{133}Cs$) and the initial activity ($^{137}Cs$) in solution. Most of the literature $Cs^+$ sorption isotherm data on clay minerals is based on the activity in solution. Often an AAS (atomic absorption spectrometry) measurement was used to determine the $^{133}Cs$ concentration in the CsCl stock solution. With these values the activity per unit of concentration can be calculated, and the concentration of $Cs^+$ in solution can be calculated based on the activity measurement. With the current detection limits of the ICP-MS very low $Cs^+$ concentrations can be measured and even active samples can be measured. The total $Cs^+$ concentration in solution was measured initially (before adding sorbent) and after 48 hours.

The $Cs^+$ solution concentrations measured by ICP-MS have a large spread (between the replicates) and are higher than the concentrations calculated from the activity in solution (Figure A2.3). The samples had to be diluted 100 times because of the matrix effect of $Ca^{2+}$ (100 mM). This implies that the samples with the lowest $Cs^+$ concentrations contained a concentration between $10^{-11}$ and $10^{-12}$ M. This range is

still measureable though the error is higher. The relatively small differences between the two datasets lead to large differences in $K_D$ (Table A2.1).

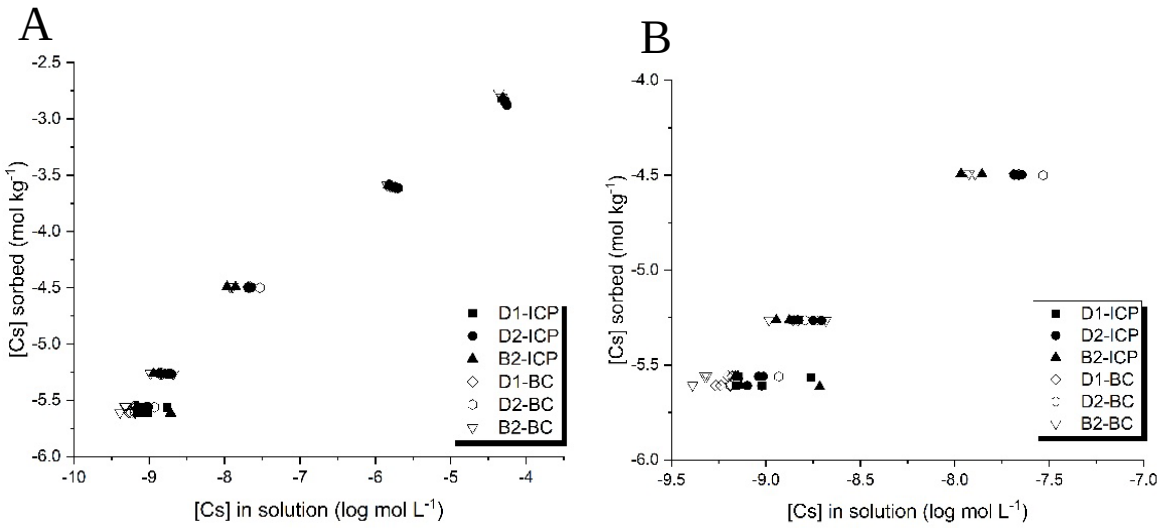


Figure A2.3A Experimental data (after 48 hours) plotted as [$Cs^+$] in solution (log mol $L^{-1}$) versus the [$Cs^+$] sorbed (mol $kg^{-1}$) with the concentrations plotted for the ICP-MS data ($^{133}Cs$) and for the beta counter (BC) data ($^{137}Cs$). Figure B a gives a more detailed section of the low concentration domain.

Table A2.1 $Cs^+$ concentrations in solution after 48 hours measured by ICP-MS and beta counter (calculated based on activity) and the related distribution coefficients.

| $K_D$ | Initial [$Cs^+$] mol $L^{-1}$ | $^{133}Cs$ mol $L^{-1}$ | $^{137}Cs$ mol $L^{-1}$ | $^{133}Cs$ L $kg^{-1}$ | $^{137}Cs$ L $kg^{-1}$ | $^{133}Cs$ log (L $kg^{-1}$) | $^{137}Cs$ log (L $kg^{-1}$) |
|---|---|---|---|---|---|---|---|
| B2 | 8 E-8 | 1.33 E-9 | 5.28 E-10 | 2300 | 4930 | 3.36 | 3.69 |
| | 9 E-8 | 6.99 E-10 | 4.80 E-10 | 3950 | 5770 | 3.60 | 3.76 |
| | 2 E-7 | 1.23 E-9 | 1.56 E-9 | 4450 | 3930 | 3.65 | 3.59 |
| | 1 E-6 | 1.24 E-8 | 1.23 E-8 | 2640 | 2610 | 3.42 | 3.42 |
| | 1 E-5 | 1.54 E-6 | 1.50 E-6 | 166 | 172 | 2.22 | 2.24 |
| | 1 E-4 | 4.95 E-5 | 4.57 E-5 | 31 | 36 | 1.49 | 1.55 |
| D1 | 8 E-8 | 8.24 E-10 | 5.60 E-10 | 3060 | 4410 | 3.49 | 3.64 |
| | 9 E-8 | 1.22 E-9 | 6.47 E-10 | 2720 | 4270 | 3.43 | 3.63 |
| | 2 E-7 | 1.44 E-9 | 1.44 E-9 | 3780 | 3790 | 3.58 | 3.58 |
| | 1 E-6 | 2.12 E-8 | 2.12 E-8 | 1500 | 1500 | 3.18 | 3.18 |
| | 1 E-5 | 1.81 E-6 | 1.77 E-6 | 137 | 141 | 2.14 | 2.15 |
| | 1 E-4 | 5.23 E-5 | 5.01 E-5 | 27 | 30 | 1.44 | 1.48 |
| D2 | 8 E-8 | 8.74 E-10 | 6.50 E-10 | 2830 | 3790 | 3.45 | 3.58 |
| | 9 E-8 | 9.42 E-10 | 9.16 E-10 | 2930 | 3260 | 3.47 | 3.51 |
| | 2 E-7 | 1.87 E-9 | 1.73 E-9 | 2900 | 3160 | 3.46 | 3.50 |
| | 1 E-6 | 2.16 E-8 | 2.52 E-8 | 1480 | 1300 | 3.17 | 3.11 |
| | 1 E-5 | 1.91 E-6 | 1.93 E-6 | 128 | 127 | 2.11 | 2.10 |
| | 1 E-4 | 5.47 E-5 | 5.31 E-5 | 25 | 27 | 1.40 | 1.42 |

### Evaluation of the model in the lower concentration domain

Table A2.2 Testing of the model in the trace $Cs^+$ concentration domain with the assumption that at trace concentration the $K_D$ depends solely on the $K_C$ (Cs/K) and the FES – type I capacity. Comparison of the calculated $K_D$ for the modelled and experimental values for the FES sites type I. The combined $K_D$ was calculated to simulate the effect of both the FES type I and type II sites taking part.

| | D1 | | D2 | | B2 | |
|---|---|---|---|---|---|---|
| | % CEC | $K_D$ (L $kg^{-1}$) | % CEC | $K_D$ (L $kg^{-1}$) | % CEC | $K_D$ (L $kg^{-1}$) |
| Modelled type I | 0.04 | 6180 | 0.06 | 6010 | 0.05 | 7400 |
| Modelled type I + type II | 1.7 | 6250 | 2.3 | 6080 | 1.9 | 7480 |
| Modelled type I + 10 times type II | 17 | 6880 | 22 | 6560 | 19 | 8200 |
| Illite FES-type I | 0.25 | 36800 | 0.25 | 27200 | 0.25 | 37500 |
| Experimental | | 7940 | | 6170 | | 5370 |
| Ratio illite type I to modelled type I | | 5.1 | | 5.9 | | 4.5 |
| Ratio experimental to modelled type I | | 1.1 | | 1.0 | | 0.89 |

The model provides a good fit with the experimental data. The modelled data differ a factor 0.89 to 1.1 from the experimental data (Table A2.2). The most relevant part of the sorption isotherm is in the $Cs^+$ trace concentration range, i.e. the environmentally relevant range. At trace concentration $Cs^+$ it can be assumed that only the FES type I sites take part in the $Cs^+$ sorption reaction (Eqn. 1). The $K_D$ was calculated based on the selectivity coefficients of illite and the modelled results. The original illite model (Bradbury and Baeyens, 2000) uses much higher FES type I capacity (0.25 vs 0.05 % of the CEC) leading to an overestimate of the $K_D$ by a factor 4.5 to 5.1. Even though the type II sites are assumed not to take part in the sorption at trace concentration $Cs^+$, the carrier CsCl in the spike contributed to a $8\times10^{-8}$ M initial $Cs^+$ concentration in solution. However, even if the type II sites take part in the sorption reaction, the effect is rather limited due to the much lower selectivity coefficients (1-1.1% difference). The optimised model predicted significantly lower capacities for the type II sites (1.7-2.2 vs 20 % of the CEC). Though, even at ten times higher type II site capacities the difference in $K_D$ remains limited (8-11 %).

### Evolution of the sorption site availability over time

The $Cs^+$ sorption potential increases with a factor 6-8 between 2 and 30 days (Bruneel et al., 2020). The total site capacity does not necessarily increase, more likely the site availability increases over time. The initial sorption occurring at the edges of the layers, both at type II and FES (type I) sites, and slowly migrating to deeper sorption sites (Figure A2.4). In addition to the microscale changes the density and size of the pores in the pellet limit the migration of $Cs^+$. The sorption isotherm was optimised for the

experimental results at four different time points (2, 7, 28 and 94 days) (Table A2.3). The capacity of the FES (type I) increases with a factor 1.6-2.1, the FES type II sites with a factor 1.4-1.7.

Table A2.3 Results of the optimisation of the three-site model at four different time points (2, 94, 28 and 94 days). The selectivity coefficients values were taken from the illite model (Bradbury and Baeyens, 2000) (log $K_c$ (Cs/K) FES 4.6, log $K_c$ (Cs/K) type II 1.5, log $K_c$ (Cs/K) planar sites 0.5). The represented capacities are the optimised values with the error on the site capacities representing the 95% confidence interval and the RMSE (residual mean squared error) of the log [$Cs_s$].

| | | | 2 d | 7 d | 28 d | 94 d |
|---|---|---|---|---|---|---|
| D1 | FES | CEC % | 0.042 ± 0.009 | 0.059 ± 0.004 | 0.074 ± 0.006 | 0.087 ± 0.008 |
| | Type II | CEC % | 1.7 ± 0.9 | 1.9 ± 0.3 | 2.1 ± 0.4 | 2.3 ± 0.4 |
| | RMSE | | 0.15 | 0.059 | 0.11 | 0.11 |
| D2 | FES | CEC % | 0.055 ± 0.005 | 0.073 ± 0.004 | 0.087 ± 0.006 | 0.10 ± 0.01 |
| | Type II | CEC % | 2.2 ± 0.6 | 2.6 ± 0.3 | 3.2 ± 0.5 | 3.7 ± 0.5 |
| | RMSE | | 0.030 | 0.055 | 0.080 | 0.095 |
| B2 | FES | CEC % | 0.049 ± 0.016 | 0.071 ± 0.003 | 0.064 ± 0.003 | 0.079 ± 0.007 |
| | Type II | CEC % | 1.9 ± 1.4 | 2.0 ± 0.2 | 2.1 ± 0.209 | 2.7 ± 0.4 |
| | RMSE | | 0.31 | 0.025 | 0.036 | 0.12 |

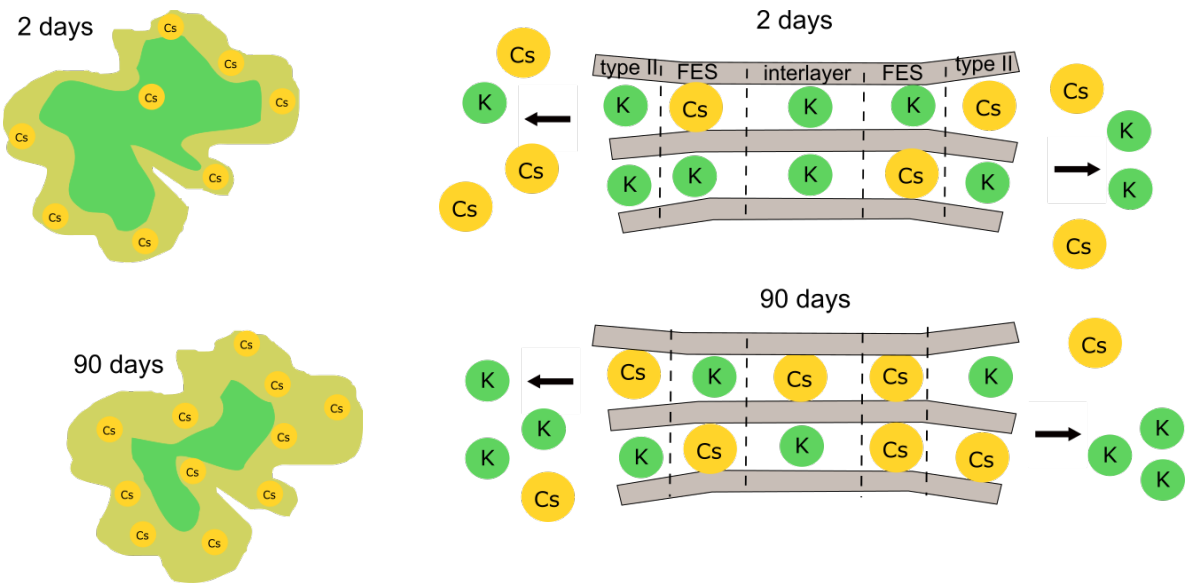


Figure A2.4 Evolution of the site capacity over time at grain level and at the clay platelet. At the level of the grain $Cs^+$ migrates through the pores, limited by diffusion. At the clay layers itself, most of the sorption occurs at the FES sites at first (2 days). $Cs^+$ sorption at the type II sites can block the access to deeper sites. At this time no sorption occurs at the interlayer sites. After 90 days the $Cs^+$ occupancy in both FES and type II sites increases. And a small fraction of the $Cs^+$ can exchange the interlayer $K^+$.

## A3. Caesium column experiments

**Effect of the solid/liquid ratio**

Until now the difference between the applied S/L ratios in the $^{137}Cs$ batch sorption studies (chapter 2 and 3) (0.013 and 0.033 g $mL^{-1}$) and standard sorption tests ($10^{-3}$ g $mL^{-1}$) were assumed to be negligible. Wauters and Cremers (1996) observed no effect on the $K_D$ within a range of 3 orders of magnitude difference in the solid/liquid ratio. Glauconite is present as in large grains (average 125-250 µm) and $Cs^+$ sorption is slower than in standard soils and clay fractions. The large grain size might slow down $Cs^+$ sorption and not all sorption sites are accessible (Bruneel et al., 2020). Using standard solid/liquid ratios of $10^{-3}$ g $mL^{-1}$ is not practical as the grains do not stay in suspension. Using smaller solid fractions (unmilled) will most probably lead to not representative sample sizes. The distribution coefficient ($K_D$) is not a thermodynamical constant, rather an integrated result of various physico-chemical processes. These processes are highly dependent on the characteristics of the solid-liquid phase. The effect of the solid liquid in a range from 0.001 to 0.03 g $L^{-1}$ on the $Cs^+$ sorption $K_D$ was tested in a batch experiment.

*Material and methods*

A batch sorption experiment was set up with sample D1 in five different solid to liquid ratios (1/30, 1/60, 1/80, 1/160 and 1/1000) to study the effect of the solid to liquid ratio on the sorption potential. The amount of solid is constant in all samples to avoid effects of unrepresentative sample size. The glauconite sand was not milled. The samples were pre-equilibrated according to the same procedure as the selectivity and sorption isotherm samples, in a background solution of 0.5 mM $K^+$ (KCl) and 100 mM $Ca^{2+}$ ($Ca_2Cl_2.2H_2O$). The supernatant was labelled with 1.5 kBq $g^{-1}$ radiocaesium, containing 0.0063 µg CsCl carrier. The $^{137}Cs$ activity concentration in solution was measured with liquid scintillation counting.

*Results and discussion*

Figure A2.1 shows the evolution of the sorption potential over time. The difference between the four highest solid/liquid samples is limited to a factor 1.5 after 30 days and 1.3 after 85 days, in the same range as the difference between the duplicates. What stands out are the $K_d$ values of the 1 g to 1000 $mL^{-1}$ samples, they are a factor 1.7 to 2.1 lower than the other S/L ratios. If the solid-liquid ratio varies within a factor 5 there is no significant impact on the sorption potential. This will be of importance when comparing $K_D$ data from the batch sorption experiments on glauconite to literature data on clays. In column experiments and in-situ the solid liquid ratio will be much higher. Wang et al. (2009) find that S/L ratios above 0.25 g $mL^{-1}$ lead to a consistent $K_D$ between batch and column experiments, representative for transport processes in the environment. Below 0.25 the $K_D$ can differ with one order of magnitude. Based on these results we can however expect higher sorption potentials in waste repository environments.

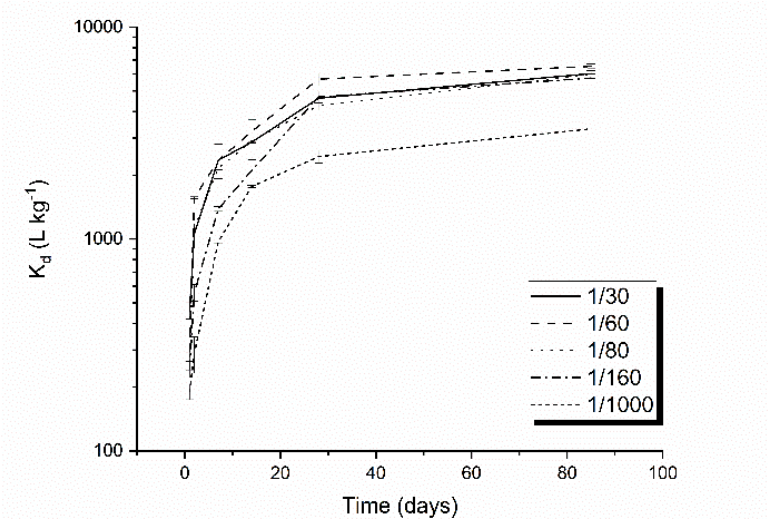


Figure A2.1 Evolution of the sorption potential (L kg$^{-1}$) over time for five different solid/liquid ratios (in g mL$^{-1}$ 1/30, 1/60, 1/80, 1/160 and 1/1000). The error bars represent the difference between the duplicates. If the solid-liquid ratio varies within a factor 5 there is little to no difference between the sorption potentials. Only the extreme 1 to 1000 g mL$^{-1}$ has significantly lower sorption potential at every time step.

**Stop flow**

A stop flow event is used to detect chemical disequilibrium flow. In the case of equilibrium flow, the increased contact time does not affect the shape of the breakthrough curve. In the case of disequilibrium flow, a dip can be expected in the breakthrough curve after restarting the flow.

Stop flow events were performed on four columns (K10A, K10B, K10D and K20A). Column K10D, K10B and K10A (with resp. flow rates 1.2, 1.2 and 1.1 m d$^{-1}$) were stopped for 12 days and after restarting the effluent was collected for four pore volumes (Figure A2.2). In column K20A (2.4 m d$^{-1}$) the flow was suspended twice, for eight and four days with a four day interval.

In K10A the effluent concentration is higher after resuming the flow. In K10B and K20A there is a small decrease. At the onset of the stop flow column K10D was only at the start of the linear concentration increase. Initially the concentration drops back to about background concentration (1.9 10$^{-9}$ M). However, within 4 pore volumes the concentration increased up to 1.4 10$^{-8}$ M. In K20A, after the initial decrease, the concentration increased to 1.4 10$^{-6}$ M, about 1.5 times the inlet $Cs^+$ concentration in four days. After the second stop flow (4 days) [$Cs^+$] reached 1.5 10$^{-6}$ M before decreasing to the inlet solution concentration. The small decreases after resuming the flow could indicate that the prolonged residence time caused an increased adsorption. None of the stop flow events on the columns were performed at exactly the right time, either at saturation or too early.

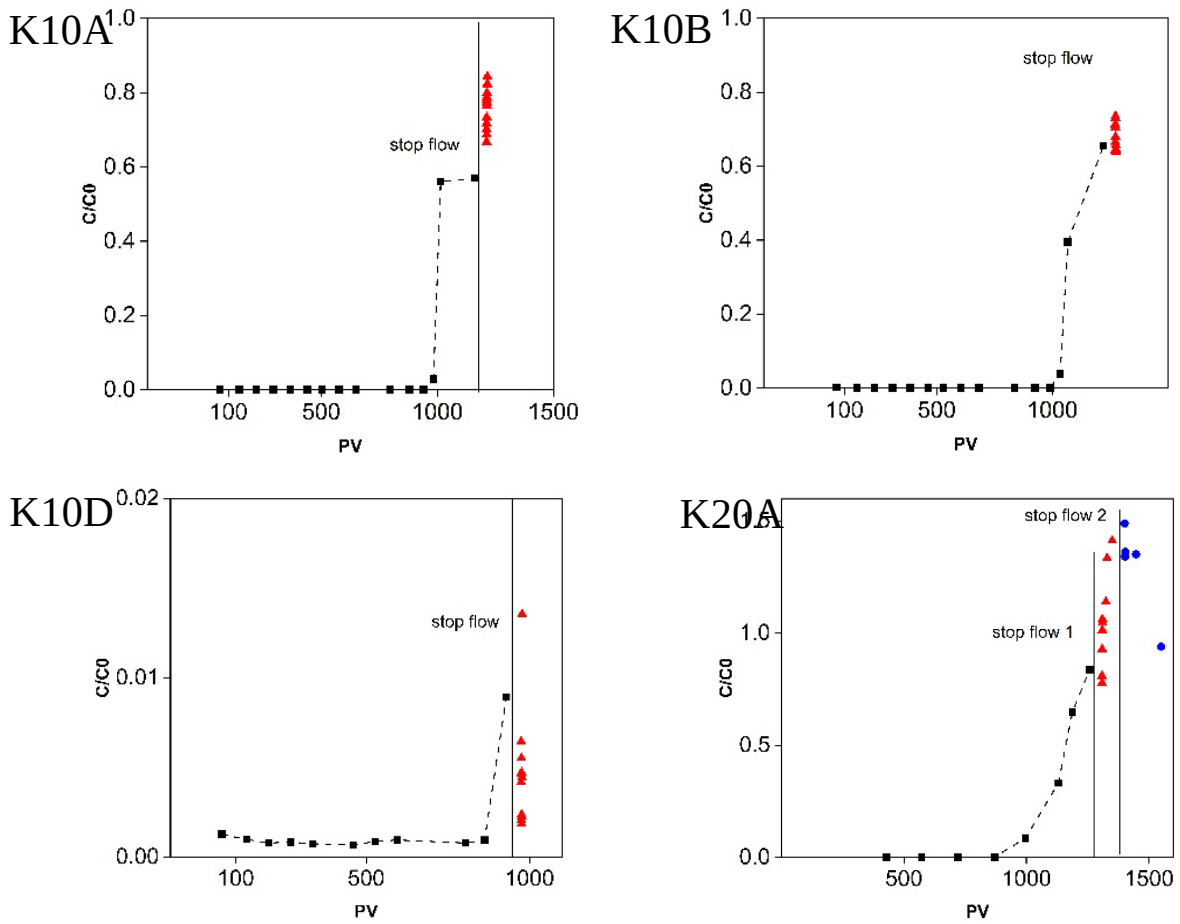


Figure A2.2 Effect of stop flow on the outflow concentration (expressed as fraction of the injected concentration). Columns K10A, K10B and K10D were stopped for 12 days and restarted for 4 pore volumes. K20A had a double stop flow, one of 8 days and one of 4 days.

**The dispersion coefficient**

The $Br^-$ breakthrough curves were fitted in STANMOD (Simunek et al., 1999) to the one-dimensional equilibrium CDE model to obtain the dispersion coefficient (D) in the column (Figure A2.3). The simulated function is optimised by using a nonlinear least-squares inversion method. The modelling input is given in Table 4.2.Table 4.2 Model parameters for a three-site sorption model at 2 days and 94 days interaction time for sample D5 (CEC 12 $cmol_c$ $kg^{-1}$) under the experimental conditions of the column set-up (1 mM KCl, 10 mM $CaCl_2$). The fitting of the equilibrium CDE model corresponds relatively well to the measured breakthrough points ($r^2$ =0.77-0.97). The longitudinal dispersivity (λ) is calculated by the ratio between D and *v* and ranges from 0.31-0.51.

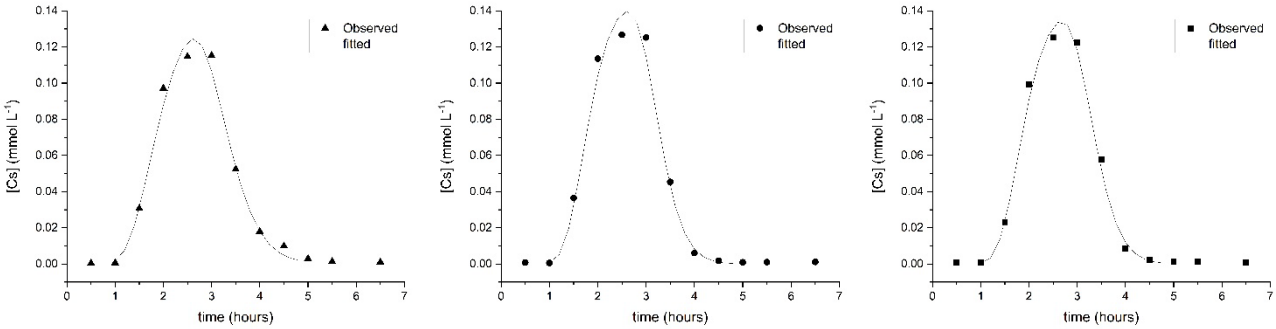


K10A
D $6.36 \times 10^{-3}$ $m^2$ $d^{-1}$
$r^2$ 0.97

K10B
D $3.84 \times 10^{-3}$ $m^2$ $d^{-1}$
$r^2$ 0.86

K10D
D $3.29 \times 10^{-3}$ $m^2$ $d^{-1}$
$r^2$ 0.77

Figure A2.3 Estimates of the dispersion coefficient (D) by the convection-dispersion model (CDE) obtained by least-square fit with STANMOD .

In HYDRUS solute transport is modelled by a combination of convection and dispersion in the liquid phase. One of the solute transport parameters is the dispersivity. The dispersion coefficient (D) ($m^2$ $d^{-1}$) and the dispersivity are linearly related by the pore water velocity (m $d^{-1}$). The dispersivity is therefore constant through the column (Merdun, 2012). By lowering D the number of pore volumes to breakthrough decreases (Figure A2.4). The infliction point of both breakthrough curves remains the same, but the time between the rise in concentration and the breakthrough is shorter.

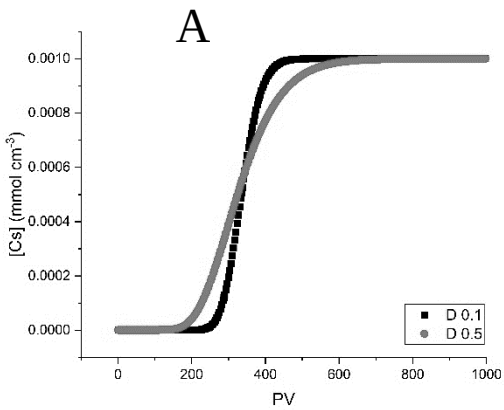


Figure A2.4 A lower dispersion coefficient (D 0.1 vs 0.5 $cm^2$ $h^{-1}$) causes a faster breakthrough and shorter time between rise in the background concentration and breakthrough (modelled with the $K_D$ at 48h in STANMOD).

## A4. Radiostrontium sorption on glauconite sands

### Comparison caesium and strontium sorption

Part of the samples represented in this paper were studied for $^{137}Cs$ sorption (Chapter 2). An overview of the combined $^{137}Cs$ and $^{85}Sr$ sorption data for these 11 samples are given in Table A3.1.

Table A3.1 The $^{137}Cs$ log $K_D$ (L $kg^{-1}$) and $^{85}Sr$ $K_D$ (L $kg^{-1}$) values of the complete glauconite sands (sand) and glauconite fraction (GL) after 35 days, means ± standard deviation of two replicates combined data of chapter 2 and 5.

| Formation | Sample | $^{137}Cs$ sorption log $K_D$ (L $kg^{-1}$) | | $^{85}Sr$ sorption $K_D$ (L $kg^{-1}$) | |
|---|---|---|---|---|---|
| | | Sand | GL | Sand | GL |
| Diest Fm | D1 | 3.46 ± 0.02 | 4.14 ± 0.03 | 51 ± 2.4 | 116 ± 0.7 |
| | D2 | 3.42 ± 0.03 | 4.16 ± 0.03 | 37 ± 11 | 89 ± 0.1 |
| | D3 | 3.36 ± 0.01 | | 35 ± 3.5 | 121 ± 1.2 |
| | D4 | 3.53 ± 0.01 | | 35 ± 0.9 | 131 ± 0.3 |
| | D5 | 3.75 ± 0.03 | | 58 ± 0.1 | 144 ± 3.6 |
| Berchem Fm | B1 | 4.25 ± 0.05 | 4.27 ± 0.01 | 86 ± 2.0 | 100 ± 3.0 |
| | B2 | 3.59 ± 0.01 | | 48 ± 4.1 | 139 ± 0.3 |
| | B3 | | 4.09 ± 0.02 | 33 ± 14 | |
| Voort Fm | V1 | 3.59 ± 0.02 | | 37 ± 7.6 | 126 ± 0.5 |
| | V2 | 3.57 ± 0.03 | | 47 ± 0.6 | |
| | V3 | 3.86 ± 0.01 | 4.26 ± 0.01 | 50 ± 1.1 | 141 ± 0.7 |
| Illite du Puy | Ref | 4.39 ± 0.05 | | 132 ± 3.2 | |
| Boom Clay | Ref | 3.54 ± 0.03 | | 70 ± 2.3 | |

### Welch test

Results of the t-test (Welch test) are given in Table A2.2. The t-test assumes unequal variances between the sample groups of weathered (W1-18) versus natural glauconite sand samples (K1, D1-D16, B1-B4, V1-V6) and the glauconite content, CEC, $Sr^{2+}$ $K_D$, $K_c$ (Sr/Ca), the total Fe content and the $Fe^{2+}$ to $Fe_{tot}$ ratio.

Table A3.2 Test statistics of the t-test (Welch) ) comparing the properties of un-weathered (subsurface) and weathered glauconite sands (Significant correlations in bold, ***p <0.001, ** p <0.01, * p <0.05).

| Categorical variable | Continues variable | Test statistics | Probability p | Degrees of freedom |
|---|---|---|---|---|
| Natural versus weathered | Glauconite content | 1.68 | 0.099 | 61.1 |
| | CEC | -2.82 | **0.0065**** | 59.9 |
| | $Sr^{2+}$ $K_D$ | -1.75 | 0.084 | 85.4 |
| | $K_c$ (Sr/Ca) | -1.55 | 0.13 | 45.7 |
| | Total Fe content | 3.21 | **0.0051**** | 17.3 |
| | $Fe^{2+}$ to $Fe_{tot}$ ratio | -7.11 | **<0.0001***** | 26.9 |

**Optical microscopy**

Optical microscopy of glauconite fractions of subsurface sands show a large variation in grain size, morphology of the glauconite grains and oxidation state. In the surface sands most of the grains are coated with or even fully transformed to iron oxide (Figure A3.1).

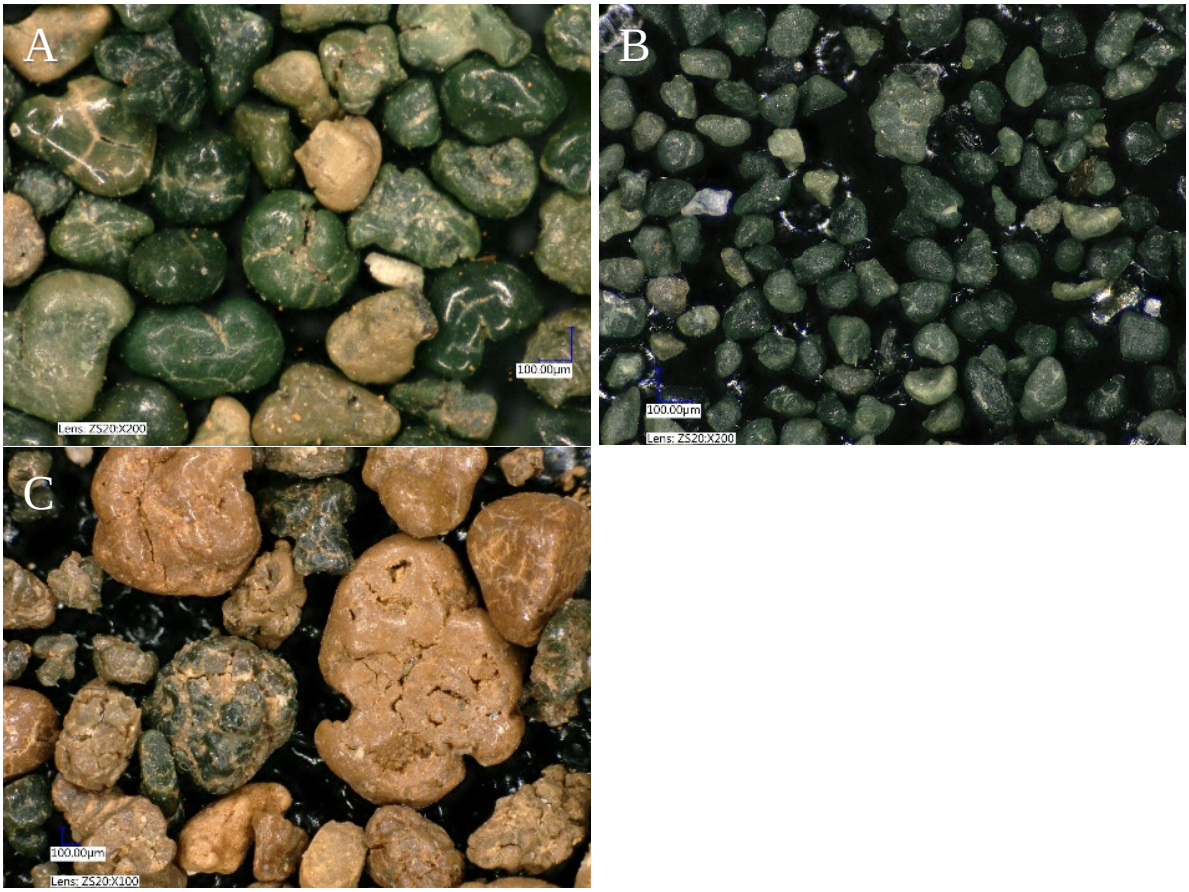


Figure A3.1 Optical microscopy of the glauconite fraction of sample D1,V1, W10, respectively A, B and C.

**XRD patterns**

In Figure A3.2-A XRD patterns of the complete glauconite sand (bulk) are given for eight glauconite sands. The bulk XRD patterns were used to determine for mineral phase identification and quantification of the glauconite, total clay and quartz content. The position of the $d_{060}$ peak was determined on XRD patterns in the 55-65° region (Figure A3.2-B). The sample is mixed with 4 wt% zincite to reduce the offset error. The analysis of the peak was done in X-ray Viewer. It is important to note that the glauconite fraction is the magnetically separated fraction. In this fraction traces of quartz, other micas and quartz might be present. The quality of the separation was checked under the microscope and repeated if necessary.

In addition to the analysis of the complete glauconite sand clay slides were made to determine the clay fraction mineralogy. The results of the quantification are presented in Table A3.3.

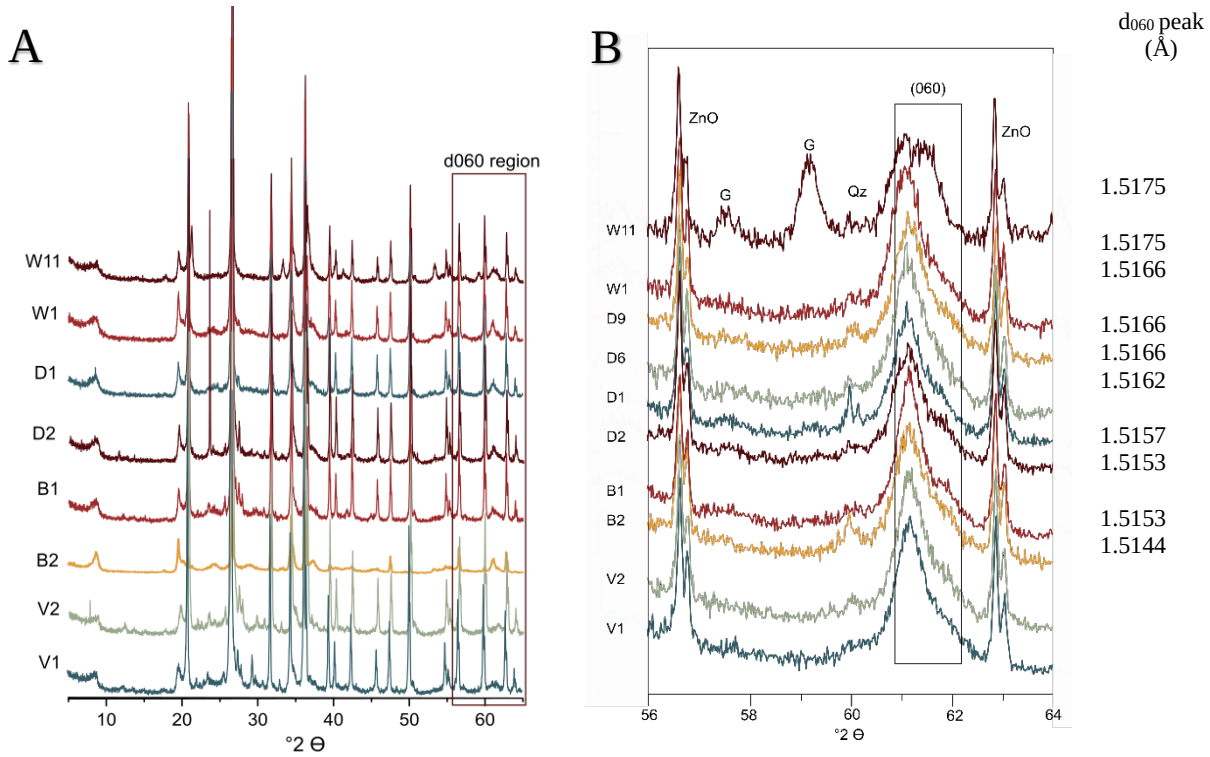


Figure A3.2 A) XRD measurement of the complete glauconite sand. The strong reflections of the quartz fraction mask the clay peaks. B) d060 peak region (56-64° 2Θ ) measured on the glauconite fraction including the $d_{060}$ peak position (Å).

Table A3.3 Extracted clay fraction mineralogy (<2 µm ). The data of sample D8 to D16 were presented in the PhD of Adriaens (2015) with %S representing % of smectite.

| | Glauconite-smectite | | Illite-smectite | | Illite | Smectite | Kaolinite | Chlorite | Fe-vermiculite |
|---|---|---|---|---|---|---|---|---|---|
| | wt % | %S | wt % | %S | wt % | wt% | wt% | wt% | wt% |
| D1 | 88 | 25 | 8 | 29 | 1 | 2 | 1 | 0 | 0 |
| D2 | 70 | 18 | 5 | 29 | 5 | 16 | 3 | 2 | 0 |
| D5 | 11 | 13 | 31 | 30 | 10 | 43 | 4 | 1 | 0 |
| D8 | 34 | 12 | 23 | 29 | 3 | 37 | 2 | 1 | 0 |
| D10 | 23 | 15 | 27 | 28 | 4 | 43 | 2 | 1 | 0 |
| D11 | 16 | 25 | 1 | 33 | 7 | 30 | 7 | 1 | 10 |
| D12 | 30 | 25 | 0 | 36 | 3 | 31 | 3 | 0 | 8 |
| D13 | 69 | 24 | 1 | 35 | 1 | 15 | 1 | 1 | 0 |
| D14 | 93 | 15 | 0 | 34 | 1 | 1 | 1 | 0 | 0 |
| D15 | 85 | 17 | 0 | 34 | 2 | 3 | 2 | 0 | 0 |
| D16 | 85 | 15 | 0 | 34 | 1 | 2 | 1 | 0 | 0 |
| B2 | 62 | 26 | 17 | 29 | 5 | 12 | 4 | 0 | 0 |
| B4 | 29 | 26 | 15 | 30 | 22 | 28 | 5 | 1 | 0 |
| V1 | 29 | 33 | 32 | 29 | 12 | 17 | 7 | 3 | 0 |
| W1 | 92 | 15 | 5 | 33 | 2 | 0 | 1 | 0 | 0 |

In addition to the linear correlations presented in Figure 5.3. Table A3.4 provides the $d_{060}$ values and corresponding expandable layer content for the < 2µm fraction of 11 glauconite samples.

Table A3.4 Positions of the $d_{060}$ peak for 11 glauconite fractions with corresponding CEC values (glauconite fraction), expandable layer content in the glauconite-Smectite and illite-smectite mixed layer and total smectite content. The $d_{060}$ and expandable layer content data of sample D9-D16 were presented in Adriaens (2015).

| | d060 | CEC GL ($cmol_c\ kg^{-1}$) | % Smectite in GL/S and I/S | Total smectite (%) |
|---|---|---|---|---|
| D1 | 1.5166 | 26.9 | 24.6 | 27.0 |
| D2 | 1.5162 | 24.2 | 13.8 | 29.6 |
| D9 | 1.5166 | 33.1 | | |
| D10 | 1.5148 | 33.6 | 11.0 | 54.0 |
| D11 | 1.5190 | 20.7 | 4.3 | 34.3 |
| D12 | 1.5170 | 21.9 | 7.4 | 38.4 |
| D13 | 1.5178 | 23.9 | 16.8 | 31.8 |
| D15 | 1.5178 | 26.0 | 14.1 | 17.1 |
| D16 | 1.5178 | 26.0 | 12.8 | 14.8 |
| B1 | 1.5157 | 24.8 | | |
| B2 | 1.5153 | 33.3 | 21.0 | 32.9 |
| B4 | 1.5144 | 33.1 | 12.2 | 40.2 |
| W1 | 1.5175 | 24.1 | 15.4 | 15.4 |

The CEC and $d_{060}$ reflection are negatively correlated ($R^2$ = 0.57). Suggesting the $d_{060}$ reflection broadens and shifts to lower $d_{060}$-values by weathering. The effect of weathering on the structure is both an increase in the number of expandable layers or smectite interlayers and a decrease of the interlayer $K^+$. This causes an increase in the interlayer width allowing access to larger (hydrated) cations. However, these changes are reflected in the $d_{001}$ reflection, at 15 Å for smectite and 10 Å for illite and glauconite.

The broadening of the $d_{060}$ reflection is not directly influenced by the K-interlayer to hydrated interlayer transition. The $d_{060}$ reflection is sensitive to the size of the cations and to the site occupancy in the octahedral sheet. However, changes in the tetrahedral and octahedral sheet will influence the charge defect and interlayer space and thereby the interlayer $K^+$ content. At this time it was not possible to conduct further mineralogical analysis on the samples to further investigate this observation.

## A5. Accelerated weathering

**Oxidation during storage**

The glauconite sands used in this study were stored for many years before being used and analysed for this study. In the case of glauconite there is often some scepticism about the stability of glauconite during storage. The presence of both $Fe^{2+}$ and $Fe^{3+}$ in the structure of glauconite indicate glauconite is not completely stable under oxic conditions. Some glauconite samples are said to turn from green to bright orange almost overnight when stored under ambient conditions, while other samples remain unaffected. In none of the samples used in this study changes of colour during storage were observed.

The glauconite sands occur in water saturated, anoxic conditions in-situ (in the investigated formations at the site in Mol). After sampling the sands of the excavation of the second shaft to HADES, they were packed in vacuum sealed bags and stored in a freezer. The samples of the cores ON-Dessel-5 and ON-Mol-1, present at the core library (NIRAS/EURIDICE) are just stored in the vacuum bags. When these bags are re-opened for sampling, often bright orange iron deposition or oxidation rings can be seen about 1 cm below the surface (Figure A4.1). This could indicate oxidation of the glauconite, though, more likely the Fe-deposition is the result of evaporation of pore water. The rim with Fe deposition was removed before sampling the cores.

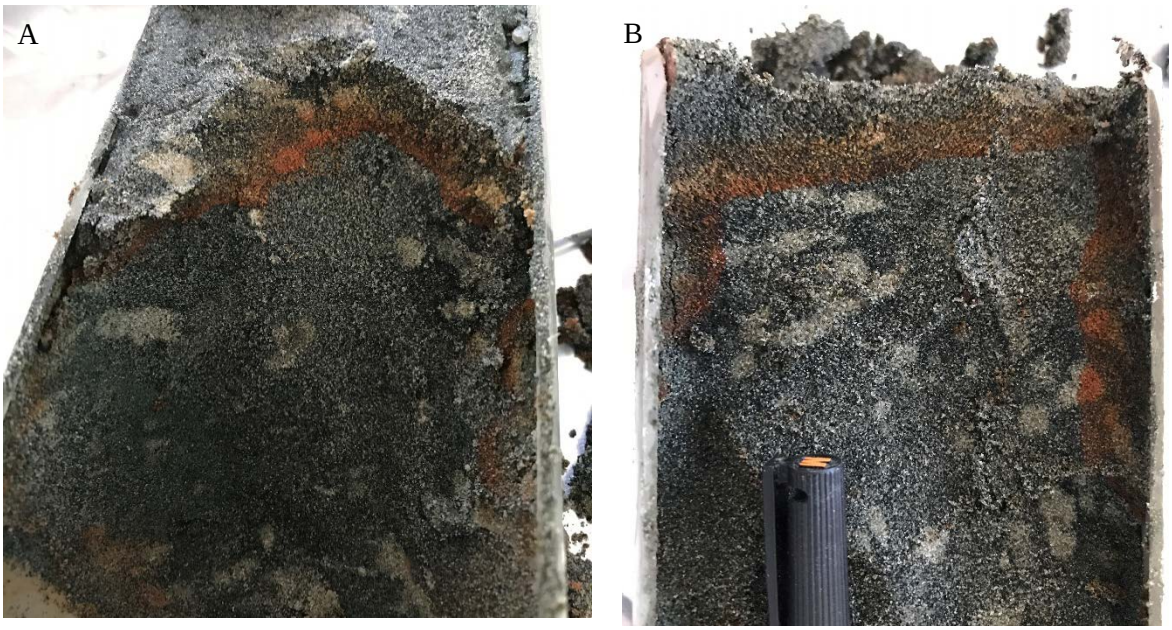


Figure A4.1 Oxidation rim/surface at about 1 cm below the top of the core (A) and surrounding the end of the core (B) in sample D3 core 30 ON-Dessel-5.

For sample D3 and D4 (resp. core 30 and 44 ON-Dessel-5) the iron speciation was determined on a sample of the oxidised rim and a sample of the apparent unaltered centre. The glauconite sands were washed (deionised water) during the sieving and separation of the glauconite fraction. The washing step removed part of the soluble Fe-oxide coating (Figure A4.2). In both samples the $Fe^{2+}$ to $Fe_{tot}$ ratio was

lower in the oxidised samples (0.12-0.15) than compared to the un-oxidised samples (0.24-0.26) (Table A4.1). Also the total iron content decreased from 14.0-14.3 (un-oxidised) to 12.5-12.7 wt % (oxidised). The decrease in $Fe^{2+}/Fe_{tot}$ indicates oxidation during storage. The decrease in total Fe could be related to the formation of iron oxides (top of the core, Figure A4.1). This hypothesis was not verified as the amount of Fe-oxide (including coating) was not quantified.


Figure A4.2 Removal of the Fe-coating with water on a strongly naturally weathered sample (W11) in two washing steps. With A) the unwashed sample, B) after one rinsing and C) after a second washing. The remaining oxidised grains are assumed fully oxidised. In the subsurface glauconite sands there is very little difference before and after washing.

Table A4.1 $Fe^{2+}$ to $Fe_{tot}$ ratios (mean ± error between triplicates) for eight glauconite fractions of un-weathered glauconite sands analysed both in 2017 and 2019, including the storage conditions for the glauconite sands between sampling in 1998 and sample preparation and analysis in 2017.

| Sample | $Fe^{2+}$ to $Fe_{tot}$ ratio | | Ratio 2019/2017 | Storage conditions |
|---|---|---|---|---|
| | Analysis 2017 | Analysis 2019 | | frozen (F)/ vacuum (V) |
| D3 | 0.24 ± 0.07 | 0.14 ± 0.01 | 0.60 | V |
| D4 | 0.26 ± 0.01 | 0.14 ± 0.05 | 0.52 | V |
| D5 | 0.17 ± 0.01 | 0.11 ± 0.03 | 0.63 | V |
| D6 | 0.17 ± 0.02 | 0.14 ± 0.01 | 0.81 | F |
| D9 | 0.15 ± 0.01 | 0.11 ± 0.05 | 0.73 | F |
| B1 | 0.18 ± 0.01 | 0.12 ± 0.03 | 0.65 | V |
| B2 | 0.22 ± 0.01 | 0.13 ± 0.02 | 0.59 | F |
| V3 | 0.15 ± 0.01 | 0.14 ± 0.03 | 0.95 | F |

**Major element analysis**

In Figure A4.3 the changes in the major element compositions of the different conditions are shown. The composition of Al, Fe, Si and Mg remained stable over all treatments. With the exception of the Mg and Si content higher in the untreated sample. The Na and Ca content increased under alkaline conditions (of young cement water), but are most probably attributed to drying in of the cement water. The Si to Al and Al to Fe ratios remained stable over all treatments. These ratios are often used to describe compositional variation in illite and glauconite minerals.

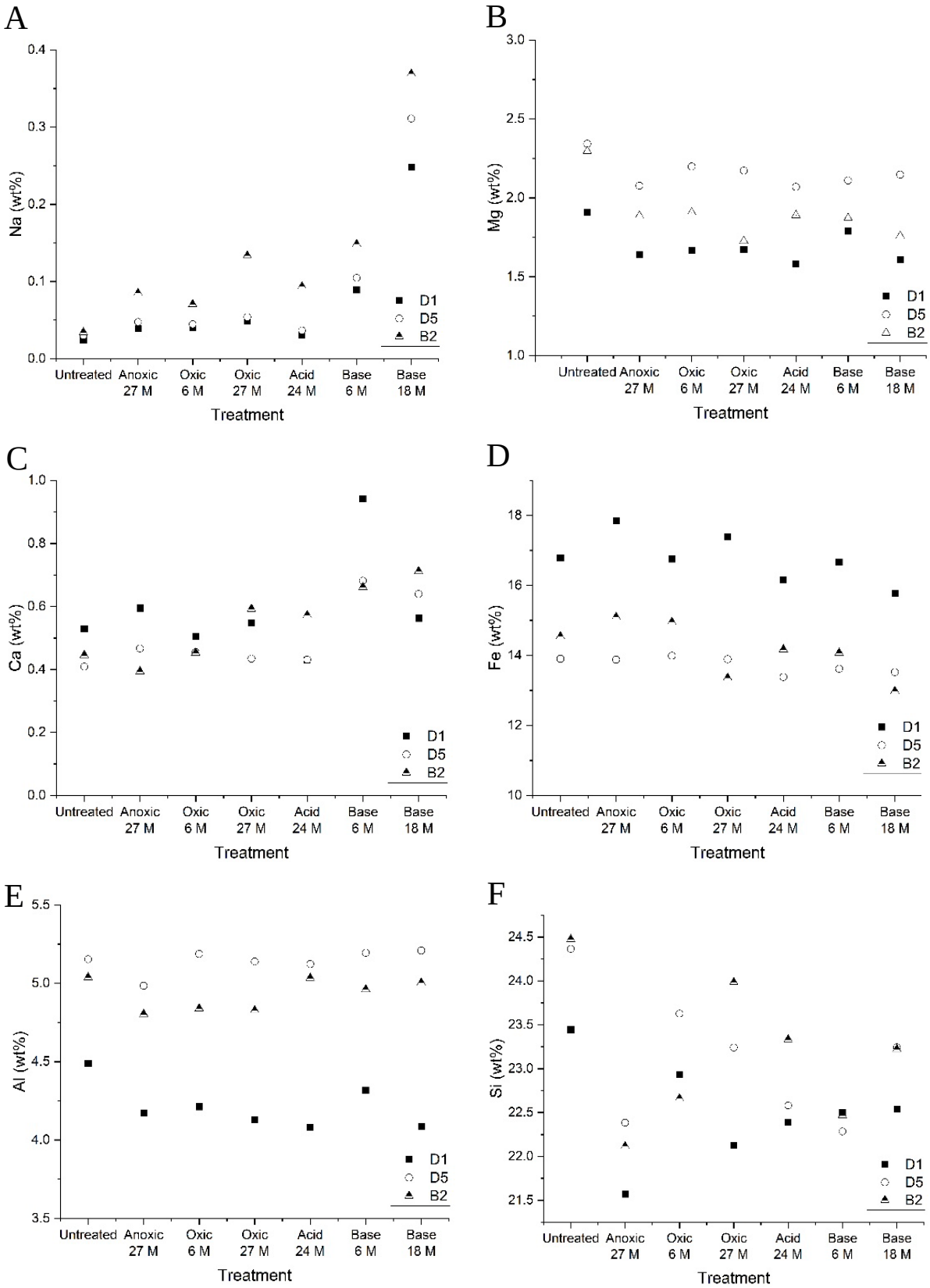
A
Na (wt%)
0.0
0.1
0.2
0.3
0.4
D1
D5
B2
Untreated
Anoxic 27 M
Oxic 6 M
Oxic 27 M
Acid 24 M
Base 6 M
Base 18 M
Treatment
B
Mg (wt%)
1.0
1.5
2.0
2.5
3.0
C
Ca (wt%)
0.0
0.2
0.4
0.6
0.8
1.0
D
Fe (wt%)
10
12
14
16
18
E
Al (wt%)
3.5
4.0
4.5
5.0
5.5
F
Si (wt%)
21.5
22.0
22.5
23.0
23.5
24.0
24.5

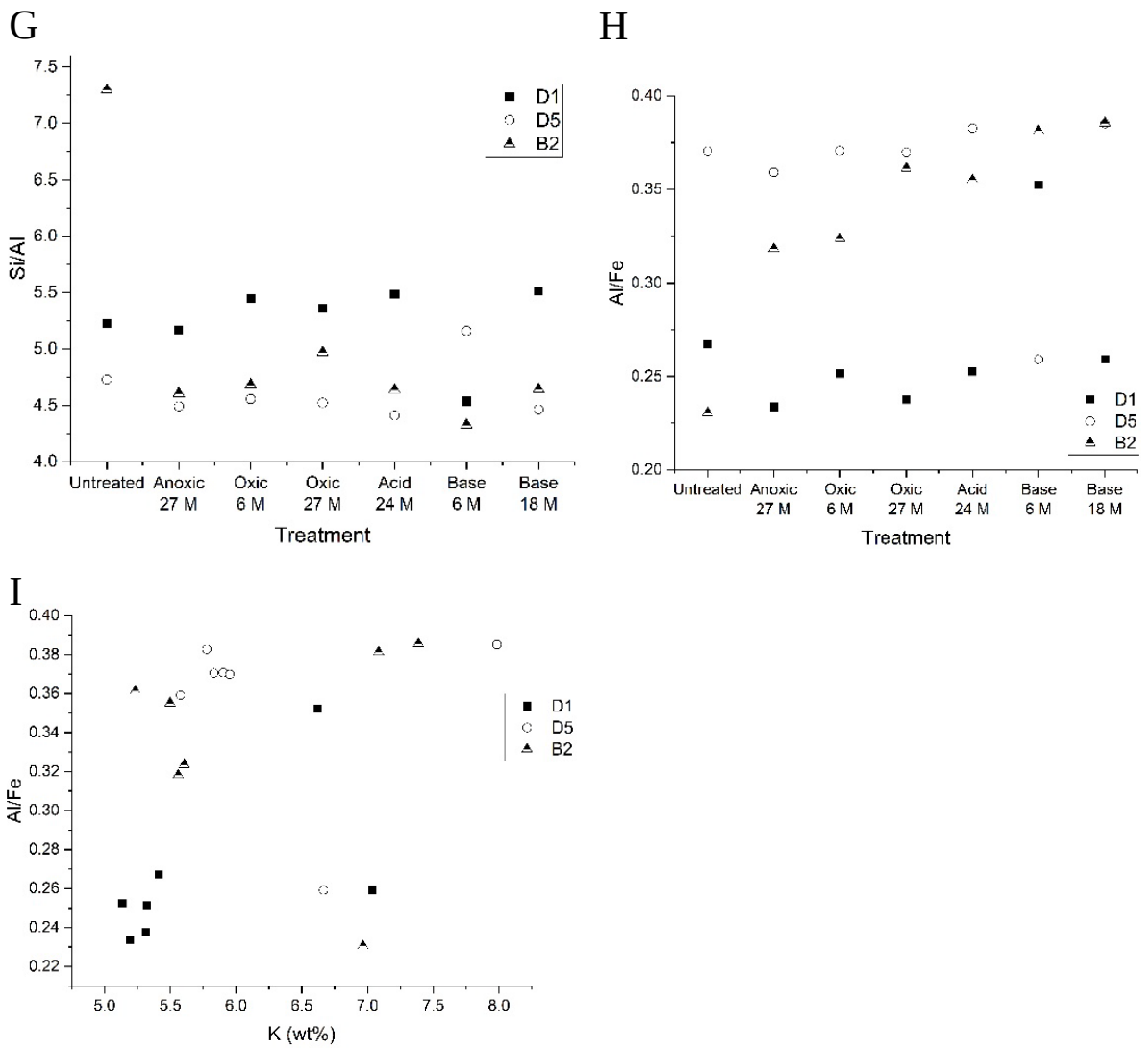


Figure A4.3 Effect of the different conditions (oxic, anoxic, alkaline, acid) on the major element composition of the glauconite fraction after different exposure times. The composition of Al, Fe remained stable over all treatments. The Na and Ca content increased under alkaline conditions (of young cement water), but are most probably attributed to drying in of the cement water. The Si to Al and Al to Fe ratios are often used to describe compositional variation in illite and glauconite minerals. Points are mean values and error bars of replicate analysis are not shown to facilitate reading.

**The effect of artificial weathering on the mineralogy**

Visually and chemically little seems to have changed in the glauconite sands after the artificial weathering in the four different environments. One sample (D1) was selected for additional mineralogical analysis. The glauconite fraction was separated from the sand (magnetical separation) to avoid matrix effects and to eliminate (most) of the high intensity reflections of the quartz fraction. The observations are however very similar. There are no significant differences between the different treatments. The quantification results (measurement and analysis performed by R. Adriaens, Qmineral) are given in Table A4.2. In the XRD pattern little differences can be observed between the samples (Figure A4.4). The main difference is the intensity of the quartz peaks. The higher quartz content in the

Alkaline sample suggests an imperfect separation of the glauconite fraction. Beside the quartz content the mineralogical composition of the sample is nearly identical.

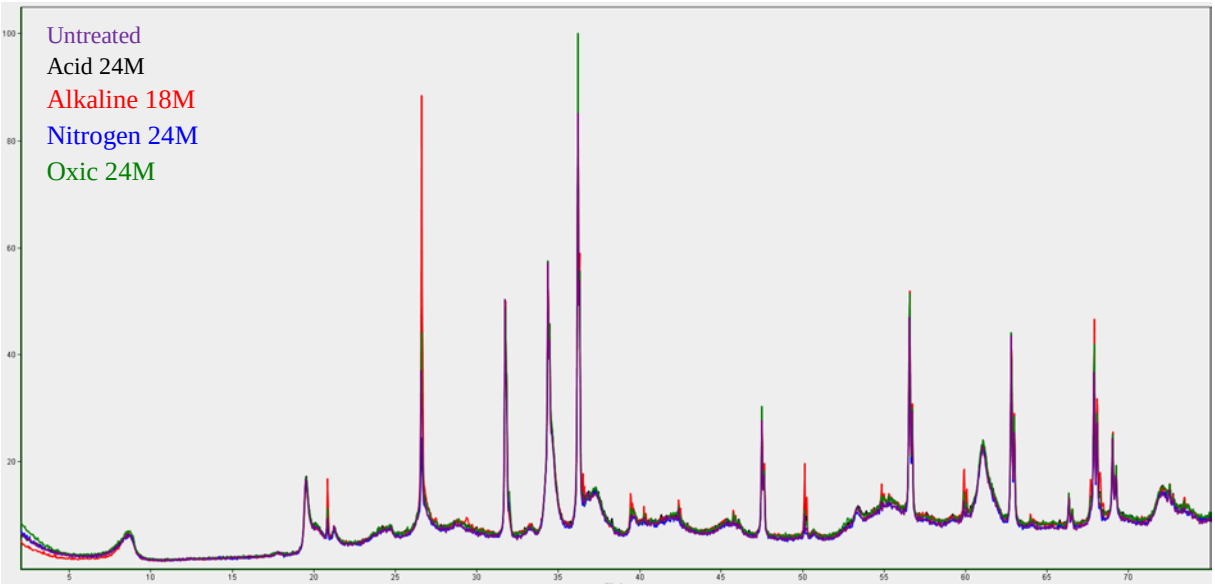


Figure A4.4 XRD pattern of the glauconite fraction of sample D1 after artificial weathering in four different environments (untreated – purple, Acid – black, Alkaline – red, Nitrogen – blue, Oxic – green).

Table A4.2 Mineralogical composition (wt%) of the glauconite fraction of sample D1 after artificial weathering. The composition is very similar for all samples. Imperfect magnetic separation of the glauconite fraction caused the largest differences in composition. To remove the effect of the separation the quartz content is removed and the sample composition is normalised.

| | | Untreated | Oxic | N2 | Alkaline | Acid |
|---|---|---|---|---|---|---|
| | Quartz | 5.5 | 6.2 | 3.3 | 11.8 | 6.9 |
| | Alkali feldspar | 1.0 | 1.1 | 0.5 | 2.0 | 1.1 |
| | Calcite | 0.0 | 0.0 | 0.0 | 1.1 | 0.0 |
| | Siderite | 1.6 | 2.2 | 1.9 | 0.6 | 1.4 |
| | Goethite | 2.9 | 1.8 | 2.1 | 2.2 | 2.3 |
| | Glauconite | 88.8 | 88.6 | 92.1 | 82.2 | 88.2 |
| | Kaolinite | 0.1 | 0.1 | 0.0 | 0.0 | 0.0 |
| | Chlorite | 0.1 | 0.0 | 0.1 | 0.1 | 0.1 |
| Normalised Without Qz | Alkali feldspar | 1.0 | 1.1 | 0.5 | 2.3 | 1.1 |
| | Calcite | 0.0 | 0.0 | 0.0 | 1.2 | 0.0 |
| | Siderite | 1.7 | 2.4 | 1.9 | 0.7 | 1.5 |
| | Goethite | 3.1 | 1.9 | 2.1 | 2.5 | 2.5 |
| | Glauconite | 94.0 | 94.5 | 95.2 | 93.1 | 94.8 |
| | Kaolinite | 0.1 | 0.1 | 0.0 | 0.0 | 0.0 |
| | Chlorite | 0.1 | 0.0 | 0.1 | 0.1 | 0.1 |

**Dunnett's test of individual samples**

The changes in mean glauconite properties (CEC, $K_D$, major element composition and Fe speciation) due to weathering are analysed per sample and treatments. In table A4.2, A4.3 and A4.4 the results of the Dunnett's test (p-values) are given.

Table A4.3 Results of the Dunnett's test for sample D1 with the effect of the treatment on the $K_D$, the CEC, the Fe speciation, the K, Al and Fe content (* $p < 0.05$, ** $p < 0.01$, *** $p < 0.001$).

| | D1 | | | |
|---|---|---|---|---|
| | Base 18 m | Acidic 24 m | Oxic 27 m | Anoxic 27 m |
| CEC | 0.99 | 0.13 | 0.007** | 0.18 |
| Al | <0.0001*** | <0.0001*** | <0.0001*** | <0.0001*** |
| Ca | <0.0001*** | <0.0001*** | <0.0001*** | 0.002** |
| Fe | 0.006 | 0.05 | 0.02* | 0.16 |
| Al/Fe | <0.0001*** | <0.0001*** | <0.0001*** | 0.0001*** |
| K | 0.13 | <0.0001*** | <0.0001*** | <0.0001*** |
| Mg | 0.01* | 0.02* | 0.002** | 0.02* |
| Na | 0.04* | 0.86 | 0.70 | 0.91 |
| Si | 0.004** | 0.08 | 0.03* | 0.001** |
| Si/Al | <0.0001*** | <0.0001*** | <0.0001*** | <0.0001*** |
| $K_D$ 85d | 0.99 | 0.03* | 0.13 | 0.03* |
| $Fe^{2+}$/ $Fe_{tot}$ | 0.022* | 0.032* | 0.99 | 0.0017** |

Table A4.4 Results of the Dunnett's test for sample D5 with the effect of the treatment on the $K_D$, the CEC, the Fe speciation, the K, Al and Fe content (* $p < 0.05$, ** $p < 0.01$, *** $p < 0.001$).

| | D5 | | | |
|---|---|---|---|---|
| | Base 18 m | Acidic 24 m | Oxic 27 m | Anoxic 27 m |
| CEC | 0.34 | 0.90 | 0.68 | 0.99 |
| Al | 1.00 | 0.28 | 1.00 | 0.91 |
| Ca | 0.34 | <0.0001*** | 0.03* | 0.005** |
| Fe | 0.61 | 0.84 | 0.90 | 0.92 |
| Al/Fe | 0.88 | 0.65 | 0.97 | 1.00 |
| K | 1.00 | 0.003** | 0.99 | 0.91 |
| Mg | 0.08 | 0.005** | 0.27 | 0.09 |
| Na | 1.00 | 0.03* | 0.99 | 1.00 |
| Si | 0.0005*** | 0.0003*** | 0.01* | 0.0002*** |
| Si/Al | 0.38 | 0.97 | 0.65 | 0.61 |
| $K_D$ 85d | 0.79 | 0.45 | 0.99 | 0.99 |
| $Fe^{2+}/Fe_{tot}$ 2017 | 0.034* | 0.043* | 0.0185* | 0.043* |
| $Fe^{2+}/Fe_{tot}$ 2019 | 0.64 | 0.39 | 0.78 | 0.007** |

Table A4.5 Results of the Dunnett's test for sample B1 with the effect of the treatment on the $K_D$, the CEC, the Fe speciation, the K, Al and Fe content (* $p < 0.05$, ** $p < 0.01$, *** $p < 0.001$).

| | B1 | | | |
|---|---|---|---|---|
| | Base 18 m | Acidic 24 m | Oxic 27 m | Anoxic 27 m |
| CEC | 0.02* | 0.18 | 0.21 | 0.35 |
| Al | 1.00 | 0.36 | 0.42 | 0.56 |
| Ca | 0.11 | 0.78 | 1.00 | 0.93 |
| Fe | 0.001** | 0.06 | 0.25 | 0.96 |
| Al/Fe | 0.10 | 1.00 | 1.00 | 0.97 |
| K | <0.0001*** | 0.13 | 0.75 | 0.28 |
| Mg | 0.08 | 0.005** | 0.01* | 0.02* |
| Na | 0.0001*** | 1.00 | 0.82 | 0.96 |
| Si | 0.003** | 0.005** | 0.004** | <0.0001*** |
| Si/Al | 0.82 | 0.77 | 0.87 | 1.00 |
| $K_D$ 85d | 0.03* | 0.04* | 0.82 | 0.0.26 |
| $Fe^{2+}/Fe_{tot}$ 2017 | 0.004** | 0.006** | 0.003** | 1.00 |
| $Fe^{2+}/Fe_{tot}$ 2019 | 0.99 | 0.26 | 0.91 | 0.01* |

## List of publications

Bruneel Y, Van Laer L, Brassinnes S, Smolders E. Radiocaesium sorption on natural glauconite sands is unexpectedly as strong as on Boom Clay. Science of the Total Environment. 2020;Vol. 720

Goolaerts, S., De Ceuster, J., Mollen, F.H., Gijsen, B., Bosselaers, M., Lambert, O., Uchman, A., Van Herck, M., Adriaens, R., Houthuys, R., Louwye, S., Bruneel, Y., Elsen, J., Hoedemakers, K., 2020. The upper Miocene Deurne Member of the Diest Formation revisited: unexpected results from the study of a large temporary outcrop near Antwerp International Airport, Belgium. Geologica Belgica 23.

Bruneel Y, Van Laer L, Brassinnes S, Smolders E. Characterisation of the highly selective caesium sorption on glauconite rich sands of contrasting geological formations. Applied Geochemistry. 2021. Vol. 128

Bruneel Y, Van Laer L, Brassinnes S, Smolders E. Radiostrontium sorption on natural glauconite sands of the Neogene-Paleogene formations in Belgium. Journal of Environmental Radioactivity. 2021. Vol. 233

Bruneel Y, Van Laer L, Brassinnes S, Smolders E. Glauconite sands are effective caesium barriers at environmentally relevant water flow rates. Applied Geochemistry.
- **Submitted**